Management thermique d'un module de batteries pour véhicules électriques : modélisation et expérimentation

Khalid Ziat

Normandie Université

THÈSE

Pour obtenir le diplôme de doctorat

Spécialité MECANIQUE DES FLUIDES, ENERGETIQUE, THERMIQUE, COMBUSTION, ACOUSTIQUE

Préparée au sein de l'Université de Caen Normandie

Thermal management of a battery pack for electric vehicles: numerical modelling and experimentation

Présentée et soutenue par
KHALID ZIAT

Thèse soutenue le 08/12/2021 devant le jury composé de		
M. BERTRAND GARNIER	Chargé de recherche HDR, Université de Nantes	Rapporteur du jury
M. NASSIM RIZOUG	Maître de conférences HDR, EC SUP TECH AERON AUTOM LAVAL	Rapporteur du jury
M. HAMID GUALOUS	Professeur des universités, Université Caen Normandie	Membre du jury
M. RACHID OUTBIB	Professeur des universités, Université Aix Marseille 1 Provence	Président du jury
MME HASNA LOUAHLIA	Professeur des universités, Université Caen Normandie	Directeur de thèse
M. PIERRE SCHAETZEL	Professeur émérite, Université Caen Normandie	Co-directeur de thèse

Thèse dirigée par HASNA LOUAHLIA et PIERRE SCHAETZEL, Laboratoire universitaire des sciences appliquées de cherbourg (Caen)

UNIVERSITÉ CAEN NORMANDIE

ED 591 PSIME

LUSAC

Résumé

L’objectif de ce mémoire est d’étudier le comportement thermique d’une batterie Li-ion pour différents courants de charge et de décharge afin de dimensionner un système de refroidissement passif, efficace lors d’utilisation dans un module de plusieurs batteries. Notre étude est basée sur une analyse expérimentale et une modélisation numérique. Un banc d’essais qui permet de charger et de décharger les batteries à courant constant a été installé. Une batterie Li-ion de capacité 60 Ah et d’une forme prismatique a été testée pour des courants de charge allant de 40 A à 60 A et des courants de décharge allant de 40 A à 100 A.

L’étude expérimentale effectuée sur une batterie a permis de conclure que la température mesurée au niveau de l'électrode positive est la plus représentative de la température au cœur de la batterie. Durant des cycles de charge et de décharge consécutifs, deux régimes thermiques sont observés : Un régime transitoire et un régime quasi-stationnaire. Des fluctuations périodiques d’une forme ‘V’ sont obtenues en régime quasi-stationnaire causées par des réversibilités thermiques. Une différence d'environ 3 °C est observée entre la température mesurée à la surface de la batterie et celle au cœur de la batterie. Des expérimentations ont été conduites afin de mesurer les coefficients d’échange thermique à la surface de la batterie, les coefficients d’entropie thermique, les flux réversibles et irréversibles ainsi que l’accumulation de chaleur au cours des phases de charge et de décharge. Des corrélations sont proposées en se basant sur les mesures expérimentales. Elles ont été introduites dans le modèle numérique afin de remonter à la distribution de la température et des flux au cœur de la batterie.

Le modèle numérique développé permet la détermination de la température en tout point de la batterie. L’équation de la chaleur tridimensionnelle en régime transitoire est résolue en utilisant la méthode implicite de direction alternée. Les paramètres thermiques et électriques des batteries sont déterminés expérimentalement et analytiquement. En effet, des mesures sont effectuées afin de déterminer la résistance électrique de la batterie durant la charge et la décharge ainsi que le coefficient d’entropie thermique. Ces mesures permettent la détermination du terme source de l’équation de la chaleur.

Deux corrélations sont proposées en se basant sur les résultats numériques pour prédire l’augmentation maximale de la température ainsi que de l’énergie thermique générée par la batterie

quelque soient les courants de charge et de décharge. Une validation est effectuée pour les corrélations suggérées avec les mesures expérimentales. Une erreur absolue moyenne maximale inférieure à 15% est obtenue sur la prédiction de l'augmentation maximale de la température tandis que l'erreur absolue moyenne maximale sur l'estimation de la génération d'énergie thermique est d'environ 9%. Les résultats de cette modélisation fine ont conduit au développement d'un deuxième modèle numérique utilisant la méthode à constantes localisées et qui simplifie le problème physique. Ce deuxième modèle permet la modélisation d'un module de plusieurs batteries sollicitées à des courants constants et dynamiques. Ce modèle a la particularité d'intégrer l'aspect refroidissement passif et définir sa capacité en fonction des puissances sollicitées. Ce deuxième modèle est validé en comparant les mesures à des résultats expérimentaux.

Enfin, un nouveau banc de test Chroma 17020 a été installé pour tester expérimentalement un module de plusieurs batteries sollicité à des courants dynamiques déterminés à partir des cycles véhicules. Les résultats expérimentaux sont comparés aux résultats prédits par le modèle proposé. Des solutions de refroidissement utilisant un matériau de changement de phase microencapsulé INERTEK 32 sont étudiées. Les résultats expérimentaux montrent une diminution de la température d'ordre de 5.9% pour un module de trois batteries combinées avec l'INERTEK 32. La masse du MCP présente dans ce cas 4.2% de la masse totale des batteries. Finalement, Le modèle développé est utilisé pour étudier l'efficacité du MCP combiné avec des modules des batteries dimensionner pour trois voitures différentes. Trois cycles de courant dynamiques (WLTC, US06 et JAP15) ont été appliqués. La masse de MCP utilisée pour chaque cas est déterminée à partir des corrélations développées pour assurer la dissipation de la chaleur produite par les modules des batteries. Les résultats numériques montrent que la diminution de la température peut atteindre 6.6% pour une masse de MCP équivalente à 4% de la masse des batteries dans certain cas.

Mots clés : Courant constant/dynamique, batterie, modèle thermique, refroidissement passif, MCP.

Abstract

The objective of this thesis is to study the thermal behavior of a Li-ion battery for different charge and discharge currents to size a passive cooling system using phase change materials (PCM) and to verify its efficiency when used with a pack of several batteries. Our study is based on an experimental and a numerical study. A test bench is implemented to charge and discharge the batteries at constant current. A prismatic Li-ion battery with a capacity of 60 Ah was tested for charge currents ranging between 40 A and 60 A and discharge currents varying from 40 A to 100 A.

The experimental study conducted on a battery show that the temperature measured on the positive electrode is the most representative of the battery core temperature. During consecutive charge and discharge cycles, two thermal regimes are observed. Periodic 'V' shaped fluctuations are obtained in the quasi-stationary regime due to the reversible heat. A difference of about 3 °C is observed between the temperature measured at the surface of the battery and the temperature of the active material. This confirms that the battery surface temperature measurements are not sufficient for efficient battery thermal management. In addition, the temperature and heat flux density measurements allowed the determination of the heat transfer coefficients as well as the entropic thermal coefficient which were introduced in the proposed numerical model.

The numerical study led to the development of a three-dimensional model. This model allows the determination of the temperature in all points of the battery. The three-dimensional transient heat transfer equation is solved using the implicit alternating direction method. The thermal and electrical parameters of the battery are determined experimentally and analytically. Indeed, two correlations are proposed based on the numerical results to predict the maximum temperature rise as well as the thermal energy generated by the battery for given charge and discharge currents. A validation is performed for the suggested correlations with experimental measurements. A maximum mean absolute error less than 15% is obtained for the maximum temperature increase while the maximum mean absolute error for the thermal energy generation is about 9%. Furthermore, a second numerical model is proposed using equivalent thermal networks which simplifies the physical problem. The second model allows the modeling of a pack of several batteries tested under constant and dynamic currents. The developed models are validated with experimental results.

Finally, a new Chroma 17020 test bench has been installed to experimentally test a battery pack at dynamic currents determined from the normalized driving cycles. The experimental results are compared to the results predicted by the proposed model. Cooling solutions using an INERTEK 32 microencapsulated phase change material are also studied. The experimental results show a temperature decrease of about 5.9% for a pack of three batteries combined with INERTEK 32. The mass of the PCM in this case is 4.2% of the total mass of the batteries. Finally, the developed model is used to study the efficiency of the PCM combined with battery packs sized for three different cars. Three dynamic current cycles (WLTC, US06 and JAP15) were applied. The mass of PCM used for each case is determined from the developed correlations to ensure the dissipation of the heat produced by the batteries. The numerical results show that the temperature decrease can reach 6.6% for a PCM mass equivalent to 4% of the battery mass in some cases.

Keywords: Constant/dynamics current, battery, thermal model, passive cooling, PCM

Acknowledgments

I would like to thank the persons who, via their help and their support, contributed to this work.

First, I thank Prof. Hamid GUALOUS, the director of the LUSAC, for welcoming me in the laboratory and for placing his trust in me.

I would like to express my sincere gratefulness to my supervisor, Prof. Hasna LOUALIA., for providing guidance and feedback throughout this project. Thanks to her advice, experience and availability, she followed up every progress step in my work and supported me along these three years. I would like to thank also my co-supervisor Prof. Pierre SCHAETZEL for his contribution in this work.

I would like to express my gratitude to Dr. Nassim RIZOUG and Dr. Bertrand GARNIER for accepting to review this work. I thank also Prof. Rachid OUTBIB for examining this work.

I would like to express my gratitude to all the staff of the LUSAC and the IUT of Saint-Lô for their kindness and their generosity. Many thanks to Ms. Adeline OZENNE who made this work less tough.

I offer my warm thanks to the actual and former members of the LUSAC laboratory in Saint-Lô. Dear fellow lab mates, you were awesome! Thanks for the fun-time we spent together, for your supportive and pertinent comments.

Finally, I dedicate this part to thank my parents Ahmad and Chafika, my brothers Hicham, Yassir and Oussama and all my family members especially my aunts Fatima and Rhimou who had trusted and supported me and for all their love and encouragement. I want also to express my unconditional love to my niece and nephews Rim, Rayan and Siraj.

Table of contents

List of figures

List of tables

Nomenclature

Latin symbols		
Symbols	**Denominations**	**Units**
$\dot{Q}$	Heat flux	W
a	Acceleration	m/s²
C	Capacity	Ah
C_g	Rolling coefficient	-
C_p	Specific heat capacity	J/ (kg. K)
C-rates	Current rates	A
C_x	Drag coefficient	-
EOC	End of charge	-
EOD	End of discharge	-
g	Gravity	m/s²
h	Heat transfer coefficient	W/ (m². K)
I	Current	A
L	Latent heat	J/kg
M	Mass	kg
Q	Heat Energy	J
R	Internal resistance	Ω
S	Area	m²
SOC	State of charge	%
SOH	State of health	%
T	Temperature	°C, K
U_{oc}	Open circuit voltage	V
V	Voltage	V
Greek symbols		
Symbols	**Denominations**	**Units**
η	Efficiency	-
λ	Thermal conductivity	W/ (m. K)
ρ	Density	kg/m^3
Φ	Heat density	W/m²
Subscripts		
Symbols	**Denominations**	
amb	Ambient	
bat	Battery	
cond, cv, rad	Conductive, Convective and Radiative	
eq	Equivalent	
gen	Generated	
max and min	Maximum and minimum	
rev, irrev	Reversible, irreversible	

General introduction

The distribution of world energy consumption shows that transportation is one of the most energy-intensive sectors. 24% of global CO_2 emissions originate from fuels combustion provided by the transport sector in 2019, according to the international energy agency [1]. In France, 31% of greenhouse gas emissions are provided by the transport sector of which 53% of this amount is emitted by vehicles in 2020, as declared by the Climate High Council [2]. The electrification of vehicles is an efficient alternative in progress to reduce the use of fossil fuels in transportation. In addition, the storage system of an electric vehicle must have high energy density to offer high driving autonomy, and also high specific power to provide or recover the power necessary for acceleration or braking respectively. Furthermore, safety, cost and lifetime are important factors to consider when choosing an energy storage system.

Many devices are proposed to be used as an energy source in electric vehicles like flywheels, capacitors, fuel cells, and batteries [3]. Lithium-ion batteries have shown their high efficiency, especially in the transport sector and power supply systems which include grid-connected as well as off-grid systems [4]. This type of battery has a high specific energy, high voltage, and low self-discharge rate and can be used in electric vehicles as a primary energy source, such as in Nissan Leaf and Mitsubishi iMiev [5]. In addition, according to ADEME [6], electric vehicles count 6.72% of France vehicles market comparing to hybrid vehicles which present 14.7%. Indeed, the progress of the electric automobile sector requires the enhancement of Li-ion batteries lifecycles and safety performances. Generally, a high amount of heat is generated inside the battery during operating time causing an increase in battery temperature. In some cases, a non-controllable battery thermal behavior may lead to a thermal runaway [7]. Moreover, The Li-ion battery aging depends not only on the internal composition of the battery but also on applied current and climate conditions. The thermal management of batteries requires a cooling system adapted to the application to avoid thermal runaway and degradation of battery performance. This work is carried out in the heat transfer and energy efficiency team of the LUSAC laboratory, aiming to perform a thermal characterization to Li-ion battery enabling the design of a passive cooling system. This thesis comprises four main chapters:

- The first chapter is a literature review on Li-ion batteries modeling approaches based on either numerical methods or equivalent thermal networks. A summary of different passive and active cooling systems is also discussed.
- The second chapter details an experimental study on a 60 Ah prismatic Li-ion battery. A description of experimental setup and an investigation of the current rates effects on battery thermal behavior are performed.
- The third chapter presents a 3D numerical model. The thermal parameters are experimentally measured and a description of measurements methods is presented. Moreover, the proposed model accuracy is validated with the experimental results.
- The fourth chapter investigates experimentally and numerically the thermal behavior of a Li-ion battery pack. A simplified model based on equivalent thermal networks is developed and validated. Furthermore, dynamic current profiles are applied to simulate real use conditions of electric vehicles. Finally, an application of a cooling system using phase change material (PCM) is performed.

Chapter I. Li-ion battery thermal management systems: state of the art

I.1 Introduction

Over the years, studies have proven the significant effect of pollution caused by the consumption of fossil fuels in the transport sector, and its negative influence due to the release of toxic substances such as carbon dioxide (CO_2) and carbon monoxide (CO). In addition, the conventional vehicle consumes about 15% of the fuel's total energy during combustion. Most of this energy is transformed to heat, which contributes directly to global warming[2]. The climate change effects are irreversible. For this reason, many alternatives are in progress and researchers are developing new technologies which enable ensuring the economic development with no greenhouse gases emissions.

The internal combustion engines (ICE) used in conventional vehicles are either combined or fully replaced by electrical motors. The research and development on the field of electric vehicles (EVs) is supported in many countries in the world and industries such as Renault and Tesla. Three main types of recent commercialized vehicles are shown in Figure I.1. The hybrid electric vehicles (HEVs) and the plug-in hybrid electric vehicles (PHEVs) which are both composed of an internal combustion engine and an electric motor. The main difference is that the HEVs recovers the energy from the braking systems and store it in the battery pack while the PHEVs could be additionally charged via an external charger. Moreover, the battery electric vehicles (BEVs) has only an electric motor [3].

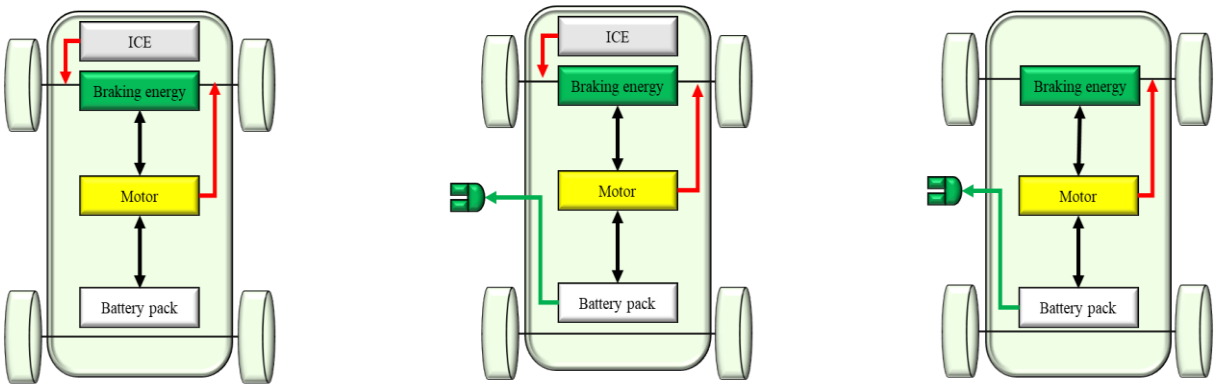

(a) (b) (c)

Figure I.1 Schematic diagram of main components of (a) hybrid electric vehicles (HEVs) (b) plug-in hybrid vehicles (PHEVs) (c) battery electric vehicles (BEVs).

Electric vehicles are equipped with Li-ion batteries which are of great interest, as they have long life cycle, low self-discharge rate, high capacity and are environmentally friendly. Despite these advantages, there are several risks concerning the use of batteries. For instance, they are not considered totally safe due to the problem of the heat production during operating time [4]. Many parameters are used to characterize the batteries as summarized in Figure I.2. The battery capacity, energy and power are the parameters identifying the amount of energy stored inside the battery while the state of charge (SOC) and the depth of discharge (DOD) are the parameters characterizing the left time during a cycle. The battery is fully charged when the SOC is equal to 1 and fully discharged when the SOC is equal to 0. Moreover, the internal resistance and the open circuit voltage are electrical parameters of the battery and depends on the materials used in the cathode and anode electrodes. Finally, the state of health (SOH) is a parameter which characterizes the battery aging.

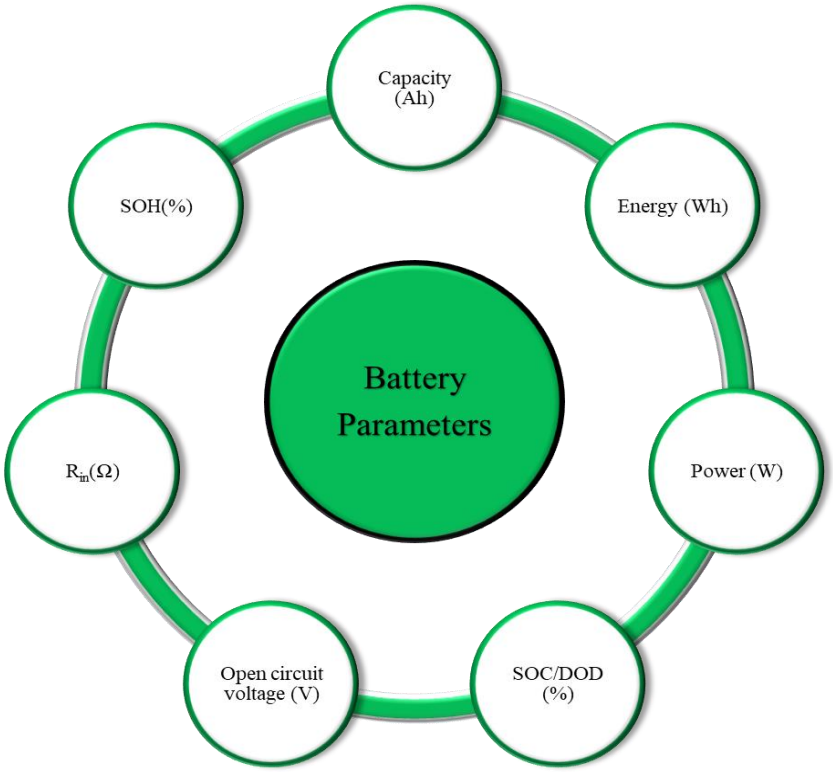

Figure I.2 Battery parameters.

Many studies have shown that Li-ion batteries internal heat generation is caused mainly by to two phenomena, reversible and irreversible heat. The reversible heat depends on the entropy change and predominates at low current rates. While, the irreversible heat is related to Joule effect and predominates

at high current rates. Moreover, due to the increasing demand for the high-rate power discharge, the thermal safety problem at high-rate is taken into consideration. So that, it is very important to perform an adequate thermal analysis on the batteries tested at different current rates. However, major challenges such as the problems of the high heat generation rate and the non-regularity of the intensity allocation are present. Also, there are several factors influencing the performance of the lithium-ion batteries including: the geometrical features, the positioning of the current gathering tabs, and working conditions. Therefore, the lithium-ion batteries require overall the identification of their thermal performance. For these reasons, modeling lithium-ion batteries should be taken into consideration in order to fully understand the thermal characteristics, to well size an efficient thermal management system. In recent published papers, many mathematical models, such as the equivalent circuit models, single particle models, 1D electrochemical thermal paired cell unit models, and 3D combined thermal models, have been improved to expect the electrochemical process, charge and discharge activities, and heat generation inside the Li-ion battery [5]. Thermal management systems with higher cooling efficiency have recently been examined to process the mentioned concerns. Creative ideas, as combining several thermally conductive systems into the battery thermal management systems (BTMS) are investigated.

In this chapter, a critical review of the available literature on the thermal behavior and thermal management systems of batteries is performed. The study carried out in this chapter guides to realize the critical gaps in lithium-ion battery thermal management study and supposed to give an effective guideline for the Li-ion battery's thermal analysis and its thermal management system design.

I.2 Modeling approach of Li-ion batteries

In this section, two modeling approaches of Li-ion batteries thermal behavior are discussed. The numerical modeling which is based on the resolution of the heat transfer equation using numerical methods such as finite difference, volume difference and finite element difference methods. This method presents the advantage of the determination of the temperature or heat generation rates in any given point inside the battery core or sides. Nevertheless, modeling a battery pack coupled with cooling systems requires the simplification of the physical model to reduce the calculation duration. For this reason, many researchers developed equivalent thermal networks based on the analogy between the thermal and electrical systems.

I.2.1 Numerical modeling

Several researchers have studied experimentally and numerically Li-ion batteries during operation time charge or discharge to ensure a controllable operating temperature [6]. In addition, Wang et al. [7] developed a numerical model to describe the thermal behavior of cylindrical Li-ion battery. ANSYS software is used to solve the heat transfer equation based on finite element method. The proposed model was validated with experimental results. Moreover, Mastali et al. [8] proposed a coupled thermo-electro-chemical model. A 3D heat transfer equation is proposed as defined in equation I.1. Where ρ designs the battery density, C_p presents the battery specific heat, λ refers to the thermal conductivity and $\dot{Q}_{gen}$ indicates the source terme.

$$\rho C_p \frac{\partial T}{\partial t} = \frac{\partial}{\partial x}\left(\lambda_x \frac{\partial T}{\partial x}\right) + \frac{\partial}{\partial y}\left(\lambda_y \frac{\partial T}{\partial y}\right) + \frac{\partial}{\partial z}\left(\lambda_z \frac{\partial T}{\partial z}\right) + \dot{Q}_{gen} \qquad \text{I.1}$$

The results of their study presented in Figure I.3 show that the temperatures near the battery tabs are higher due the high amount of heat generation related to Joule effect in the electrodes. However, Vetter et al. [9] confirmed in their study that not only high operating temperature damage battery performances but also low operating temperature. Thus, the design of battery thermal management system must be preceded by an investigation to the battery's internal heat generation and operating temperature conditions [10].

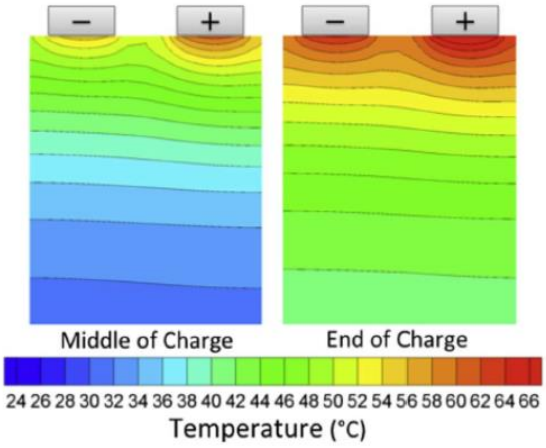

Figure I.3 Battery cell temperature distribution during charge [8].

The development of numerical model simulating batteries thermal behavior requires the determination of thermophysical parameters such as specific heat capacity and thermal conductivity, besides other parameters characterizing the irreversible and reversible heat generation as the internal resistance and entropic heat coefficient. Richter et al. [11] experimentally measured the thermal conductivity of commercial batteries electrodes and separators. The thermal conductivity varies from 0.13±0.02 $Wm^{-1}k^{-1}$ to 0.61±0.02 $Wm^{-1}k^{-}1$ for dry electrodes and from 0.07±0.02 $Wm^{-1}k^{-1}$ to 0.18±0.02 $Wm^{-1}k^{-1}$ for dry separators. Drake et al. [12] measured the thermal conductivity of two cylindrical cells and found a radial thermal conductivity of 0.15 and 0.2 $Wm^{-1}k^{-1}$, while the axial thermal conductivity was large (32 and 30.42 $Wm^{-1}k^{-1}$). This difference in thermal conductivity was analyzed by Huang et al. [13]; the internal structure of battery cells is leading to this anisotropic phenomenon. Moreover, Tang et al. [14]summarized in their review experimental methods to measure the specific heat capacity of batteries in which accelerating rate calorimeter is the most used. An experimental study of the effect of temperature and state of charge was performed by Bazinski et al. [16]. Their measurements show no effect of SOC on specific heat capacity while an increase of temperature cause a slight rise on it. Lin et al. [15] measured the specific heat capacity of a 40Ah prismatic LFP battery using an accelerated rate calorimeter and compared it to an obtained value based on mass-weighted calculation, a difference of 7.5% was noticed. In addition, the entropy coefficient could be determined experimentally using potentiometric and calorimetric methods according to Zhang et al. [16], those methods were discussed in Jalkanen et al. [17] and Sheng et al. [18]. Other experimental methods were recently evolved such as the pulse relaxation method [21] and electro-thermal impedance spectroscopy method [22]. Furthermore, Pan et al. [19] compared the internal resistance of a battery measured by different methods, (V-I) method, (OCV-V) method and (HPPC). They concluded that (HPPC) method based on voltage drop during intermittent discharge is the more accurate method.

I.2.2 Equivalent thermal networks

The development of equivalent thermal networks to model the thermal behavior of Li-ion battery presents the advantage of simplifying the studied physical problem. As the complexity of the internal phenomenon inside the battery causing mass and heat transfer due to chemical reactions of insertion and disinsertion of Li-ion during charge and discharge processes requires the determination of several chemical, electrical and thermal parameters which is not always possible especially in commercialized batteries. In this section, a literature review is presented to show different equivalent thermal networks models.

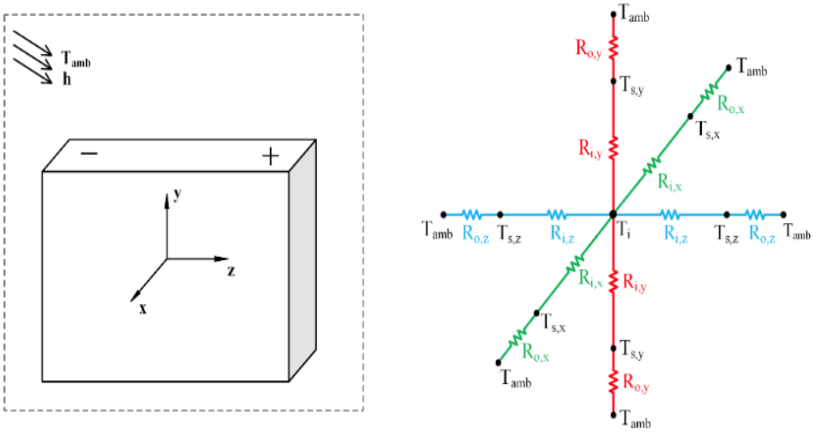

Figure I.4 3D thermal lumped model proposed by Akbarzadeh et al. [20].

First, Akbarzadeh et al. [20] developed a lumped 3D thermal model as illustrated in Figure I.4 to investigate battery cell and a 48V battery module. Their results show that during 2C discharge cycle, battery module temperature is higher than optimal temperature range. The developed thermal network includes various nodes and resistances. Each node represents a temperature while resistances are equivalent to conduction and convection heat transfer. Moreover, Toman et al. [21] elaborated the efficiency of use of a dynamic thermal network to simulate the thermal behavior of cylindrical battery during discharge. First, the produced heat in the battery core is transmitted to the sides via conduction, and afterward it is dispersed to the environment by convection. Second, this model is characterized by supposing that both mass and the battery specific heat capacity are gathered at battery core. On the other hand, the second study proposed by Dey et al. [22] has chosen the radial thermal model for the cylindrical shaped Li-ion battery cell. The proposed model enables analyzing the battery surface and core temperature to develop a diagnostic algorithm. As clarified above, the energy balance is simulated by an equivalent electric circuit, where capacitors and resistances are respectively equivalent to storage and dissipation terms while the current source is used to model the heat source term. An investigation of two lumped models is performed by Forgez et al. [23] as shown in Figure I.5 to study simplified equivalent resistances inside resistance and outside resistance with complete equivalent resistances model containing radiative, convective and conductive resistances. The proposed models allow the prediction of battery core temperature which was validated with experiments results. In addition, another study carried out by Herrera et al. [24] have shown that the energy balance of a given cell can be written as defined in equation I.2 :

$$\mathrm{MC_p}\frac{\partial \mathrm{T}}{\partial \mathrm{t}} = \dot{\mathrm{Q}}_{\mathrm{cv}} + \dot{\mathrm{Q}}_{\mathrm{rad}} + \dot{\mathrm{Q}}_{\mathrm{gen}} \qquad \text{I.2}$$

The term M represents the battery mass while the term C_p stands for specific heat capacity; the heat exchange is transmitted by both convection Q_{conv} and radiation Q_{rad} and the Q_{gen} which represents the heat generation term.

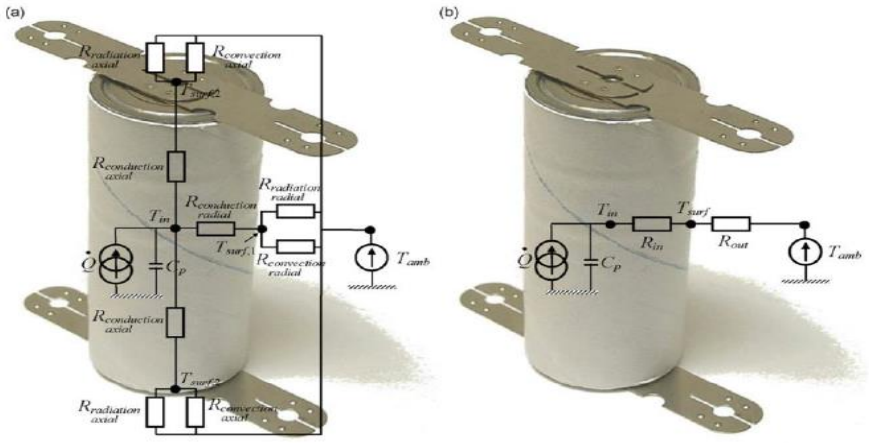

Figure I.5 Cylindrical cell equivalent thermal network suggested by Forgez et al. [23].

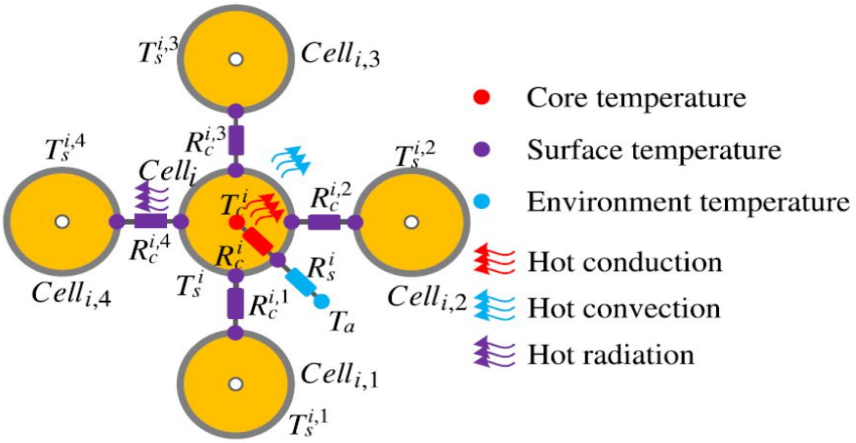

Figure I.6 Battery pack equivalent thermal model developed by Tian et al. [25].

It is necessary to mention that modeling one battery cell isn't sufficient to study the real use conditions of batteries in electric vehicles. For this reason, researchers are doing effort to propose equivalent thermal models enabling the analyze of battery pack thermal behavior. One of the proposed

models in literature shown in Figure I.6 is developed by Tian et al. [25] to study the sensor fault diagnosis scheme. In more details, a precise thermal model can be fundamental to examine the battery thermal behavior in advance.

I.3 Battery thermal management systems

Batteries are manufactured to work only between given temperature ranges. Heat is generated during the operating time. An efficient cooling system should be designed to maintain the battery operating under optimal temperatures, therefore, increasing lifespan and avoiding any damage to the batteries. The cooling of batteries could be carried out either via external or internal cooling systems. Moreover, there are two main types of battery thermal management systems (BTMS): active systems, and passive systems. The active ones depend on forced circulation of a specific fluid such as air or water. While the passive ones use different methods such as phase change materials, heat pipes and fins. The passive method has the advantage of no energy consumption. Many studies have been performed based on combining the passive and the active method. Figure I.7 illustrates a schematic diagram of different battery thermal management systems types.

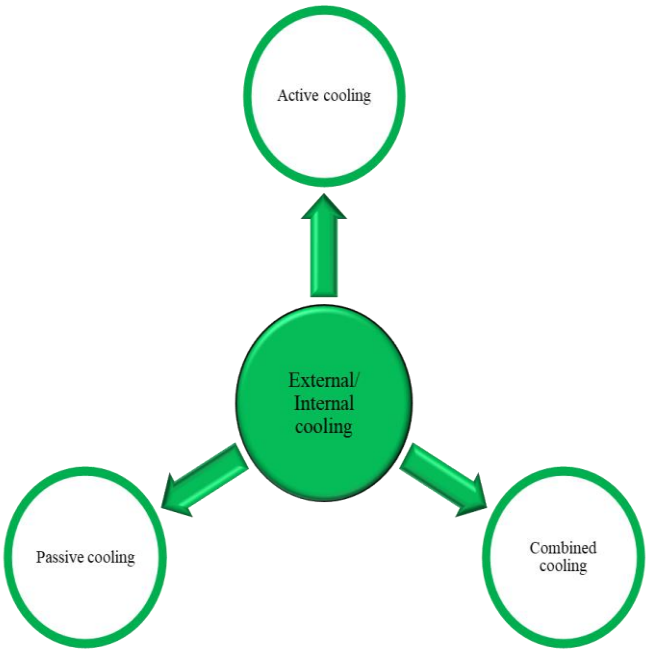

Figure I.7 Schematic of different battery thermal management system types.

I.3.1 Air cooling

Air cooling systems use air as the thermal medium. Several researches studied experimentally and numerically different air-cooling systems applied on batteries under different current rates. The optimization of cooling systems based on air require the analysis of the effect of several parameters as illustrated in Figure I.8.

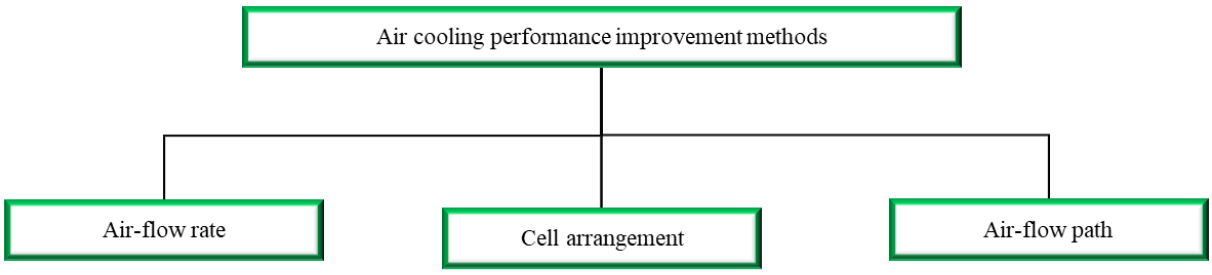

Figure I.8 Schematic of methods to enhance air cooling systems performance.

The air flow rate has a strong influence on the transfer heat coefficient. The cell arrangement and the air flow path have a remarkable impact on the distribution of the battery's temperature. The parallel air-cooled configuration was investigated by Chen and al. [26], by minimizing the ΔT_{max} (maximum temperature difference) in a battery pack. Among various BTMSs, the most commonly used solutions are the parallel air-cooled system. Chen and al. [26] optimized the battery pack configuration in this system by arranging the spacings among the battery cells for cooling performance improvement by combining two models: the flow resistance network model and the heat transfer model. The results showed a decrease in ΔTmax by 42%. Also, the numerical results showed that the cooling performance of the BTMS has improved quite well after optimization. Figure I.9 shows a comparison of the original BTMS and the optimized one under a current rate of 5C. The results show a decrease of ΔTmax by 1.8 K after optimization.

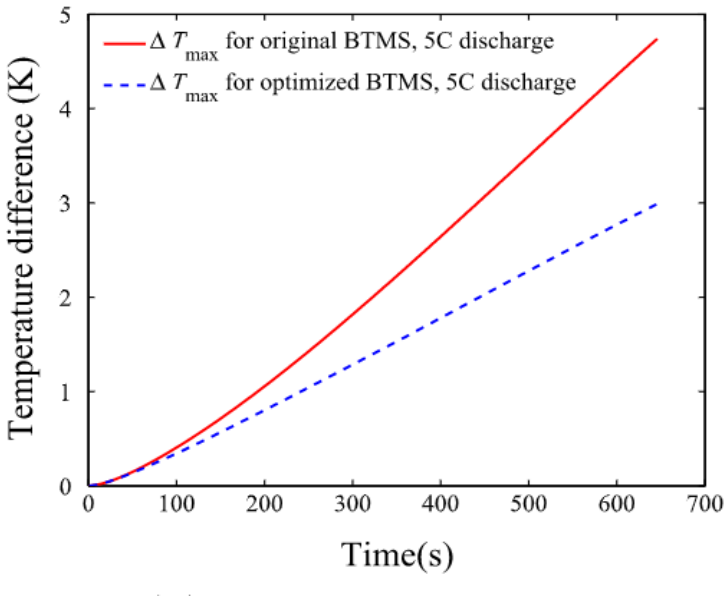

Figure I.9 Optimization of maximum temperature difference during discharge [26].

Afterwards, in another study Chen et al. [27] optimized the homogeneity of airflow rate across the channels by minimizing the cooling channel width. In the parallel air-cooled BTMS the cells in the pack are distributed to increase the spacing in order to improve the system's cooling efficiency. The computational fluid dynamics (CFD) calculation verifies the effectiveness of the model. And the CFD method is validated by the experimental air-cooled system with aluminum blocks. According to the obtained results found by the authors, the cooling efficiency of the BTMS is improved remarkably after applying the cell spacing optimization strategy. This study has also shown that compared to the original BTMS, the maximum temperature of the battery pack for the optimized BTMS is reduced by about 4 °C, and the maximum cell temperature difference is reduced by more than 69% for various inlet airflow rates. Compared to the optimized BTMS in the authors' previous study [26] , the maximum cell temperature difference for the present optimized BTMS is reduced by more than 25% for various inlet airflow rates. Moreover, to design an optimal flow pattern system with high cooling performance, Chen and al. [28] investigated as well the use of CFD method 9 different system with various inlet and outlet airflow region. They found that the symmetrical BTMS with the inlet and outlet, achieves high cooling efficiency. It is noticed that the optimized BTMS has better cooling performance than other BTMSs. Compared to the typical BTMS with Z-type flow, the maximum temperature and the maximum cell temperature difference of the optimized BTMS are reduced by 4.5 °C and 7.7 °C, respectively.

On another hand, the battery packs in electric vehicles usually operate at high current discharge rates which leads to higher heat generation. This may have safety issues and negative impact on the battery performance over the period. In this context, Li and al. [29] suggested a methodology to improve the design performance of an air-cooling system applied on a battery module with eight prismatic cells as illustrated in Figure I.10.

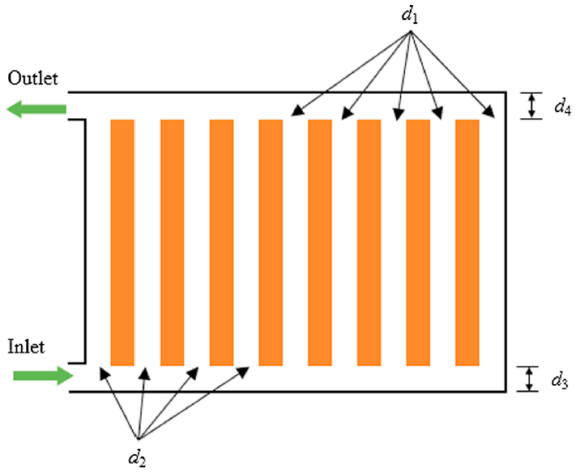

Figure I.10 Air cooling systems investigated by Li et al.[29].

Four steps were realized: the design of air-cooling battery in ANSYS, setup of the CFD codes, design of experiments, evaluation and selection of the surrogate models. The optimization results have shown a reduction of 51.9% of the maximum temperature difference and the optimized air-cooling battery module has higher thermal performance. The proposed methodology will be useful for industrial battery pack design process to reduce maximum temperature, temperature difference and the volume of battery pack. Furthermore, Yang and al. [30] validated a coupled thermal and fluid numerical simulations model with experimental result of a single cell. A strong impact of aligned and staggered arrangement was proved. This study provides a comparative analysis of thermal performances on different arrangements of cylindrical cells for a LiFePO4 battery pack. A decrease in average temperature rise was found for an increasing longitudinal interval of aligned arrangement while the augmentation of the transverse interval causes an increasing of the battery temperature rise for staggered arrangement as shown in Figure I.11.

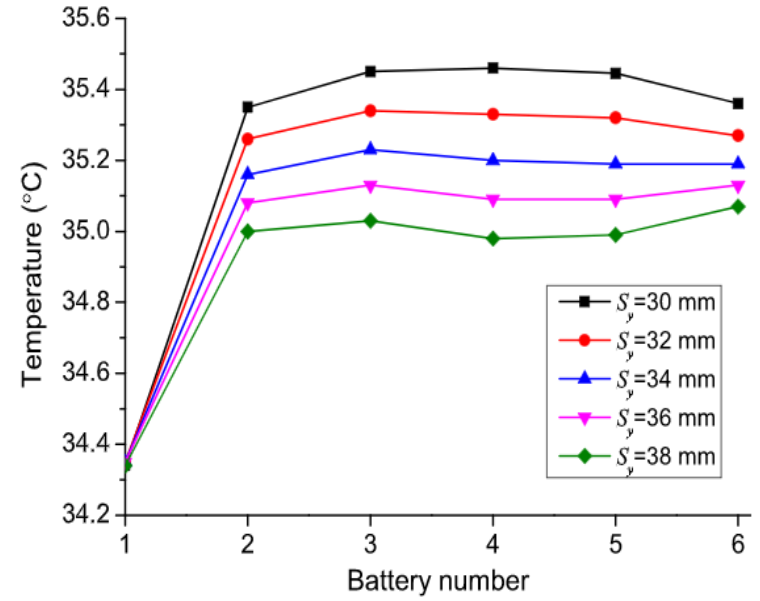

(a)

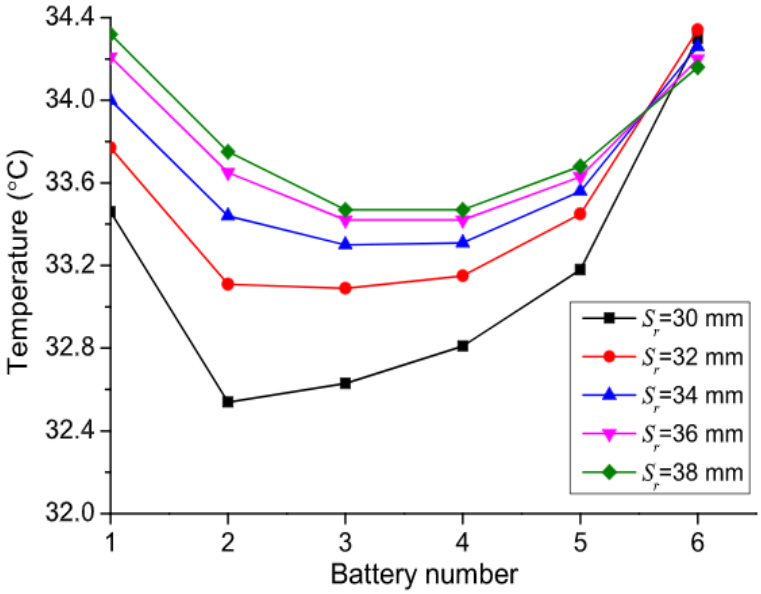

(b)

Figure I.11 Battery pack temperatures increase for (a) aligned arrangement (b) staggered arrangement [30].

Li and al. [31] suggested a battery air cooling system based on a double silica plate coupled with copper mesh. As a result, this study has proved that this strategy could be an effective and appropriate air-cooling system for thermal management. Moreover, Sun and al. [32] developed a 3D battery pack thermal model to size a "Z-type" flow battery pack with optimal thermal behavior. They describe a cooling strategy development method for an air-cooled battery pack with lithium-ion pouch cells used in a hybrid electric vehicle (HEV). Initially, a three-dimensional battery pack thermal model was developed. An analytical study is performed to examine the effects of cooling strategies including geometries of the cooling channel, cooling plate, and corrugation on battery pack thermal behavior, and to identify the design concept of an air-cooled battery pack to maximize its durability and its driving range. Fan and Khodadadi [33] developed a three-dimensional transient thermal analysis of an air-cooled module that contains prismatic lithium ion cells operating under an aggressive driving profile were performed using a commercial computational fluid dynamics code. It was found that lowering the gap spacing and/or increasing the flow rate of the fan lead to a decrease in the maximum temperature rise. For the given module, operating with a uniform gap spacing of 3 mm and an air flow rate of 40.8 m^3/h appears to be the best choice that satisfies the requirements of maximum temperature rise and temperature uniformity. Considering the variety of the design change options and their combinations, it is concluded that, the temperature gradients along the air flow direction can be affected, but are generally unavoidable. Additionally, Park [34] have also developed theoretically and numerically a specific design of air-cooled battery system as shown in Figure I.12. The result of their analysis show that an efficient cooling strategy could be achieved by employing the tapered manifold and pressure relief ventilation even without changing the layout/design of the existing battery system.

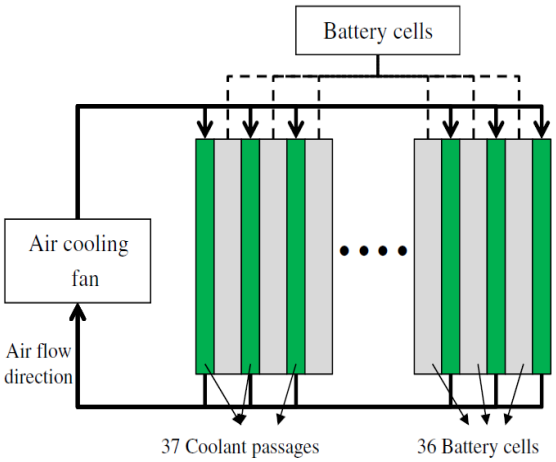

Figure I.12 Schematic diagram of air cooling systems proposed by Park et al. [34].

Jiaqiang et al. [35] explored the thermal characteristic of the 18650-battery module which consists of 60 pieces of cells and standard battery holders by using the computational fluid dynamics (CFD) method and lumped model of single cell. The results indicated that, the cooling performance of the inlet and outlet located on the different sides is better than on the same side and the use of the baffle plate can highly improve the thermal performance of air-cooling strategies with the lateral inlet and outlet. Cen et al. [36] have tried to investigate a lithium-ion battery thermal management (BTM) system using the electric vehicle (EV) air conditioning refrigerant to cool the battery pack directly. Experimental results have shown that the BTM system can control the battery pack's temperature in an appropriate preset value easily under extreme ambient temperature, as high as 40 °C. The temperature difference within the pack is less than 4 °C in the constant discharge rate of 0.5 C, 1 C, 1.5 C laboratory tests, and 1.5 °C in normalized driving cycles. Additionally, regarding the importance of the Lithium-titanate batteries that have become an attractive option for battery electric vehicles and hybrid electric vehicles, experiments were conducted by Giuliano et al. [37] using Altair nano's 50 Ah cells over a range of charge-discharge cycle currents at two airflow rates. The results showed that an airflow of 1100 m/s per cell restricts the temperature rise of the coolant air to less than 10 °C over ambient even for 200 A charge-discharge cycles. Wang et al. [38] have used thirty cylinder 18650-type cells that fabricated a 6S5P battery module with a 2-mm spacing between cells to evaluate exothermic trajectories. The efficiency of the developed forced-air cooling system was 73% in case 1 with a 1 C discharge rate, the temperature difference was less than 5°C, and the maximum temperature (T_{max}) for this case was below 45 °C showing uniform heat distribution. Moreover, extreme heat accumulation developed inside the module and damaged the adjacent LIBs during the fast 2 C discharge test. Yang et al. [39] investigated the thermal performance of axial flow air cooling for lithium-ion battery pack. As a result, increasing the radial interval leads to a slight average temperature rise but benefits from the temperature uniformity of the battery pack. A larger radial interval can significantly reduce the power cost of the cooling system. However, this might decrease space efficiency slightly. Along with this, an air-based BTMS was optimized by Li et al. [40] in a battery module with 36 battery lithium-ion cells. At this point, three metrics are used to evaluate the BTMS thermal performance, including

- the maximum temperature in the battery module
- the temperature uniformity in the battery module
- the pressure drop.

It is found that increasing the air flow rate and a large spacing size may result in a more non-uniform distribution of temperature. Results show that the maximum temperature difference of the cooling air is

reduced from 23.9 °C to 2.1 °C by 91.2%, and the maximum temperature difference among the battery cells is reduced from 25.7 °C to 6.4 °C by 75.1%. Regarding the importance of thermal management mentioned previously, another research conducted by Xun et al. [41] discusses the thermal behavior during the discharging process of the flat-plate and cylindrical stacks as illustrated in Figure I.13.

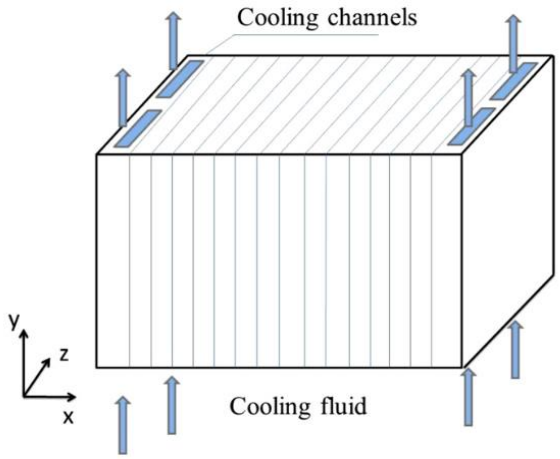

Figure I.13 Schematic battery pack air cooling developed by Xun et al. [41].

The results have shown that changing the channel size and the number of channels results in similar average battery temperatures for the same volume ratio for cooling channels and battery of flat-plate design. Yet, increasing the channel size improves the cooling energy efficiency but leads to more unevenly distributed temperature and vice versa. Hence, a counter-flow arrangement of the cooling channels or changing the flow direction of the co-flow arrangement periodically may also help the thermal management. Another study was carried by Lu et al. [42] to investigate the effects of cooling channel size and air supply strategy on the thermal behavior of battery. The numerical results illustrate that the best cooling performance is when the airflow inlet and outlet are on the top of battery pack. Besides, the analysis indicates that packing more batteries along flow direction is an appropriate solution for cooling requirements. Since the thermal management of traction battery systems for electrical-drive vehicles directly affects vehicle's dynamic performance , Mahamud, R., and Park, C [43] have proposed a new battery thermal management method using a reciprocating airflow for cylindrical Li-ion ($LiMn_2O_4$/C) cells. They suggested the use of: two-dimensional computational fluid dynamics (CFD) model, a lumped-capacitance thermal model for battery cells and flow network model.

They found that the reciprocating flow can reduce the cell temperature difference of the battery system by about 4 °C (72% reduction) and the maximum cell temperature by 1.5 °C for a reciprocation period of 120 s compared with the unidirectional flow case. On the other hand, a new structure was analyzed by Na et al. [44] by reversing layered airflow for Li-ion battery thermal management to improve the temperature consistency of the battery pack. This study revealed that the reverse layered air flow (RLAF) decreases the highest temperatures and the maximum average temperature difference of the battery pack more than that of the unidirectional air flow (UDAF). The compared configurations of air flow are given in Figure I.14.

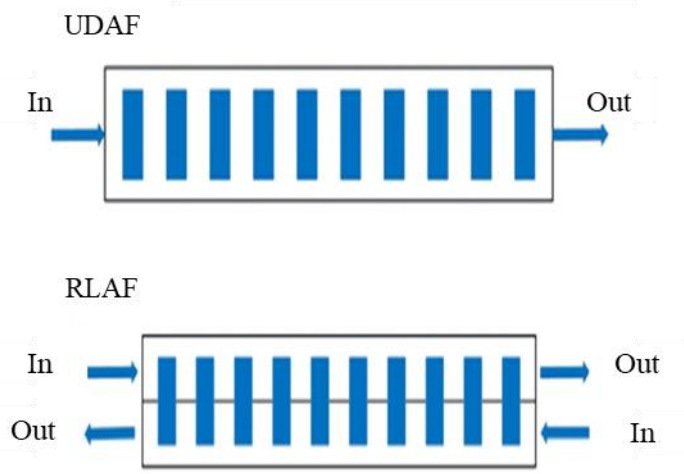

Figure I.14 Air flow configurations studied by Na et al. [44].

Xie et al. [45] have investigated the importance of the forced air-cooling system, which is of great significance in the battery thermal management system because of its simple structure and low cost. The results have shown that the best cooling performance obtained is under the condition of 2.5° air-inlet angles, 2.5° air-outlet angles and equal channels width. With the optimization method, the maximum temperature and the temperature difference decreased by 12.82% and 29.72% respectively. A three-dimensional anisotropic heat transfer model was developed by Yu et al. [46] to describe the thermal behavior of the lithium-ion batteries with the integration of heat generation theory, and was validated through both simulations and experiments. Moreover, the simulations and experiments show that the maximum temperature can be decreased to 33.1°C through the new thermal management system compared to 42.3°C through the traditional ones. Also, the temperature uniformity of the lithium-ion battery packs is enhanced significantly. To summarize the different air-cooling results in literature the Table I.1 presents a comparison between different studies performed on battery air cooling systems.

Table I.1 Summary of air-cooling results from literature.

Author (s)	Design variables	Number of cells	Capacity (Ah)	Discharge rate	Air flow rate
Fan et al. [47]	Aligned, staggered, crossed cells	32 cylindrical	3.5	0.5,1.0,2.0 C	0.6,1.0,2.0,3.0,4.0 m/s
Shahid et al. [48]	Aligned cells	32 cylindrical	2.5	2 C	2.8,2.0,2.2 m/s
Wang et al. [49]	1×24, 3×8 and 5×5 arrays rectangular arrangements, 19 cells hexagonal arrangement and 28 cells circular arrangement	24,28 cylindrical	1.5	1, 2, 3 C	-
Saw et al.[50]	Aligned cells	24 cylindrical	8	0.1 C	
Yu et al. [46]	Aligned cells	12 prismatic	18	1 C	0.125 to 2.0 m^3/min
Chen et al. [51]	N×M cuboid battery cells	N×M prismatic		4, 5 C	1.0 to 4.0 m/s
Chen et al. [52]	Cell spacing	12 prismatic	12	5 C	0.005, 0.0075, 0.010 m^3 /s
Ho et al. [53]	Connected in series	10 prismatic	52.3	1, 2, 3, 4, 5 C	-
Xie et al. [45]	Inlet and outlet angle, width of air channel	10 prismatic	-	0.2 C	0.7, 1.5 m/s

I.3.2 Liquid cooling

In this section, another active cooling system is discussed related to the use of liquids. The main coolant used in this system is water, nevertheless the efficiency of other refrigeration fluids is recently examined in several studies. The liquid cooling system has a good cooling performance thus it is the most commonly used BTMS. There are two types of liquid cooling systems; the direct-contact and the indirect-contact liquid cooling. For direct-contact where the liquid directly encounters battery cells. While, for indirect-contact where the liquid indirectly encounters the battery cells, a possible layout can be either a jacket around the battery module, discrete tubing around each module, placing the battery modules on a cooling plate or combining the battery module with cooling fins and plates. However, the indirect systems create better isolation between battery module and surrounding, which make them safer than the direct systems. The studies on the liquid cooling system focus on the development of the physical design of the cooling plate and its channels and by targeting the parameters like; coolant pressure drop across the channels of the cooling plates and cell core temperature. The liquid cooling system designs developed by several experts ensure safe and long life-time lithium-ion battery-based systems, and prevent fires or explosions that may result from high and non-controlled temperatures in the battery. Xu et al. [54] developed a mini channel cooling system combined with the battery as illustrated in Figure I.15.

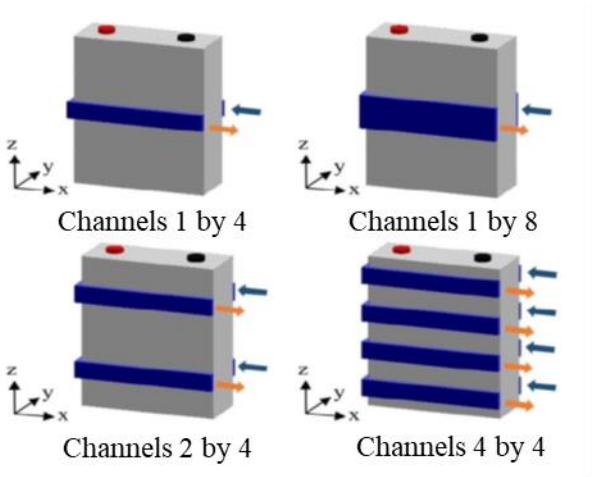

Figure I.15 Mini channels configurations proposed by Xu et al. [54].

This technique succeeded to keep temperature at controlled levels through thermal distribution among cells, therefore, preventing serious battery overheating consequences. However, Lan et al. [55] had developed a new BTMs design. This design is based on aluminum mini channel tubes where a single prismatic lithium-ion cell is used as the energetic source of the design. Under different charge rates of the lithium-ion cell, the team studied the different thermal changes of the system. the maximum cell temperature at a discharge rate of 1C is less than 27.8 °C, and the temperature difference across the cell is less than 0.80 °C using flow rate at 0.20 l/min. while higher flow rates are required at higher discharge rates to keep the same thermal amounts. It turned out in this experiment that it is needed about 0.8 l/min of flow rate for 1.5C and 2.0 l/min for 2C. On the other hand, the system could keep a perfect thermal distribution (less than 0.1C°) for the whole unit. These unique results and perfect thermal management show that mini channel tubes might be one of the ideal solutions for BTMs. Huo et al. [56] designed a BTM system with mini channel cold plate aiming a long life cycle and safe run for electric vehicles. The design was established in 3D model using a rectangular lithium-ion battery. The investigation of mass, flow direction temperature and temperature distribution showed that the increase of channels number and inlet mass flow rate leads to the battery maximum temperature decreases. In addition, Jarrett el al. [57] have designed an optimal battery cooling plate shown in Figure I.16 based on a parametrical study on channels geometry.

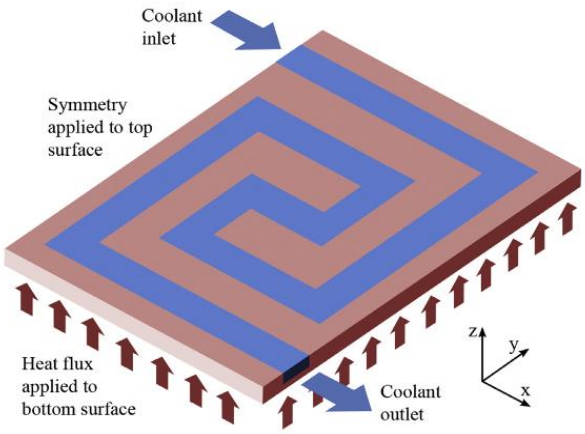

Figure I.16 Battery cooling plate investigated by Jarrett et al. [57].

Three important performance measures were considered: temperature uniformity, mean temperature, and pressure drop. Between the three measures, the temperature uniformity was most sensitive to the operating conditions, especially with respect to the distribution of the input heat flux, and also to the

coolant flow rate. Electric vehicle development-imposed necessity to update batteries thermal management. Liquid cooling is recently adopted more than the other cooling strategies. Ye et al. [58] designed a standard model with two cooling plates equipped with a lithium iron phosphate battery. The results analyzed through the orthogonal and the surrogate models have shown that both pressure and the battery temperature decreased due to cross section and coolant channel number increase, scoring between 9.5% temperature reduction to 16.88% of pressure reduction under constant inlet flow rates. An et al. [59] suggested a thermal management system working with flow boiling through mini channel. This experiment studied the thermal management at different discharge rates using a dielectric hydrofluoroether liquid which boiling point is 34°C. In this experiment, the cooling system, could manage the uniform temperature and reduce the maximum temperature of the whole system under high discharge rates. The boiling heat transfer ensured appropriate temperature for all the system which increased cooling safety and safe discharge conditions.

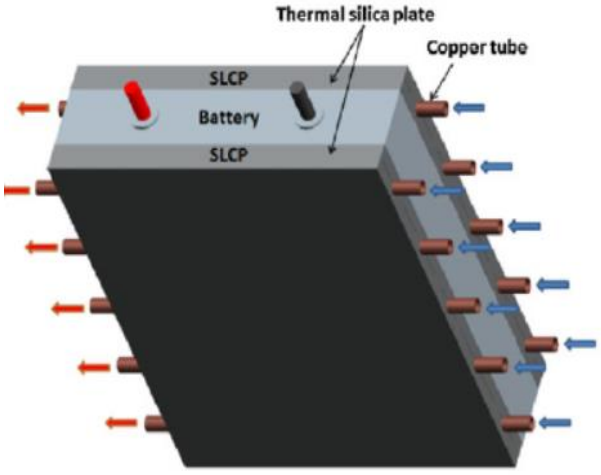

Figure I.17 Schematic of the proposed cooling system by Wang et al. [60].

Wang et al. [60] suggested a new design for prismatic Li-ion batteries, which is a thermal silica plates based BTMs associated with liquid cooling channels as shown in Figure I.17. The battery temperature decreases inversely with the cooling channels and thermal plates increase. Increase of the inlet flow rates improved the thermal performance while the flow direction did not affect the system in anyway. At 3 C discharge with 0.1 m/s inlet flow rates the system was perfectly cooled down, for 5 C-rate the suitable flow rate was 0.25 m/s. Shang et al. [61] designed lithium-ion liquid battery cooling system with changing contact surface. The maximum temperature is limited with the increase of inlet mass flow while the uniformity temperature rates couldn't be controlled with this latter. Battery

performance is affected by mass flow, width of cooling plate and inlet temperature. The best BTM performance is recorded with 18°C of inlet temperature, a 70 mm width cooling plate and a 0.21 kg/s flow rate. Optimization method helped achieving ideal pump consumption and rates of temperature and temperature uniformity of the battery. Since typical and hybrid vehicles are of complex combinations, run with such high energy of lithium-ion batteries these kinds of heavy systems face serious safety, thermal, durability and cost issues. These problems lead to various limitations in lithium-ion batteries run based vehicles. Deng et al. [62] suggested a novel leaf-like channels with loops for li-ion battery to maintain ideal temperature for a liquid cooling BTM system. A double layer channel is formed with four channels to control the system temperature. This study investigated the effect of width, length ratio, channel thickness and bifurcation angle on the maximal temperature of the system, the rate of inlet mass flow was also investigated. Perfect thermal rates are found at 3/4 width and a 0.5 length ratio with 30–50° bifurcation angel. Optimal heat is obtained with the increase of the inlet mass flow enhanced by pressure drop. This suggested design reduced the maximum temperature from 60 °C to 32 °C making it a useful design for future cold plates cooling systems. To summarize the different liquid-cooling results in literature the Table I.2 presents a comparison between different studies performed on battery liquid cooling systems.

Table I.2 Summary of liquid-cooling results from literature.

Author (s)	Design variables	Number of cells	Capacity (Ah)	Discharge rate	Liquid	Remarks
Rao et al. [63]	Liquid cooling based thermal management system	24 cylindrical cells	3	3C	Water	Li-ion battery system weight, pump power consumption and cooling performance
Panchal et al. [64]	mini-channel cold plates placed on a prismatic lithium-ion battery	1 prismatic cell	20	1C and 2C	Water	Li-ion battery
Zhou et al. [65]	Liquid cooling method with half-helical duct	9 cylindrical cells	3	5C	Liquid	Li-ion battery
Al-Zareer et al .[66]	liquid-to-vapor phase change cooling systems	3 Prismatic cells 12 cylindrical cells	12	5C and 6C	Propane Ammonia	Li-ion battery Promising options for hybrid and electric vehicles
Wang, et al. [67]	liquid cooling structure in large battery modules	90 cylindrical cells	13.2	5C	Water	Li-ion battery coupling single-factor analysis with orthogonal test
Wang et al. [68]	modular liquid-cooled battery thermal management system	20 cylindrical cells	2.2	3C	Water	Li-ion battery numerical simulation and experiment to study the effect of coolant flow rate and cooling mode
Zhu et al. [69]	liquid cooled battery module with collaborative heat dissipation in both axial and radial directions	80 cylindrical cells	-	3C	Water	Multi-objective optimization
Huang et al. [70]	liquid cooled battery thermal management system	48 cylindrical cells	-	1C and 5C	Water	The transient and ultimate thermal behaviors of the battery module as controlled by water-cooled BTM embedded system

I.3.3 PCM cooling

There are various methods for use as a thermal management system in electric vehicles and other electronic devices to regulate the temperature in operating limits without any energy consumption. One of those methods is the use of phase change material (PCM). PCM provides good thermal management.

The use of PCM as battery cooling systems should satisfy the below conditions:

- The melting temperature must be lower than the maximum temperature of the battery.
- High specific heat capacity, heat latent and thermal conductivities are required.
- Low volume change during phase change process.
- Availability and low cost.

Phase change material (PCM) is a cooling technique which achieves high levels of natural convection and heat dissipation. To examine this passive thermal management system, Javani et al. [71] designed an experimental BTM design for EV using PCM at the battery cells' level. PCM of porous foam is infused in foam layers between the lithium-ion cells as a method for passive thermal management in battery packs of electric vehicles. The result of this examination met with the ability to reduce the peak temperature of the system by 7.3°C and provide uniformity of temperature distribution throughout the battery cell. Moreover, the purpose of the study in which Li et al. [72] combined a phase change material as a cooling system of the battery pack with a structure of metal foam was to test thermal conductivity. A sandwiched cooling structure using the permeable metal foam of cooper combined with PCM was designed and compared with clear PCM combined with an air-cooling mode. The result of this comparative experience showed that the cooling structure of copper foam decreases the battery's surface temperature and enhances the uniformity of the temperature distribution due to its effective thermal conductivity. Furthermore, using carbon fiber-based PCM can also be used as a thermal management system. Khateeb et al. [73] investigated various modes of heat dissipation. The purpose of this study was to test the thermal management system of a Li-ion battery designed for electric scooter applications using phase change material to limit the temperature rise of the battery. Figure I.18 illustrates the tested battery pack composed of 18 cylindrical cells. The results of the experiment implied that the best mode used was the use of aluminum foam with PCM, which causes a significant temperature decrease of about 50% and gives a temperature uniformity compared to the other cases of thermal management.

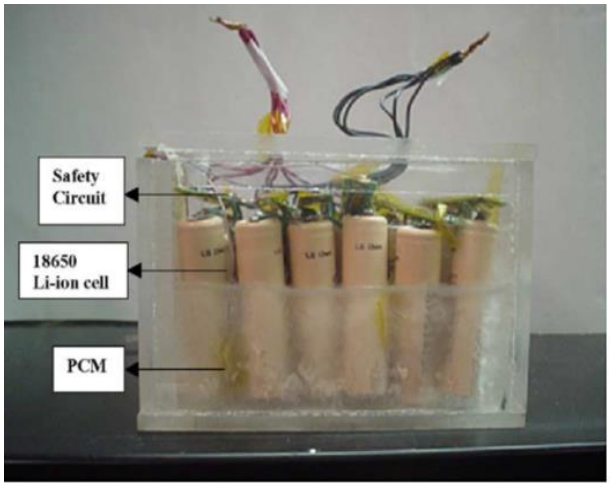

Figure I.18 Li-ion battery pack filled with phase change material [73].

The purpose of this study performed by Babapoor et al. [74] was to introduce a thermal management system for lithium-ion batteries based on phase change material. The result of the experiment implied that a preferable thermal management can be achieved using carbon fiber in PCM of 2 mm and a reduce of temperature by 45% was measured. In addition, Lithium-ion phosphate battery (LiFePO4) has been widely used in electric vehicles due to its low toxicity, low cost, significant performance, and long-term stability. Azizi et al. [75] examined the thermal system management of phase change material (PCM) and aluminum wire mesh plates in the LiFePO4 battery of electric vehicles. The result of the experiment implied a significant decrease in the surface temperature of the battery in the hot zones and improved performance of the battery cell. Jiang et al. [76] suggested a lithium-ion battery design using phase change material. The purpose of this study was to provide an expanded graphite composite phase change material for thermal management system in lithium-ion batteries. The used PCM is Poly Ethylene Glycol 1000 characterized by a melting temperature range between 35 °C-40 °C. A temperature decrease of 26% was obtained for an applied current rate of 3C. Lv et al. [77] provided a thermal management technology system for cooling using primarily a PCM. Low density polyethylene (LDPE)-enhanced composite PCM (L-CPCM) was developed in this study. The results showed that L-CPCM technology implies preferable cooling effect compared to natural air cooling, and improves the heat transfer performance if combined with fins. In addition, The purpose of the study directed by Yan et al. [78] was to investigate the application of phase change material (PCM) as a thermal management system in the dynamic cycling of batteries in electric vehicles as shown in Figure I.19.

Figure I.19 Tested PCM cooling system with battery pack [78].

The result of this application showed that PCM with a melting temperature of 45°C is recommended to be used in the battery pack system. Thermal management systems based on phase change materials can be combined with additional pieces like fins to control the temperature characteristics of the battery. Ping et al. [79] studied the design of PCM-fins systems as illustrated in Figure I.20. The system was developed and tested on five cells to optimize PCM species, thickness, fins thickness and spacing. A high thermal performance was observed for the optimized system with a maximum battery temperature less than 51°C.

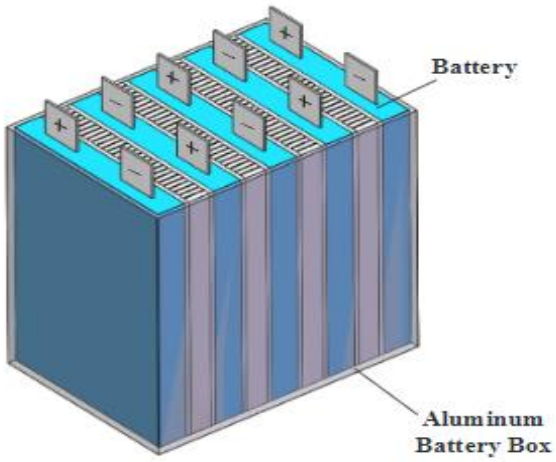

Figure I.20 Side view of PCM-fins cooling system with battery pack developed by Ping et al. [79].

In addition, Wang et al [80] developed a novel BTM system based on composite phase change materials (C-PCM) with aluminum boxes. 30 battery packs with and without (C-PCM) of 3.3 Ah connected (10S3P) are tested on discharge rate of (1C,2C). The main conclusion obtained are summarized as follows, the addition of C-PCM ensures a well-controlled average temperature of the battery pack with a notable reduction during the discharge rate of 2C than the discharge rate of 1C. Meanwhile, the temperature uniformity of the battery pack is improved. The (C-PCM) melting negatively affects the thermal control; hence a reasonable estimation of (C-PCM) dosage is needed for PCM application. Finally, we conclude that the PCM enhances the temperature uniformity and decreases the temperature.

Phase change material (PCM) uses several materials like paraffin, salt hydrates, and fatty acids as mentioned in Ling et al. [81] study. This study focused on a suitable material to enhance the reduced-temperature performance of lithium-ion cells. Composite phase change material of expanded graphite with fumed silica was studied. The results showed that composite PCM can decrease the temperature differences, and the combination of PCM displays the main role in providing a uniform temperature distribution to improve the matchmaking of the battery performance. Moreover, Hussain et al. [82] studied the BTM of a Li-ion battery using a PCM combined with graphene-coated nickel foam. This study aimed to provide a thermal management system for the Li-ion battery. The thermal management of Li-ion batteries was achieved by using Graphene coated nickel (GCN) foam saturated with paraffin as a phase change material. They showed that the battery surface temperature growth is less when using graphene-coated nickel foam saturated with PCM of paraffin as compared to other thermal management systems. Furthermore, Zou et al. [83] prepared a composite phase change material and examined its locally enhanced heat transfer for power battery module. The method prepared was highly thermal conductive phase change material. They showed an improvement in the temperature consistency of the battery module. Huang et al. [84] suggested a combination method for thermal management of a Li-ion battery pack with the application of different flexible form-stable composite PCM. Their study allowed Li-ion battery pack to work safely for a long period without exceeding upper-temperature limits. Luo et al. [88] study tested a temperature control system of graphite film combined with a phase change material for thermal management in batteries of electric vehicles. Lastly, Nofal et al. [85] introduced a new PCM structure using the 3D technique. A 3D printed PCM type, named selective self-binding laser is introduced to identify the performance of the thermal system of a lithium-ion battery. The results showed that the newly designed 3D printed PCM is capable to provide thermal management functions and well thermal characteristics compared with other PCM composites. In each study a different PCM

type was chosen by the authors to investigate its efficiency on battery cooling, Table I.3 presented below summarize different used PCM types in literature.

Table I.3 Thermo-physical properties of phase change materials in literature.

Author (s)	Melting point(°C)	Latent heat (J/g)	Specific heat capacity (J/kg. K)	Thermal conductivity (W/m. K)	Density (kg/m^3)
Babapoor et al. [74]	42-49	242	-	0.21	ρ_{solid}=912 ρ_{liquid}=768
Azizi et al. [75]	56	195	1770	λ_{solid}=0.29 λ_{liquid}=0.21	ρ_{solid}=910 ρ_{liquid}=822
Wang et al. [80]	37.8	200.66	2300	0.245	800
Ling et al. [81]	43.1	232	2500	0.24	-
Hussain et al. [82]	38-41	-	2300	0.19	ρ_{solid}=880 ρ_{liquid}=760
Zhu et al.[86]	54.8	238	Cp_{solid}=1905 Cp_{liquid}=2318	0.21	ρ_{solid}=920 ρ_{liquid}=795
Arora et al. [87]	27-29	250	2000	0.2	ρ_{solid}=880 ρ_{liquid}=770

I.3.4 Heat pipe cooling

Heat pipes are one of the efficient cooling devices. The thermal management systems imply the processes of temperature control through thermodynamics and heat transfer technology, involving conduction, convection, and radiation. Whether used alone or coupled with PCM or air/ liquid thermal managing systems, the heat pipes provide a good performing atmosphere. Many experiments were conducted on the heat pipe effect on the thermal phenomena of an electric drive system. Liu et al. [88] investigated the cooling/heating characteristics (dynamic thermal characteristics) of the ultra-thin micro heat pipe (UMHP) as shown in Figure I.21. Different heating and cooling processes of the UMHP were undertaken and the performance and efficiency were assessed. The results showed that the heat transfer characteristics of the UMHP were high-efficient with low-energy consumption, valid to guide thermal analysis and optimization of heat pipe Battery Thermal Management (BTMSs).

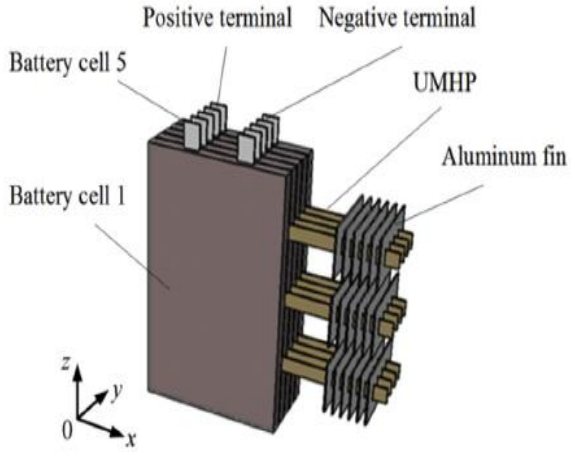

Figure I.21 Battery cooling system using heat pipes as proposed by Liu et al. [88].

Weng et al. [89] Tested heat pipe with PCM. This study aimed to explain the various thermal performances of a heat pipe linked with PCM for electronic cooling system. They coupled in this experiment a PCM with storage container at the level of the adiabatic section of heat pipe. This storage container stores and releases thermal energy that it receives from a condenser's fan and evaporator performance. In this study, the team investigated the thermal variations using different types of phase change materials, different fan speeds, different PCM volumes and different released heating powers of the PCM system under distinct charge and discharge conditions of test. The thermal distribution results of all the previous mentioned experiments revealed that about 46% of the transmitted power from the condenser fan could be saved by Tricosan PCM system. Rao et al. [90] had experienced thermal management of electric vehicle battery with heat pipe. The purpose of the investigation was to introduce a thermal design of heat pipes for energy saving in the thermal management system of batteries in an electric vehicle. The result of the experiment in this study showed that heat pipes can be effectively used in the thermal management system for energy savings.

Greco et al. [91] studied lithium-ion battery thermal management for electric vehicles using heat pipes. The study aimed to analyze and develop precise methods to use heat pipes as a guide for the battery thermal management system (BTMS). The thermal analysis model of the computational model and the thermal model of heat pipes was used in Li-ion batteries. The results of the study showed a highly effective performance that heat pipes provide in managing batteries pack temperature. Wang et al. [92] suggested an experimental study to provide a complete experimental description of cooling and heating via the heat pipe battery covering a range of unusual battery conditions. Two typical battery

cells and an alternate heat source of 2.5 to 40 W / cell were built. The results implied that under the unusual battery conditions of environmental overheating or overcooling, the heat pipe operates effectively to maintain the battery temperature. Furthermore, Li-ion batteries are frequently used in portable electronics due to their high electric capacity, they are distinguished by a high ratio in the ability to produce and store electricity. Discharge rates are one of the characteristics of any battery, the low thermal conductivity of the lithium batteries causes overheating problems due to high discharge rates. Deng et al. [93] experimental study aimed to examine the battery thermal system using a heat pipe for cooling combined with an aluminum plate which regulates the temperature through the surface of the battery. The method used resulted in a reduction of the temperature rise in (Li-ion) battery leading to a long lifetime and better safety of battery which may deteriorate due to high discharge rates and overheating.

Despite the high usage of lithium-ion batteries in various types of electric vehicles due to its electricity-saving properties, lithium-ion batteries need protection circuit or heat pipes to maintain voltage and thermal management within safe limits. Tran et al. [94] investigated the performance of the heat pipe in lessening the temperature of the battery packs in the hybrid electric vehicle. The flat heat pipe was used in this study and the result showed that the flat heat pipe is capable to handle the overheating and lowering heat resistance by the cooling method. The effect of inclination on the heat pipe cooling efficiency is illustrated in Figure I.22. A low variation is remarked less than 2 K which prove the efficiency of heat pipe use under different inclinations.

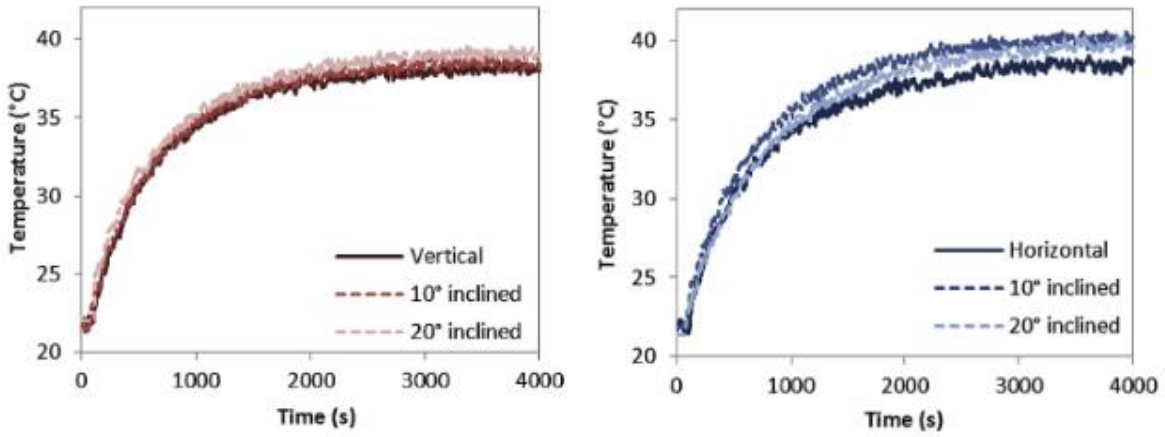

Figure I.22 Effect of inclination on Heater/heat pipe interface [94].

Heat pipes do not contain moving mechanical parts and do not usually require any maintenance, but non-condensable gases that circulate through the walls of the tube, as a result of working fluid failure or when impurities remain in the material, can reduce the tube's effectiveness in transferring heat. Tran et al. [95] had also investigated a hybrid and a typical electric vehicle system aiming to design a heat pipe for cooling the battery pack of Hybrid electric vehicles and electric vehicles. The result of the experiment showed that heat-pipes combined with a ventilation apparatus is an effective instrument to save the battery from overheating through its working.

Lithium as a metal shows instability especially during the charging process. Thus, recent research experiments start to go with non-metal lithium-ion batteries because of its ability to produce electricity and rechargeable advantage, even though lithium-ion batteries are susceptible to overheating caused by fast charging. Ye et al. [96] had numerically analyzed the thermal system in his study to provide a system of heat pipe for the thermal management of batteries during fast charging. An optimized heat pipe thermal management system was presented in this study for lithium-ion battery cells. The result of the experiment showed that heat pipes have the ability to improve the thermal management system of the battery cell during fast charging.

The goal of Battery Thermal Management System (BTMS) is to increase battery lifetime by regulating temperature and distribution, this occurs through various heat-controlling methods, such as heat pipes that had shown to be an effective way to transfer heat, or heat energy, from one point to another. Zou et al. [97] experimental study investigates the thermal performance of the heat pipe heat exchanger (HPHE) for the EV battery practice. The method used for this investigation includes an experimental test bench of HPHE and heat pump air conditioning on car chairs. The results of the investigation came up with a well, effective working system of thermal management.

Recent research articles suggest several cooling techniques in Electric Vehicles (EV) by applying heat pipes for the management of the battery thermal system of EV. Heat transfer through these heat pipes occurring such as thermal conduction and unpredictable thermal conditions through the segments of the battery pack which may cause unequal thermal distributions.

The design of the types of thermal management systems in most batteries in an electric vehicle is usually based on the selection of materials and the development of related components that somehow either increase or reduce heat transfer by conduction and radiation. Oscillating Thermal Pipes (OTP) or oscillating heat pipes (OHP) are new two-stage heat transfer apparatus based on the oscillating flow of

the inner liquid and vapor components in a long miniature tube that bends in many turns. The purpose of Chi et al. [98] study was to present an Oscillating Heat Pipe (OHP) as a new heat regulator and cooling system in Electric vehicle batteries. The parameters of heat pipe were used in top heating/bottom cooling mode in Lithium-ion batteries. The result showed that the Oscillating heat pipe is performable for use in the battery cooling system. Qu et al. [99] conducted a battery based study using flexible heat pipes. The purpose of this study was to test flexible oscillating heat pipes (FOHPs) in electric vehicle batteries to evaluate the effects of adiabatic length and structural components and style of the flexible pipe on thermal characteristics. The result of the experiment showed that FOHPs plays an important solution for battery thermal management system in electric vehicles using several structural styles of FOHPs and large adiabatic length. Li-ion batteries are used for the storage and conversion of energy for various technologies mainly electric vehicles especially when combined with heat pipes. The purpose of the experimental study suggested by Feng et al. [100] was to investigate the experimental monitoring of the strain and temperature through the charge and discharge processes in the Li-ion battery pack by using a heat pipe cooling device to reduce the temperature. The results of the experiment showed that the device used was effective in managing the reduction of strain and temperature through various charge-discharge processes. Figure I.23 illustrates a schematic of the used heat pipe cooling device (HPCD) combined with batteries during operating time.

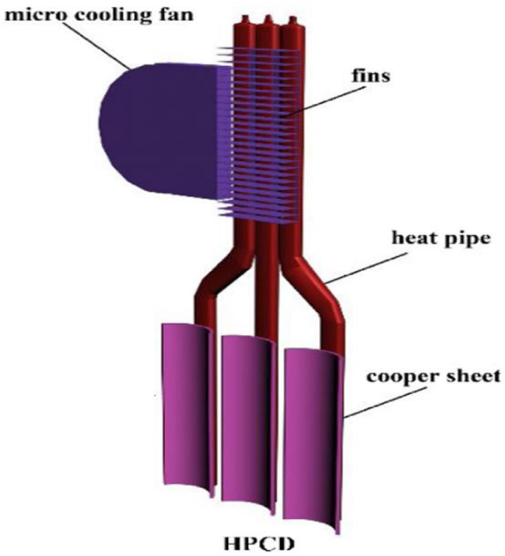

Figure I.23 Schematic of the heat pipe cooling device used by Feng et al. [100].

The term passive cooling refers to the set of technologies or design features used for cooling a device without energy consumption. To investigate the main standards and criteria of this system, Rizk et al. [101] studied a passive thermal management system by using heat pipes in electric vehicles lithium-ion batteries. The thermal system of the battery of heat pipes with fins was studied in repetitive charge/discharge cycles at different current rates by using thermocouples placed on the battery surface and the heat pipe. The result of the experiment showed that using more than one heat pipe with fins cools the battery surface temperature better than using one heat pipe with a fin.

The application of a battery pack thermal management system for cooling remains an evolving and searchable challenge in electric vehicles. Wei et al. [102] had designed an experimental protocol of a binary ethanol aqueous battery cell, oscillating heat pipe. The purpose of this study was to introduce a plug-in oscillating heat pipe (OHP) for cooling the battery cell with binary-fluid mixtures of ethanol aqueous of electric vehicles. The result of the experiment implies that heat-pipe with cooling performance takes a hopeful elect for battery thermal management system of batteries in electric vehicles.

I.3.5 Combined cooling

Providing the suitable cooling system for electric vehicles lithium-ion battery ensuring better performance conditions, safety and saving energy become a necessity to think about while designing a lithium-ion energy project. Basic thermal management systems might show failures under some specific conditions. Including charge/ discharge cycles, external thermal conditions and the system thermal as well energetic capacity. For this reason, researchers are doing effort to propose cooling systems combining either between different passive cooling or between both passive and active cooling to benefits from the advantages of each cooling system. Weng et al. [89] designed an experimental heat pipe and PCM cooling system to study the influence of PCM on heat pipe thermal behavior. They coupled in this experiment a PCM in the adiabatic zone of heat pipe as illustrated in Figure I.24. Moreover, several types and volumes of PCM, different fan speeds and different heating powers were tested. The results unveiled that about 46% of the fan consumption could be reduced when using PCM type Tricosane. Those results prove the importance of several cooling systems which can lead to energy saving and reduce the cooling system cost as passive cooling system are cheaper and require less interventions. Furthermore, Chen et al [103] exposed the four cooling system’s effect on the performance, weaknesses and validity concerning the thermal control of lithium-ion batteries. Their

result show that the weight of cooling system is highest when using fins as cooling system while air cooling requires the most energy consumption. Direct and indirect liquid cooling were also tested and the indirect cooling is more performant.

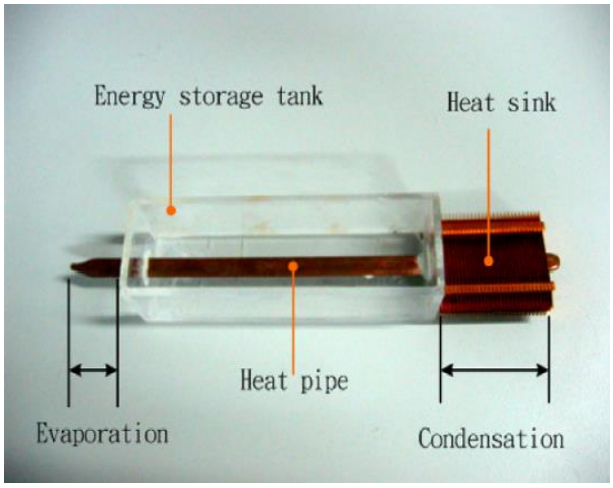

Figure I.24 Tested heat pipe with PCM in adiabatic zone Weng et al. [89].

Additionally, Zhao et al. [104] proposed a combined heat pipe with a condenser wetted by water to enhance cooling by evaporation. Four types of heat pipe and natural convection method are examined to be compared with the heat pipe and wet cooling method on two battery packs, 3Ah and 8 Ah (4S1P), during high-intensity discharge (1C,2C,3C). The results showed a lower temperature gradient and temperature rise in discharge tests in the combined cooling system as for the 3Ah battery pack the temperature elevations during tests are below 4 °C while for 8 Ah battery pack, the proposed system is able to ensure temperature under 30 °C with only four sprays of water. Despite the fact that cooling systems based on phase change materials (PCMs) overcome the lithium-ion batteries heating, they might show some thermal control failure due to some circumstances. A study of Ling et al.[105] took the heat accumulation caused by the bad conditioned cooling air for the PCMs cooling system. A forced air convection was implemented to test its ability to keep the lithium batteries under a PCMs based cooling system among the safety temperature of 60°C. Opposed to the passive thermo-physical properties of PCMs which leads to an over heat of the battery, the forced air convection succeeded to keep the battery heat under the limits of 50°C. This study added more prospects and solutions to the PCMs cooling system of lithium-ion batteries. Wu et al.[106] proposed a novel combined heat pipe assisted PCM system, experimental measurements were done to evaluate maximum temperature rise and temperature distribution. A comparison between no cooling system and heat pipe assisted PCM demonstrates the

efficient of this system as it increases operation time before attending 50°C in the system. Forced air convection ameliorate the system performance but increasing air velocity leads to fluctuation in PCM phase transition process. This study ended with new prospects for future designs and optimization of lithium-ion battery systems. Yamada et al. [107] inspected the thermal runaway of Lithium ion batteries resulting from abnormal heat generation inside batteries. A combined heat pipe and PCM system illustrated in Figure I.25 was designed and tested experimentally and numerically, obtained results show 30 °C degrees of reduction of battery temperature when using combined heat pipe and PCM comparing to only heat pipe-cooling system.

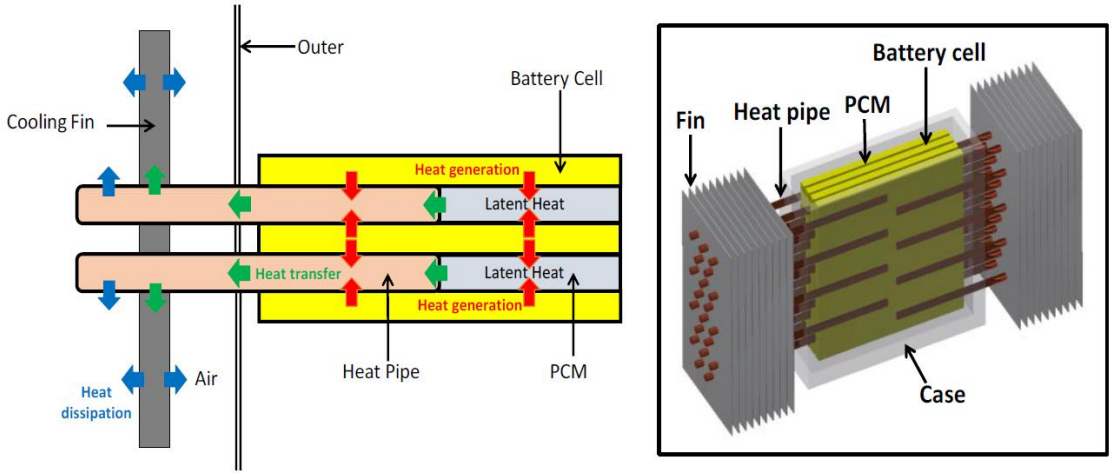

Figure I.25 Schematic diagrams of combined heat pipe and PCM suggested by Yamada et al. [107].

In addition, Zhao et al. [108] designed an air combined (HP/PCM) as presented in Figure I.26 aiming to analyze the performance on battery thermal control. The tested PCM reduces up 33.6% of the temperature rise and 28.9% of decrease when PCM is assisted with heat pipe compared to PCM. Moreover, a simple design of hybrid cooling system was constructed by Wei et al. [109] to test its efficiency in cooling lithium-ion batteries. This design was similar to the air-cooling system design with additional a duct allowing the coolant to move around through an inlet and an outlet linked with a duct. To release the heat from the battery, the design contained also a collection of hydrophilic fiber channels with water coolant, the forced air theory was applied at this point. This hybrid cooling system was able to keep the main aimed results within the norms. It succeeded to maintain the average surface temperature within an excellent average only 30.5 °C. It, also decreased the temperature uniformity starting from 12.5 °C as a primary temperature no cooling case to only 2.1 °C as a controlled temperature

under the experimental conditions. This hybrid cooling design allows a decrease of temperature up to 73.5% to 85.7%. The air-cooling and the water-cooling systems couldn't reach only 32 °C to 50% compared to the other typical water or air-cooling systems. This hybrid design ensured a better performance with low thermal averages for a lithium-ion energy-based system.

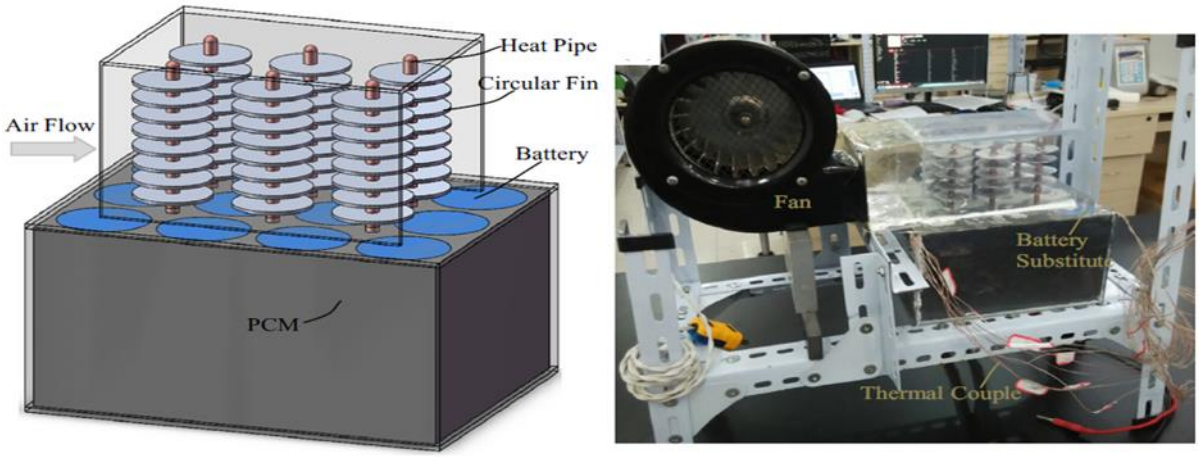

Figure I.26 Schematic diagrams of combined air (HP/PCM) proposed by Zhao et al. [108].

Huang et al. [110] experimentally investigated cooling system for cylindrical batteries. PCM heat pipe air-cooling/ liquid systems were tested. This study took phase-change materials PCM as the main material to design the experimental cooling system. A lithium-ion battery module was used in this experiment and a large capacity and heat resistance PCM cooling system was designed. The cooling system included a cylindrical lithium-ion battery, a heat pipe linked with air assisted phase change material (PCM/ HP-AIR), another heat pipe coupled with liquid assisted phase change material (PCM/HP-Liquid) see Figure I.27. During discharge cycle and under and applied discharge current of 3C rates. The results show that the temperature of battery module reaches 44 °C after 1160 s when testing the PCM/HP combined with liquid cooling system as shown in Figure I.28. This temperature is achieved after 1124s for the PCM/HP combined with air cooling and finally for only PCM cooling, the battery module temperature rises to 44 °C after 1103s.

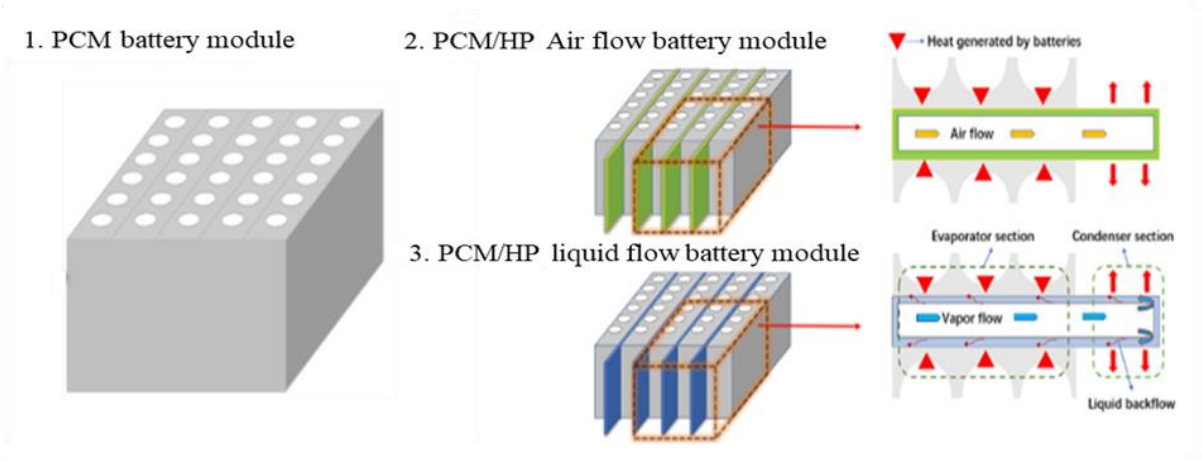

Figure I.27 Proposed battery cooling configurations investigated by Huang et al. [110].

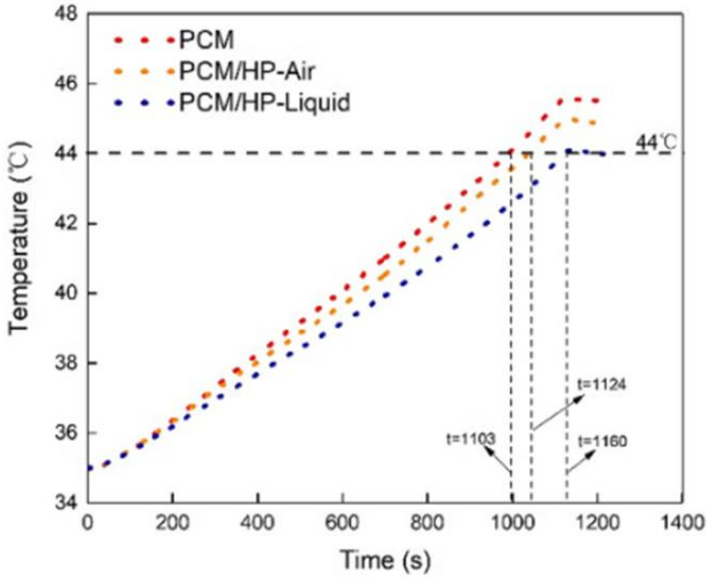

Figure I.28 Comparison of temperature variation for the three studied configuration under 3C rate during discharge cycle [110].

Additionally, a response surface methodology (RSM) based study was conducted by Ling et al. [111] to provide higher cooling system with low weight. This study was conducted by minimizing the PCM mass by adopting an optimization method, which adopts both active and passive cooling systems in parallel. The analyses of the variables PCM system, the active/passive cooling variables has shown a wide effect on the system thermal performance and configuration. Adopting a certain size and weight couldn't be done without making an optimal design for this hybrid TMS system, which ended up with

saving over 94.1% of the PCM system mass and 55.6% if the volume. These experimental conditions provided till 37°C ending out the standards of less than 3 °C. Providing this ideal low weight in parallel with high performance to the cooling system in addition to its practical structure, the hybrid system proved its efficiency with comparison to the conventional liquid cooling system. Deeper, one of the primary criteria that an effective thermal management system should reflect is its large capacity to maintain high amounts of temperature for higher safety and performance of lithium-ion battery-based systems. Therefore, Bai et al. [112] investigated the phase change slurry (PCS) based thermal management and mini channel cooling plate for the lithium-ion pouch battery module. In order to balance between the energy consumption and the PCS cooling performance, these elements were tested through a three-dimensional thermal modal design linking the cooling plate with mini channel following the orthogonal matrix experimental method. Despite the practicality phase changed material has shown through high temperature reduction and low costs, this latter has limited development chances due to low thermal conductivity. As a solution, Qu et al.[113] in their experimental study increased the PCM system thermal performance by adopting an oscillating heat pipe working as a thermal transfer device. In the experimental design, a regular OHP and 3D-OHPs were implemented for a better PCM thermal performance. Two experiments were conducted to test the thermal performance of the PCM system with two distinct designs based on OHP, for the first one, PCM linked with two kinds of novel 3D-OHPs (4 layers 3D-OHP and 3 layers 3D-OHP) and for the second one PCM coupled with multiple 2D-OHPs system. For the regular OHP case, paraffin wax melted faster than the 3D-OHP former system. Consequently, the 4 doubled layers' paraffin wax took less time to solidify again. This study revealed that paraffin wax/3D-OHP system provides better thermal condition for an efficient PCM system. Figure I.29 presents the proposed oscillating heat pipes systems tested by Qu et al.[113] to enhance the PCM efficiency. To summarize the different combined-cooling results in literature the Table I.4 presents a comparison between different studies performed on battery combined cooling systems.

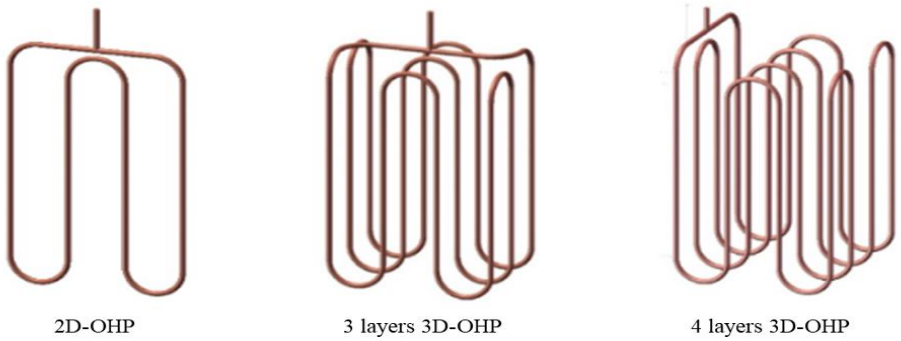

Figure I.29 Proposed oscillating heat pipes systems developed by Qu et al.[113].

Table I.4 Summary of combined cooling results from literature.

Author (s)	Number of cells	Cooling systems	Characteristics	ΔT	Remarks
Mashayekhi et al. [114]	3 cylindrical cells	hybrid cooling	PCM and Al2O3 nanofluid in aluminium minichannels	15.5% in active method and 8.5% in hybrid method	TMS using heat cartridges to model Li-ion batteries
Behi et al.[115]	24 cylindrical cells	Air and heat pipe cooling	heat pipe with copper sheets (HPCS)	42% compared to natural air cooling	cell spacing, air velocity, different ambient temperatures
Heyhat et al. [116]	1 cylindrical cells	hybrid cooling	Thermal energy storage composites of PCM, metal foam, fin and nanoparticle	Metal foam: up to 4°C and 6°C	Phase change material Battery thermal management system heat transfer enhancement
Kong et al.[117]	24 cylindrical cells	PCM+liquid cooling	PCM and optimized controllable strategy different ambient temperatures	4°C	cell-to-cell spacing cell-to-tube distance
Kiani et al.[118]	9 cylindrical cells	Nanofluid cooling	Active/passive methods	77% of maximum temperature reduction	Lithium-ion battery thermal management Al2O3/AgO/CuO nanofluids and phase change material
Dan et al.[119]	96 prismatical cells	Array-air cooling	Micro heat pipe	2°C	equivalent thermal resistance model is developed for MHPA based on thermal circuit method
Gan et al.[120]	12 cylindrical cells	Heat pipe and cooling plate	Heat pipe Thermal equivalent circuit model	14°C	Heat pipe-based thermal management system for a Li-Ion battery.

I.3.6 Internal cooling

After discussing in previous section different active and passive external battery thermal management systems. In this section, another promising internal cooling system is in progress in last years. Highlighting the internal cooling in our study is very important and will display the gap in this part to researchers. In this context, Mohammadian et al. [121] performed a numerical study to compare the internal and external cooling methods using electrolyte as a coolant by micro channels inside the electrodes of the lithium-ion battery. The results show that internal cooling causes increasing the convection heat transfer and a regulation better than the external cooling. Moreover, the study performed by Shah et al. [122] aimed to investigate the cooling of Li-ion battery using an air flow inside a centered annular channel in a case and heat pipe fixed in the central axis to cool the battery core as show in Figure I.30 based on experimental and numerical models. The method used for the investigation indicates that the cooling was effective and causes a well thermal reduction through to the cell core higher than 18°C in the case of heat pipe cooling. Furthermore, as discussed below Phase change material (PCM) could be used as an efficient cooling system to ensure limiting battery temperature rise. Thus, Zhao et al. [123] proposed an internal cooling system based on PCM . They tested the battery internal cooling system by optimization of a phase change material using 40 cylindrical batteries. The results prove that the internal cooling is a space-saving method that eases the implementation of the high energy density of the lithium-ion battery pack. In addition, Gou et al. [124] designed a cooling method based on PCM and PCM combined with heat pipe as novel internal cooling system. The obtained temperature for PCM cooling is limited on 35.5°C while it decreases to lower than 31.5°C when PCM is combined with heat pipe.

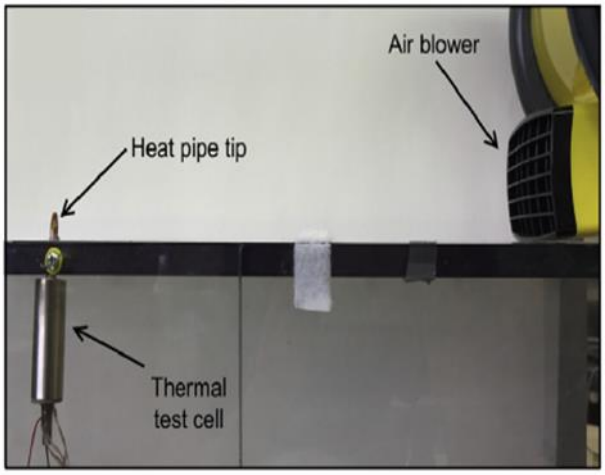

Figure I.30 Proposed internal heat pipe cooling system by Shah et al. [122].

The battery thermal management system ensures longer life and better performance of the lithium-ion batteries through a simplified heat cooling system. It controls the batteries heat with low costs and energy waste. More experimental studies are recommended to be performed to analyze different internal cooling strategies and to propose optimized systems.

I.4 Synthesis and Conclusion

This bibliographic study highlights technical issues limiting the progress of Li-ion batteries use in electric vehicles. During operating time, two main heat sources are generated due to entropy change and Joule effect which cause an undesirable thermal behavior of Li-ion battery. As the chemical properties are often unknown due to the confidentiality adopted by the manufacturers to the internal composition of batteries, and as they are also strongly impacted by the applied current, the experimental characterization of the commercialized battery is primary to analyze and its thermal behavior and to develop an accurate the thermal model. Li-ion batteries are subjected to unfavorable operating conditions, especially when grouped in packs, and in applications requiring high power. In some cases, the maximum temperature recommended by the manufacturers may be exceeded. To avoid safety risks, improve performance and increase battery life, researchers are developing technologies to keep batteries within the optimal temperature range.

In fact, understanding the thermal behavior of a Li-ion battery is the main key factor to enable sizing an efficient cooling system. Many studies have elaborated an analysis to batteries thermal behavior based on experimental measurements and numerical models. The most of efforts were concentrated on testing different current rates especially during discharge as high current may be applied during discharge compared to charge cycles. This why we think that applying consecutive charge and discharge cycles will contribute to a better understanding to the thermal behavior of Li-ion batteries and the maximum temperature rise could be defined for a given charge and discharge current.

In Addition, developing a numerical model requires the determination of several parameters characterizing the thermal behavior of Li-ion battery such as the internal electrical resistance, the entropic heat coefficient, the specific heat capacity, the thermal conductivities and the heat transfer coefficients. Those parameters may be determined either experimentally or based on given data in literature. Furthermore, the determination of those parameters is essential to solve the heat transfer equation. However, it is evident that the development of simplified correlation enabling fast

determination of the battery thermal behavior will attract the attention of scientist and industries working on batteries.

Many cooling systems were tested in different studies to ensure controlling the temperature rise of batteries during operating time and under different test conditions. The active cooling systems is widely used in EVs. Recently, researchers are more focusing on studying the efficiency of some passive cooling systems based on phase change material (PCM) and heat pipe as they present an advantage on no energy consumption. Nevertheless, more concentration should be given to the efficiency of those systems taking in consideration the rise on cooling system mass impact on the required electrical motor power.

Finally, based on our state of art study on the battery thermal management systems. Our experimental and numerical study will focus on a description of the thermal behavior of a Li-ion battery first. Then, a numerical model is developed and validated with experimental measurements. The developed numerical models in this thesis are able to solve heat transfer equation in one battery using alternating directive method (ADI) in a side and also able to predict the temperature rise of a battery pack combined with PCM under both constant and dynamic current deduced from normalized driving cycles.

Chapter II. Experimental study of a Li-ion battery thermal behavior

II.1 Introduction

The literature review presented in the previous chapter shows the necessity of understanding the thermal behavior of Li-ion batteries which will enable the proposition of an efficient cooling strategy. For this motive, in this chapter, an experimental study has been performed in order to investigate and analyze the thermal behavior of a prismatic 60Ah LFP battery during consecutive charge and discharge cycles. A description of the experimental test bench is presented as well as measurements methods. Different currents rates were applied and obtained results of temperature and heat flux measurements are discussed. An analysis of temperature distribution on the battery sides and its symmetry is carried out. The results presented in this chapter are used to develop the 3D thermal model and in sizing an efficient cooling system.

II.2 Description of the experimental test bench

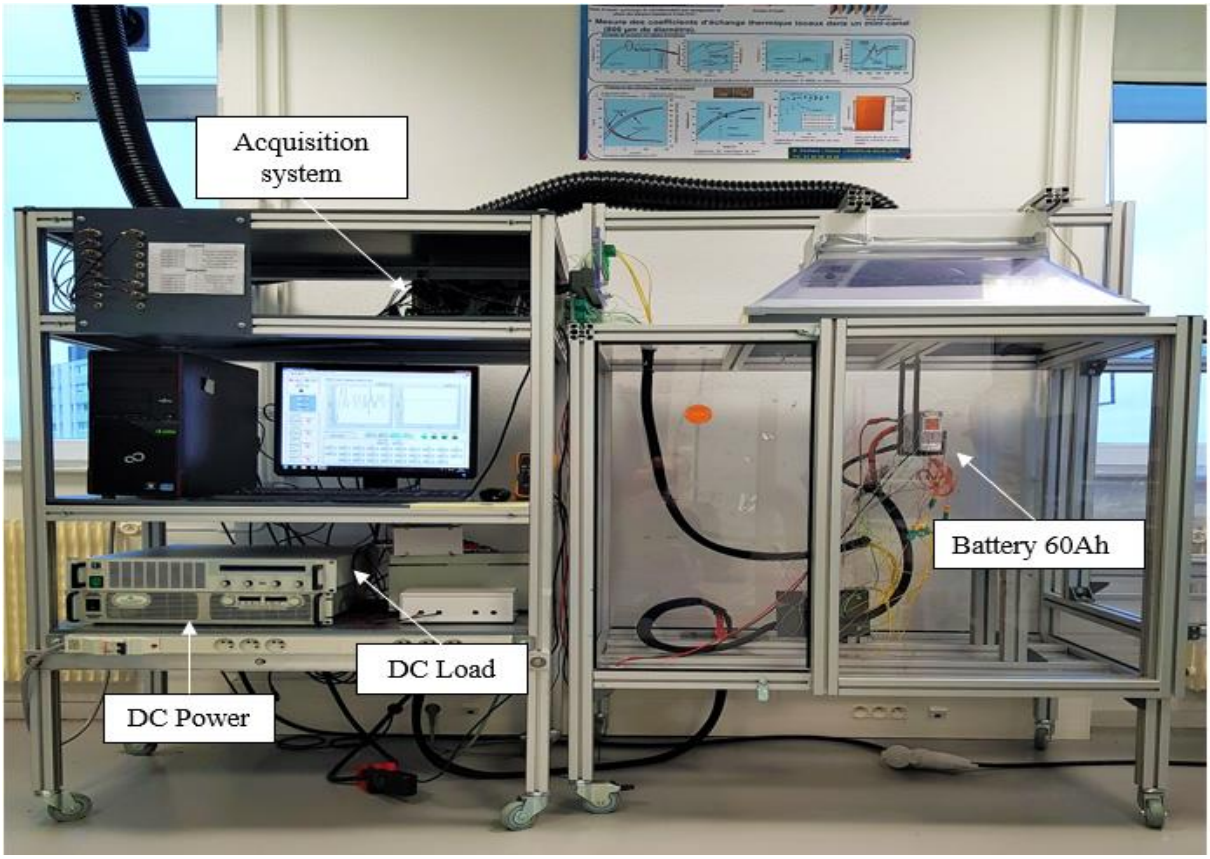

(a)

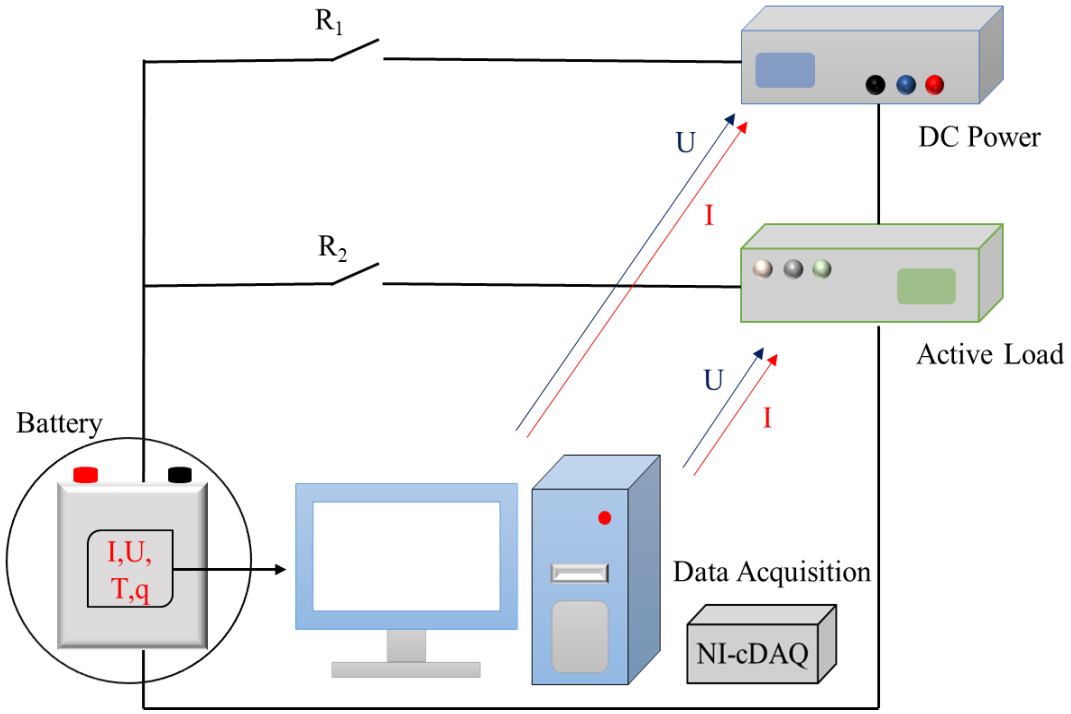

(b)

Figure II.1 Experimental setup (a) components (b) electrical circuit scheme.

The experimental test bench illustrated in Figure II.1.a. is implemented to carry out the thermal characterization of a prismatic LFP battery during charge and discharge cycles. It is composed of a DC power supply, a DC Load, several thermocouples and heat flux sensors, a voltmeter, a current probe and a National Instrument DAQ device for data sampling. The CALB (CA60AHA) LFP battery is tested in the operating voltage range of 2.6V and 3.6V see Figure II.1.b The DC power supply used to charge the battery is the GEN40-125 (fabricated by GENSYS). The power supply characteristics are maximal voltage, current and power values of 40V, 125A and 5000W, respectively. The battery is subsequently discharged by the DC active load EA-EL 9080-200 (constructed by Elektro-Automatik). The DC load characteristics are a maximal voltage, current, and power of 80V, 200A and 2400W, respectively see Table II.1 The characteristics of used equipment's in experimental setup.. Measurements are collected using the National Instrument (NI-cDAQ) device, with a data sampling of 1mes/second.

Figure II.2 illustrates the LabVIEW user interface used all along the tests to perform both the charge and discharge cycles. Particularly, both the charge and discharge current, the maximal and minimal voltage, and the SOC values are controlled.

Table II.1 The characteristics of used equipment's in experimental setup.

Equipment	Specifications	Uncertainties/Range
The CALB (CA60AHA)	Prismatic LFP battery	60 Ah
GEN40-125	DC power supply	(0V-40V) (0A-125A)
EA-EL 9080-200	DC Load	(0V-80V) (0A-200A)
Pico technology TA167	Current, I(A)	10 mV/A
115 Fluke, voltmeter	Voltage, U(V)	±0.2 V

Figure II.2 LabVIEW program user interface.

Moreover, Figure II.3 shows the flow diagram implemented in the LabVIEW program. During each test the battery is 'N' times charged and discharged. Tests are performed in the same voltage range (min 2.6V-max 3.6V) fixed to ensure the fully charge and discharge range of the battery.

The purpose of those tests is to study the effect of increasing current on battery temperature and heat generation. Consecutive cycles are applied to experimentally visualize the thermal regimes which are transient regime and quasi-stationary regime. Experimental data are analyzed first in both transient regime and quasi-stationary regime to study the local surface temperature. Then, different current ratios are applied to the battery. According to literature [125], high temperatures should be measured for high C-rate due especially to the irreversible heat which is proportional to the square of the current. Coulomb counting method is used to estimate the battery SOC, the principle of this method is supposing the existence of a fixed quantity of energy and normalized as (1), if battery is fully charged [126].

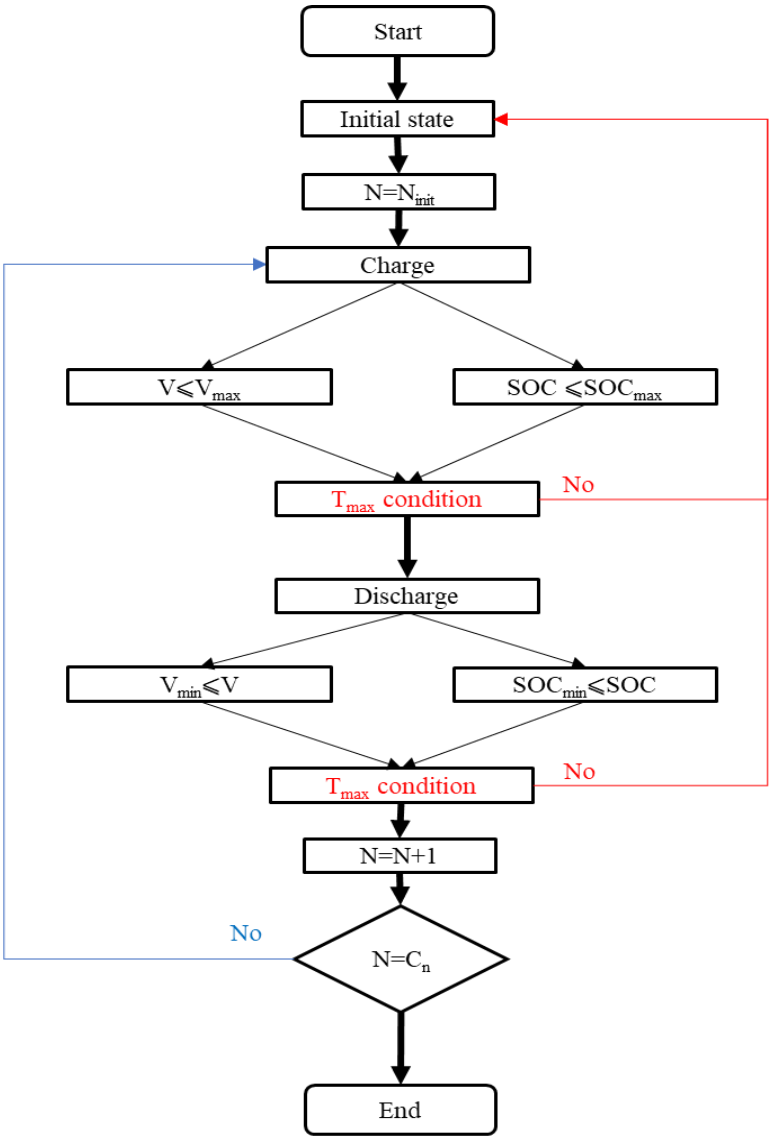

Figure II.3 Flow diagram of LabVIEW program.

II.2.1 Battery instrumentation

Figure II.4 shows thermocouples and heat flux sensors inserted on the battery surface. 5 K-type thermocouples were embedded inside the battery shell which has a thickness of 4mm; a thermal adhesive was used to fix them. The heat flux sensors used are the OMEGA (HFS4); each one of them is equipped with a K-type thermocouple. A thin copper plate was attached to the HFS to ensure the contact with the battery surface. The K-type thermocouples were attached on the battery external surface by an aluminum tape.

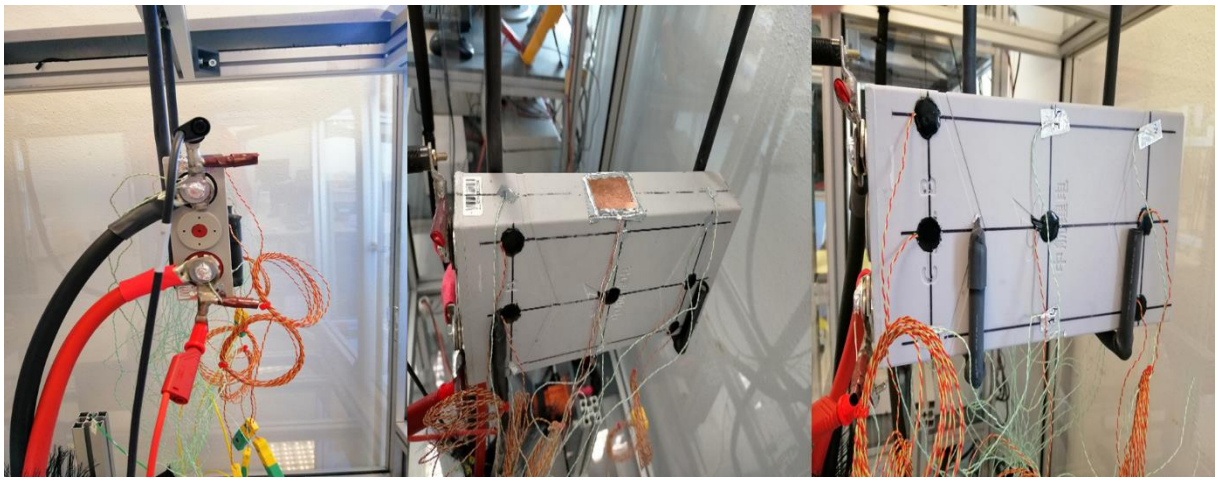

Figure II.4 Pictures of thermocouples and heat flux sensors inserted on the battery.

Moreover, the thermocouples' numbers and their locations on the tested battery are proposed in Figure II.5 Five thermocouples (T_{24}, T_{25}, T_{26}, T_{27}, T_{28}) are embedded in the battery shell to measure the active material temperature. While, three heat flux sensors were inserted on the center of battery front, right, and base sides.

A P600 precision thermometer and a Poylstat 36 thermostatic bath are used to calibrate K-type thermocouples. Figure II.6 illustrates an example of calibration curve for a K-type thermocouple. Furthermore, the heat flux measurements are obtained using the transfer function provided by the sensors' manufacturer. The thermocouples and heat flux sensors uncertainties are given in Table II.2.

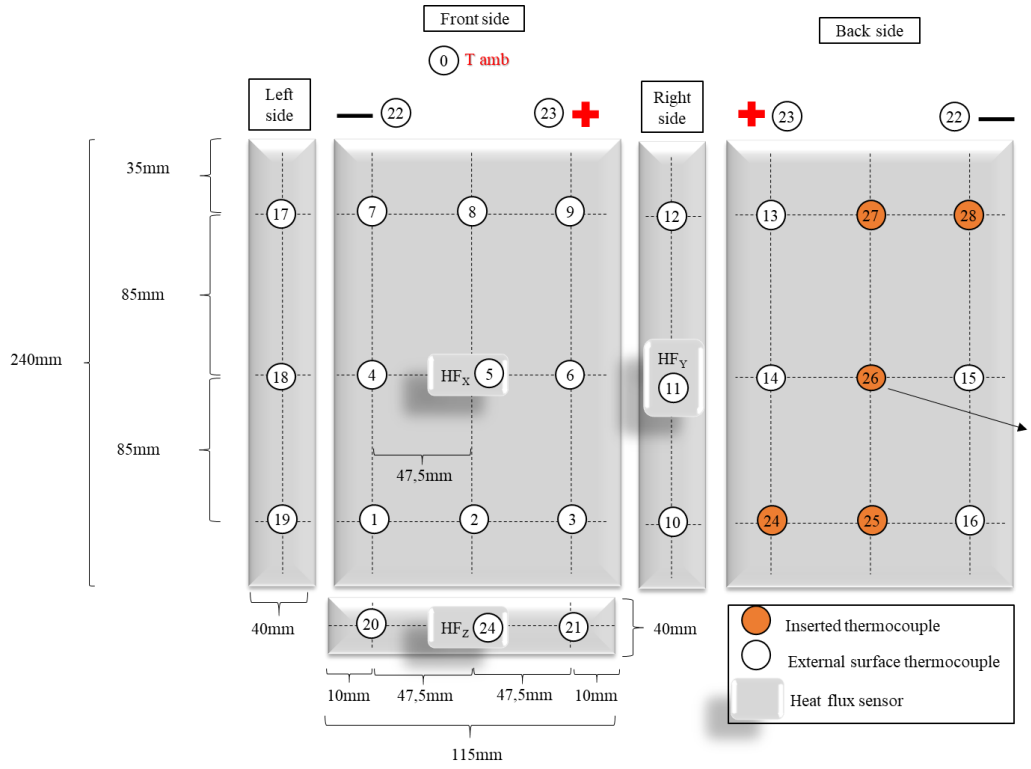

Figure II.5 Scheme of the thermocouples and heat flux sensors location on the battery.

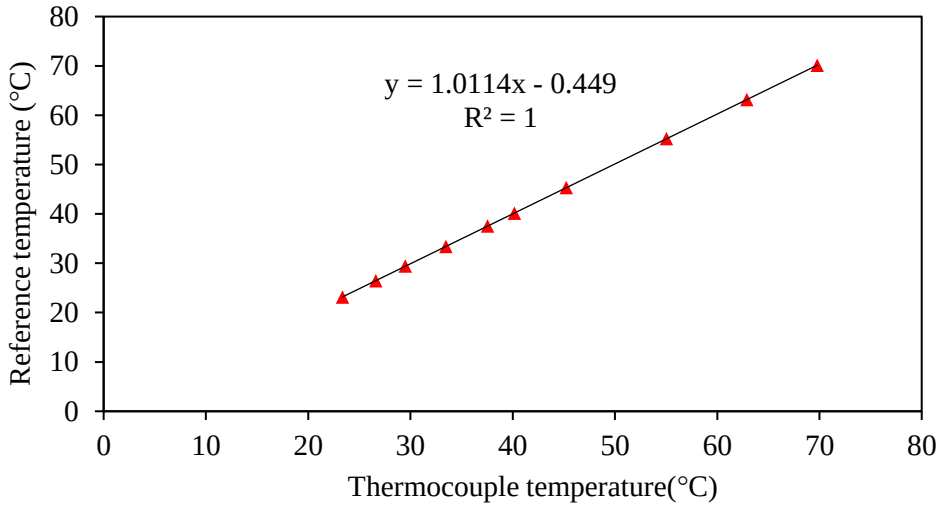

Figure II.6 Calibration curve of one thermocouple.

Table II.2 Uncertainties for different parameters involved in the experimental tests.

Parameter	Uncertainty
Temperature, T (°C)	$\pm 0.3\ °C$
Heat flux, Φ (W/m^2)	$\pm 3\%$

II.2.2 Battery internal composition

The chemical reactions inside the battery during operating time cause several mass and heat transfer phenomena. Analyzing the battery internal composition is a key factor to better describe its thermal behavior. The battery core is composed of a graphite anode, LFP cathode and a separator. The internal composition of the tested battery is presented in Figure II.7 The internal architecture of the battery is composed of layers, the decomposition of our commercialized battery at Elecsys France shows that the different layers are parallel to the (yz) plane. During the charge process, Lithium ions leave the positive electrode and are inserted into the crystalline structure of the negative electrode, while during the discharge process, these ions are extracted from the negative electrode and are intercalated into the structure of the positive electrode. This migration of lithium ions takes place through the electrolyte. In addition, the released electrons are transferred through the external circuit to the negative electrode during the charge process and to the positive electrode during the discharge process, which provides the generation of an electric current.

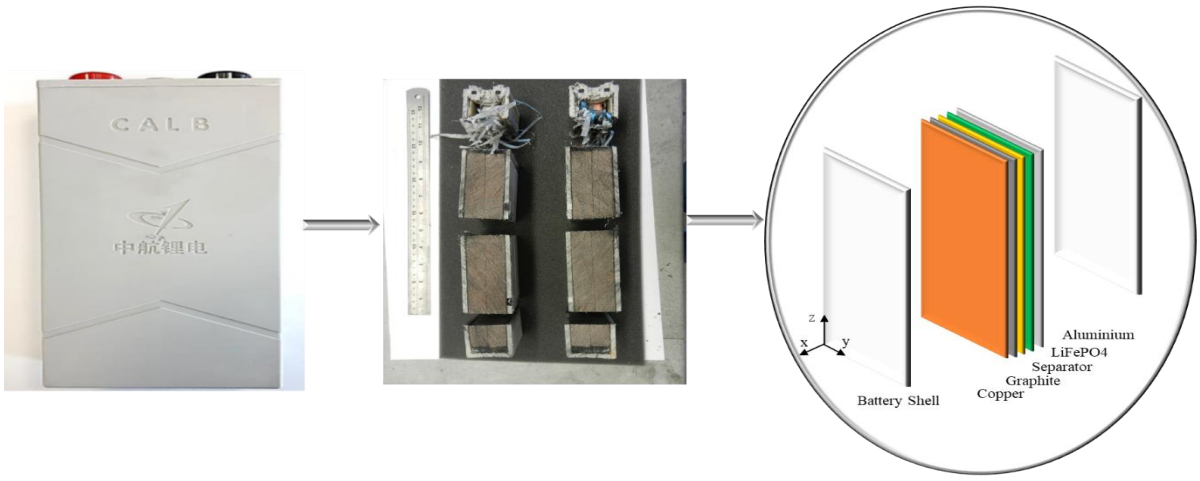

Figure II.7 Decomposition of tested battery and its internal components.

Indeed, the non-controllable thermal behavior of batteries appears when high currents rates are applied [127], which causes the battery aging [128] . Furthermore, the heat produced by the battery could be defined as the sum of the Joule heat which is the irreversible part and the heat due to the entropy change which forms the reversible part [129]. The irreversible heat is due to the current flow inside the battery during charge and discharge. While the reversible heat is caused by the entropy change during the insertion and disinsertion of Li-ions in the structure of electrodes. Moreover, two other sources of heat could exist in during battery operating time: the heat generated by secondary reactions and the heat of mixing. The secondary reactions are related to aging and could be neglected when using a new battery. The heat of the mixture is caused by the creation and relaxation of internal concentration gradients. Thus, the cumulative heat absorption and release is zero and this term can then be neglected [130].

The heat generation amount depends on several factors such as SOC, current, battery initial temperature and battery SOC. In this study, the electrical properties are considered to be dependent to the SOC, and therefore on time. Experimental tests are carried out first to study the thermal symmetry of the battery external surfaces.

II.2.3 Preliminary test

II.2.3.1 Capacity measurements

The preliminary test conducted on the battery are capacity measurements to enable the determination of the SOC. The Constant current (CC) mode is widely used as a battery charge and discharge protocol. To determine the capacity of battery, the battery is first charged via CC mode until reaching the maximum recommended voltage 3.6 V. Then a constant voltage protocol is applied until reaching a current of 0.1 A. At this point the battery is considered charged at 100%. Same CC-CV protocol is applied during discharge until reaching the minimal recommended voltage of 2.6 V. Figure II.8 shows the obtained profiles of current and voltage during applied CC-CV protocol to measure the battery capacity. The obtained capacity calculated during discharge is 60.76 Ah.

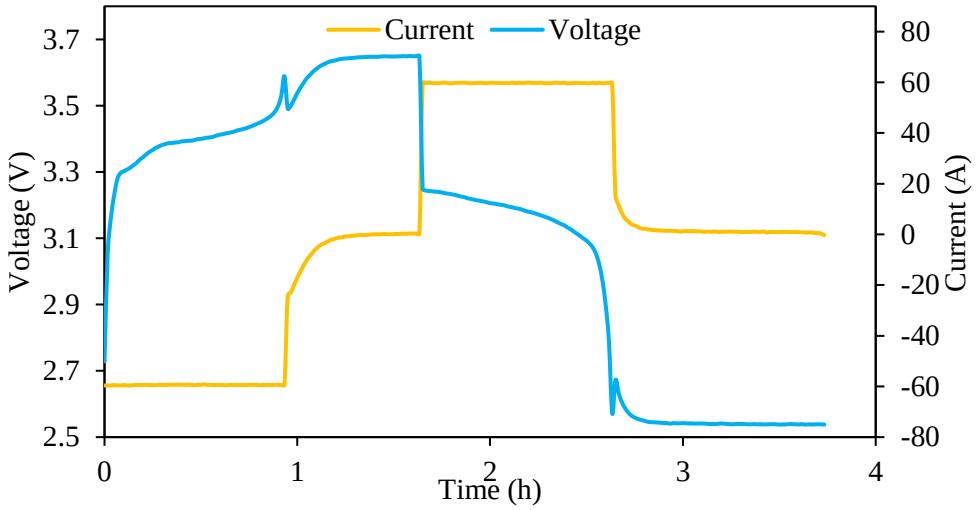

Figure II.8 Battery Capacity measurement test.

The upper and lower voltage recommended by the battery manufacture are (3.6 V, 2.6 V) and the maximum current during charge and discharge are respectively 60 A (1 C) and 120 A (2 C). To highlight the effect of current on battery capacity three charge currents were applied (40 A, 50 A, 60 A) and five discharge currents were tested (40 A, 50 A, 60 A ,80 A, 100 A). Figure II.9 show the voltage variation versus battery capacity during charge and discharge. Only CC mode were applied. The comparison shows that the capacity could be considered similar during charge and discharge. Based on these results, we could define a normalized SOC which will enable us to compare the temperature and heat flux for different C-rates versus the battery SOC (see equation II.1).

$$SOC = SOC(t-1) - \frac{I(A)t(h)}{C(Ah)} \qquad \text{II.1}$$

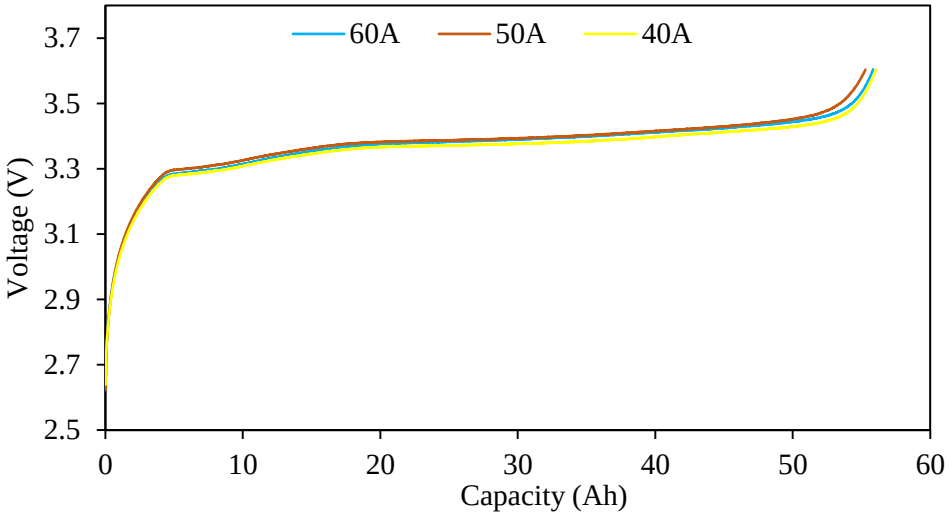

(a)

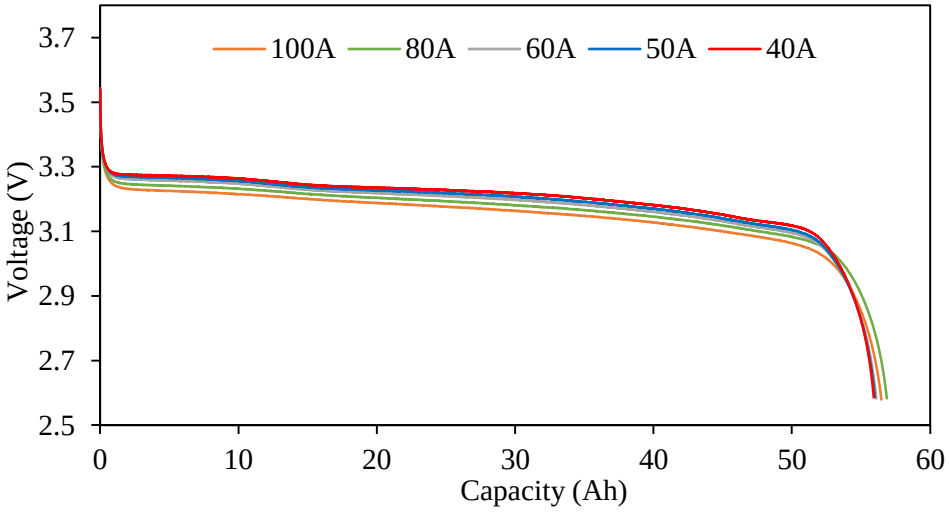

(b)

Figure II.9 Voltage variation versus battery capacity during (a) charge (b) discharge.

II.2.3.2 Initial temperature

The experimental tests are conducted under natural convection. The ambient temperature isn't necessarily the same during test time. To ensure the repeatability of the experimental test same current rates on the tested battery in different tests and the experimental results were compared. Figure II.10

presents the results of the battery temperature rise measured by one chosen thermocouple and the ambient temperature. The initial temperature isn't similar in the test and ambient temperature shows a different profile during test time. Moreover, the comparison of the battery temperature and ambient temperature difference shows similar profiles (see the yellow and green curves). Based on this conclusion the comparison of the test will be performed taking in consideration the effect of ambient temperature. In addition, Figure II.11 illustrates the comparison of the temperature difference during both tests 1 and 2. The results show repetitive results as the maximum difference obtained between both tests was obtained in thermocouple (15) and the calculated difference is 0.34 °C. This difference is equal to the uncertainty of measurement of the thermocouples given in Table II.2.

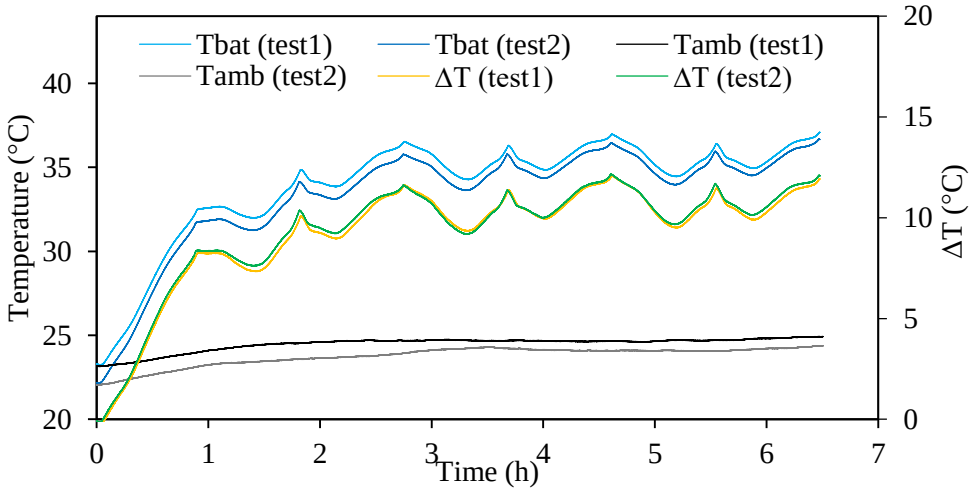

Figure II.10 Effect of initial temperature test1 (25/06/2019) test 2 (20/06/2019).

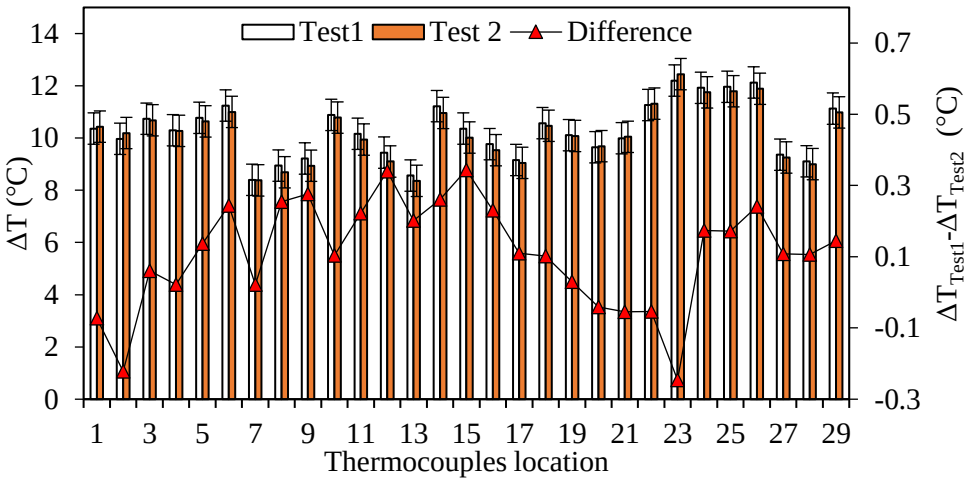

Figure II.11 Comparison of temperature difference for all thermocouples.

II.3 Characterization of thermal regimes

II.3.1 Consecutive charge/discharge cycles

Experimental measurements of battery surface temperature are conducted for 1 C charging/discharging cycles. 3.4 V was defined as the cut-off voltage for this test, which permits performing more cycles during the test. 11 charge/discharge cycles were applied. During each cycle period constant current is imposed and the voltage varies from 2.6 V to 3.4 V. A direct switch from charge to discharge with no imposed rest time. Heat is then generated inside the battery during all test time and a quasi-steady state is supposed to be reached as the battery is tested under natural convection. Figure II.12.a presents the curves of voltage and current during battery operating time. Moreover, Figure II.12.b shows a comparison between the measured temperature in the battery front and back sides, while Figure II.12.c illustrates this comparison in the battery left and right sides and Figure II.12.d displays the comparison between obtained local measured temperature in battery base and top sides. It is possible to notice two thermal regimes: transient and quasi-stationary regime. The maximum temperature of 35.5 °C is obtained at the end of the discharge cycle. This is mainly related to a rise in heat generation. It is also possible to state that, the maximum temperature is obtained in the center of the battery (T26). Therefore, the active material temperatures measured by the internal thermocouples (T25, T26) are higher than the surface temperatures given by T2, T5, T8 due to the battery shell effect. Finally, the lowest temperature is obtained in battery upper front side (T8) where no active material is implemented, in accordance with the battery internal composition shown in Fig.6. A difference of 3°C approximately, is obtained between the maximal temperature (T26) and the minimal temperature (T8) in quasi-stationary regime. Concluding, even if the measured temperatures profiles show similar trends, it is possible to state that, their values vary with respect to the distance between the sensors' position and the battery active material location. Consequently, a real difference between the measured surface temperature and the internal battery temperature is stated.

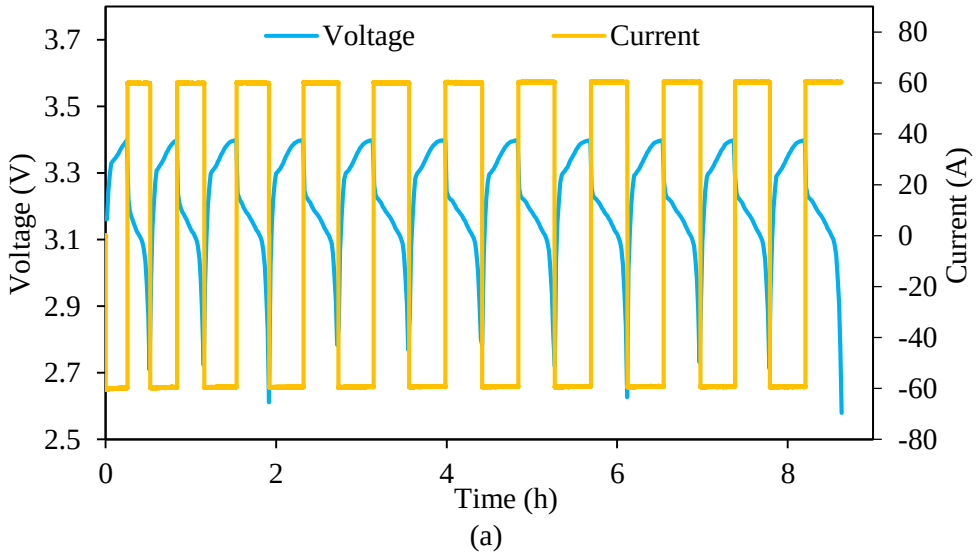
Voltage
Current
Voltage (V)
Current (A)
Time (h)
3.7
3.5
3.3
3.1
2.9
2.7
2.5
80
60
40
20
0
-20
-40
-60
-80
0
2
4
6
8

(a)

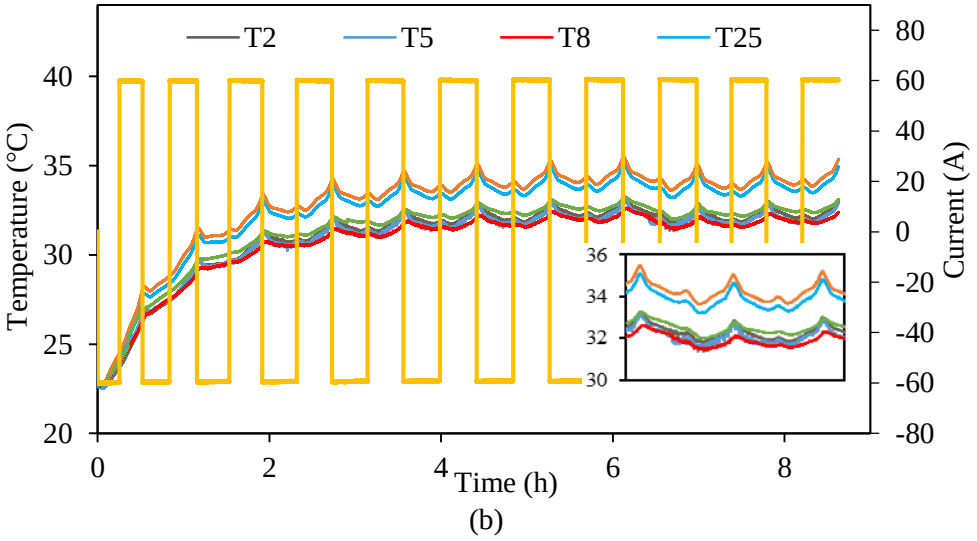
T2
T5
T8
T25
Temperature (°C)
Current (A)
Time (h)
40
35
30
25
20
80
60
40
20
0
-20
-40
-60
-80
0
2
4
6
8
36
34
32
30

(b)

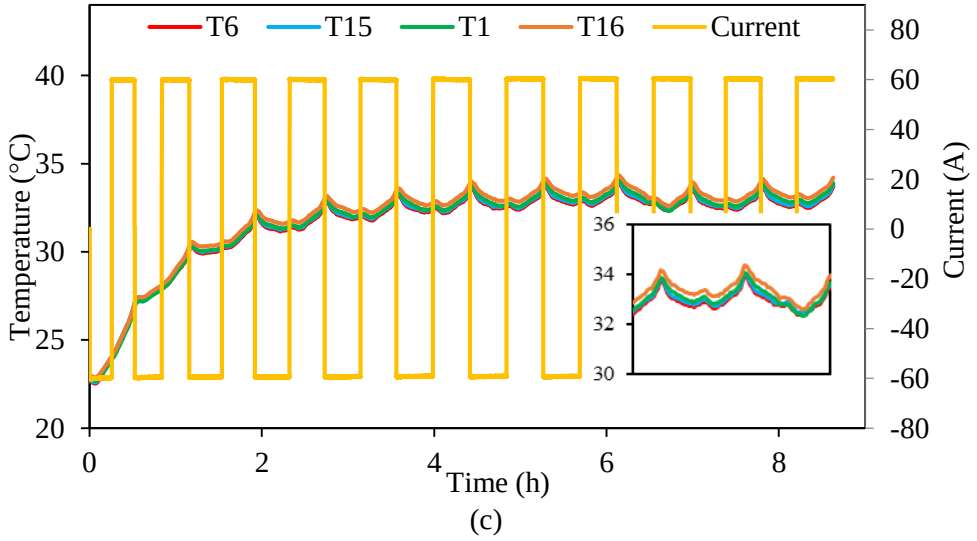
T6
T15
T1
T16
Current
Temperature (°C)
Current (A)
Time (h)
40
35
30
25
20
80
60
40
20
0
-20
-40
-60
-80
0
2
4
6
8
36
34
32
30

(c)

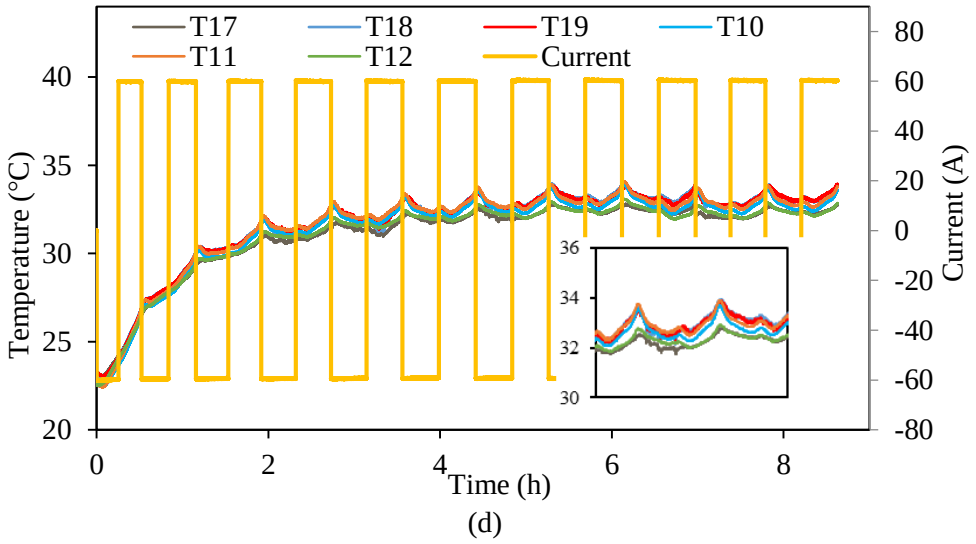

Figure II.12 Battery surface temperature profiles during 1C rate (a) voltage and current profiles, (b) surface and embedded thermocouples, (c) surface thermocouples in front and back side, (d) left and right side.

II.3.2 Maximum local temperature measurements

The experimental tests are first conducted to verify the symmetry. A comparison between the measurement taken by each thermocouple in (front/back) sides, (right/left) sides and (base/top) sides. This comparison helps in verifying the symmetry of temperature rise in each side and to display the effect of battery external shell. Figure II.13 illustrates this comparison between the obtained temperatures during a consecutive charge and discharge test with an applied current of 60A. It is to be noticed that in Figure II.13.a. the comparison is performed between thermocouples inserted in the battery sides and others embedded inside the battery shell (locations 2,3,5,7 and 8). This comparison is very important as it clarifies the effect of battery shell, the difference between the thermocouples in location is about 2.31 °C which proves the importance of not neglecting the internal thermal state on characterizing the battery thermal behavior. Moreover, the difference between thermocouples in location 8 is 0.25 °C even though one thermocouple is inserted in battery side (T_8) and the symmetrical one is embedded inside the shell (T_{27}). This result is justified by the internal composition of the battery, as we remarked, after the decomposition of the battery that no active material is placed in this part which causes no heat generation in this part. Besides, the symmetrical thermocouples inserted in the external surface show approximately same temperatures in both right and left sides (see Figure II.13.b).

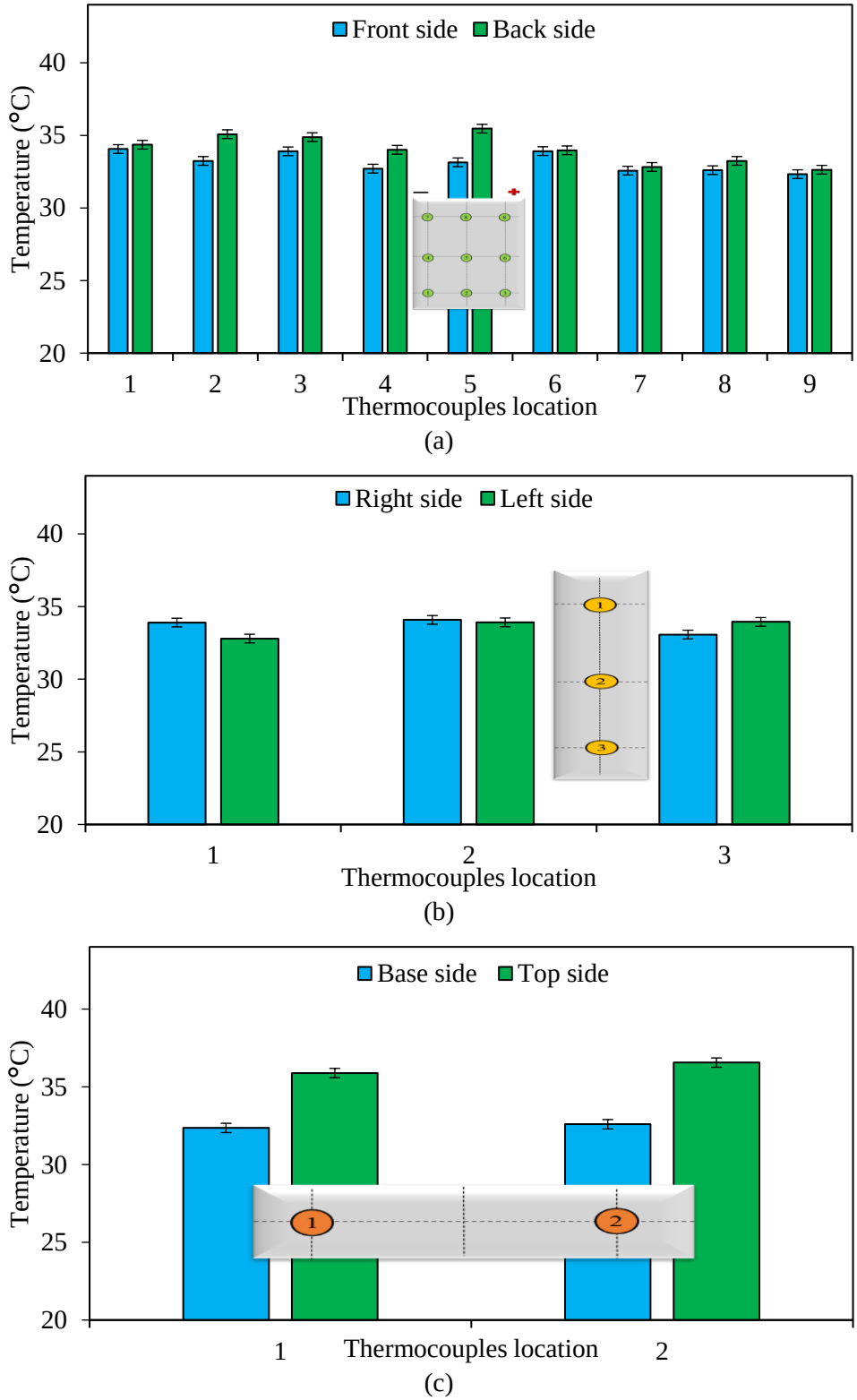

Figure II.13 Maximum local temperature (a) front and back side (b) left and right side (c) base and top side.

Additionally, the comparison between thermocouples in battery base and top sides presented in Figure II.13.c shows a large difference due basically to electrode collectors' which reflects more the battery core temperature.

II.4 Electrodes collectors' temperatures measurements

Consecutive charge and discharge cycles were applied on the tested battery to characterize its' thermal behavior. Figure II.14.a presents the curves of voltage and current measured during this test, the C-rate is kept constant at 1C rate during charge and discharge cycles, and the voltage variation is limited in the range of 2.6 V to 3.6 V. Figure II.14.b. shows the battery maximum and minimum local temperatures (T_{max},T_{min}), which are respectively measured by thermocouples (T_{26}) and (T_8), the electrodes temperatures (T_{e+},T_{e-}) are measured by thermocouples (T_{23}, T_{21}). Moreover, it illustrates that the temperature measured at the negative electrode (black profile) is lower than the temperature measured at the positive electrode (red profile), because of the different electrical resistance of aluminum (Al) and cupper (Cu) materials used in the positive and negative electrodes which provides different Joule heat generation in electrodes. However, both the electrodes' temperatures profiles are closed to the internal highest temperature profile measured by (T_{26}). This behavior is consistent with the heat generation rate, which is supposed to be higher at the battery electrodes [131] , such as for the active material of the battery core. Furthermore, also for the temperatures measured at the electrodes, a difference of about 3 degrees can be stated with the minimum temperature measured at the center of battery upper front side (T_8). Focusing on the quasi-stationary regime of the highest temperatures' profiles, it is possible to state that the occurrence of the temperature local maxima is in phase with the load variation introduced by the charge/discharge cycling switch, while the local minima are located in the middle of the charge and discharge steps. During the charge cycle (constant negative current), temperature decreases from the local maximum value. A similar behavior is observed during the discharge cycle. Moreover, during the quasi-stationary regime, the maximum local temperature is approximately equal to negative electrode temperature in the beginning of charging cycles in the quasi-stationary regime while it is approximately equal to the positive electrode temperature in the beginning discharging cycles.

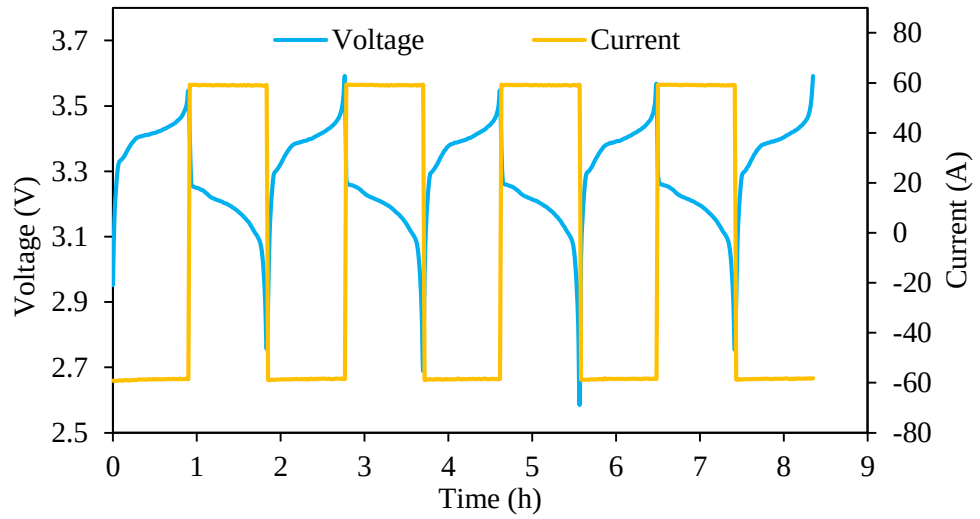

(a)

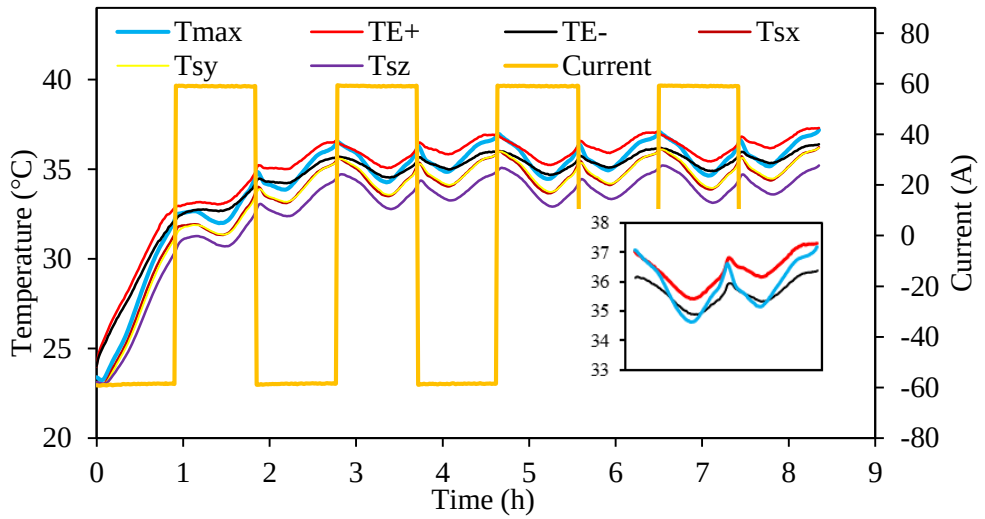

(b)

Figure II.14 Consecutive charge and discharge cycles for 1C rate (a) voltage and current curves (b) temperature profiles.

II.5 Effect of current on battery temperature rise

Tests are conducted for numerous charge/discharge cycles applied on the tested battery to analyze its thermal response. For fully charge/discharge tests, three different currents (40 A, 50 A, 60 A) were

applied during the charge phase, as 1 C-rate (60 A) is the maximum current recommended by the manufacturer in charging cycle. While five currents rates (40 A, 50 A, 60 A, 80 A, 100 A) were tested during the discharge cycle. To simplify analyzing the results we define a ratio between charge current and discharge current as defined in equation II.2.

$$R_{current} = \frac{I_{charge}}{I_{discharge}} \qquad \text{II.2}$$

II.5.1 $R_{current}=1$

First tests were performed for three different currents' values (40 A, 50 A, 60 A) at the same C-rate in the charge and discharge cycles. The maximum local battery temperature profiles measured per each tested current are illustrated in Figure II.15.a. In transient regime, temperatures increase drastically until reaching 6 °C, 7.5 °C and 8.5 °C at 40 A, 50 A, 60 A, respectively. Once the quasi-stationary regime is attained, a 'V' shape profile is obtained for the three tests. This behavior is consistent with the reversible heat generation which is proportional to the current. A temperature fluctuation around these levels can be noted, due to the impact of the charge and discharge cycles and consequently to the battery SOC variation. While in quasi-stationary regime, it is possible to observe that during these fluctuations the gradient between the local maxima and minima of the temperatures' profiles remains the same (about 2.5 °C) independently of the current values imposed during the tests. Concluding, even if the average value of temperature oscillations is still depending on the different currents, the amplitude of the oscillations is not changing with them. Effect of the battery state of charge on the battery maximum local temperature is shown in Figure II.15.b. For the tested charge/discharge C-rates, temperature profiles decrease during charging cycle until reaching a minimum value in a state of charge between 30% and 40%, and then increase until the end of the charging cycle. A symmetrical behavior is observed during the discharge cycle. Battery temperature variation during charging/discharging cycles is due to the internal battery heat generation where the entropy heat could be either endothermal or exothermal, while the Joule heat generation is always exothermal.

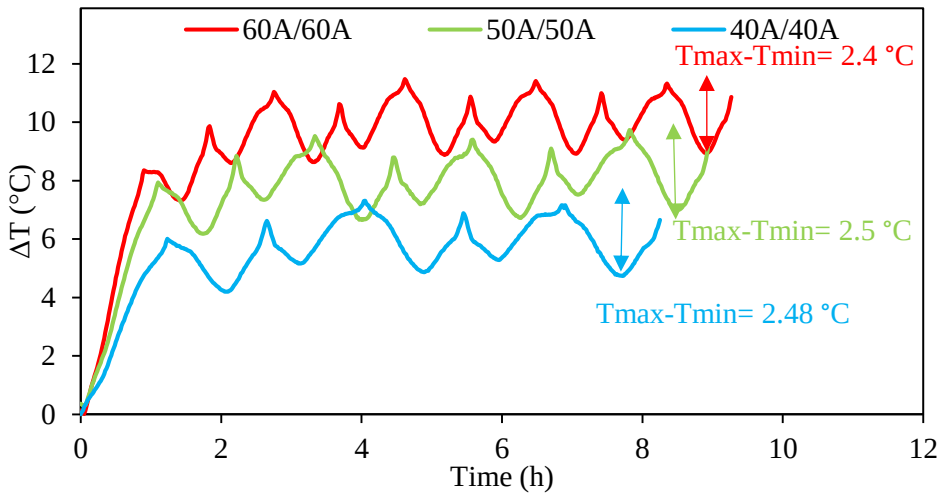

(a)

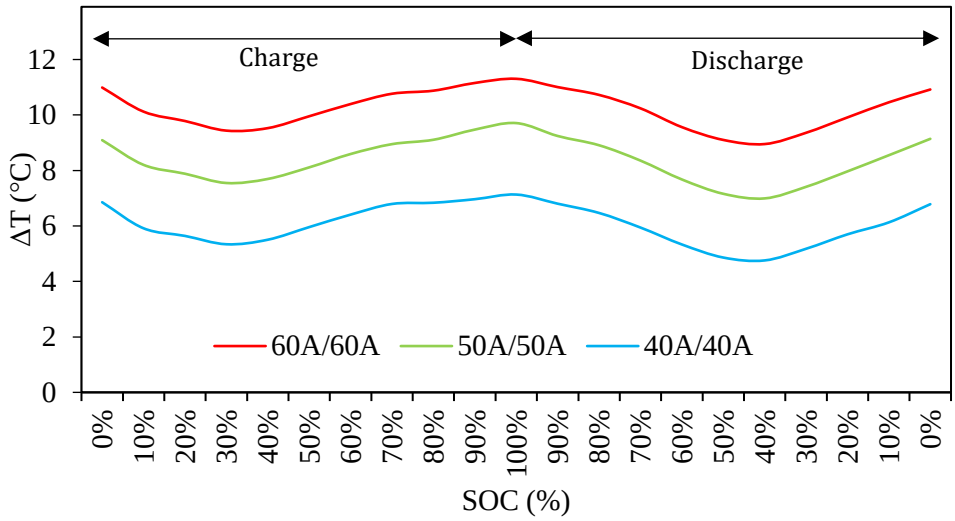

(b)

Figure II.15 Temperature rise for Rcurrent=1 (a) consecutive cycles (b) charge and discharge cycle in quasi-stationary regime.

The measurements of local temperatures are essential when determining the distribution of temperature in battery surfaces. An illustration is presented in Figure II.16 showing this distribution via Y and Z plane sides for three different currents rates. The temperature given in each point presents an average of the local temperatures measured via the concerned plane. As an example, for the first points

which corresponds to 0mm in Y plane, the given values present an average to temperatures measured by thermocouples (T_{17}, T_{18} and T_{19}). The obtained results of the local temperature for Y plane are presented in Figure II.16 a while the results of the Z plane are presented in Figure II.16.b. For both Y and Z planes, Higher temperatures are obtained for higher currents rates. A notable remark to be mentioned in Z plane that a decrease of temperatures is noticed at 200 mm for the three applied currents. At this level no active material was found when decomposing the tested battery.

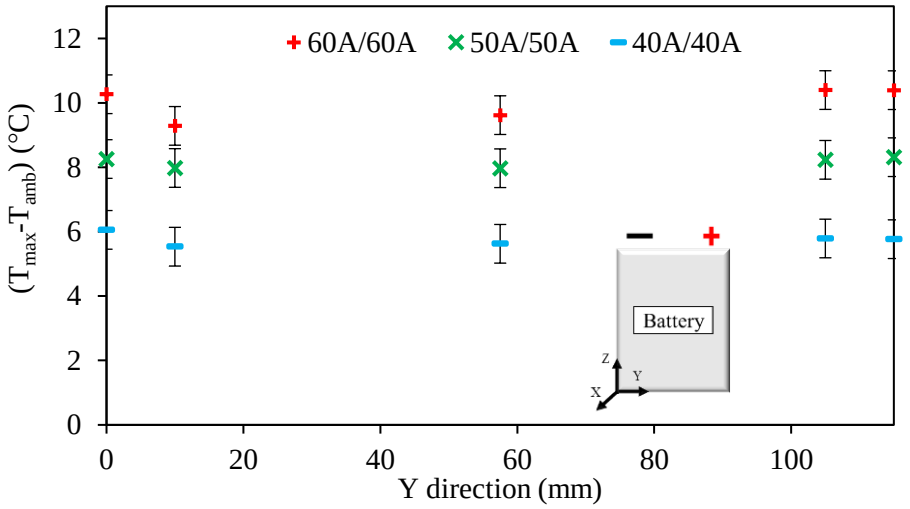

(a)

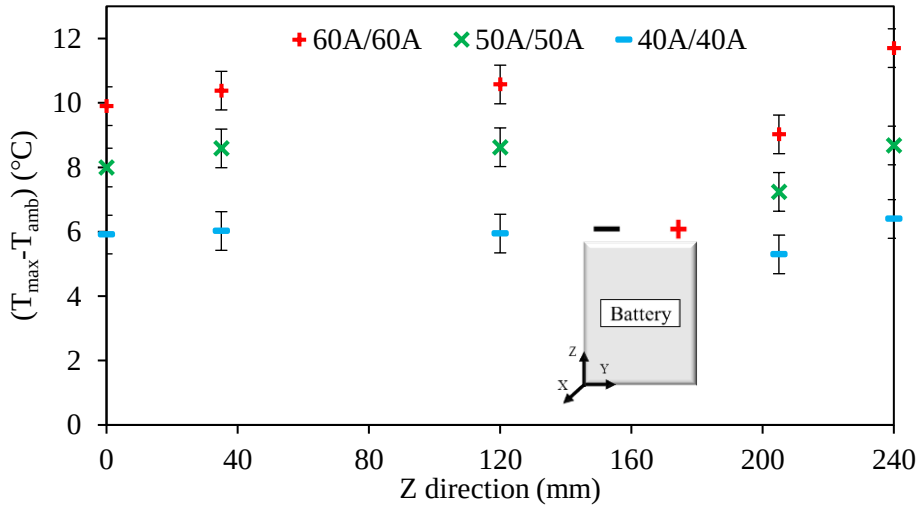

(b)

Figure II.16 Temperature distribution via battery sides (a) Y direction (b) Z direction.

The maximum temperature measurements carried out for the three different charge/discharge currents are shown in Figure II.17 Five temperatures are presented for each applied current. The temperature T_{max} and T_{min} are measured by thermocouples (T_{26}) and (T_8) While the T_{sx}, T_{sy} and T_{sz} are obtained by thermocouples (T_5, T_{11} and T_{24}). In addition, T_{E-} and T_{E+} are the temperatures taken by thermocouples (T_{22} and T_{23}). A difference of 3.25 °C is obtained between the maximum and minimum temperature for an applied current of 60 A while this difference is lower for currents of 50 A and 40 A, it is equal to 2.87 °C and 1.88 °C. Moreover, a similar difference between temperature measurement in the three tests is observed. In next sections, to simplify the comparison between different tests the maximum temperature measured by thermocouple (T_{26}) is chosen to analyze the effect of current rate on the battery thermal behavior.

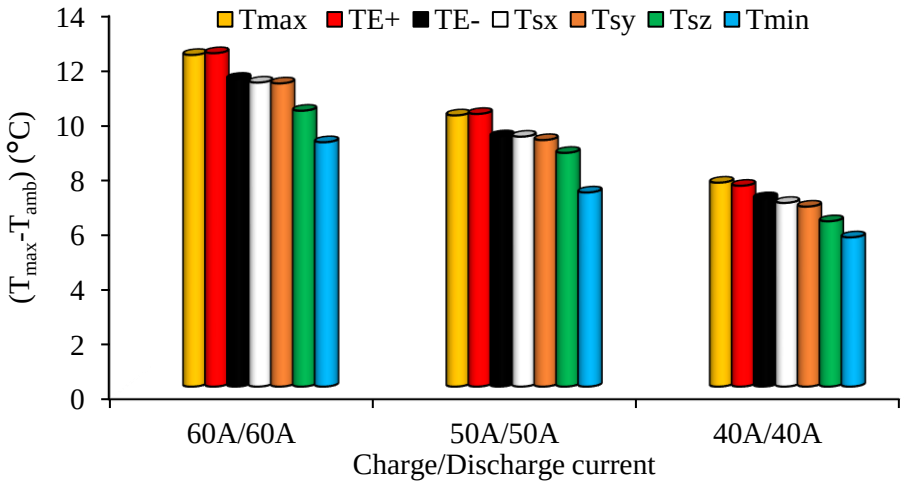

Figure II.17 Comparison of maximum temperature rise for three different tests.

II.5.2 $R_{current}\neq1$

The new tests are performed imposing different charge/discharge current ratios. The purpose of those tests is to visualize the thermal behavior and temperature profiles when applying consecutive charge and discharge cycles for $R_{current}\neq1$. The Figure II.18 shows a comparison of obtained results for 15 tests. Different charge and discharge currents were applied and the maximum temperature rise obtained by thermocouple (T_{26}) is presented. For all tested cases, higher temperature is obtained for higher currents. In the following part of this section. The effect of different tested current during both transient and quasi-stationary regime besides the effect of SOC on temperatures profiles is investigated.

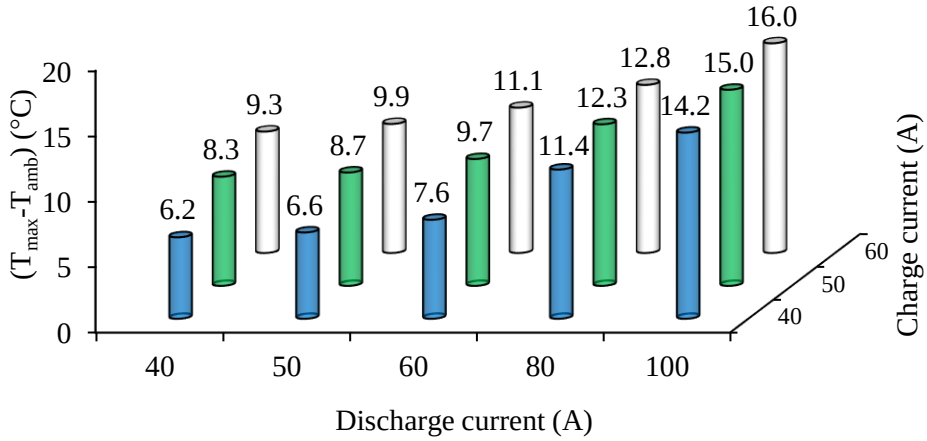

Figure II.18 Maximum temperature difference obtained for different charge and discharge current.

Figure II.19 shows the battery local maximum temperature profiles for different states of charge. Four different current rates (40 A, 50 A, 60 A, 80 A and 100 A) were applied for three different charge current (60 A ,50 A and 40 A). The obtained results for the given charge current are presented respectively in Figure II.19a, Figure II.19.b and Figure II.19.c. Moreover, it can be seen that increasing the discharge current leads to higher temperature rise and to a change of the temperature profiles. Particularly, for discharge current values lower or equals to the charging current value a decrease and an increase of the battery temperature are obtained during both charge and discharge cycles, as previously discussed. While, increasing the discharge current over the charging rate, a temperature decrease is observed all along the charge cycle, followed by the temperature increase during the discharge cycle. Consequently, it is possible to state a relevant change in temperatures fluctuation profiles in quasi-stationary regime. Furthermore, to better compare the temperature profiles during quasi-stationary regime an illustration is presented in Figure II.20.a, Figure II.20.b and Figure II.20.c. Only the last charge and discharge cycle obtained for each given charge and discharge current were presented versus the SOC as the duration of the cycle depends to the current rate. The local minima, which are previously observed around the 40% of the SOC during both the charge and discharge cycles, are converging in the 100% of the state of charge (corresponding to the end of the charge cycle and to the beginning of the discharge cycle), and the shape of the temperature profile is collapsing in a bathtub curve.

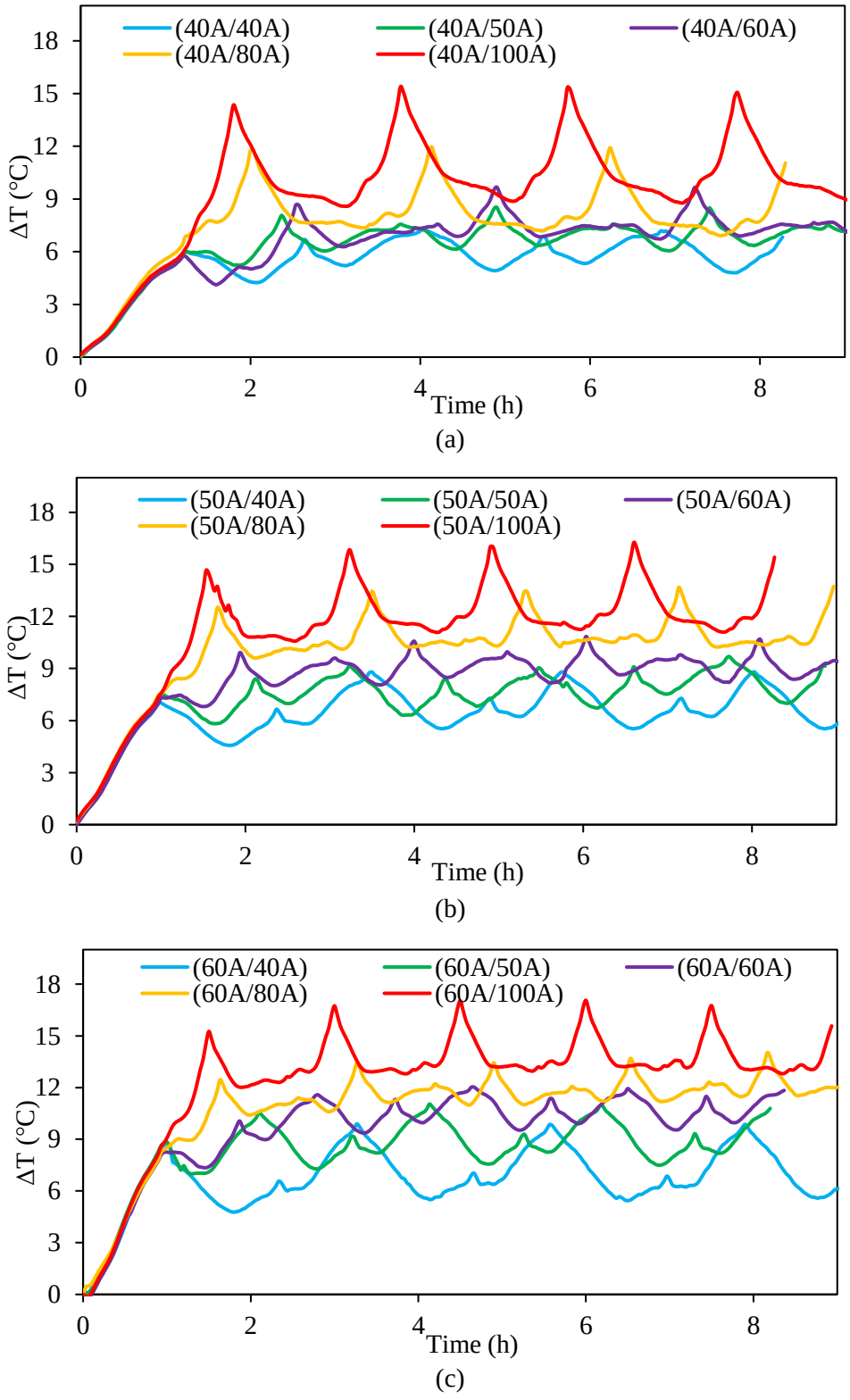

Figure II.19 Comparison of temperature rise for increasing discharge current: (a) Ic=40 A, (b) Ic=50 A, (c) Ic=60 A.

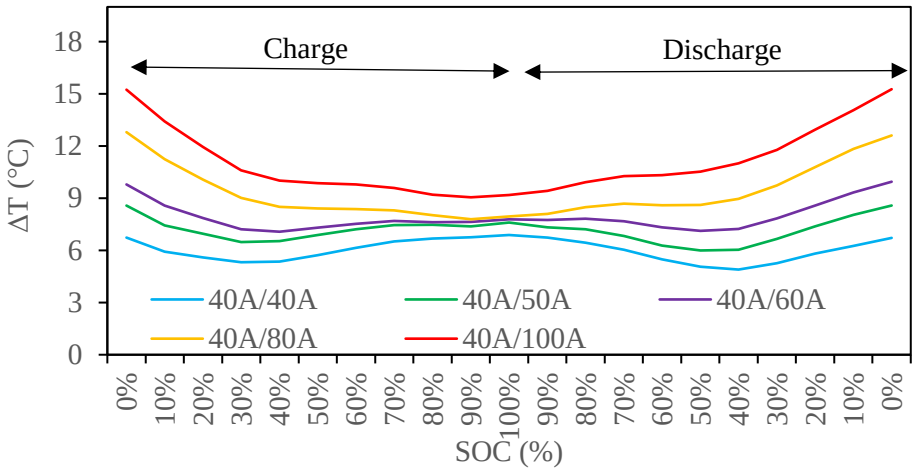

(a)

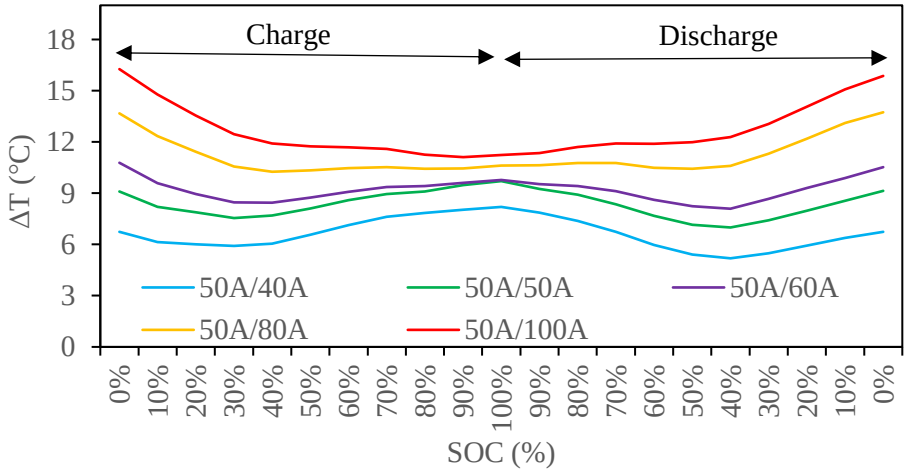

(b)

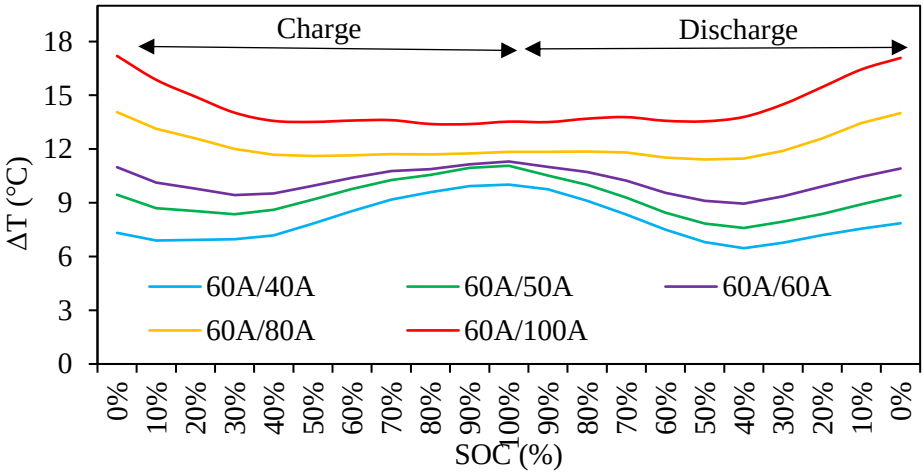

(c)

Figure II.20 Temperature profiles during quasi stationary regime versus SOCs: (a) Ic=40 A, (b) Ic=50 A, (c) Ic=60 A.

Other series of tests are performed for the same discharge currents (40 A, 60 A and 100 A) and three different charge C-rates (40 A, 50 A, 60 A). The aim of these experiments is to define the impact of the charge current variation on the battery temperature for different states of charge. Figure II.21 shows the evolution of the temperature profiles obtained for increasing charge current, with respect to the reference discharge current of 40A, 60A and 100A in Figure II.21.a, Figure II.21.b and Figure II.21.c respectively. Additionally, the last charge and discharge cycle for each given discharge current are presented in Figure II.22.a, Figure II.22.b and Figure II.22.c . The local maxima of the temperature profiles show similar values at both 0% and 100% of the battery SOC. While for charge current higher than discharge current conditions Figure II.22.a higher temperature variation can be observed for the SOC values higher than the 30%, both in the charge and discharge cycles. Consequently, the local maximum occurring at the 100% of the battery SOC is significantly increased over the local maxima values occurring at the 0% of the SOC. Finally, for discharge current higher than charge current (Figure II.22.c), the decreasing and increasing trends of the temperature are dominant in the charge and discharge cycles, respectively, and the local maximum at 100% of the SOC value disappear.

All the presented variations in temperature profiles underline that, during its real operations, the battery is exposed to different thermal cycling, depending on the C-rate variations imposed during the charge and discharge phases. In order to enhance the battery lifespan, these variations must be integrated in the battery thermal management system.

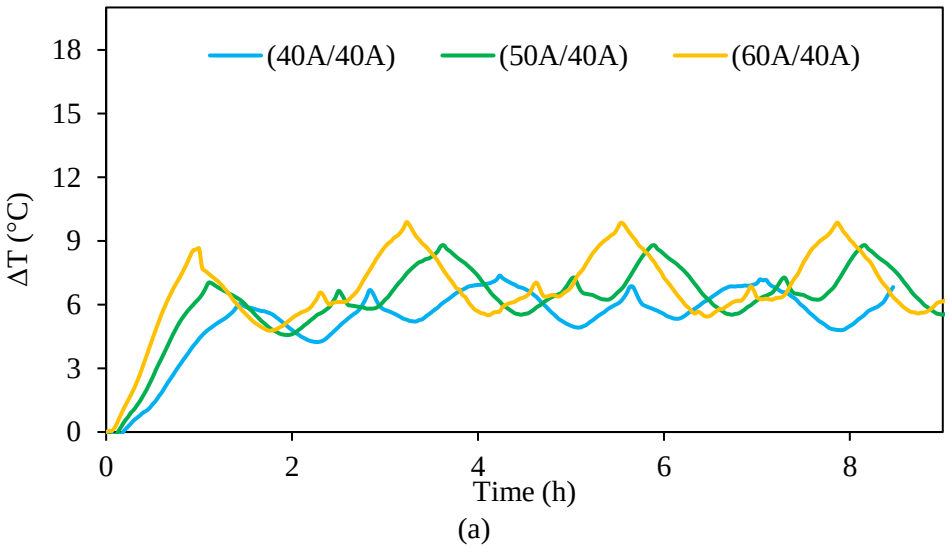

(a)

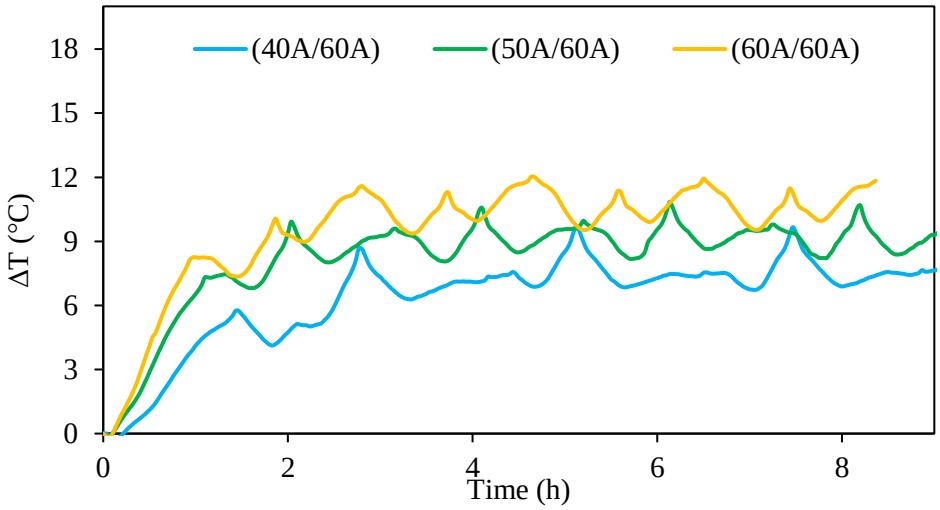

(b)

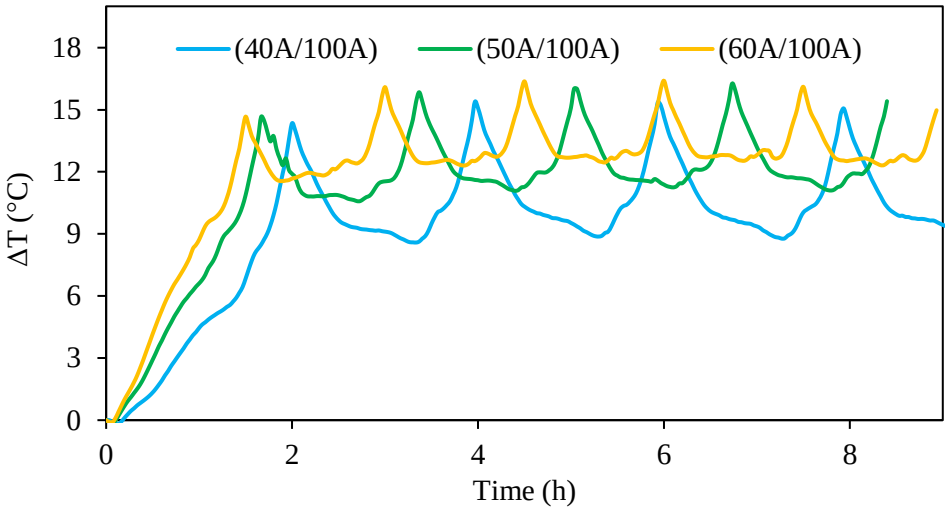

(c)

Figure II.21 Comparison of temperature rise for increasing charge current: (a) Id=40 A, (b) Id=60 A, (d) Id=100 A.

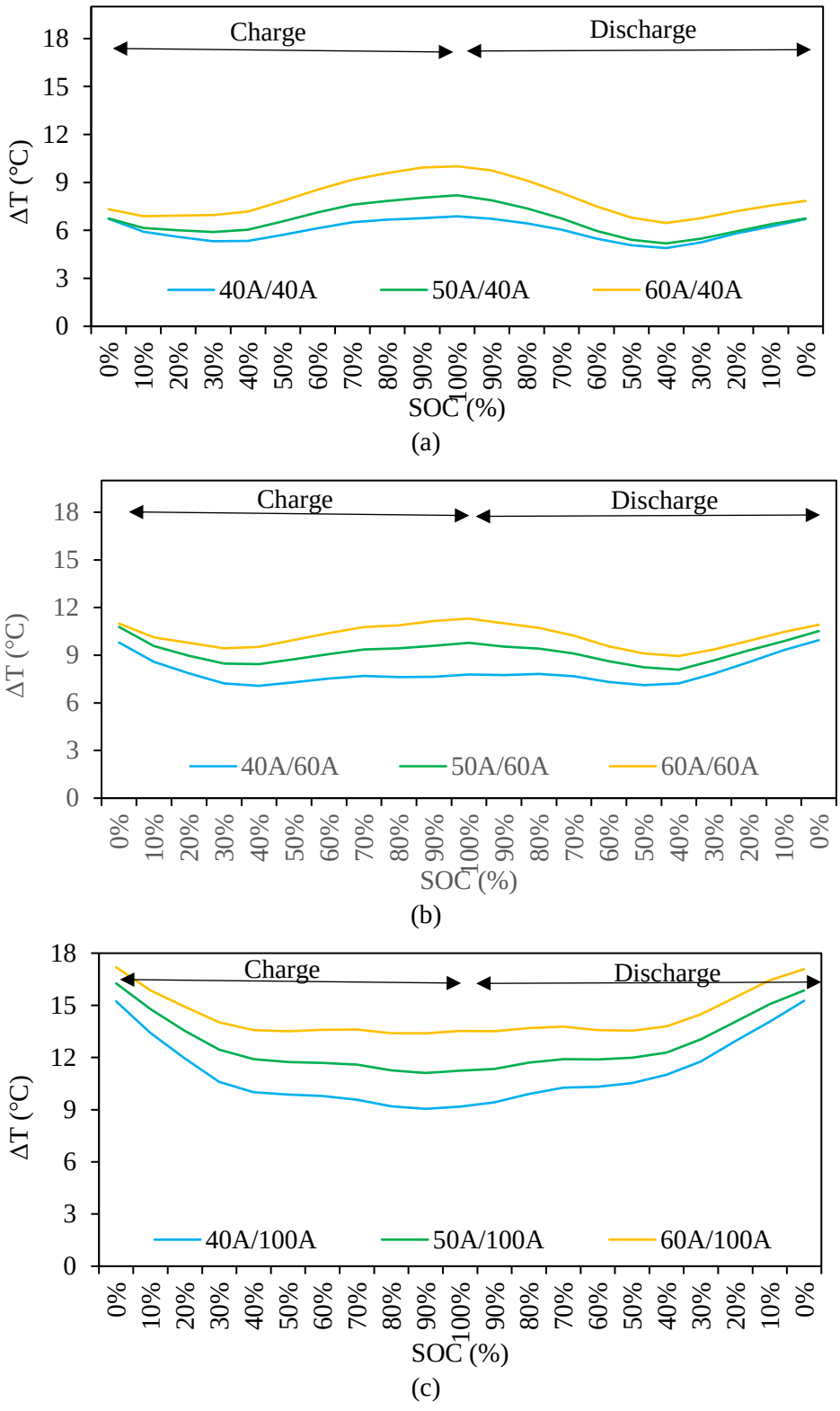

Figure II.22 Temperature profiles during quasi stationary regime versus SOCs: (a) Id=40 A, (b) Id=60 A, (d) Id=100 A.

Figure II.23 compares the gradients of the temperature fluctuations, which are observed in the quasi-stationary regime during the different charge/discharge cycles presented in this paragraph, with respect to the different current ratios ($R_{current}$). A temperature variation of about 3 °C is observed for the $R_{current}$ values closed to 1 (zone 2), resulting in the lowest measured value. The measured gradient rises with the current ratio decreasing (zone 1) until reaching its maximum value for $R_{current}$=0.4, and a similar behavior, but with a lower rising slope can be observed in case of the current ratio increasing (zone 3).

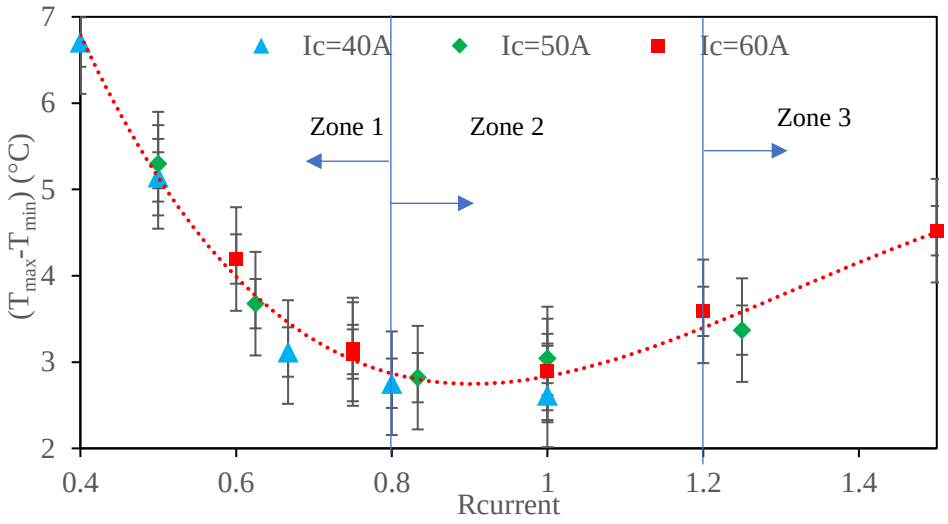

Figure II.23 Difference between maximum and minimum temperature rising during quasi-stationary regime for different C-Rates.

II.6 External heat dissipation measurements

II.6.1 Determination of total external heat dissipation

The internal generation of heat is responsible on the temperature increase inside the battery. However, an amount of this energy is dissipated to the outside. In this section, we aim to present the experimental measurements performed by three heat flux sensors inserted on 3 sides of the battery Front, right and bottom side. Only three heat flux sensors were inserted because the obtained results using thermocouples prove the symmetry. An illustration of local heat dissipation measured in center of battery front, right and bottom sides is shown in Figure II.24. The results are obtained during the application of consecutive charge and discharge cycles under a constant current of 60 A. Similar profiles are obtained for local heat flux and the previous presented curves of temperatures. Moreover, the

measured local heat flux on the front and right sides are approximately equals as the heat transfer coefficient and the ambient temperature remain identical. It is noticed that the heat flux on the bottom side is slightly higher at the other faces, this is justified by the change of the thermal properties of the battery in the lower part, due to the existence of a small layer without active material

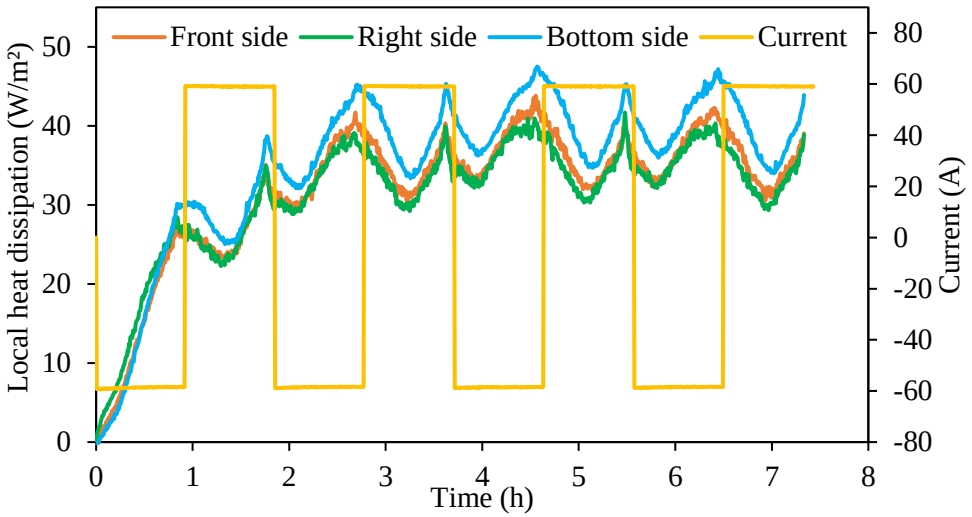

Figure II.24 Local heat dissipation measured in center of battery front, right and bottom sides.

The total dissipated heat flux is calculated by summing the measured local heat fluxes assuming symmetry in the dissipation across all sides as defined in equation II.3.

$$\dot{Q}_{measured} = 2(\Phi_{front}S_{front} + \Phi_{right}S_{right} + \Phi_{bottom}S_{bottom}) \qquad \text{II.3}$$

The heat transfer coefficient is determined for each using equation II.4. Where n designs the normal vector to the battery surface. The temperature and heat flux measured by each heat flux sensor is used to determine the heat transfer coefficient in front, right and bottom sides.

$$h_n = \frac{\Phi_n}{(T_n - T_{amb})} \qquad \text{II.4}$$

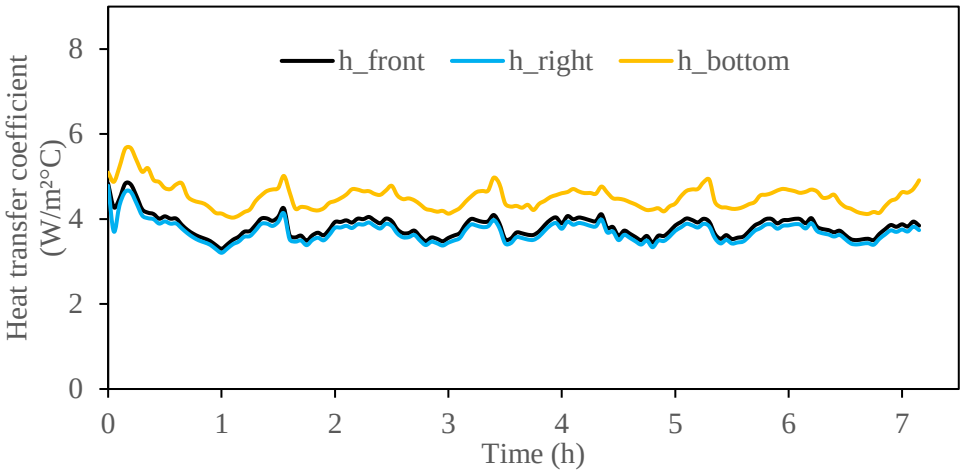

Figure II.25 Heat transfer coefficients curves for front, right and bottom sides.

Figure II.25 shows the profiles of variation of the obtained heat transfer coefficient. Moreover, a comparison is performed between predicted and measured total heat dissipation to evaluate the roughness of the hypothesis when using three heat flux sensors and summing their obtained data to obtain the measured. The predicted total heat dissipation is calculated by multiplying the averaged heat transfer coefficient of the three battery sides deduced from equation II.4 with the average temperature of thermocouples inserted in battery surface and electrodes from (T_1) to (T_{23}). The results presented in Figure II.26 show a good accuracy between the both obtained results. The equation II.5 will be used further in this work to determine the measured total heat dissipation

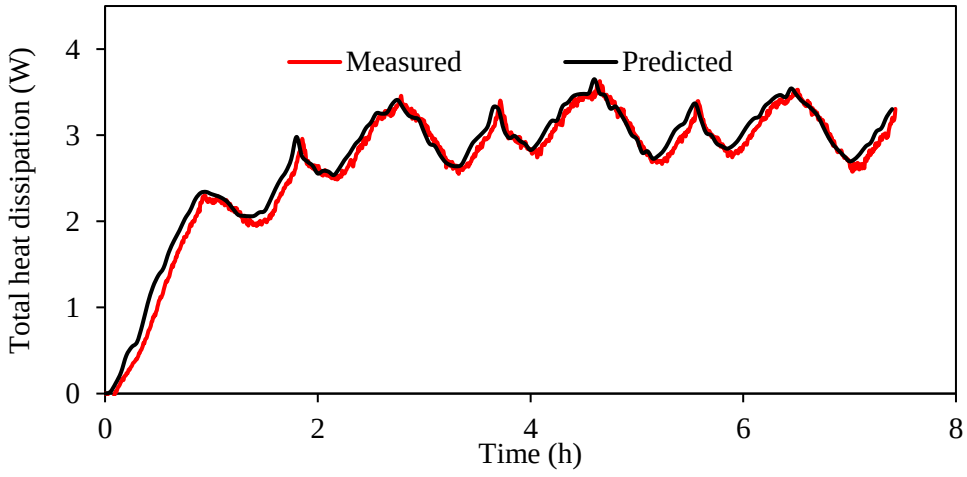

Figure II.26 Comparison of measured and predicted total heat dissipation.

$$\dot{Q}_{predicted} = h_{averaged} A_{battery} (T_{averaged} - T_{amb}) \quad \text{II.5}$$

II.6.2 Effect of current on total external heat dissipation

The total dissipated heat measured using heat flux sensors is presented for $R_{current}=1$ in Figure II.27.a. and for $R_{current}\neq1$ in Figure II.27.b. For $R_{current}=1$ three different current rates were applied (60 A, 50 A and 40 A), the results show the existence of two transient regimes and a 'V' shape during the quasi-stationary regime. Moreover, higher total heat dissipation is obtained for higher current rates. Additionally, for $R_{current}\neq1$ two different discharge current (40 A and 100 A) were tested with same discharge current 60 A. The results show a same increase in the beginning of the test as in this transient thermal regime same current is applied (Charge cycle). When applying 100 A during discharge the total heat dissipation rises strongly in the first discharge cycles while it decreases during the application of 40 A. The difference remarked in total heat flux profiles is due mainly to the effect of discharge current on internal heat generation. Battery heat generation is dependent on ambient temperature, SOC, C-rates, and battery characteristics (internal resistance, entropic heat coefficient...) [132]. In the next chapter a numerical study is performed enabling the determination of reversible and irreversible heat generation.

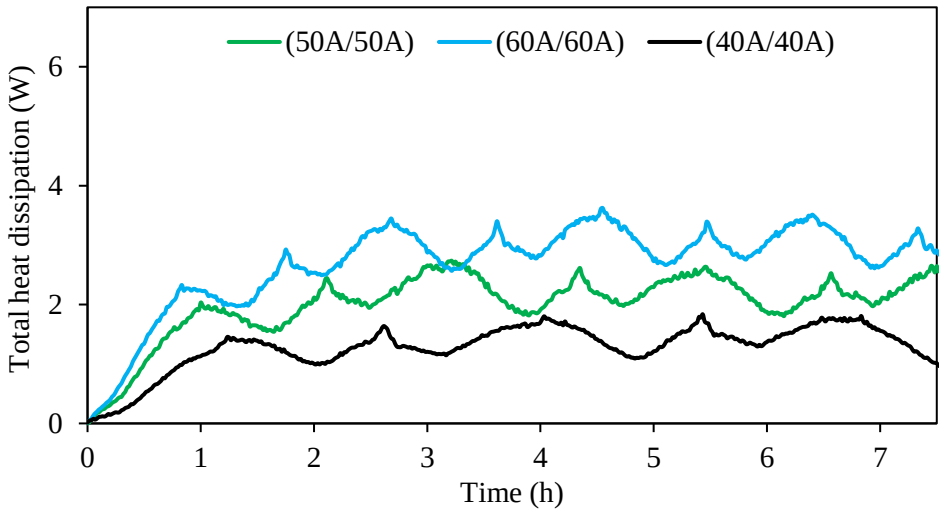

(a)

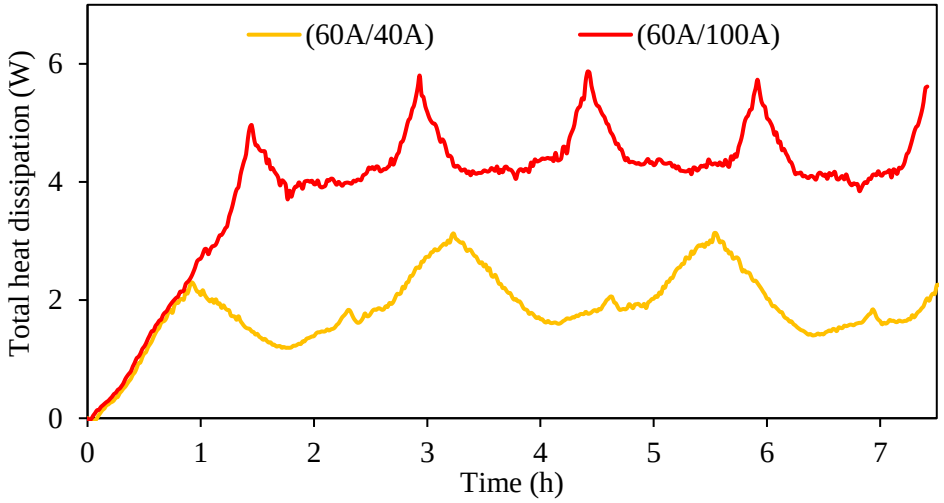

(b)

Figure II.27 Total heat dissipation profiles during consecutive charge and discharge cycles for (a) $R_{current}=1$ (b) $R_{current}\neq 1$.

II.7 Conclusion

In this Chapter, the thermal behavior of a 60 Ah Li-ion battery is investigated for different constant currents rates. Based on temperature and heat flux measurements, the effect of current rates on battery thermal behavior is examined.

Two thermal regimes are observed during consecutive charging and discharging cycles. A transient regime is followed by a quasi-stationary regime. The reversible heat generation affects strongly the temperature profile in quasi-stationary regime. Moreover, the irreversible heat generation is exothermic. A difference of about 3 °C is observed between the temperature measured on the battery surface and the temperature of the active material measured on the battery core. This confirmed that the measurements of the battery surface temperature are not sufficient to ensure efficient battery thermal management. In fact, the measured electrodes temperatures are higher than the battery surface temperature and approximately equal to maximum temperature measured on the center of the battery front side. This proves that tracking the electrodes temperature could be a main key in analyzing the battery thermal behavior. The temperature profile in quasi-stationary regime depends strongly to charge and discharge current ratio. Particularly, the temperature rise has a “V” shape in quasi stationary regime at a current

charge/discharge ratio ($R_{current}$) of 1. However, the temperature profiles drastically change while reducing or increasing this current ratio ($R_{current}$). The measurements performed on local heat flux and total heat dissipation carried using heat flux sensors show same behavior. Those measurement are primary in the determination of the heat transfer coefficient and the entropic heat coefficient which will be used in developing the numerical models in the next chapters.

Concluding, all the presented variations in temperature profiles underlined that, depending on the C-rate variations imposed during the charge and discharge phases, the battery can be exposed to different thermal cycling during real operations. Then, to enhance the battery lifespan, these variations must be integrated in the battery thermal management system. Thermal modeling of a prismatic Li-ion battery.

Chapter III. Thermal modeling of a prismatic Li-ion battery

III.1 Introduction

During operating time, heat is generated inside the battery due to chemical reactions. The battery temperature increases then which causes in some non-controllable cases the deterioration of the battery. The experimental study proposed in the previous chapter gave an idea about the thermal behavior of a prismatic 60Ah Li-ion battery tested for different current rates. However, this study is limited to the measurement of temperatures and heat flux densities. It is therefore necessary to develop a thermal model enabling the determination of the internal heat generation as it is the main key factor to well conceive an efficient battery thermal management system. In this Chapter, a 3D thermal model is proposed to the tested battery. First, the thermal parameters such as entropic heat coefficient and electrical parameters such as internal resistance are determined which enable the estimation of the reversible and irreversible heat amounts. In addition, the model is solved using the alternating directive method (ADI). A validation of the results predicted using the developed numerical model is performed. The proposed model is used to suggest two correlations enabling the fast determination of the internal heat energy generation and maximum temperature rise for given charge and discharge current.

III.2 3D thermal numerical model

A prismatic lithium iron phosphate battery is tested under different C-rates to characterize its thermal behavior. Experimental data was used to determine battery thermal parameters and a 3D battery thermal model is developed. In this section, the energy balance equation and boundary conditions are first defined and then the alternating direction method is used. Finally, the calculation procedures to solve the constructed tri-diagonal matrix is described.

Based on energy balance equation, battery heat accumulation is equal to the sum of internal volumetric heat generation and heat conduction see equation III.1. Where ρ is the battery density, C_p is the specific heat capacity, while λ_x, λ_y and λ_z are respectively the thermal conductivities in x, y and z directions. V_{bat} designs the battery volume. Internal volumetric heat generation is defined as the sum of irreversible and reversible heat [133]. The determination of battery internal resistance (R) and entropic heat coefficient ($\frac{dU_{OC}}{dT}$) versus SOC are necessary to solve the heat transfer equation. ρ, C_p, λ and h_n are defined as constant during battery operating time. equation III.2 presents the boundary conditions and the value of heat transfer coefficient h_n is experimentally calculated from heat flux measurements.

Where n designs the normal vector to the battery, $T_{s,n}$ presents the surface temperature measured by each of the heat flux sensors.

Battery heat transfer equation :

$$\rho C_p \frac{\partial T}{\partial t} = \lambda_x \frac{\partial^2 T}{\partial x^2} + \lambda_y \frac{\partial^2 T}{\partial y^2} + \lambda_z \frac{\partial^2 T}{\partial z^2} + \frac{1}{V_{bat}} (RI^2 - IT \frac{dU_{OC}}{dT}) \quad \text{III.1}$$

Boundary conditions :

$$-\lambda_n \frac{\partial T}{\partial n} = h_n (T_{s,n} - T_{amb}) \quad \text{III.2}$$

The development of the model is based on experimental methods to determine the internal electrical resistance and the entropic heat coefficient and the thermal parameters (the thermal conductivities and the specific heat capacity) are obtained from bibliographic data. The heat transfer coefficient is determined from the measurements of temperature and heat flux presented in chapter II. After determining the extrinsic and intrinsic parameters helping in the resolution of the heat transfer equation, a 3D thermal model is programed manually using Fortran language. Finally, a validation of the obtained numerical results is done for different experimental conditions to prove the model accuracy. Figure III.1 illustrates a flowchart describing the process of the numerical model development.

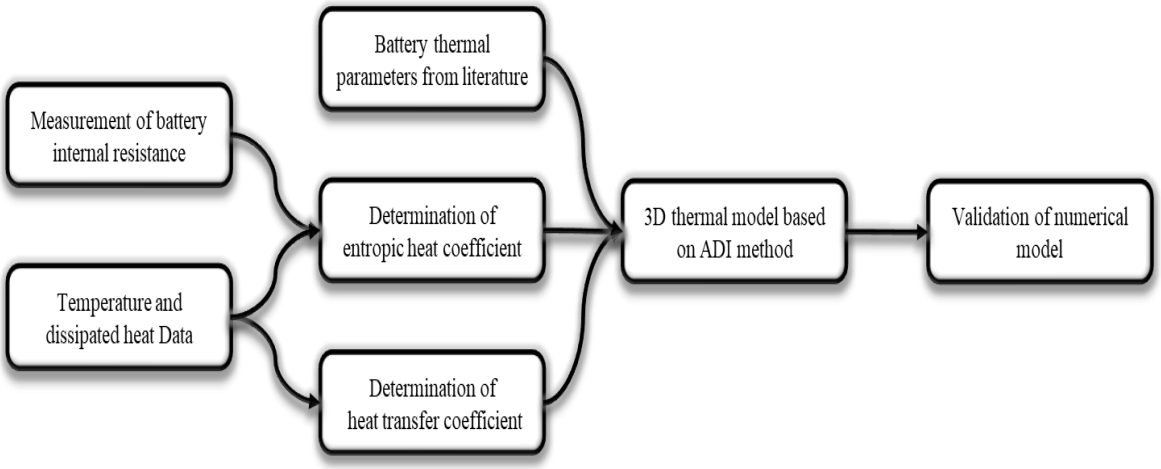

Figure III.1 Flowchart of the model development process.

III.2.1 ADI method

The alternating directive method (ADI) used to solve the battery heat transfer equation was developed first by Peaceman and Rachford [134] to solve elliptic and parabolic equations in 2D and 3D. This method is unconditionally stable. As a conclusion to this stability condition lower calculation time and computer storage is needed. The numerical discretization of the heat transfer equation is presented in equations III.3, III.4 and III.5. The tridiagonal matrix is used to calculate the temperature in each step.

$$\rho Cp\frac{T_{i,j,k}^{*}-T_{i,j,k}^{n}}{\frac{\Delta t}{2}}-\lambda_x\frac{T_{i+1,j,k}^{*}-2T_{i,j,k}^{*}+T_{i-1,j,k}^{*}}{\Delta x^2}-\lambda_y\frac{T_{i,j+1,k}^{n}-2T_{i,j,k}^{n}+T_{i,j-1,k}^{n}}{\Delta y^2}-\lambda_z\frac{T_{i,j,k+1}^{n}-2T_{i,j,k}^{n}+T_{i,j,k-1}^{n}}{\Delta z^2}=\frac{1}{V_{bat}}\left(RI^2-IT_{i,j,k}^{n}\frac{dU_{OC}}{dT}\right) \quad \text{III.3}$$

$$\rho Cp\frac{T_{i,j,k}^{**}-T_{i,j,k}^{n}}{\frac{\Delta t}{2}}-\lambda_x\frac{T_{i+1,j,k}^{*}-2T_{i,j,k}^{*}+T_{i-1,j,k}^{*}}{\Delta x^2}-\lambda_y\frac{T_{i,j+1,k}^{**}-2T_{i,j,k}^{**}+T_{i,j-1,k}^{**}}{\Delta y^2}-\lambda_z\frac{T_{i,j,k+1}^{n}-2T_{i,j,k}^{n}+T_{i,j,k-1}^{n}}{\Delta z^2}=\frac{1}{V_{bat}}\left(RI^2-IT_{i,j,k}^{n}\frac{dU_{OC}}{dT}\right) \quad \text{III.4}$$

$$\rho Cp\frac{T_{i,j,k}^{n+1}-T_{i,j,k}^{**}}{\frac{\Delta t}{2}}-\lambda_x\frac{T_{i+1,j,k}^{*}-2T_{i,j,k}^{*}+T_{i-1,j,k}^{*}}{\Delta x^2}-\lambda_y\frac{T_{i,j+1,k}^{**}-2T_{i,j,k}^{**}+T_{i,j-1,k}^{**}}{\Delta y^2}-\lambda_z\frac{T_{i,j,k+1}^{n+1}-2T_{i,j,k}^{n+1}+T_{i,j,k-1}^{n+1}}{\Delta z^2}=\frac{1}{V_{bat}}\left(RI^2-IT_{i,j,k}^{n+1}\frac{dU_{OC}}{dT}\right) \quad \text{III.5}$$

The parameters i, j and k represent the steps in direction of x, y and z respectively. The domain is divided following each direction in Nx, Ny and Nz time with a step in each direction Δx, Δy and Δz. The Figure III.2 illustrates a simplified schematic of battery domain meshing.

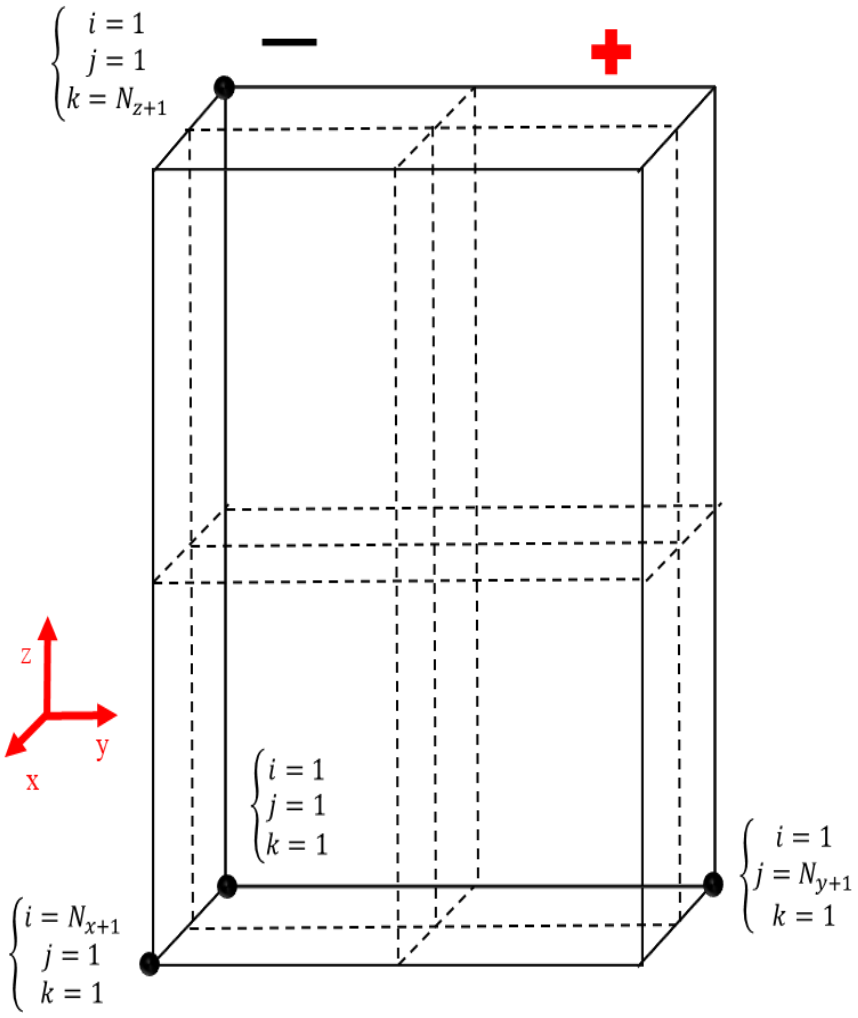

Figure III.2 Simplified schematic of the mesh construction.

Additionally, the calculation in each step requires the determination of temperature using boundary conditions for (i=1, Nx+1), (j=1, Ny+1) and (k=1, Nz+1). as described respectively in equations III.6, III.10, III.11, III.15, III.16 and III.20.

The ADI method consists in calculating the spatial derivatives of the temperatures at an instant p (*) with respect to the spatial derivatives of the temperatures at a later instant p+1 (**). The unconditional stability of the implicit method implies the convergence of the method whatever the chosen time step. This makes it possible to choose a longer time step, and thus increase the computational speed. The time step is equals to $t+\Delta t/2$, the temperature at $t+\Delta t/2$ is calculated from the previous temperature T (t). Equations below show the used discretization in each step.

- **Step 1:**

For i=1, the boundary condition is applied to determine $T^*_{1,j,k}$.

$$T^*_{1,j,k} = \frac{1}{h_x + \frac{\lambda_x}{\Delta x}}\left(\frac{\lambda_x}{\Delta x} T^*_{2,j,k} + h_x T_{amb}\right) \quad \text{III.6}$$

For i=2, the defined equation of $T^*_{1,j,k}$ is replaced in equation III.3.

$$\begin{aligned}\left(\frac{2\rho C_p}{\Delta t} + \frac{2\lambda_x}{\Delta x^2} - \frac{{\lambda_x}^2}{\Delta x^3\left(h_x + \frac{\lambda_x}{\Delta x}\right)}\right) T^*_{2,j,k} - \frac{\lambda_x}{\Delta x} T^*_{3,j,k} \\ = \left(\frac{2\rho C_p}{\Delta t} - \frac{2\lambda_y}{\Delta y^2} - \frac{2\lambda_z}{\Delta z^2} - \frac{I\frac{dU_{OC}}{dT}}{V_{bat}}\right) T^n_{2,j,k} \\ + \frac{\lambda_y}{\Delta y^2}\left(T^n_{2,j+1,k} + T^n_{2,j-1,k}\right) + \frac{\lambda_z}{\Delta z^2}\left(T^n_{2,j,k+1} + T^n_{2,j,k-1}\right) \\ + \frac{\lambda_x h_x}{\Delta x^2\left(h_x + \frac{\lambda_x}{\Delta x}\right)} T_{amb} + \frac{RI^2}{V_{bat}}\end{aligned} \quad \text{III.7}$$

For i= [3, Nx-1], the equation III.3 is rearranged and the temperature in instant (*) is written in function of known temperatures in instant (n).

$$\begin{aligned}-\frac{\lambda_x}{\Delta x^2} T^*_{i-1,j,k} + \left(\frac{2\rho Cp}{\Delta t} + \frac{2\lambda_x}{\Delta x^2}\right) T^*_{i,j,k} - \frac{\lambda_x}{\Delta x^2} T^*_{i+1,j,k} \\ = \left(\frac{2\rho Cp}{\Delta t} - \frac{2\lambda_y}{\Delta y^2} - \frac{2\lambda_z}{\Delta z^2} - \frac{\frac{dU_{OC}}{dT}}{V_{bat}}\right) T^n_{i,j,k} \\ + \frac{\lambda_y}{\Delta y^2}\left(T^n_{i,j+1,k} + T^n_{i,j-1,k}\right) + \frac{\lambda_z}{\Delta z^2}\left(T^n_{i,j,k+1} + T^n_{i,j,k-1}\right) + \frac{RI^2}{V_{bat}}\end{aligned} \quad \text{III.8}$$

For i=Nx, the defined equation of $T^{*}_{Nx+1,j,k}$ is replaced in equation III.3

$$-\frac{\lambda_x}{\Delta x^2}T^{*}_{Nx-1,j,k}+\left(\frac{2\rho C_p}{\Delta t}+\frac{2\lambda_x}{\Delta x^2}-\frac{{\lambda_x}^2}{\Delta x^3(h_x+\frac{\lambda_x}{\Delta x})}\right)T^{*}_{Nx,j,k}$$
$$=\left(\frac{2\rho C_{p,}}{\Delta t}-\frac{2\lambda_y}{\Delta y^2}-\frac{2\lambda_z}{\Delta z^2}-\frac{I\frac{dU_{OC}}{dT}}{V_{bat}}\right)T^{n}_{Nx,j,k} \qquad \text{III.9}$$
$$+\frac{\lambda_y}{\Delta y^2}\left(T^{n}_{Nx,j+1,k}+T^{n}_{Nx,j-1,k}\right)+\frac{\lambda_z}{\Delta z^2}\left(T^{n}_{Nx,j,k+1}+T^{n}_{Nx,j,k-1}\right)$$
$$+\frac{\lambda_x h_x}{\Delta x^2(h_x+\frac{\lambda_x}{\Delta x})}T_{amb}+\frac{RI^2}{V_{bat}}$$

For i=Nx+1, the boundary condition is applied to determine $T^{*}_{Nx+1,j,k}$

$$T^{*}_{Nx+1,j,k}=\frac{1}{h_x+\frac{\lambda_x}{\Delta x}}\left(\frac{\lambda_x}{\Delta x}T^{*}_{Nx,j,k}+h_x T_{amb}\right) \qquad \text{III.10}$$

The ‘i’ iterations explained following the x plane directions are done for Y and Z plane to determine the iterations ‘j’ and ‘k’. For the iteration ‘j’ the temperature is given in instant (**) and written in function of previous temperatures in instants (*) and (n). Moreover, For the direction ‘k’ the temperature is given in instant (n+1) and written in function of previous temperatures in instants (**) and (*).

- **Step 2:**

For j=1

$$T^{**}_{i,1,k}=\frac{1}{h_y+\frac{\lambda_y}{\Delta y}}\left(\frac{\lambda_y}{\Delta y}T^{**}_{i,2,k}+h_y T_{amb}\right) \qquad \text{III.11}$$

For j=2

$$\left(\frac{2\rho C_p}{\Delta t}+\frac{2\lambda_y}{\Delta y^2}-\frac{\lambda_y^2}{\Delta y^3\left(h_y+\frac{\lambda_{y,}}{\Delta y}\right)}\right)T_{i,2,k}^{**}-\frac{\lambda_y}{\Delta y}T_{i,3,k}^{**}$$
$$=\left(\frac{2\rho C_p}{\Delta t}-\frac{2\lambda_z}{\Delta z^2}-\frac{I\frac{dU_{OC}}{dT}}{V_{bat}}\right)T_{i,2,k}^{n}+\frac{\lambda_x}{\Delta x^2}\left(T_{i+1,2,k}^{*}-2T_{i,2,k}^{*}+T_{i-1,2,k}^{*}\right) \quad \text{III.12}$$
$$+\frac{\lambda_z}{\Delta z^2}\left(T_{i,2,k+1}^{n}+T_{i,2,k-1}^{n}\right)+\frac{\lambda_y h_y}{\Delta y^2\left(h_y+\frac{\lambda_y}{\Delta y}\right)}T_{amb}+\frac{RI^2}{V_{bat}}$$

For j=3, Ny-1

$$-\frac{\lambda_y}{\Delta y^2}T_{i,j-1,k}^{**}+\left(\frac{2\rho Cp}{\Delta t}+\frac{2\lambda_y}{\Delta y^2}\right)T_{i,j,k}^{**}-\frac{\lambda_y}{\Delta y^2}T_{i,j+1,k}^{**}$$
$$=\left(\frac{2\rho Cp}{\Delta t}-\frac{2\lambda_z}{\Delta z^2}-\frac{\frac{dU_{OC}}{dT}}{V_{bat}}\right)T_{i,j,k}^{n}+\frac{\lambda_x}{\Delta x^2}\left(T_{i+1,j,k}^{*}-2T_{i,j,k}^{*}+T_{i-1,j,k}^{*}\right) \quad \text{III.13}$$
$$+\frac{\lambda_z}{\Delta z^2}\left(T_{i,j,k+1}^{n}+T_{i,j,k-1}^{n}\right)+\frac{RI^2}{V_{bat}}$$

For j=Ny

$$-\frac{\lambda_y}{\Delta y^2}T_{i,Ny-1,k}^{**}+\left(\frac{2\rho C_p}{\Delta t}+\frac{2\lambda_y}{\Delta y^2}-\frac{\lambda_y^2}{\Delta y^3\left(h_y+\frac{\lambda_{y,}}{\Delta y}\right)}\right)T_{i,Ny,k}^{**}$$
$$=\left(\frac{2\rho C_p}{\Delta t}-\frac{2\lambda_z}{\Delta z^2}-\frac{I\frac{dU_{OC}}{dT}}{V_{bat}}\right)T_{i,Ny,k}^{n}+\frac{\lambda_x}{\Delta x^2}\left(T_{i+1,Ny,k}^{*}-2T_{i,Ny,k}^{*}+T_{i-1,Ny,k}^{*}\right) \quad \text{III.14}$$
$$+\frac{\lambda_z}{\Delta z^2}\left(T_{i,Ny,k+1}^{n}+T_{i,Ny,k-1}^{n}\right)+\frac{\lambda_y h_y}{\Delta y^2\left(h_y+\frac{\lambda_y}{\Delta y}\right)}T_{amb}+\frac{RI^2}{V_{bat}}$$

For j=Ny+1

$$T_{i,Ny+1,k}^{**}=\frac{1}{h_y+\frac{\lambda_y}{\Delta y}}\left(\frac{\lambda_y}{\Delta y}T_{i,Ny,k}^{**}+h_y T_{amb}\right) \quad \text{III.15}$$

- **Step 3:**

For k=1

$$T_{i,j,1}^{n+1} = \frac{1}{h_z + \frac{\lambda_z}{\Delta z}}\left(\frac{\lambda_z}{\Delta z} T_{i,j,2}^{n+1} + h_z T_{amb}\right) \quad \text{III.16}$$

For k=2

$$\left(\frac{2\rho Cp}{\Delta t} + \frac{2\lambda_z}{\Delta z^2} + \frac{I\frac{dU_{OC}}{dT}}{V_{bat}} \frac{\lambda_z^2}{\Delta z^3\left(h_z + \frac{\lambda_z}{\Delta z}\right)}\right) T_{i,j,2}^{n+1} - \frac{\lambda_z}{\Delta z^2} T_{i,j,3}^{n+1}$$
$$= \frac{\lambda_x}{\Delta x^2}\left(T_{i+1,j,2}^{*} - 2T_{i,j,2}^{*} + T_{i-1,j,2}^{*}\right) + \left(\frac{2\rho Cp}{\Delta t} - \frac{2\lambda_y}{\Delta y^2}\right) T_{i,j,2}^{**} \quad \text{III.17}$$
$$+ \frac{\lambda_y}{\Delta y^2}\left(T_{i,j+1,2}^{**} + T_{i,j-1,2}^{**}\right)$$
$$+ \frac{\lambda_z h_z}{\Delta z^2\left(h_z + \frac{\lambda_z}{\Delta z}\right)} T_{amb} + \frac{RI^2}{V_{bat}}$$

For k=3, Nz-1

$$-\frac{\lambda_z}{\Delta z^2} T_{i,j,k-1}^{n+1} + \left(\frac{2\rho Cp}{\Delta t} + \frac{2\lambda_z}{\Delta z^2} + \frac{I\frac{dU_{OC}}{dT}}{V_{bat}}\right) T_{i,j,k}^{n+1} - \frac{\lambda_z}{\Delta z^2} T_{i,j,k+1}^{n+1}$$
$$= \frac{\lambda_x}{\Delta x^2}\left(T_{i+1,j,k}^{*} - 2T_{i,j,k}^{*} + T_{i-1,j,k}^{*}\right) + \left(\frac{2\rho Cp}{\Delta t} - \frac{2\lambda_y}{\Delta y^2}\right) T_{i,j,k}^{**} \quad \text{III.18}$$
$$+ \frac{\lambda_y}{\Delta y^2}\left(T_{i,j+1,k}^{**} + T_{i,j-1,k}^{**}\right) + \frac{RI^2}{V_{bat}}$$

For k=Nz

$$-\frac{\lambda_z}{\Delta z^2} T_{i,j,Nz}^{n+1} + \left(\frac{2\rho Cp}{\Delta t} + \frac{2\lambda_z}{\Delta z^2} + \frac{I\frac{dU_{OC}}{dT}}{V_{bat}} \frac{\lambda_z^2}{\Delta z^3\left(h_z + \frac{\lambda_z}{\Delta z}\right)}\right) T_{i,j,Nz+1}^{n+1}$$
$$= \frac{\lambda_x}{\Delta x^2}\left(T_{i+1,j,Nz+1}^{*} - 2T_{i,j,Nz+1}^{*} + T_{i-1,j,Nz+1}^{*}\right) + \left(\frac{2\rho Cp}{\Delta t} - \frac{2\lambda_y}{\Delta y^2}\right) T_{i,j,Nz+1}^{**} \quad \text{III.19}$$
$$+ \frac{\lambda_y}{\Delta y^2}\left(T_{i,j+1,Nz+1}^{**} + T_{i,j-1,Nz+1}^{**}\right)$$
$$+ \frac{\lambda_z h_z}{\Delta z^2\left(h_z + \frac{\lambda_z}{\Delta z}\right)} T_{amb} + \frac{RI^2}{V_{bat}}$$

For k=Nz+1

$$T_{i,j,Nz+1}^{n+1} = \frac{1}{h_z + \frac{\lambda_z}{\Delta z}}\left(\frac{\lambda_z}{\Delta z} T_{i,j,Nz}^{n+1} + h_y T_{amb}\right) \quad \text{III.20}$$

Based on previous given equations of the model discretization using ADI method is performed. Three tridiagonal matrixes are built to calculate the temperature in the three instants (*), (**) and (n+1).

An example of the decomposition method is given for the first step and same method is applied in the other steps.

First for i=[2, Nx] the given system of equations could be written via the given matrix in equation III.21 and the coefficient are given bellow in equations III.22,III.23 and III.24.

$$\begin{pmatrix} b_2 & c_2 & 0 & \cdots & \cdots & 0 \\ a_3 & b_3 & c_3 & \cdots & \cdots & 0 \\ 0 & \ddots & \ddots & \ddots & \ddots & \vdots \\ \vdots & \ddots & a_i & b_i & c_i & \vdots \\ \vdots & \ddots & \ddots & \ddots & \ddots & 0 \\ \vdots & \ddots & \ddots & a_{Nx-1} & b_{Nx-1} & c_{Nx-1} \\ 0 & \cdots & \cdots & 0 & a_{Nx} & b_{Nx} \end{pmatrix} \times T^* = f \qquad \text{III.21}$$

$$b_2 = b_{Nx} = \frac{2\rho C_p}{\Delta t} + \frac{2\lambda_x}{\Delta x^2} - \frac{{\lambda_x}^2}{\Delta x^3 (h_x + \frac{\lambda_x}{\Delta x})} \qquad \text{III.22}$$

$$b_i = \frac{2\rho C_p}{\Delta t} + \frac{2\lambda_x}{\Delta x^2} \qquad \text{III.23}$$

$$a_i = c_i = -\frac{\lambda_x}{\Delta x^2} \qquad \text{III.24}$$

The given matrix is decomposed as the product of a lower triangular matrix L and an upper triangular matrix U according as shown in equation III.25. The lower triangular matrix L is presented in equation III.26 while the upper triangular matrix U is defined in equation III.27. Furthermore the coefficient of each matrix are also presented below in equations III.28, III.29, III.30, III.31 and III.32.

$$\begin{pmatrix} b_2 & c_2 & 0 & \cdots & \cdots & 0 \\ a_3 & b_3 & c_3 & \cdots & \cdots & 0 \\ 0 & \ddots & \ddots & \ddots & \ddots & \vdots \\ \vdots & \ddots & a_i & b_i & c_i & \vdots \\ \vdots & \ddots & \ddots & \ddots & \ddots & 0 \\ \vdots & \ddots & \ddots & a_{Nx-1} & b_{Nx-1} & c_{Nx-1} \\ 0 & \cdots & \cdots & 0 & a_{Nx} & b_{Nx} \end{pmatrix} = L \times U \quad \text{III.25}$$

$$L = \begin{pmatrix} 1 & 0 & 0 & \cdots & \cdots & 0 \\ l_3 & 1 & 0 & \cdots & \cdots & 0 \\ 0 & \ddots & \ddots & \ddots & \ddots & \vdots \\ \vdots & \ddots & l_i & 1 & 0 & \vdots \\ \vdots & \ddots & \ddots & \ddots & \ddots & 0 \\ \vdots & \ddots & \ddots & l_{Nx-1} & 1 & 0 \\ 0 & \cdots & \cdots & 0 & l_{Nx} & 1 \end{pmatrix} \quad \text{III.26}$$

$$U = \begin{pmatrix} g_2 & c_2 & 0 & \cdots & \cdots & 0 \\ 0 & g_3 & c_3 & \cdots & \cdots & 0 \\ 0 & \ddots & \ddots & \ddots & \ddots & \vdots \\ \vdots & \ddots & 0 & g_i & c_i & \vdots \\ \vdots & \ddots & \ddots & \ddots & \ddots & 0 \\ \vdots & \ddots & \ddots & 0 & g_{Nx-1} & c_{Nx-1} \\ 0 & \cdots & \cdots & 0 & 0 & g_{Nx} \end{pmatrix} \quad \text{III.27}$$

$$g_2 = b_2 \quad \text{III.28}$$

$$g_i = b_i - l_i \times c_{i-1} \quad \text{III.29}$$

$$g_{Nx} = b_{Nx} - l_{Nx} \times c_{Nx-1} \quad \text{III.30}$$

$$l_i = \frac{a_i}{g_{i-1}} \quad \text{III.31}$$

$$l_{Nx} = \frac{a_{Nx}}{g_{Nx-1}} \quad \text{III.32}$$

The equation III.21 could be written then as defined in equation III.33. To solve the equation a vector Y is defined as the product of the upper triangular matrix U and the Temperature vector as presented in equation III.34. Finally, the coefficient of the E vector and temperatures $T^*_{i,j,k}$ are given in equations III.35, III.36, III.37 and III.38.

$$L \times U \times T^{*} = f \quad \text{III.33}$$

$$E = U \times T^{*} \quad \text{III.34}$$

$$e_2 = f_2 \quad \text{III.35}$$

$$e_i = f_i - l_i \times e_{i-1} \quad \text{III.36}$$

$$T^{*}_{Nx,j,k} = \frac{e_{Nx}}{g_{Nx}} \quad \text{III.37}$$

$$T^{*}_{i,j,k} = \frac{e_i - c_i \times T^{*}_{i+1,j,k}}{g_i} \quad \text{III.38}$$

III.2.2 Calculation procedures

Figure III.3 illustrates the flow chart of the numerical model calculation. The thermal parameters of the battery as well as charge and discharge current rates are the inputs of the numerical model. The calculation process includes two cases depending on the first cycle process either it is charge or discharge. The SOC of charge is then initialized based on the chosen case and the ADI method is used to solve the heat transfer equation in each iteration. The SOC is calculated in each iteration and the next cycle start after achieving the end of the previous cycle. The charge and discharge cycle are repeated consecutively to simulate the same experimental conditions. In next sections, experimental measurements are performed to determine the thermal and electrical parameters. Those parameters are exploited to solve the numerical model.

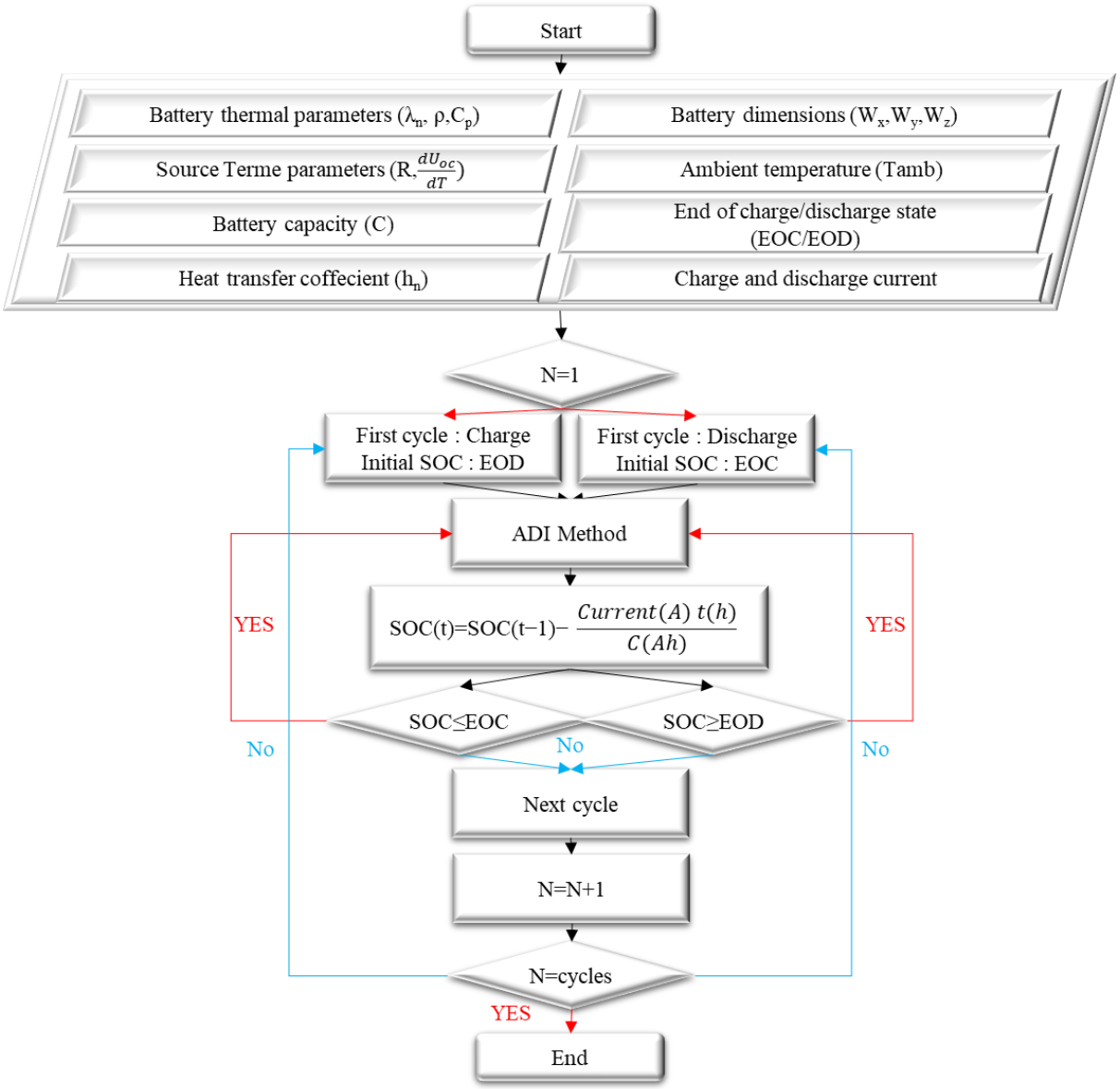

Figure III.3 Flow chart of the program.

III.3 Identification of battery thermal parameters

III.3.1 Calculation of ρ,Cp, λ_n and h_n

The chemical reactions inside the battery during operating time cause several mass and heat transfer phenomena. Many researchers simplify the physical problem of batteries models by considering it as a

block [135],[46]. Battery thermal parameters are then calculated based on its volume. The battery density is calculated based on equation III.39. Besides, the specific heat capacity is determined using the equations III.40. In addition, the thermal conductivity is determined taking in consideration the internal this structure's arrangement which is in series along the battery thickness (direction x) while it is in parallel for the height and width directions (y and z). Figure III.4 illustrates a simplified schematic of equivalent thermal conductivity for layers in series and in parallel. The equation III.41 are used to determine battery thermal conductivity in each direction. Furthermore, the battery heat transfer coefficient is experimentally determined based on heat flux measurements in battery sides equation III.42. Where n designs the normal vector to the battery surface.

Density :

$$\rho = \frac{m_{battery}}{V_{bat}} \qquad \text{III.39}$$

Specific heat capacity :

$$C_p = \frac{\sum_{i=1}^{n}(\rho V)_i C_{pi}}{\sum_{i=1}^{n}(\rho V)_i} \qquad \text{III.40}$$

Thermal conductivity :

$$\lambda_x = \frac{\sum_{i=1}^{n} e_i}{\sum_{i=1}^{n} \frac{e_i}{\lambda_i}} \quad ; \quad \lambda_y = \lambda_z = \frac{\sum_{i=1}^{n} \lambda_i\, e_i}{\sum_{i=1}^{n} e_i} \qquad \text{III.41}$$

Heat transfer coefficient :

$$h_n = \frac{\Phi_{n,dissipated}}{(T_{s,n} - T_{amb})} \qquad \text{III.42}$$

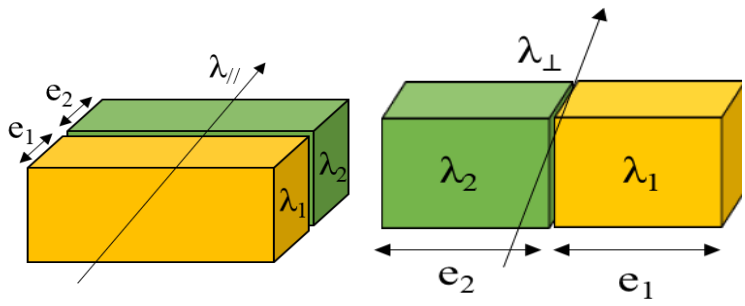

(a) (b)

Figure III.4 Schematic representation of equivalent thermal conductivity for layers in (a) Series (b) Parallel.

The characteristics of each component are extracted from literature [136] and listed in Table III.1. The index (i) represents a component of the battery structure. While The dimensions and battery parameters used in the numerical model are listed in Table III.2.

Table III.1 Battery thermal parameters.

Material	**Thickness, ei (µm)**	**Density ($kg \cdot m^{-3}$)**	**Cp ($J \cdot kg^{-1} \cdot K^{-1}$)**	**Porosity**	**λ ($W \cdot m^{-1} \cdot K^{-1}$)**
Graphite	120	1347	1437	0.3	1.04
Copper	10	8930	386	0	398
Electrolyte	0	1223	1375	0	0.59
Separator	40	1400	1551	0.47	0.35
LiFePO4	180	3500	700	0.25	0.27
Aluminum	20	2710	902	0	237
Shell	4000	1290	975	0	0.3

Table III.2 Dimensions and battery parameters.

Parameters	**Value**
Size of battery; (mm)	$240 \times 40 \times 115$
Battery mass; (kg)	1.97
Capacity; (Ah)	60
Density; (kg/m3)	1784
Specific heat; (J/kg. K)	964
Thermal conductivity; (W/m. K)	$\lambda_x = 0.31$; $\lambda_y = \lambda_z = 2.31$
Heat transfer coefficient; (W/m^2. K)	$h_n = 4.32$

III.3.2 Internal electrical resistance

Irreversible heat generated by Li-ion batteries during operating time is caused by electrical losses called usually Joule effect. This heat is equal to the product of internal electrical resistance and the current square. Thus, the determination of internal resistance is primary to determine the source term of the heat transfer equation. Internal resistance is determined based on test profile mentioned in Freedom Car manual [137] illustrated in Figure III.5.

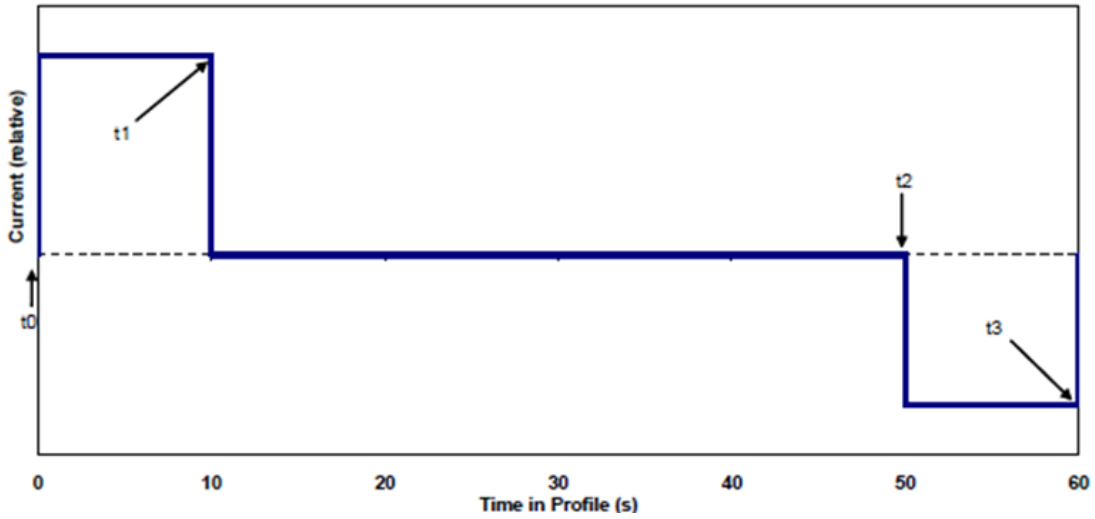

Figure III.5 Test profile applied to measure the internal resistance [137].

First a 10s discharge cycle is set followed by 40s rest, then finally a 10s charge cycle is applied. Equations III.43 and III.44 are then used to calculate charge and discharge internal resistance. For each of the following SOC (0 %, 20 %, 40 %, 60%, 80 % and 100 %), This experimental procedure was applied on the battery for three different currents (40 A, 60 A, 100 A) to study the effect of current on internal resistance for different SOC. An illustration is presented in Figure III.6 showing the obtained curves of current and voltage during the applied test of profile during three different SOC 0%, 60% and 100%.

$$R_{Charge} = \frac{\Delta V_{Charge}}{\Delta I_{Charge}} \quad \text{III.43}$$

$$R_{Discharge} = \frac{\Delta V_{Discharge}}{\Delta I_{Discharge}} \quad \text{III.44}$$

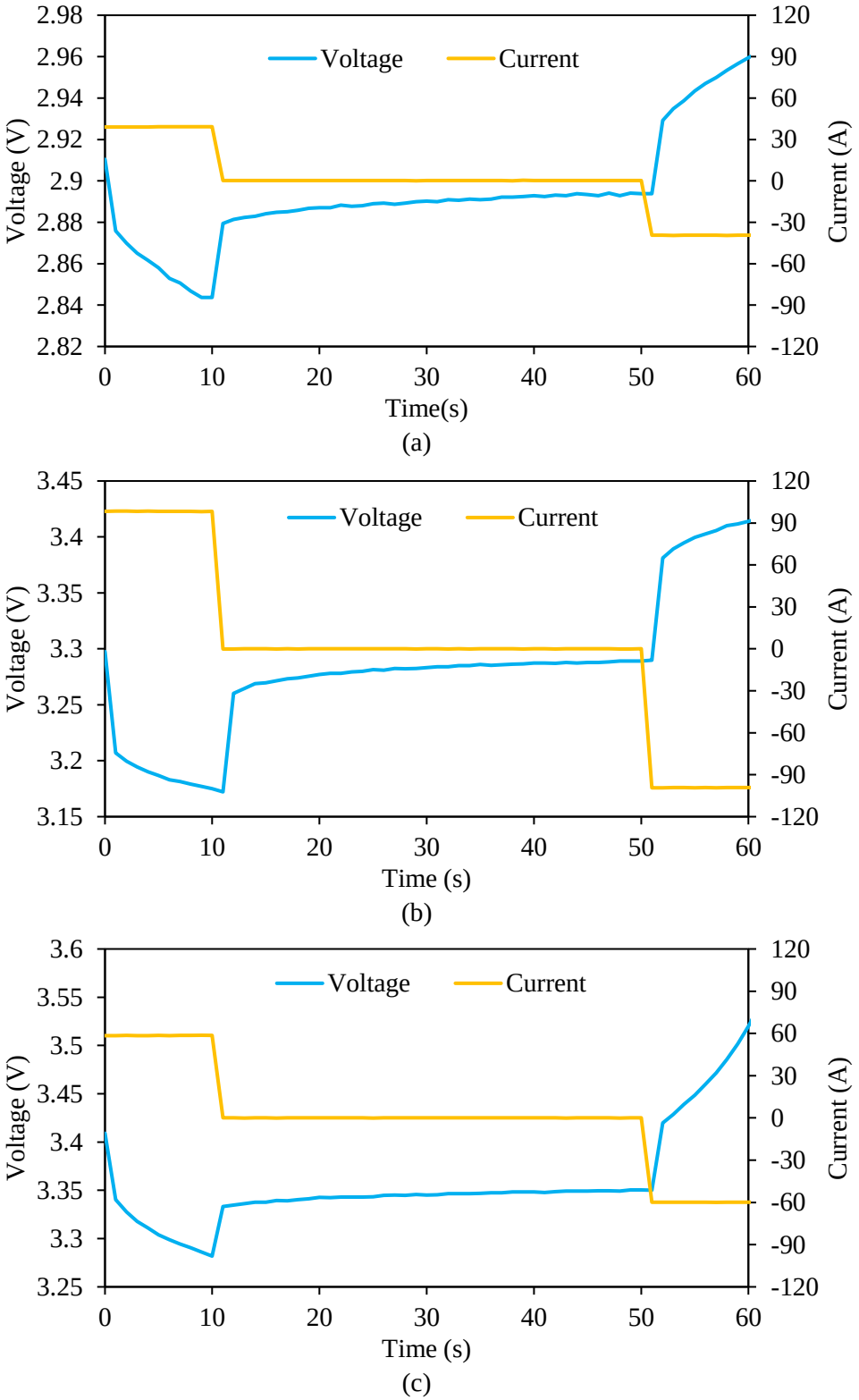

Figure III.6 HPPC protocol for three different SOC (a) 0 % (b) 60 %(c) 100 %.

Moreover, the results illustrated in Figure III.7 show no current effect on Internal resistance for SOC varying from 20% to 80% during charge and discharge cycles. For SOC equals to 0% and 100%, the internal resistance was found to be higher which is due to voltage strong drop/rise.

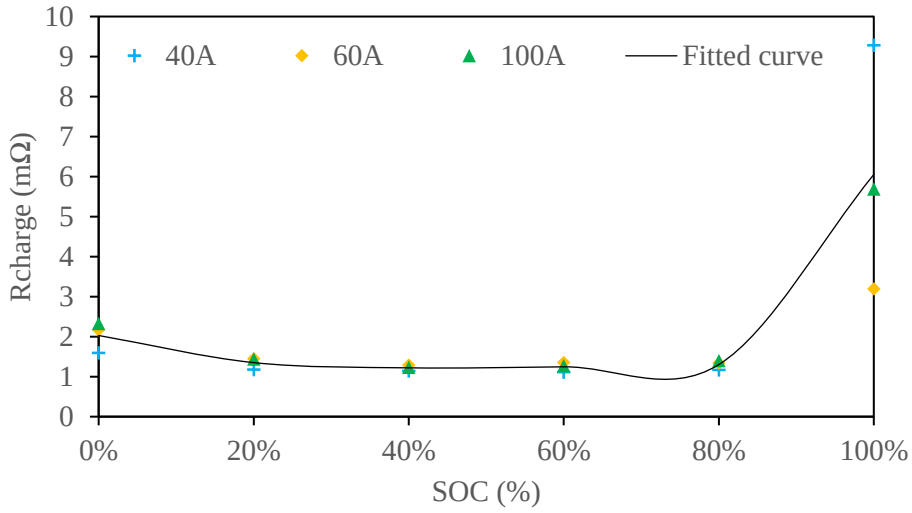

(a)

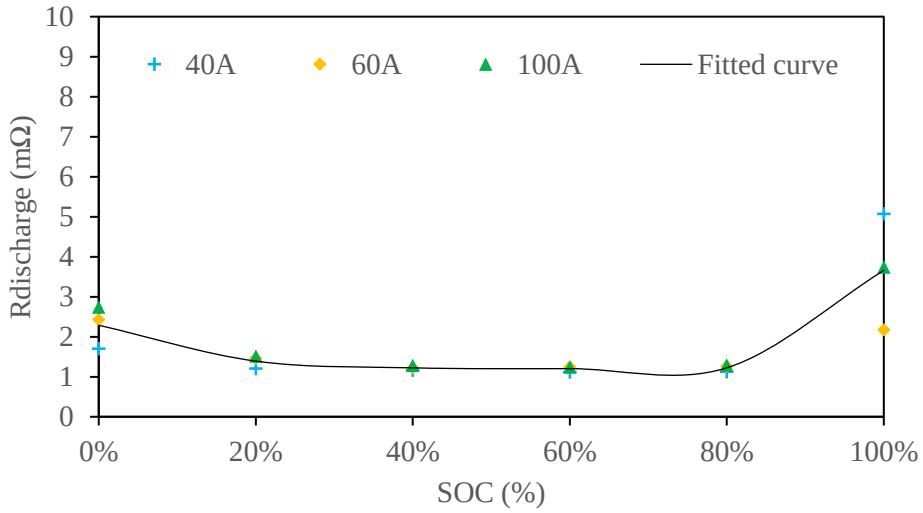

(b)

Figure III.7 Effect of current on battery internal resistance. (a) during charge, (b) during discharge.

The obtained internal resistance during charge and discharge were interpolated versus SOC, see equation III.45 and III.46. These equations are then integrated to solve the numerical 3D model.

$$R_{Charge} = 117.88\,SOC^5 - 228.89\,SOC^4 + 148.67\,SOC^3 - 32.435\,SOC^2 - 1.2015\,SOC + 2.0277 \quad \text{III.45}$$

$$R_{Discharge} = 52.193\,SOC^5 - 92.029\,SOC^4 + 46.132\,SOC^3 + 0.9382\,SOC^2 - 5.8643\,SOC + 2.2877 \quad \text{III.46}$$

III.3.3 Entropic heat coefficient

Energy accumulation is defined as the difference of heat generation due to chemical reactions and heat dissipation [138] see equation III.47. The internal heat generation is defined based on equation III.48 and heat dissipation is extracted from heat flux sensors measurement. The maximum local temperature experimentally measured in the center of the large side of battery by the thermocouple embedded inside the shell is used in the calculation of reversible heat as it reflects the battery internal temperature. The used equation to determine the entropic heat coefficient is as presented bellow in equation III.49.

$$\dot{Q}_{accumulated} = \dot{Q}_{generated} - \dot{Q}_{Dissipated} \quad \text{III.47}$$

$$\dot{Q}_{generated} = RI^2 - IT\frac{dU_{oc}}{dT} \quad \text{III.48}$$

$$\frac{dU_{oc}}{dT} = \frac{RI^2 - \dot{Q}_{accumulated} - \dot{Q}_{Dissipated}}{IT} \quad \text{III.49}$$

The entropic heat coefficient (EHC) obtained based on energy balance equation is illustrated in Figure III.8 during charge and discharge for both $R_{current}=1$ and $R_{current}\neq 1$. Our analytical method presents a particularity, comparing it to proposed experimental and analytical methods in literature as it leads to the determination of the entropic heat during both charge and discharge cycles. Indeed, the measurements of entropic heat coefficient performed by Geifes et al. [139] show low current effects, same profile for three tested currents and negative entropic heat coefficients for a SOC lower than 20%. Moreover, experimental results published by Samba et al. [127] show a difference between entropic heat

coefficient during charge and discharge. This difference is justified by the hysteresis phenomena of open circuit voltage in function of SOC. Obtained results for the tested 60 Ah battery show that the entopic coefficient is in same cycle exothermic and endothermic which explains our remarks concerning the "V" shape of temperature profile in quasi-stationary regime. During charge and discharge for a SOC lower than 35% the EHC is endothermic while it is exothermic for a SOC between (35%-85%). for higher SOC values the EHC is endothermic during charge while it keeps increasing during discharge. This phenomenon is due basically to the difference of materials used in each electrode which provides different electrical reactions during the insertion or desertion of lithium ions.

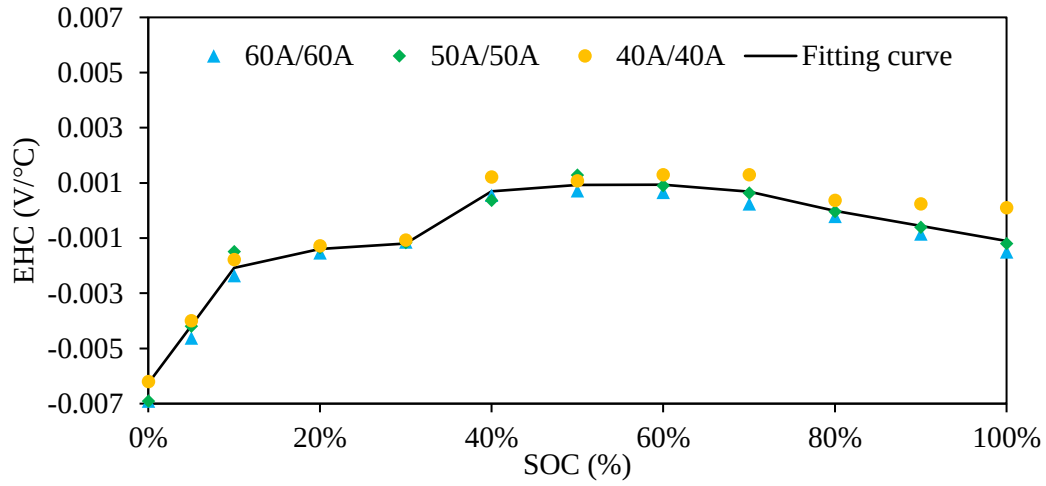

(a)

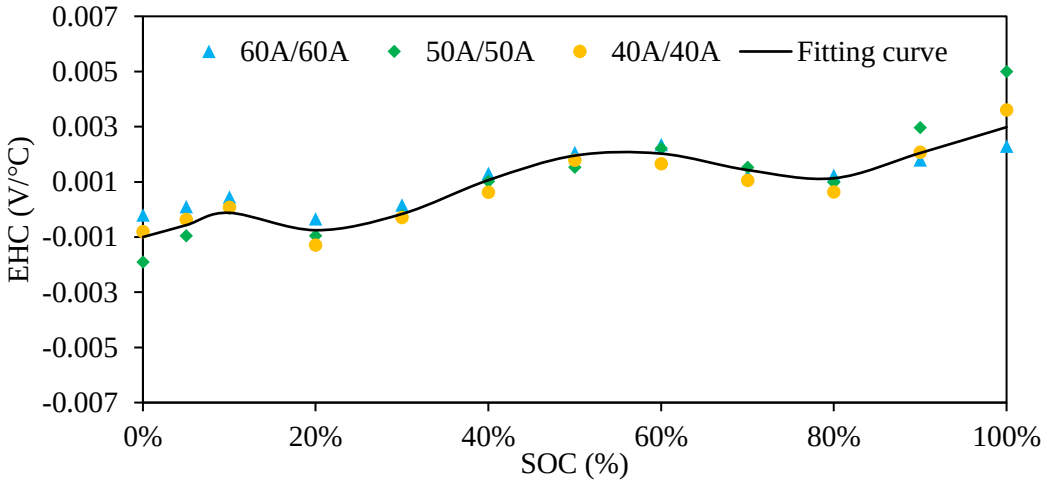

(b)

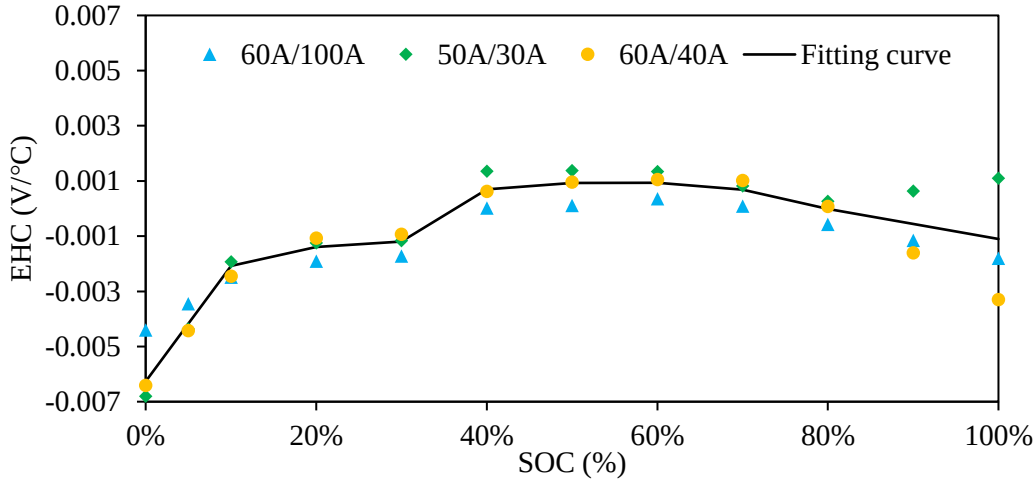

(c)

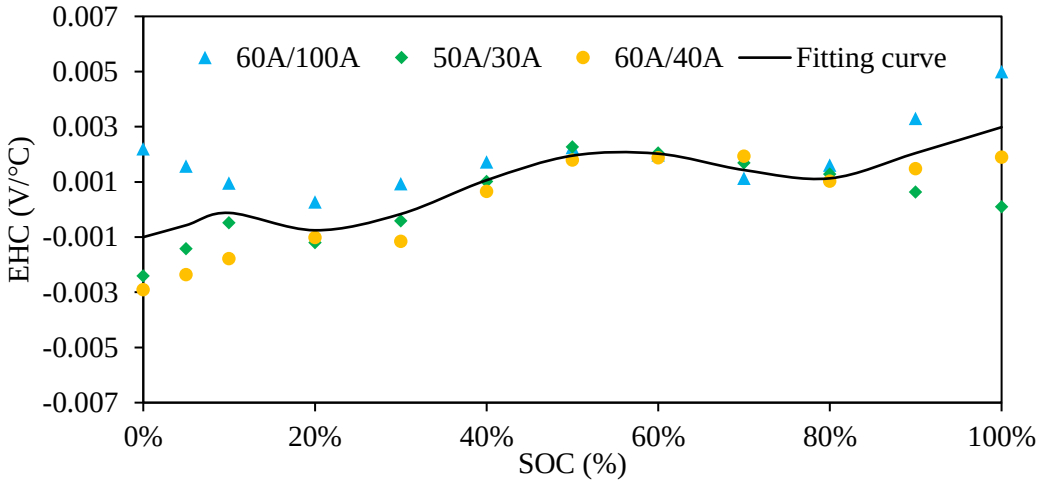

(d)

Figure III.8 Entropic heat coefficient. (a) during charge $R_{current}=1$ (b) during discharge $R_{current}=1$ (c) during charge $R_{current}\neq1$ (d) during discharge $R_{current}\neq1$.

The EHC is averaged for each state of charge and for all given current and is then interpolated versus SOC in equations III.50 and III.51.

$$\left(\frac{dU_{oc}}{dT}\right)_{Charge} = -0.6069SOC^6 + 2.0061SOC^5 - 2.5295SOC^4 + 1.5163SOC^3 - 0.4524SOC^2 + 0.0716SOC - 0.0064 \quad \text{III.50}$$

$$\left(\frac{dU_{oc}}{dT}\right)_{Discharge} = -0.8579SOC^6 + 2.6712SOC^5 - 3.0749SOC^4 + 1.5891SOC^3 - 0.35285SOC^2 + 0.0294SOC - 0.0011 \quad \text{III.51}$$

III.4 Battery temperature and heat dissipation model validation

In this section, temperature and heat flux measured during consecutive charge/discharge cycles for an applied current of 60A is compared to the numerical model results. The thermal parameters of battery (thermal conductivity, specific heat, heat transfer coefficient, internal resistance, entropy coefficient and ambient temperature) are fixed inputs and the validation with the experimental tests is conducted by modifying the charge and discharge currents.

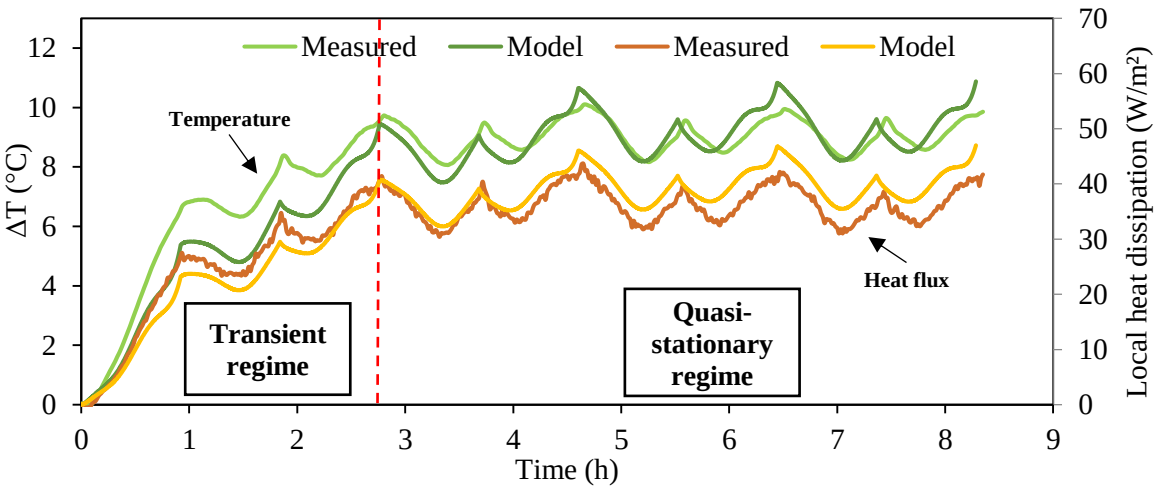

(a)

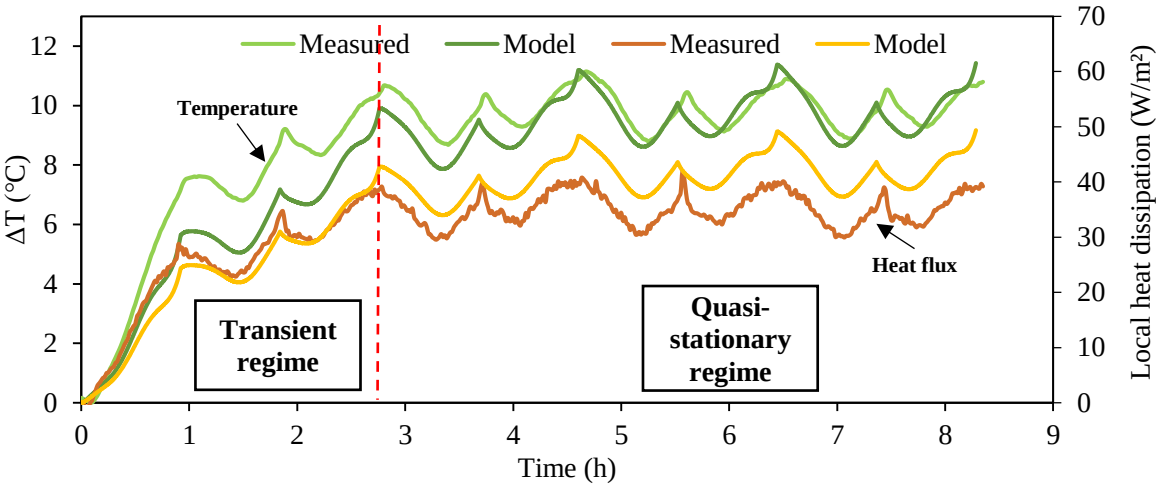

(b)

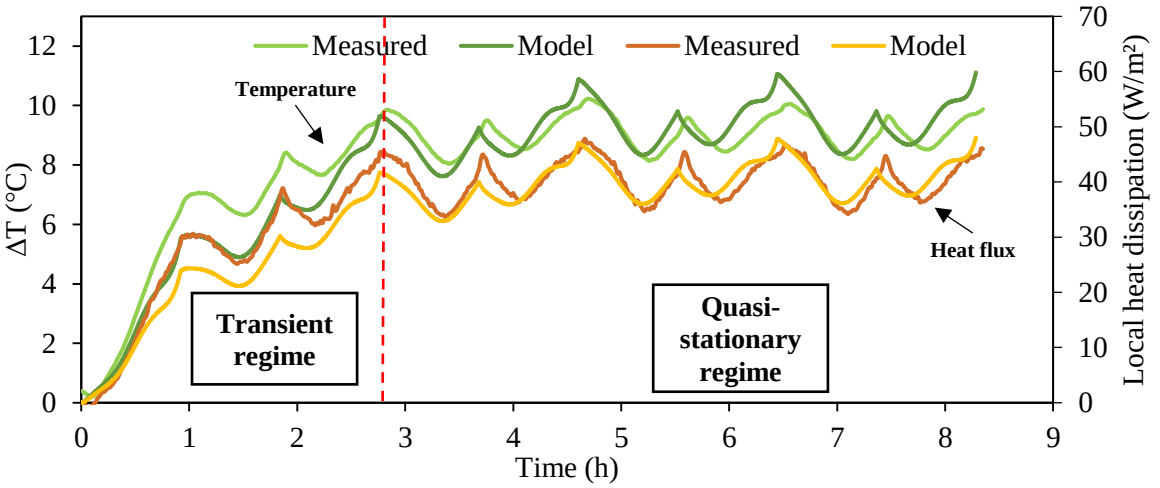

(c)

Figure III.9 Validation of temperature rise and dissipated heat for 1C rate. (a) front side (b) right side (c) bottom side.

Figure III.9 illustrates the experimental and numerical obtained results for three battery sides (front side, right side and bottom side). The accuracy of the numerical model is good during both transient and quasi-stationary regimes. The mean absolute error (MAE%) between measured and predicted temperatures are (9.65 %, 11.57 %, 9.22 %) for respectively the front, right and bottom sides. While the MAE of the dissipated heat measured locally in the center of the three sides are (8.56 %, 13.11 %, 8.73 %) for respectively the front, right and bottom sides. Moreover, Figure III.10 shows the obtained

experimental results and predictions by the model for three different charge/discharge currents: 40A/60A, 60A/60A and 60A/40A. The mean absolute errors are of 3.8 %, 4,7 % and 11.2 % respectively for the battery front, right and bottom sides.

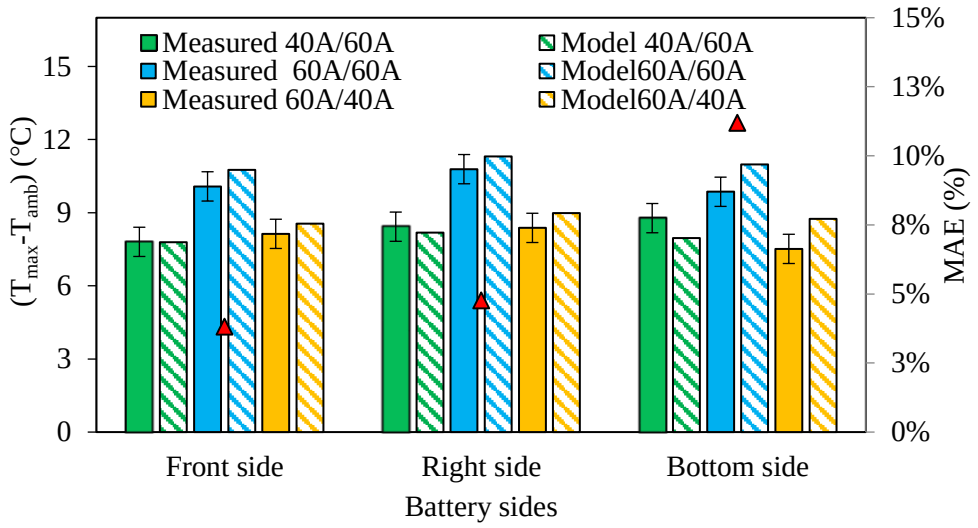

Figure III.10 Validation of maximum temperature rise for different C-rates.

The battery temperature is strongly dependent to charge/discharge current which is the main factor affecting the battery thermal behavior. For this reason, the total heat dissipation on the battery sides, predicted by the model is compared to the experimental measurements for the same charge and discharge current ratios ($R_{current}$=1) using three currents rates (40 A, 50 A, 60 A). Experimental tests were performed by charging and discharging the battery until reaching the maximum and minimum cut-of voltage (2.6 V-3.6 V). The thermal model is compiled for same state of charge (5%-95%). As shown in Figure III.11, the comparison of the experimental data and the thermal model presents an accurate prediction to the thermal profiles of heat dissipation. It can be seen that higher heat was dissipated for higher applied current. For each cycle, the profile of heat dissipation during quasi-stationary regime has a 'V' shape, due to the entropy variation during a cycle. Furthermore, the heat dissipated via battery sides is the consequence of the internal generation. As discussed previously, an amount of the internal heat is accumulated inside the battery and transferred by dissipation to the external environment. An illustration is shown in Figure III.12 describing the obtained numerical profiles of irreversible, reversible, accumulated and dissipated heat besides the temperature rise curve. The results show a strong variation of irreversible and reversible heats versus time due specially to change of the SOC which causes a variation of the internal electrical resistance and the entropic heat coefficient.

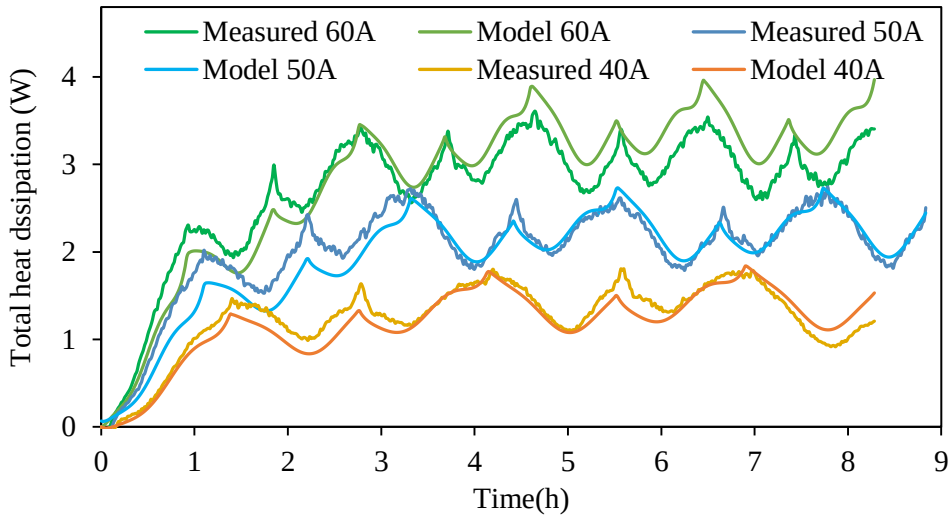

Figure III.11 Comparison of the measured and predicted battery total heat dissipation for $R_{current}$=1.

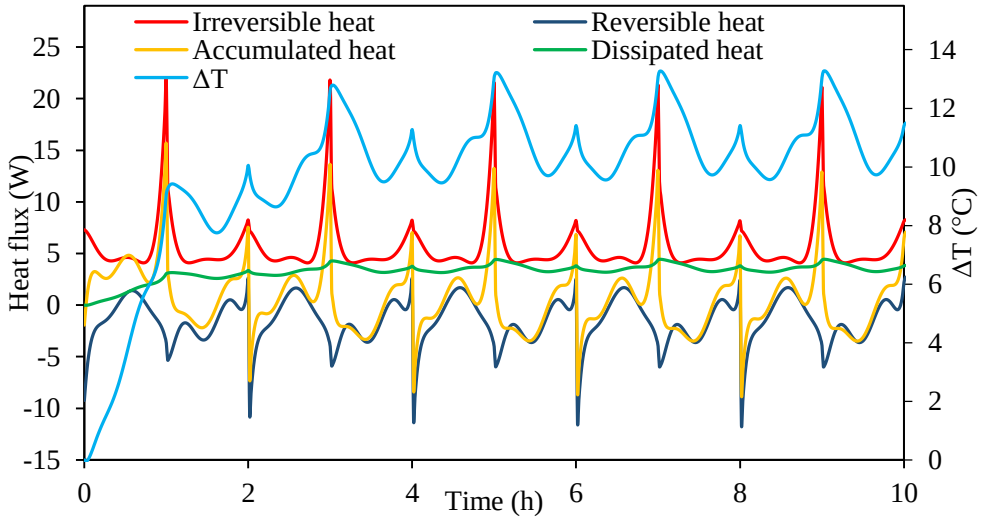

Figure III.12 Battery heat flux and temperature rise profiles for 1C-rate.

Additionally, the numerical model is used to determine the amount of each heat types for different current rates. Figure III.13 illustrates the amounts of irreversible, reversible, accumulated and dissipated heats for increasing charge current and a constant discharge current of 60 A during both transient and quasi-stationary regimes. The irreversible heat presents 80.57 % during transient regime while during quasi-stationary regime, this amount decreases to 77.58 % due basically to the increase of reversible heat amount from 19.43 % to 22.24 % as it is proportional to the temperature of the battery. Moreover, the battery dissipated heat during transient regime presents only 37.34 % while in in quasi-stationary

regime this amount increases to 90 %. The accumulated heat amount during transient regime is about 62% while during the quasi-stationary regime this amount presents less than 10 %.

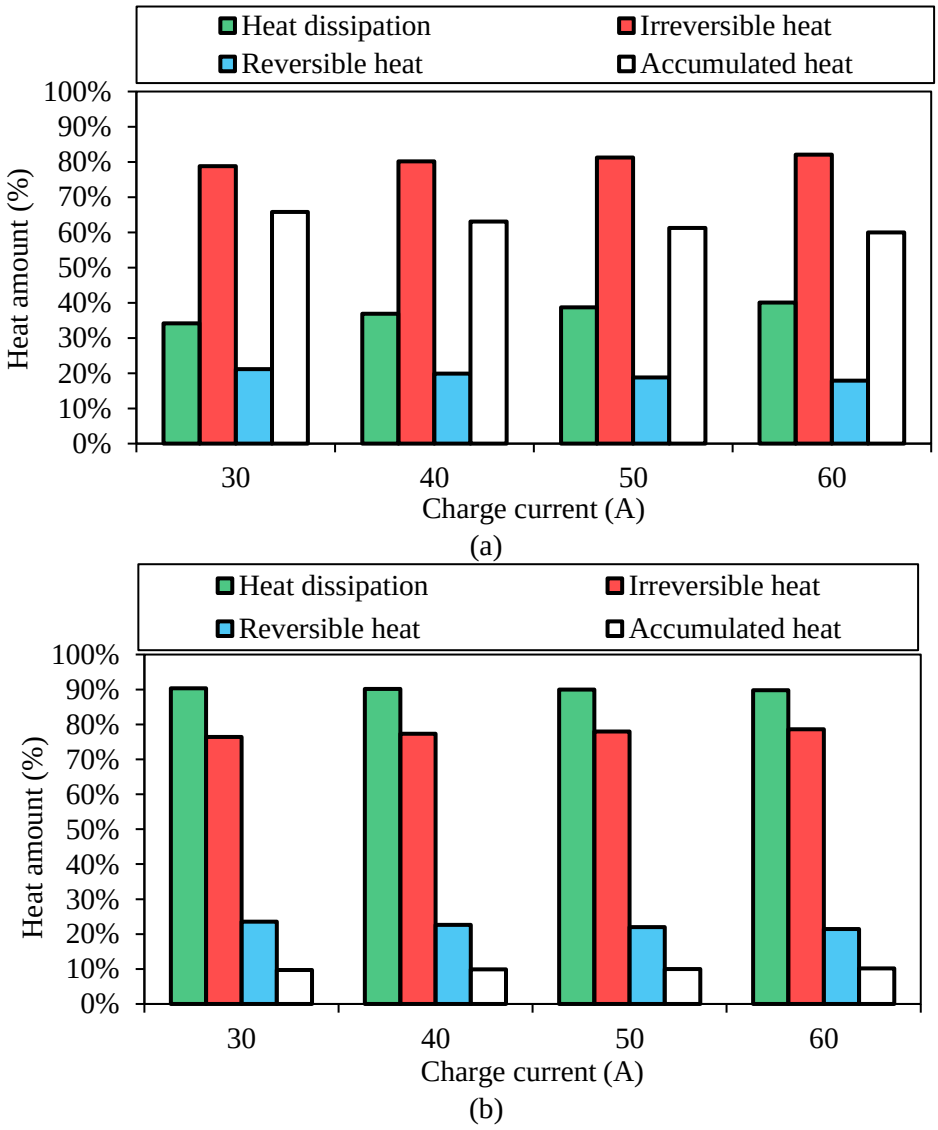

Figure III.13 Percentage of heat for a constant Discharge current of 60 A (a) transient regime (b) quasi-stationary regime.

Moreover, Figure III.14 illustrates the amounts of irreversible, reversible, accumulated and dissipated heats for increasing discharge current and a constant charge current of 60 A during both transient and quasi-stationary regime. During Transient regime, the irreversible heat amount for a discharge current presents 78.5 % while this amount increases to 86.5 % for a discharge current of 120 A which proves the domination of irreversible heat for high currents. Inversely, the reversible heat

amount is equals to 21.5 % for an applied current of 30 A while this amount decreases to 13.5 % for a tested current of 120 A. Furthermore, the battery dissipated heat during transient regime presents 62 % while in in quasi-stationary regime for a current of 30 A this amount increases to 90 % during quasi-stationary regime. The accumulated heat amount during transient regime is about 77.26 % for a tested current of 120 A while during the quasi-stationary regime this amount decreases to only 11.8 %. The high accumulation rate during transient regime is related to the reduced duration of cycle for high current.

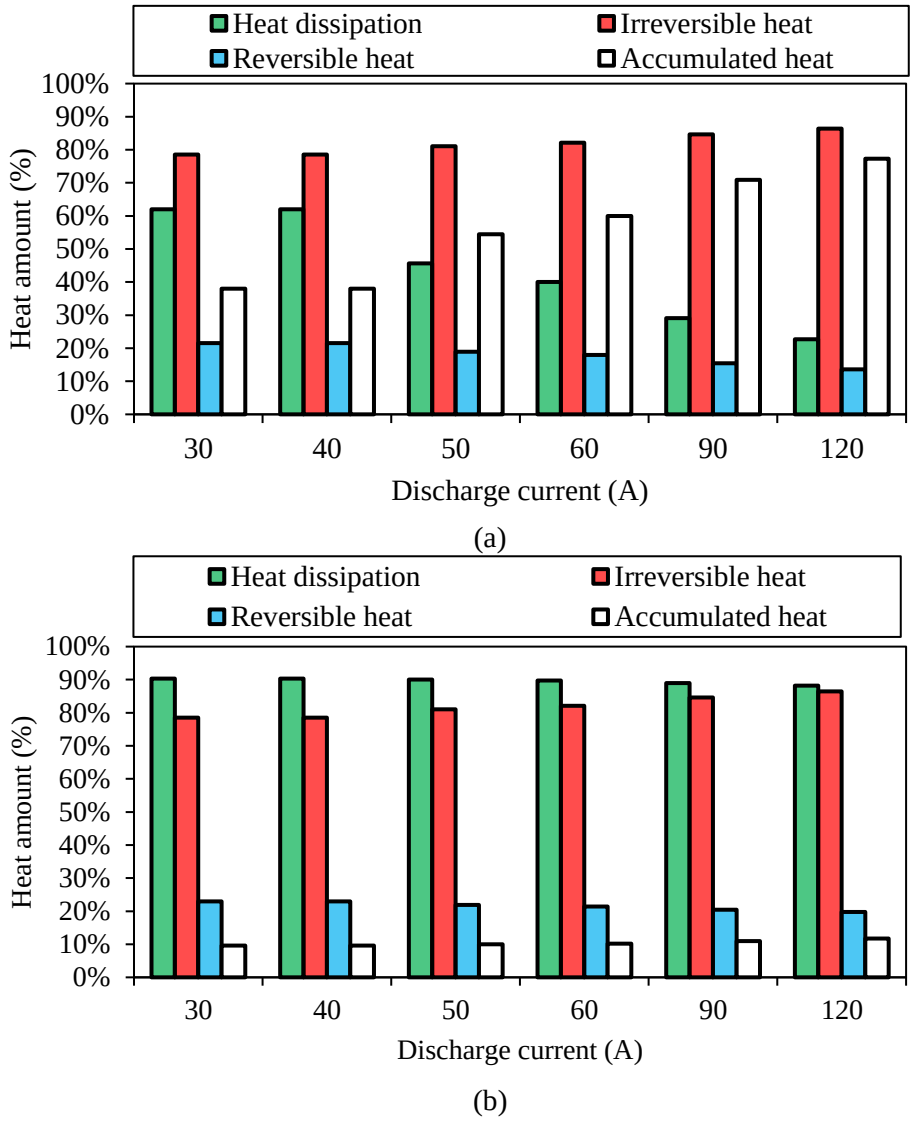

Figure III.14 Percentage of heat for a constant charge current of 60 A (a) transient regime (b) quasi-stationary regime.

III.5 Effect of the state of charge on the battery temperature

In this section, the effect of SOC as well as the first cycle prosses (charge or discharge) are studied to clarify their impact on the battery temperature rise and heat dissipation profile during both transient and quasi-stationary regimes. First, the model was validated by comparing the battery temperature and heat dissipation measured and predicted in transient and quasi-stationary regimes. The state of charge is varied between 20%-80%. Experiments and modeling are conducted for the same charge/discharge current of 60A. Figure III.15 shows the transient distribution of the battery temperature and heat dissipation during the charge and discharge cycles. It can be seen that the temperature rise and heat dissipation obtained in both transient and quasi-stationary regime were higher for the cycling test starting with charge process. This is justified by the effect of exothermic entropic heat coefficient in the end of charge cycle at a SOC of 80% while for discharge process, the entropic heat is endothermic in the SOC of 20%.

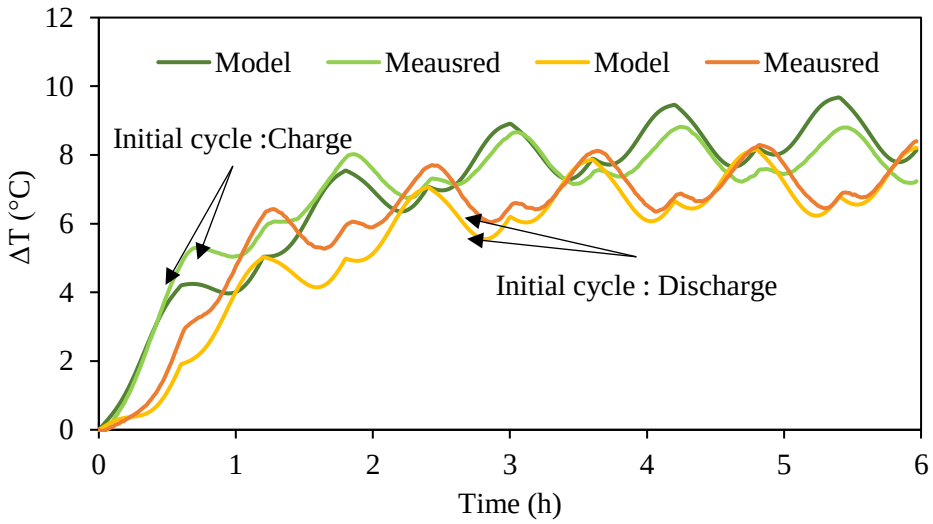

(a)

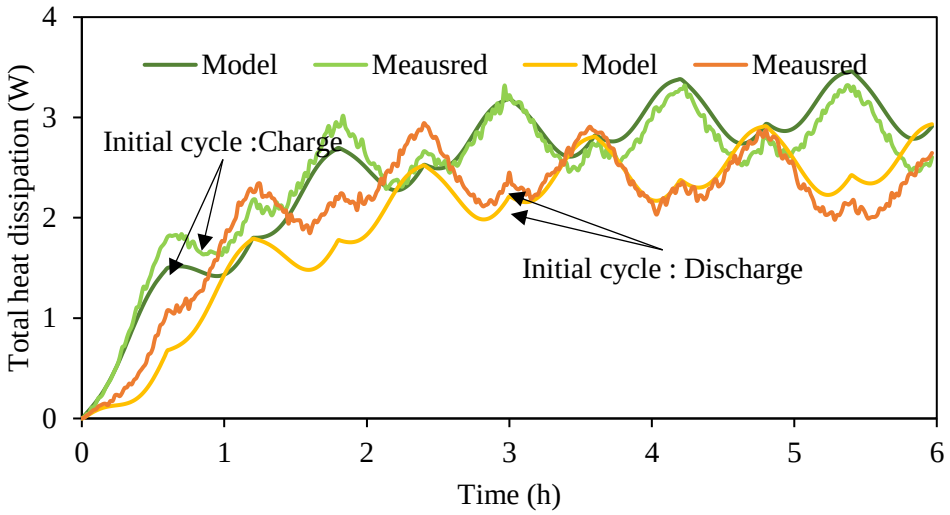

(b)

Figure III.15 Model validation for SOC range (20%-80%) for 1C-rate (a) battery temperature (b) heat dissipation.

Figure III.16.a. and Figure III.16.b. illustrate the obtained results of three different SOC ranges (0%-100%), (0%-50%) and (50%-100%) for three charge/discharge currents. The same cycling duration is used for (0%-50%) and (50%-100%). The range (0%-100%) is chosen to be the reference. The maximum mean temperature rise is obtained by computing the difference between the mean battery temperature as defined in equation III.52 and the ambient temperature.

$$T_{mean} = \frac{\sum_{i=1}^{Nx+1}\sum_{j=1}^{Ny+1}\sum_{k=1}^{Nz+1} T_{i,j,k}(t)}{\text{number of nodes}} \qquad \text{III.52}$$

The heat energy dissipation during charge/discharge cycles, is found by integrating the dissipated heat via battery surfaces as proposed in equation III.53

$$Q_d = \int_{t=0}^{t_{end}} \dot{Q}_d(t)\, dt \qquad \text{III.53}$$

Obtained results show higher temperature rise and heat energy loss for the SOC ranging from 50% to 100% compared with the study case for SOC range (0%-50%) which is due mainly to the dominance

of exothermic part of reversible heat. The battery temperature rise for SOC range (50%-100%) reached for the three tested currents is the same temperature rise for a SOC range between (0%-100%). The highest amount of energy is produced for a SOC higher than 80% due basically to drastic increase of the internal resistance which causes higher irreversible heat generations.

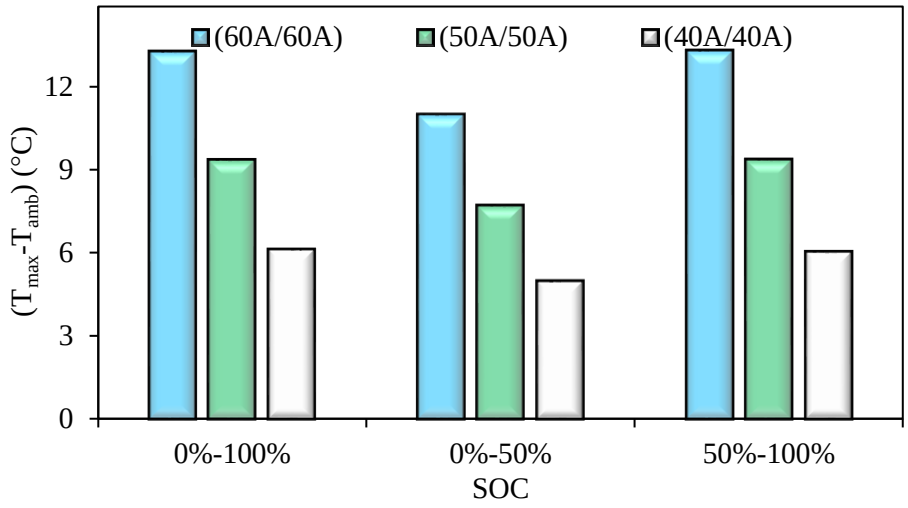

(a)

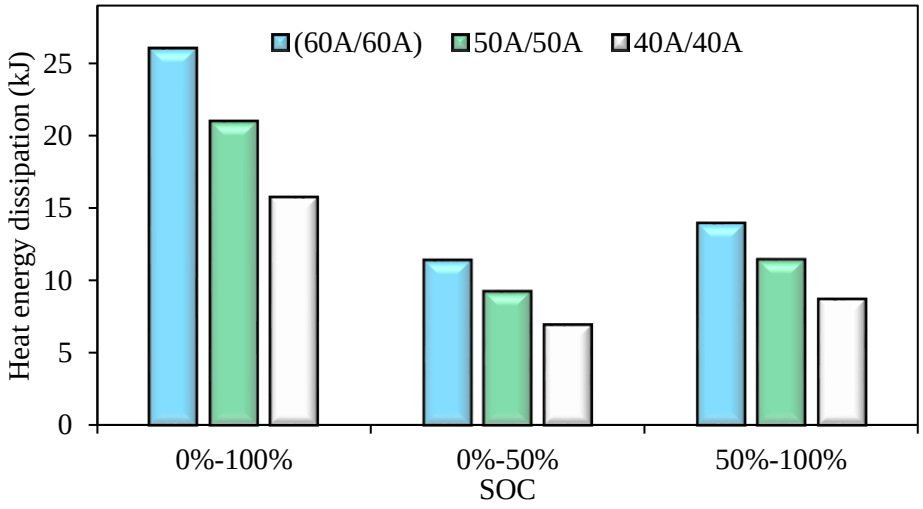

(b)

Figure III.16 The SOC effect on (a) the maximum temperature rise (b) heat energy dissipation.

Figure III.17 illustrates the effect of the state of charge range (ΔSOC) on the battery maximum temperature rise and heat energy dissipation computed for one cycle in quasi-study state. 0% is used as the initial SOC for all the studied cases, but the final state of charge is variable from 10 to 100%. The results in this figure show that the heat energy dissipation is mainly dependent on the SOC range. The amount of heat energy dissipated during charge and discharge cycle for a SOC from 0% to 100% is 26.8 kJ, this amount decreased to 12.35 kJ for a SOC ranging from 0% to 50%. The maximum temperature rise has no linear dependency versus SOC range due mainly to the strong effect of reversible heat in the quasi-stationary regime. For an optimal thermal use of the battery, avoiding a complete charge and discharge cycle may lead to increasing battery life cycle. For a SOC higher than 80% the internal resistance of the battery drastically increases. This phenomenon provides higher heat generation and battery temperature increase.

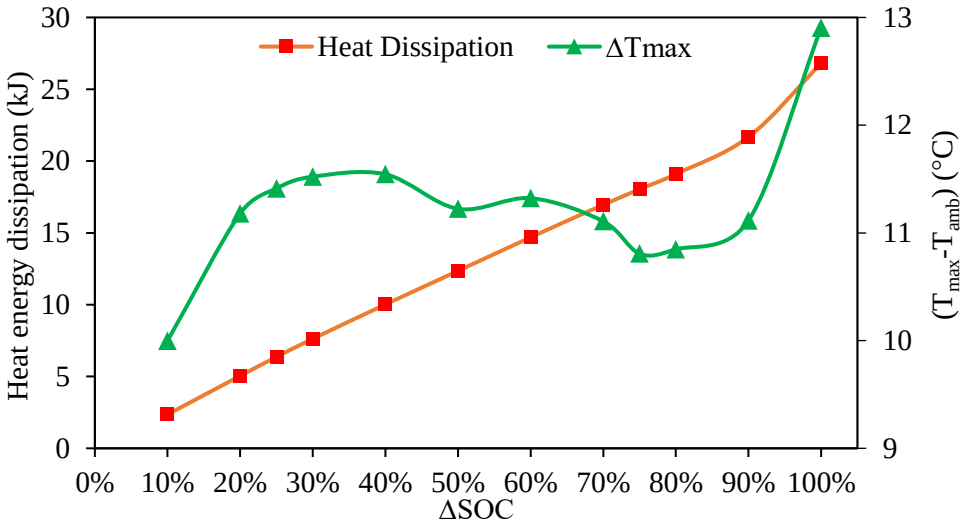

Figure III.17 Effect of SOC ranges on maximum temperature rise and heat generation.

III.6 Prediction of the maximum battery temperature rise and heat energy generation

The battery maximum mean temperature is computed for a fixed value of charge current in the range of 10 A to 60 A using the developed model. Figure III.18 illustrates the obtained results in the quasi-stationary regime for $R_{current}$ variable until 6. The discharge current is between 10 A and 120 A. It can be seen that higher temperature rise is found for higher current which is due to the higher amount of internal heat generation. Furthermore, based on the results presented in Figure III.18, a new correlation is proposed to allow a fast prediction of the battery maximum temperature rise. The developed

correlation is presented in equation III.54. Where the discharge and charge currents ratio are defined respectively by equations III.55 and III.56.

$$\Delta Tmax = 0.48108 + 7.592{R_{CC}}^{1.742} + 19.384{R_{DC}}^{1.826} + 1.57{R_{CC}}^{1.742}{R_{DC}}^{1.826} \quad \text{III.54}$$

$$R_{DC} = \frac{I_{discharge}}{I_{discharge,max}} \quad \text{III.55}$$

$$R_{CC} = \frac{I_{charge}}{I_{charge,max}} \quad \text{III.56}$$

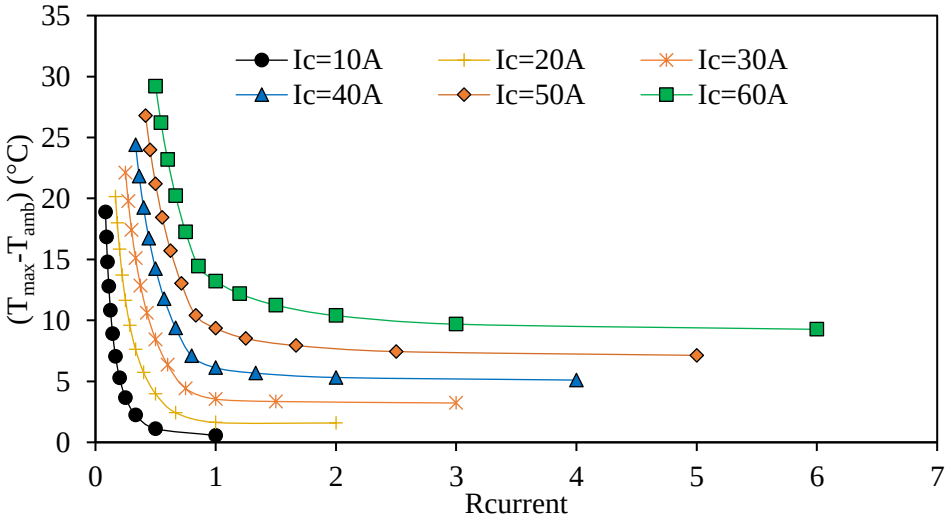

Figure III.18 Maximum temperature rise for different $R_{current}$ in quasi-stationary regime.

The results predicted by the proposed correlation are compared to the experimental data as presented in Figure III.19. Most of validated experimental results have a mean absolute error lower than 15%.

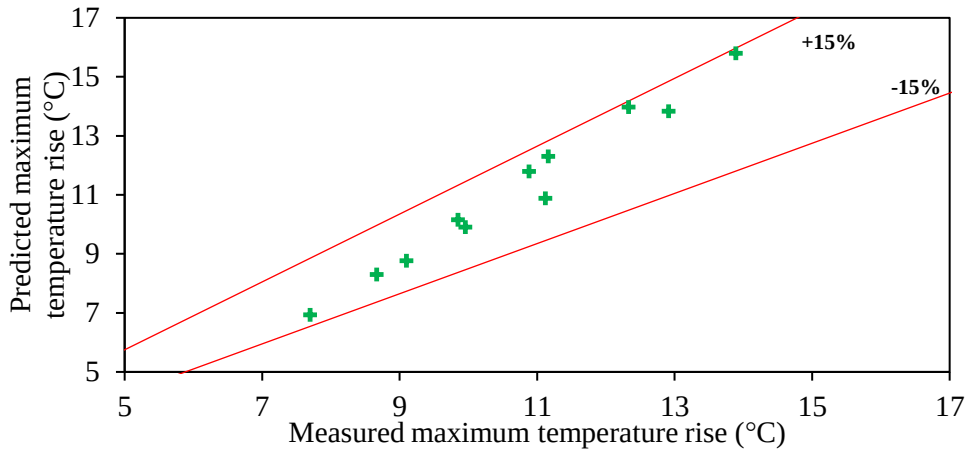

Figure III.19 Validation of new developed correlation to estimate the battery maximum temperature rise.

Figure III.20 illustrates the total heat energy generated during a charge/discharge cycle in quasi-stationary regime for different C-rates. A strong dependency to current is obtained and higher heat energy amounts were obtained for higher current values. About 90% of the heat energy generation is dissipated to ambient via battery sides, nevertheless an accurate thermal management system must be integrated to ensure keeping battery under normal operating conditions. The generated energy is correlated by the equation III.57 defined bellow.

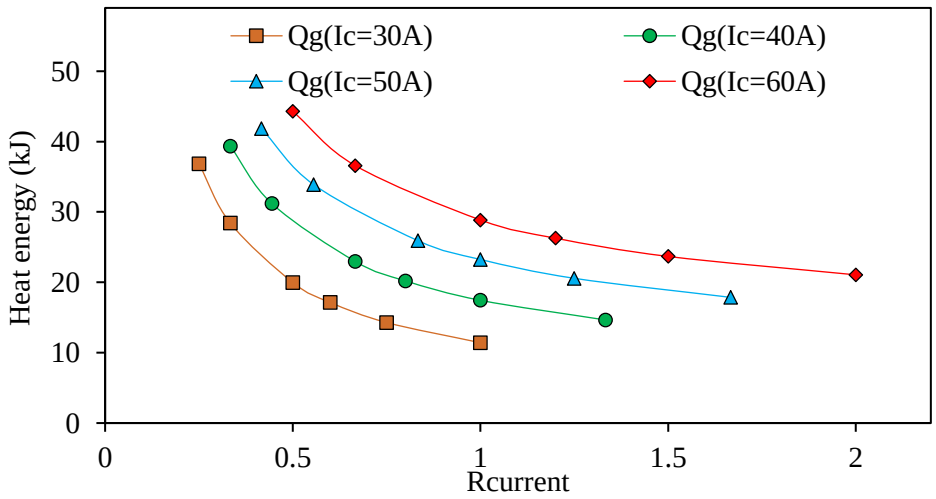

Figure III.20 Total heat energy generated and dissipated during a cycle for different C-rates.

$$Q_g = -16.124 + 27.129{R_{CC}}^{0.598} + 37.748{R_{DC}}^{0.931} - 4.442{R_{CC}}^{0.598}{R_{DC}}^{0.931} \quad \text{III.57}$$

Equation III.57 presents an efficient solution to fast estimate the amount of energy generated by the battery during operating time. The proposed correlation estimates heat generation with high accuracy lower than 10% compared to the experimental measurements (Figure III.21).

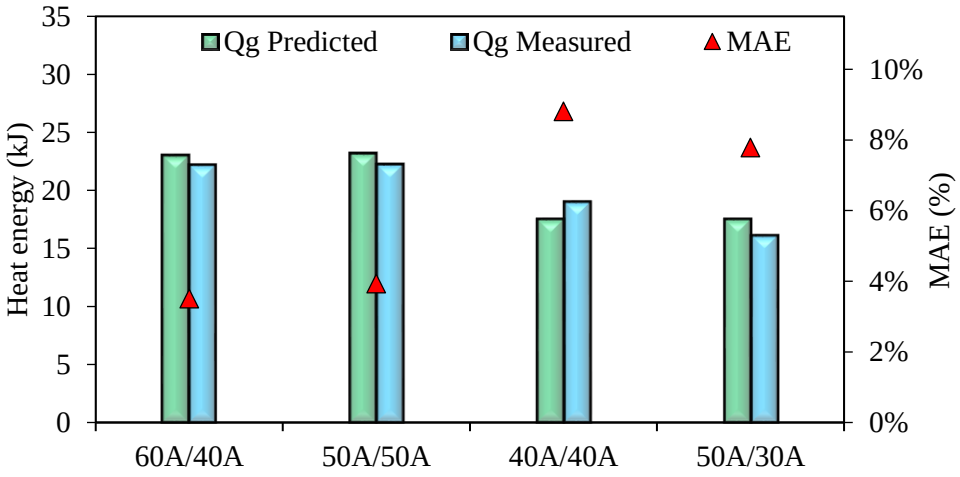

Figure III.21 Validation of new developed correlation to estimate heat energy generation.

III.7 Conclusion

In this chapter, a three-dimensional transient model was developed to predict the thermal behavior of a 60 Ah prismatic lithium-ion battery tested under different charge and discharge currents. Thermal and electrical parameters were determined experimentally and analytically. The calculations are based on experimental data such as heat flux densities and temperatures and extracted physical parameters from literature data. Based on defined inputs parameters, the proposed 3D thermal model is solved using ADI method and a validation with experimental results is performed to ensure the model accuracy. Two correlations were developed in this chapter enabling the prediction of those parameters for given charge/discharge currents. The proposed correlations on this chapter are important to fast predict the maximum temperature of a battery for given conditions and to size an efficient battery thermal management system. A validation is performed for suggested correlations with experimental data and a maximum mean absolute error lower than 15% is obtained for the prediction of maximum temperature rise while the maximum mean absolute error for the heat energy generation is about 9%.

Chapter IV. Experimental and numerical applications of PCM as cooling method of battery pack

IV.1 Introduction

The experimental and numerical study of a Li-ion battery performed respectively in chapter II and III enables the characterization of its thermal behavior. The measurement of local temperatures and heat flux carried out for different charge and discharge current rates show the possibility to track the temperature of the battery by measuring the temperature on the positive electrode. The 3D numerical model presented in chapter III allows the validation of the thermal parameters characterizing the tested battery. We have also calculated two correlations helping on fast predicting the battery maximum temperature and heat energy.

In this chapter, both an experimental and numerical study are performed to describe the thermal behavior of a Li-ion battery pack. First a simplified model based on equivalent thermal networks is developed and validated for one battery. Moreover, a novel test bench system Chroma 17020 is implemented to analyze the thermal behavior of various batteries, for different ambient temperatures. Finally, a pack of batteries is tested experimentally and numerically for constant current and dynamic current using normalized driving cycles. A cooling system using microencapsulated PCM is investigated to ensure the battery temperature control.

IV.2 Battery equivalent thermal network

In the literature review presented in chapter I, two main modeling approaches of Li-ion batteries were discussed. The first one is a numerical modeling which is based on the resolution of the heat transfer equations using mathematical methods such as finite difference, volume difference or finite element methods. The second approach is the equivalent circuit modeling which requires the use of the analogy between electrical and thermal systems. An equivalent thermal circuit should be developed and electrical laws are used such as the laws of knots and the low of meshes.

As seen in the previous chapter, the battery model is based on solving the 3D heat transfer equations using ADI method. The developed model was validated for different experimental conditions and used to predict the temperature and the heat generation rates of the tested battery for a large variety of inputs conditions. The proposed model helped in providing two correlations enabling the characterization of the thermal behavior of a Li-ion battery. The prediction of battery temperature and heat generation for given charge and discharge currents is very important in order to avoid damages to the battery during

operating time. Nevertheless, in electric vehicles a pack of batteries is usually used to supply electric power to the motor as shown in Figure IV.1 . It is therefore necessary to model the battery pack to simulate the real conditions of work of each Li-ion battery in the pack. However, modeling a pack of several batteries besides other cooling systems such as PCM requires the simplification of the studied physical model. Thus, in this section a battery equivalent thermal network is presented and validated for one battery. Later an extension of this model is performed and validated for a pack of batteries under natural convection and combined with PCM for both constant and dynamic currents.

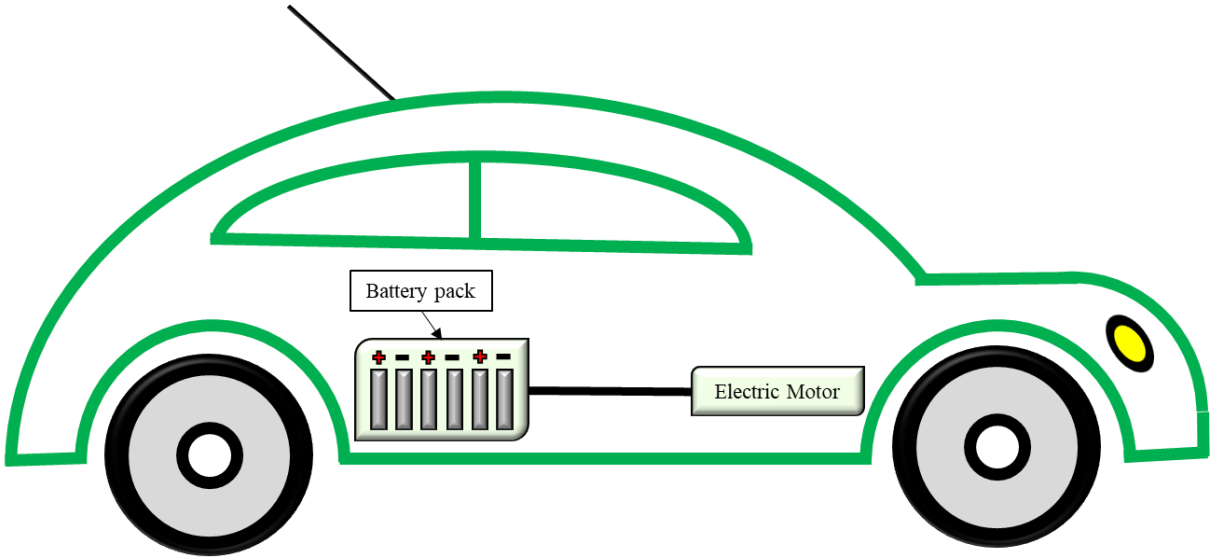

Figure IV.1 Schematic diagram of an electric vehicles.

In this model the battery is considered as a one block model composed of nodes, resistances, capacitances, current and voltage sources. The principle of the thermal network is based on the analogy between electrical and thermal systems. Figure IV.2 illustrates a 3D thermal network of a prismatic battery. In the battery core a node called T_{in} connected to the source term which is modelled by a capacitance and a current source in parallel. Moreover, all six battery sides are modeled by a node connected to the core node via a thermal resistance. In addition, the external heat dissipation is modeled by a voltage source connected in series with a thermal resistance representing the convective heat exchange. All used parameters in the previous chapter to simulate the specific heat capacity, thermal conductivities, internal electrical resistance, the entropic heat coefficient and the heat transfer coefficients are considered as inputs to the lumped thermal model. The conductive and convective thermal resistances equations are given bellow in equation IV.1 and IV.2. n designs the normal vector to the battery surface.

$$R_n = \frac{e_n}{2\lambda_n S_n} \quad \text{IV.1}$$

$$R_{cv,n} = \frac{1}{hS_n} \quad \text{IV.2}$$

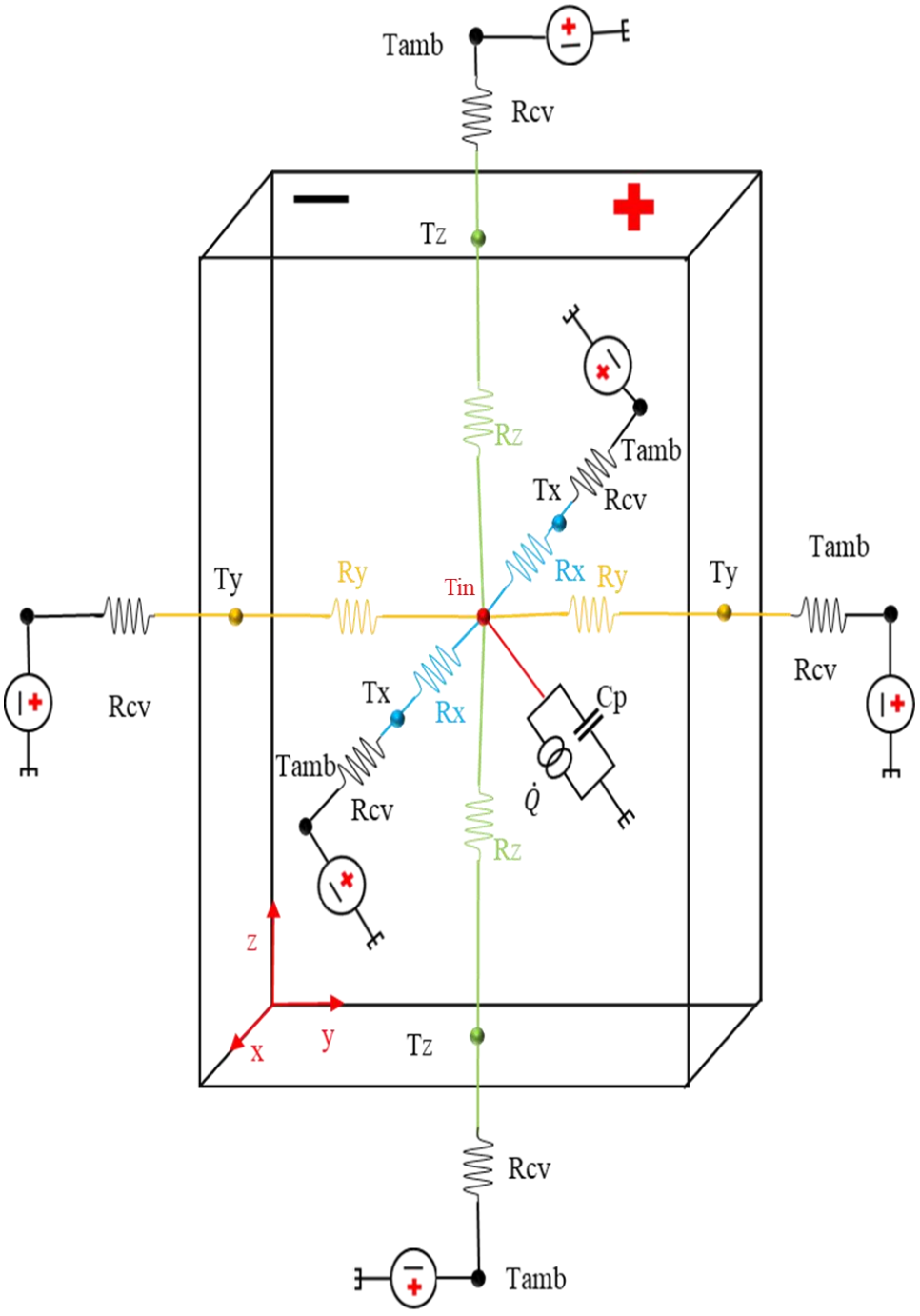

Figure IV.2 Battery 3D equivalent thermal network.

The calculated values of thermal resistances are given in Table IV.1.

Table IV.1 Conductive and convective thermal resistances.

Thermal resistance	**(K/W)**
R_x	2.33
R_{cvx}	8.38
R_y	2.59
R_{cvy}	24.11
R_z	11.29
R_{cvz}	50.32

The 3D lumped model presented in Figure IV.2 is simplified using assumptions discussed below.

- Assumption 1: Taking in consideration the symmetry of temperature discussed in chapter II. only three main nodes may be connected to battery core node.

- Assumption 2: The connected conductive and convective thermal resistances in series are simplified in this model to an equivalent thermal resistance R_i. i holds for the sides.

- Assumption 3: The three resistances in parallel are represented by an equivalent resistance $R_{eq.}$ Figure IV.3 shows the presentation of the thermal networks based on the simplified assumption. In addition, the thermal resistance presented are given in equations IV.3, IV.4, IV.5 and IV.6 while in Table IV.2 the value of each used thermal resistance is shown.

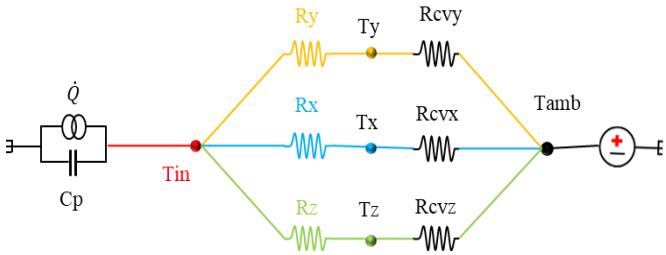

(a)

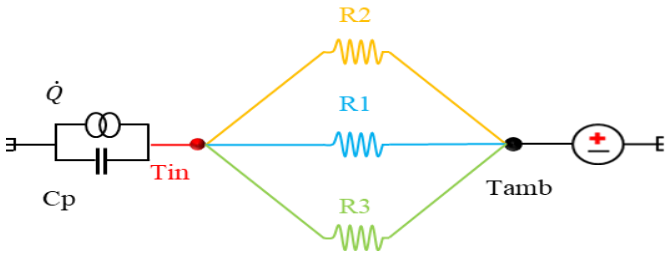

(b)

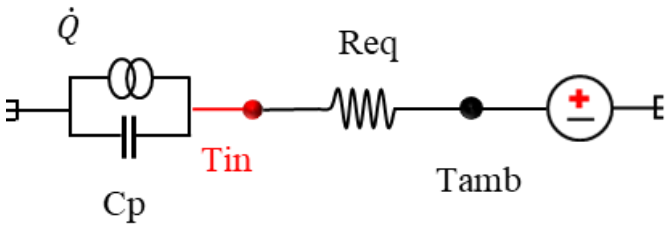

(c)

Figure IV.3 Simplified battery equivalent thermal network. (a) assumption 1 (b) assumption 2 (c) assumption 3.

$$R_n = \frac{e_n}{4\lambda_n S_n} \quad \text{IV.3}$$

$$R_{cv,n} = \frac{1}{2hS_n} \quad \text{IV.4}$$

$$R_i = R_{cv_n} + R_n \quad \text{IV.5}$$

$$R_{eq} = \left(\frac{R_1 R_2 R_3}{R_1 R_3 + R_2 R_3 + R_1 R_2}\right) \quad \text{IV.6}$$

Table IV.2 Equivalent thermal resistance used in simplified models.

Thermal resistance	**(K/W)**
R_x	1.16
R_{cvx}	4.19
R_y	1.29
R_{cvy}	12.05
R_z	5.64
R_{cvz}	25.16
R_1	5.35
R_2	13.34
R_3	30.8
R_{eq}	3.39

The heat transfer equation based on the assumptions illustrated in Figure IV.3 are given in Equation IV.7. This equation is solved using Runge-Kutta 4th order and a Fortran language program is developed to calculate T_{in}, temperature in the core of the battery. The algorithm of resolution of the heat transfer equation is defined in equations IV.8, IV.9, IV.10, IV.11 and IV.12, The thermal parameters defined in chapter III are reused in this part and the validation of the model is illustrated in Figure IV.4 The test conditions used in the validation of the model are performed for an applied current of 60A during both charge and discharge cycles. The temperature of the positive electrode, which represents the core of the battery as discussed in chapter I, is compared to the numerically predicted temperature. Moreover, the heat dissipated, experimentally measured and numerically calculated are compared for the same test conditions. An acceptable accuracy is observed and the model is validated then for battery temperature measured in the front, right and bottom sides.

$$R(t)I^2 - IT_{in}(t)\frac{dU}{dT}(t) - MCp\frac{dT_{in}(t)}{dt} = \frac{T_{in}(t) - T_{amb}}{R_{eq}} \quad \text{IV.7}$$

$$T_{in}(t+1) = T_{in}(t) + \frac{\Delta t}{6}(K_1 + 2K_2 + 2K_3 + K_4) \quad \text{IV.8}$$

$$K_1 = \frac{1}{MCp}\left(R(t)I^2 - IT_{in}(t)\frac{dU}{dT}(t) - \frac{T_{in}(t) - T_{amb}}{R_{eq}}\right) \quad \text{IV.9}$$

$$K_2 = \frac{1}{MCp}\left(R\left(t+\frac{\Delta t}{2}\right)I^2 - I\left(T_{in}(t) + \frac{\Delta t}{2}K_1\right)\frac{dU}{dT}\left(t+\frac{\Delta t}{2}\right) - \frac{\left(T_{in}(t) + \frac{\Delta t}{2}K_1\right) - T_{amb}}{R_{eq}}\right) \quad \text{IV.10}$$

$$K_3 = \frac{1}{MCp}\left(R\left(t+\frac{\Delta t}{2}\right)I^2 - I\left(T_{in}(t) + \frac{\Delta t}{2}K_2\right)\frac{dU}{dT}\left(t+\frac{\Delta t}{2}\right) - \frac{\left(T_{in}(t) + \frac{\Delta t}{2}K_2\right) - T_{amb}}{R_{eq}}\right) \quad \text{IV.11}$$

$$K_4 = \frac{1}{MCp}\left(R\left(t+\frac{\Delta t}{2}\right)I^2 - I\left(T_{in}(t) + \Delta tK_3\right)\frac{dU}{dT}\left(t+\frac{\Delta t}{2}\right) - \frac{\left(T_{in}(t) + \Delta tK_3\right) - T_{amb}}{R_{eq}}\right) \quad \text{IV.12}$$

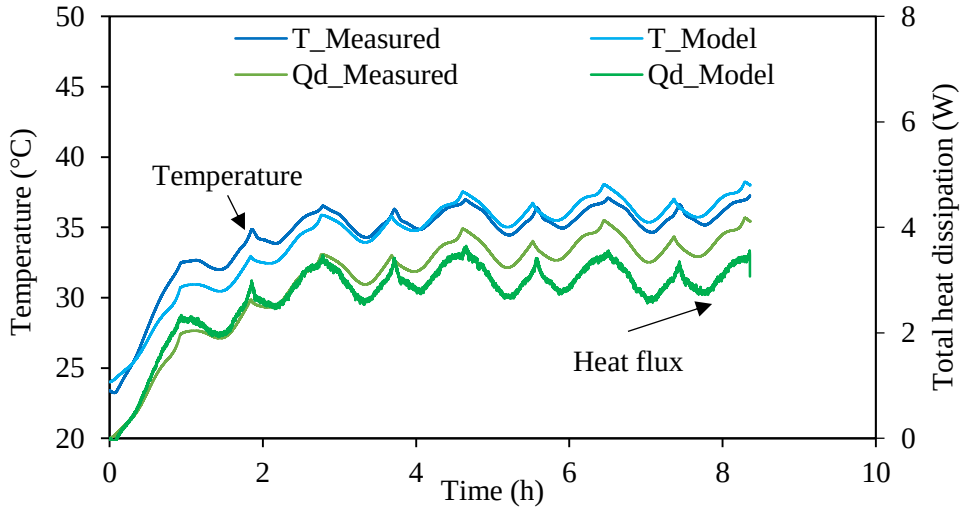

Figure IV.4 Model validation of core temperature and heat dissipation.

A mean temperature is defined for each battery sides using measurement of surface temperature in front, right and bottom sides. Furthermore, the sides temperatures (T_x, T_y and T_z) are estimated in the model based of the proposed equivalent thermal network. See equations IV.13, IV.14 and IV.15. Figure IV.5 presents the model validation of temperatures measured in each battery sides. A good accuracy is obtained with a MAE of 9.1 %, 1.3 % and 5.2 % for respectively front, right and bottom sides.

$$\frac{T_{in} - T_x}{R_x} = \frac{T_x - T_{amb}}{R_{cvx}} \quad \text{IV.13}$$

$$\frac{T_{in} - T_y}{R_y} = \frac{T_y - T_{amb}}{R_{cvy}} \quad \text{IV.14}$$

$$\frac{T_{in} - T_z}{R_z} = \frac{T_z - T_{amb}}{R_{cvz}} \quad \text{IV.15}$$

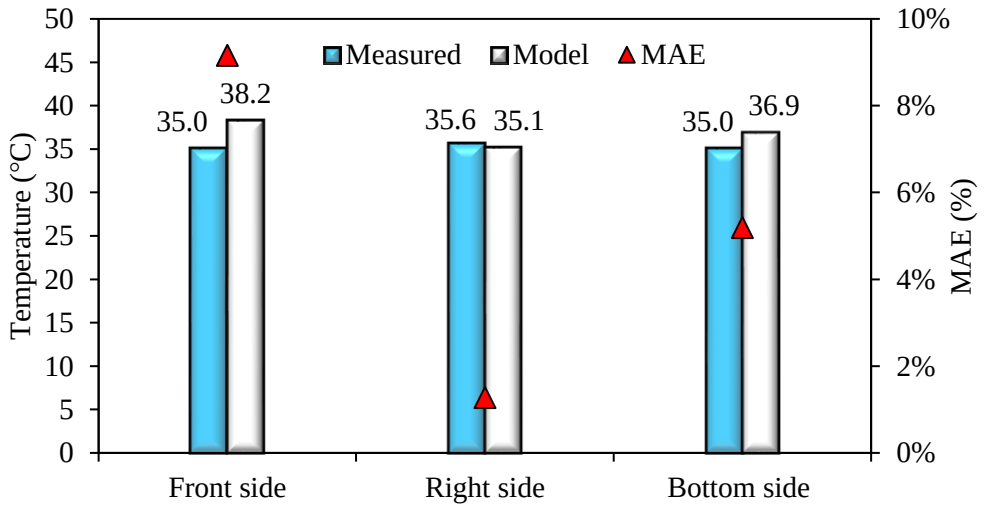

Figure IV.5 Model validation of battery surface temperatures.

IV.3 Effect of ambient temperature on batteries thermal behavior

In the present section, both a thermal behavior study and thermal parameters characterization were performed for several applied ambient temperatures. Consecutive charge discharge cycles were performed on five Li-ion batteries tested in a climate chamber. The effect of ambient temperature on batteries thermal behavior was investigated then measurements of battery thermal parameters were carried out to explain the thermal behavior.

The charge and discharge experimental cycles were conducted using the Chroma 17020 test bench. It is equipped by 8 charge/discharge chains with a maximum power and current of (1200 W,60 A) in each chain. Furthermore, the ambient temperature was controlled by the climate chamber Weisstechnik. Figure IV.6 illustrates the test bench and the five Li-ion batteries tested. Moreover, Table IV.3 summarizes the characteristics of the tested batteries. Two types of batteries were chosen i.e. LFP and NMC. This choice is justified by their wide use as energy storage systems in electric vehicles. All batteries were tested under their 1C-rate. Consecutive charge discharge cycles were applied. The voltage cut-off of each battery is determined by the recommendation of its manufacture. T-type thermocouples were inserted in each battery and an average battery surface temperature is then determined to enable the comparison with other batteries. The Chroma 17020 was connected to Battery Pro graphical interface permitting the system control and data acquisition.

Figure IV.6 Experimental setup and tested batteries inside the climate chamber.

Table IV.3 Tested batteries.

Cathode material	Geometry	Capacity (Ah)	Voltage range (V)
LFP	Prismatic	72	(2.6-3.6)
LFP	Prismatic	60	(2.6-3.6)
LFP	Prismatic	20	(2.7-3.7)
NMC	Prismatic	53	(2.9-4.3)
NMC	Cylindrical	3	(2.6-4.1)

The measurement of batteries specific heat capacity and thermal conductivities were performed using a heat flow meter (HFM446), as illustrated in Figure IV.7. This test bench allows to test samples with a maximum size of 203 mm, 203mm, 51mm. The applied temperature range varies from -20°C to 90°C. A high accuracy of measurement is ensured by the heat flow meter with an accuracy better than 2% as given by its manufacture.

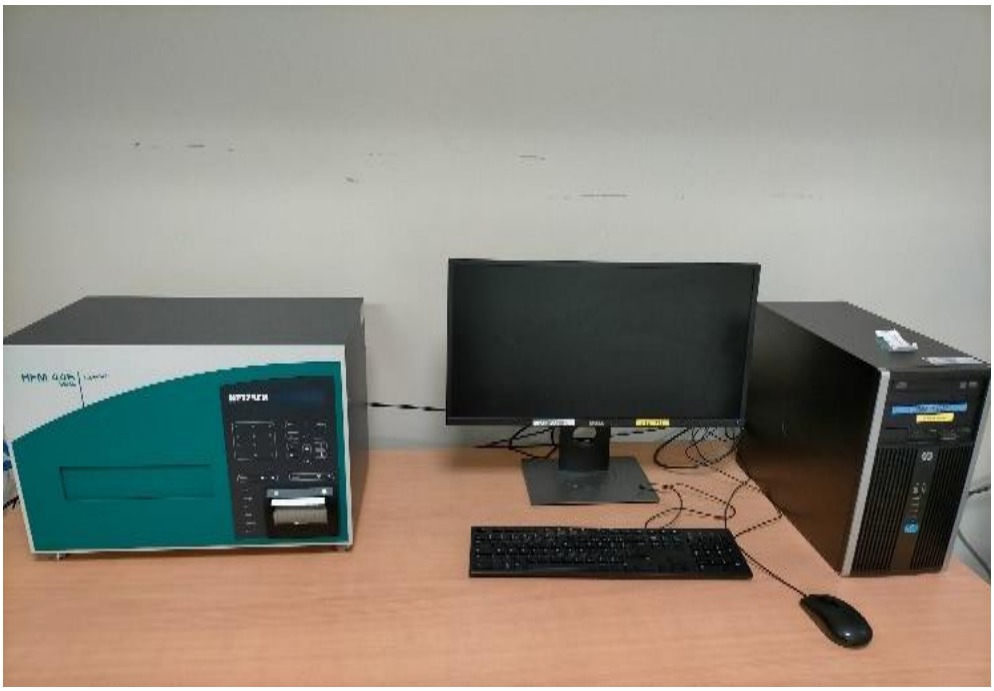

Figure IV.7 Heat Flow Meter test bench.

IV.3.1 Comparison of batteries thermal behavior for different chemistries

The effect of ambient temperature on battery temperature during quasi-stationary regime for 60Ah battery is presented in Figure IV.8 Same temperature profile was obtained for all tested ambient temperatures. The results show lower battery surface temperature rise for higher ambient temperature. In the beginning of charge cycle, temperature decreases slightly then increases until the end of the cycle. Temperatures in the starting instant of the charge cycle obtained for ambient temperature of 0°C, 10°C, 20°C and 30°C are respectively 6.87°C ,6.08°C, 4.36°C and 3.43°C while in the end of the cycle are (6.40°C,5.36°C, 4.32°C and 3.31°C). The temperature profile in the discharge cycle has the same "V" shape profile as in the charge cycle. Nevertheless, the minimal temperature rise obtained in the discharge cycle is slightly lower than the obtained in the charge cycle. This is caused mainly by the difference in the entropy coefficient during the charge and discharge cycle [153].

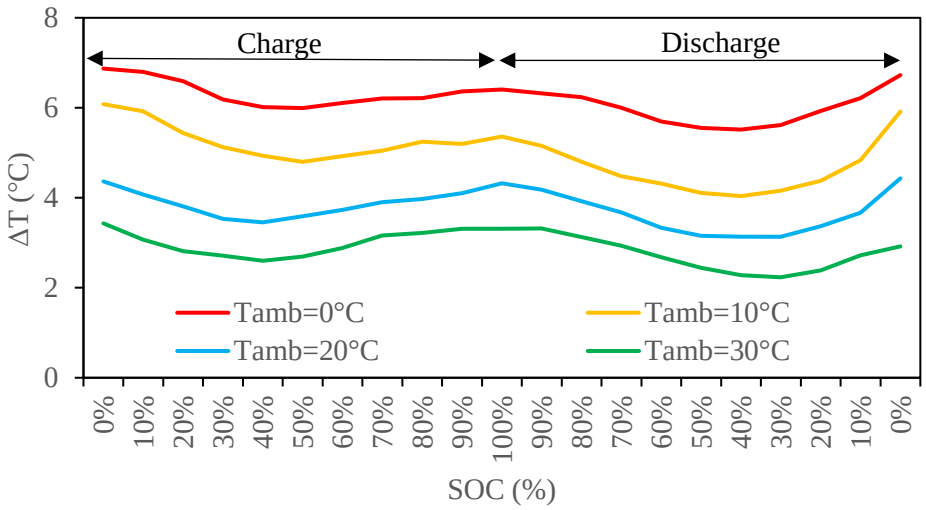

Figure IV.8 Effect of temperature on 60Ah battery temperature rise.

A comparison of the temperature profile for three different batteries (NMC 53Ah, LFP 20Ah, NMC 3Ah) tested under a temperature of 10°C is illustrated in Figure IV.9. The decrease of temperature in the beginning of the charge cycle is related directly to the endothermic part of the entropic heat coefficient for a SOC of charge lower than 40% followed by an exothermic stage [154]. The slight difference between temperature profile in charge and discharge cycles is due mainly to the difference between the entropic coefficient during charge and discharge studied for three different batteries' type (NCA, LCO, LFP) [155]. The results show the hysteresis of the entropy coefficient. Higher entropy

during charge compared to discharge explains our experimental results showing the difference between the temperature profiles. Moreover, even though all the three batteries were tested under 1C-rates different temperature rise were obtained. This is justified by the difference of applied current on each battery. The NMC 53Ah battery's temperature is the highest as the applied current for this battery is the highest.

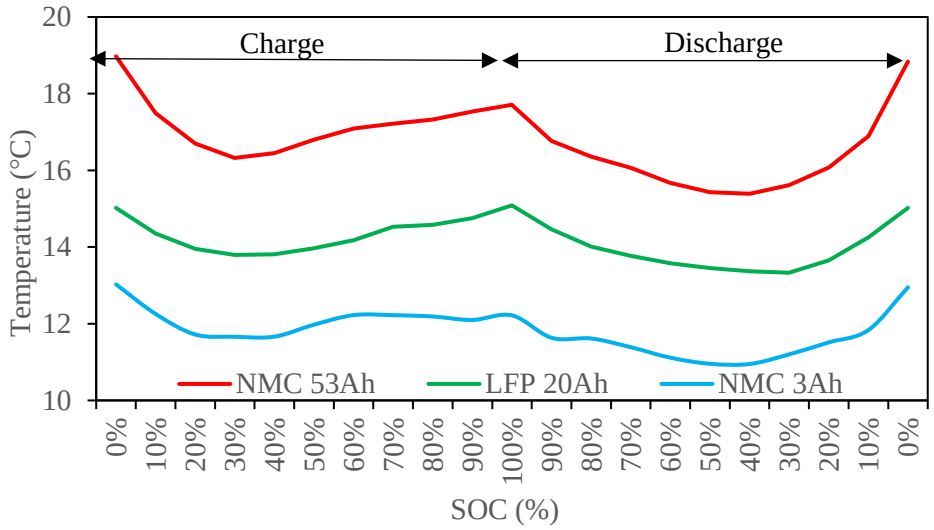

Figure IV.9 Comparison of temperature profiles of different batteries in quasi-stationary regime (T_{amb}=10 °C).

Figure IV.10 illustrates the maximum temperature rise obtained for the five tested batteries and for 4 different applied ambient temperature (0 °C,10 °C,20 °C,30 °C). For all tested batteries, the temperature shows a strong dependency to the ambient temperature. The temperature of batteries rises, which is basically due to internal heat generation, as the applied current is the same in all ambient temperatures for each battery. The dependency of the battery temperature to the environmental temperature could be explained by a change in the battery thermal properties. The internal resistance of the battery tested by Wu et al. [140] was found to be dependent to the ambient temperature. It decreases for increasing ambient temperatures. This decrease is about 25% for an applied temperature ranging from 0°C to 25°C. The effect of ambient temperatures on the variation of the battery entropy was investigated. The experimental study conducted by Bazinski et al. [141] shows no dependency of the battery entropy on the ambient temperature. Additionally, the temperature obtained for the three LFP batteries was higher for higher battery capacities. Besides, the temperature of the NMC 53Ah battery

was found to be higher than the one tested on the LFP batteries even if these have higher capacity. This is due mainly to the strong thermal stability of LFP batteries comparing to NMC batteries [142].

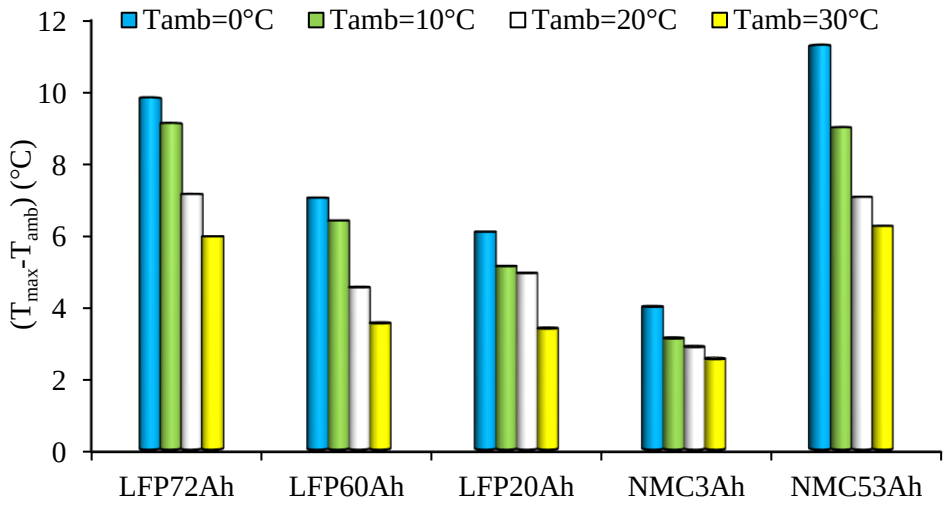

Figure IV.10 Different batteries maximum temperature rise for different ambient temperatures.

IV.3.2 Comparison of batteries thermal parameters

In the previous section, five Li-ion batteries thermal behavior was investigated for different climate conditions. A strong dependency of battery temperature to climate conditions was proven. This dependency is justified by the dependency of battery thermal parameters to environmental conditions. In this section the specific heat is measured for three batteries (LFP 60Ah, LFP 72Ah, NMC 53Ah). Same ambient temperatures were applied to measure the battery specific heat capacity. The results shown in Figure IV.11 present the specific heat capacity of three batteries versus temperature. A linear increase of the specific heat is obtained for increasing temperature. This result may give an appropriate explanation to the thermal behavior. For higher applied environmental temperature, the battery heat store capacity increases. Lower heat is dissipated via the battery surface which explains the lower temperature rise.

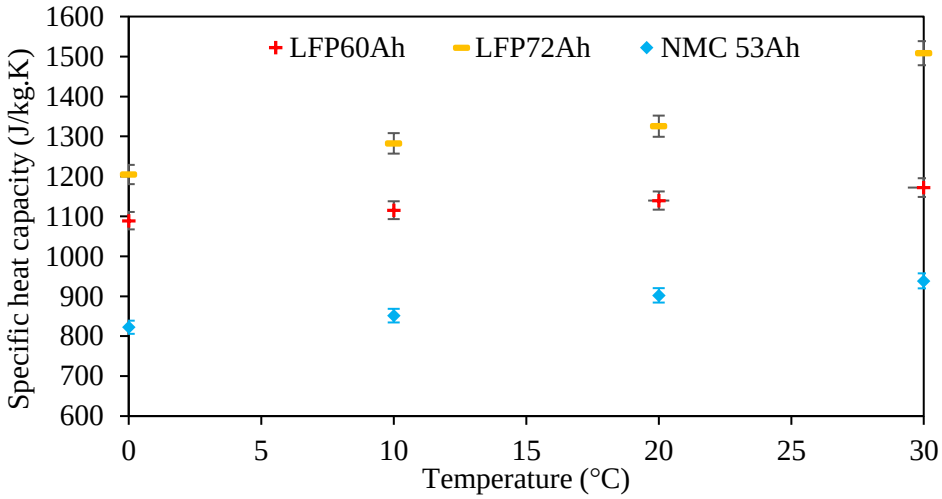

Figure IV.11 Measured specific heat capacity versus temperature.

In this section, the thermal conductivity of tested batteries is discussed. The effect of temperature on battery thermal conductivity is illustrated in Figure IV.12. Three ambient temperatures were applied (10°C, 20°C, 30°C). Obtained experimental results show no dependency of thermal conductivity to ambient temperature.

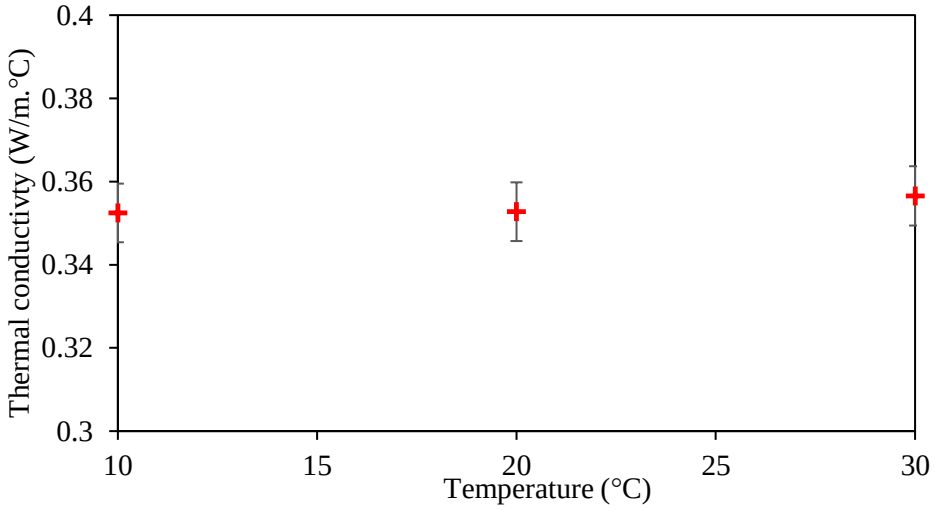

Figure IV.12 Measured thermal conductivity of the 60Ah LFP battery.

Figure IV.13 shows the results of the thermal conductivity measurement for three batteries under a temperature of 20°C. The LFP 60Ah has a low thermal conductivity compared to the LFP 72Ah and NMC 53Ah. This is due basically to the effect of the external shell which is made from plastic material.

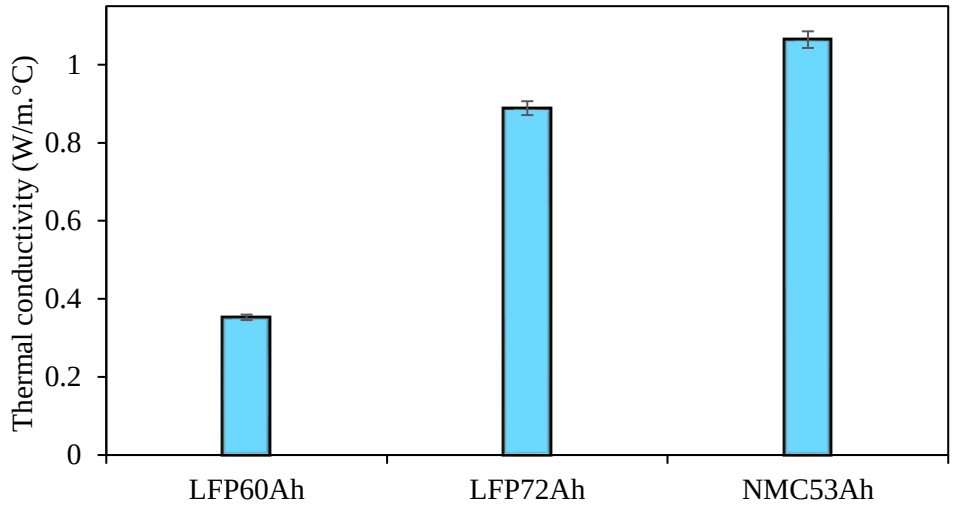

Figure IV.13 Comparison of the measured thermal conductivity of different batteries.

As discussed above, the ambient temperature has a remarkable effect on the battery thermal behavior. In addition, the use of the battery is performed all year. To reinforce the numerical model, the effect of ambient temperature on the battery thermal parameters should be taken into consideration. A first proposed step is performed to improve the domain of validation of the numerical model based on the measurement of thermal parameters for different ambient temperatures performed by the HFM446. The specific heat of the LFP 60Ah battery increases linearly for an increasing ambient temperature as discussed in Figure IV.11. The four experimental points were interpolated with the linear equation IV.16. This new developed equation is declared as an input of the numerical model to numerically visualize the effect of ambient temperature on battery temperature rise. An illustration of the model validation for different ambient temperature is presented in Figure IV.14.

$$Cp(T) = 2.72\ T + 1088.1 \qquad \text{IV.16}$$

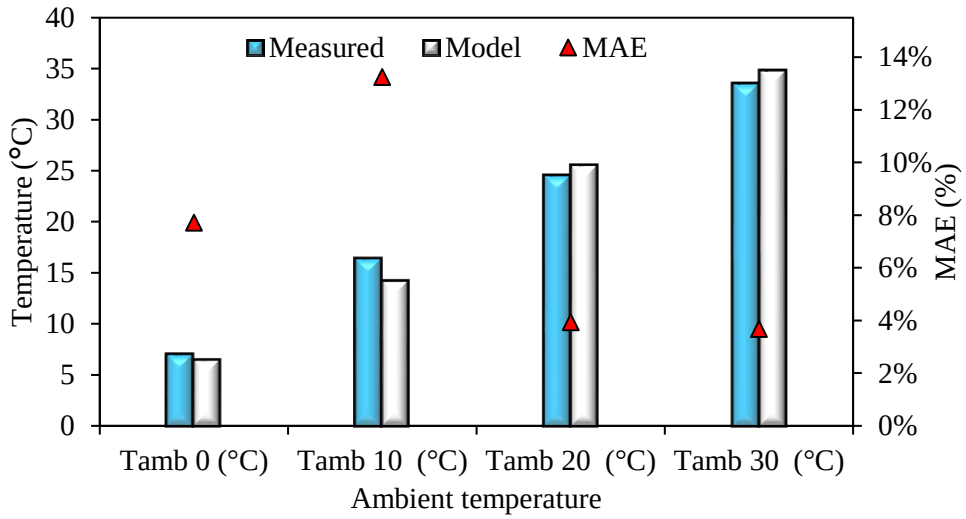

Figure IV.14 Model validation for different ambient temperature.

IV.4 Battery pack equivalent thermal network

In the previous chapter a 3D thermal model is developed to characterize the thermal behavior of one Li-ion battery. Considering the complexity of a physical model composed of a battery pack coupled with other cooling systems, a simplified numerical model based on thermal networks is proposed in this chapter. The proposed simplified model is presented and validated in the previous section for only one battery while this section is dedicated specially to establish the proposed model to a battery pack based on equivalent thermal networks. An illustration is shown in Figure IV.15 presenting the proposed battery pack configuration and the proposed 3D and 1D equivalent thermal networks.

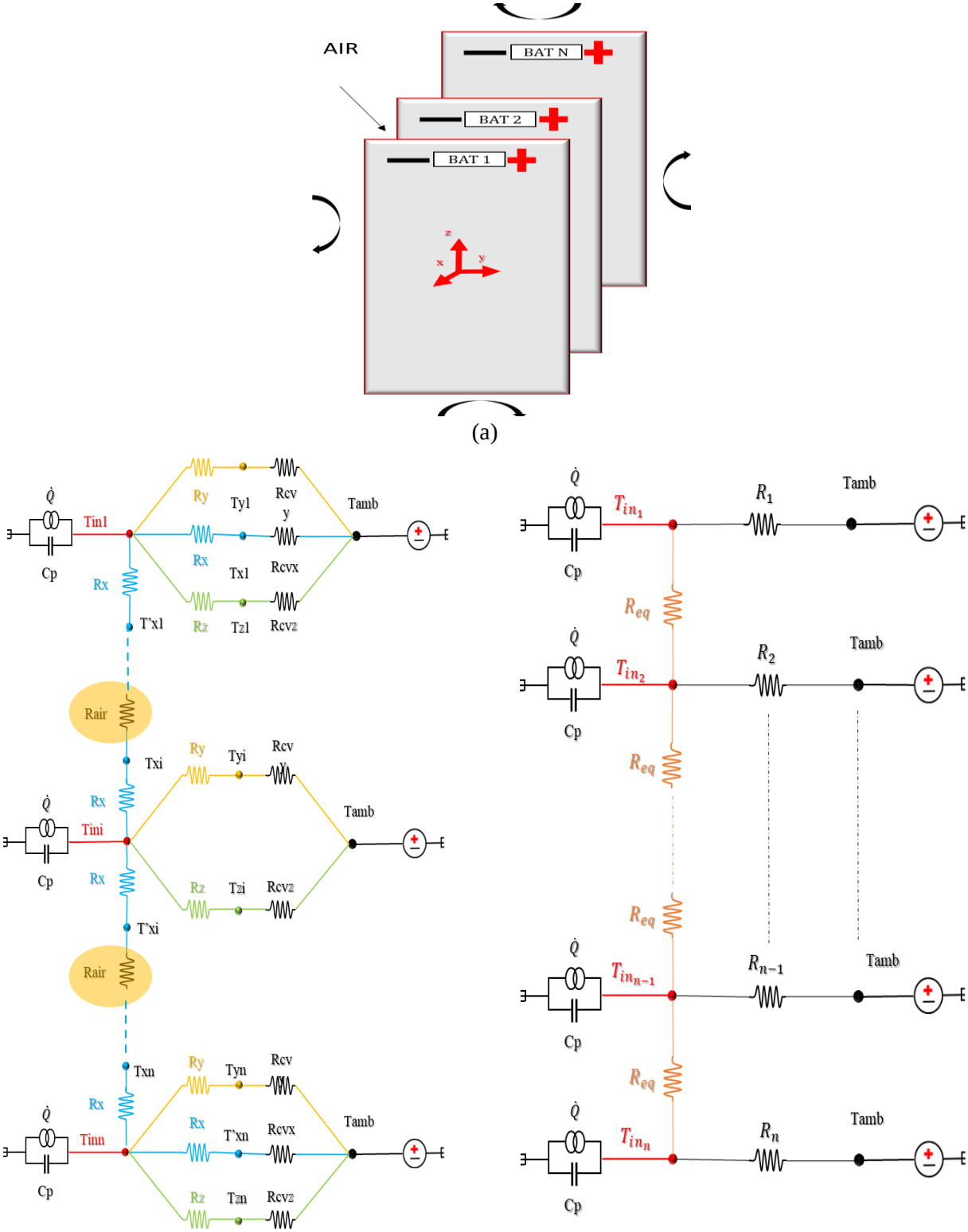

Figure IV.15 Equivalent thermal network of a battery pack (a) battery disposition (b) 3D model (c) 1D model.

First the 1D model resistances are determined with equations (IV.17, IV.18 and IV.19). The calculated values of each equivalent thermal resistance presented in Figure IV.15.c are given in Table IV.4. A system of ordinary differential equation is then used to describe the physical problem enabling the calculation of battery core temperature in each battery when studying a battery pack. The system is defined in equation IV.20 and solved using Runge-Kutta 4th.

Table IV.4 Thermal resistance values for battery pack**.**

Thermal resistance	**(K/W)**
R1= Rn	2.33
Ri	8.96
Req	26.37

$$R_1 = R_n = \frac{(R_x + R_{cx})(R_y + R_{cy})(R_z + R_{cz})}{2((R_x + R_{cx})(R_z + R_{cz}) + \frac{(R_y + R_{cy})(R_z + R_{cz})}{2} + (R_x + R_{cx})(R_y + R_{cy}))} \quad \text{IV.17}$$

$$R_i = \frac{(R_y + R_{cy})(R_z + R_{cz})}{2(R_y + R_{cy} + R_z + R_{cz})} \quad \text{IV.18}$$

$$R_{eq} = 2R_x + R_{air} \quad \text{IV.19}$$

$$\begin{cases} RI^2 - IT_{in1}\frac{dU}{dT} - MCp\frac{dT_{in1}}{dt} = \frac{T_{in1} - T_{amb}}{R1} + \frac{T_{in1} - T_{in2}}{Req} \\ RI^2 - IT_{in2}\frac{dU}{dT} - MCp\frac{dT_{in2}}{dt} = \frac{T_{in2} - T_{amb}}{R2} + \frac{T_{in2} - T_{in3}}{Req} - \frac{T_{in2} - T_{in1}}{Req} \\ \vdots \\ RI^2 - IT_{in_n}\frac{dU}{dT} - MCp\frac{dT_{in_n}}{dt} = \frac{T_{in_n} - T_{amb}}{Rn} - \frac{T_{in_{n-1}} - T_{in_n}}{Req} \end{cases} \quad \text{IV.20}$$

Using the Chroma 17020 system, a pack of 3 LFP 60 Ah batteries were tested under an applied current of 60A during consecutive charge and discharge cycles (Figure IV.16). In addition, a comparison

of experimental and numerical maximum temperature for the battery pack is shown in Figure IV.17. First, in Figure IV.17.a. the validation is performed for thermocouples inserted in the positive electrode of the three batteries. The battery core temperature is based on the resolution of the numerical model. The temperature of the battery in the middle of the pack is higher than the temperature of the two other batteries. This is due to a lower surface direct contact with the environment. Moreover, a symmetry is observed between both the first and the third battery. This is justified by a same internal heat generation as the same current were applied in all batteries. The validation of the model shows same profiles of temperature and an acceptable accuracy is noticed. Furthermore, in Figure IV.17.b. the validation is performed for temperature measured in the exposed to air battery external sides. A good accuracy is obtained for both core and surface temperatures.

Figure IV.16 Tested 60Ah Li-ion battery pack.

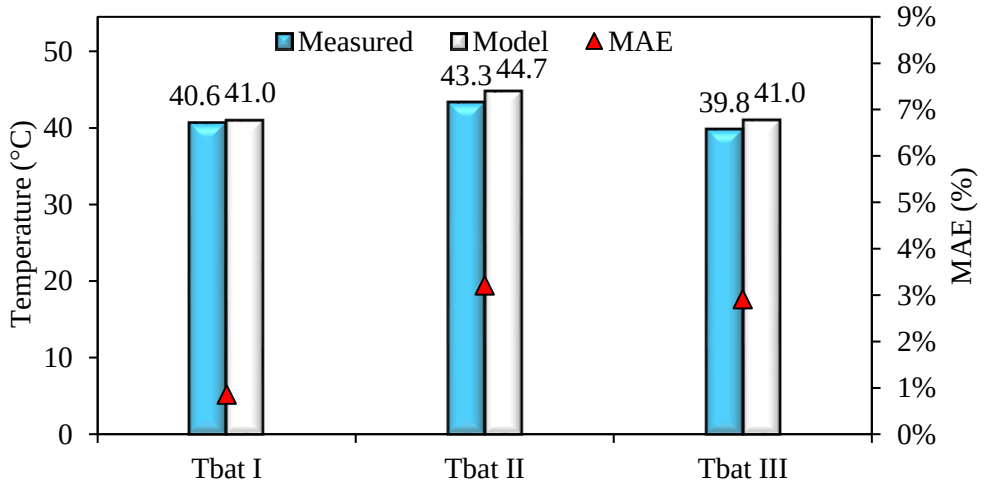

(a)

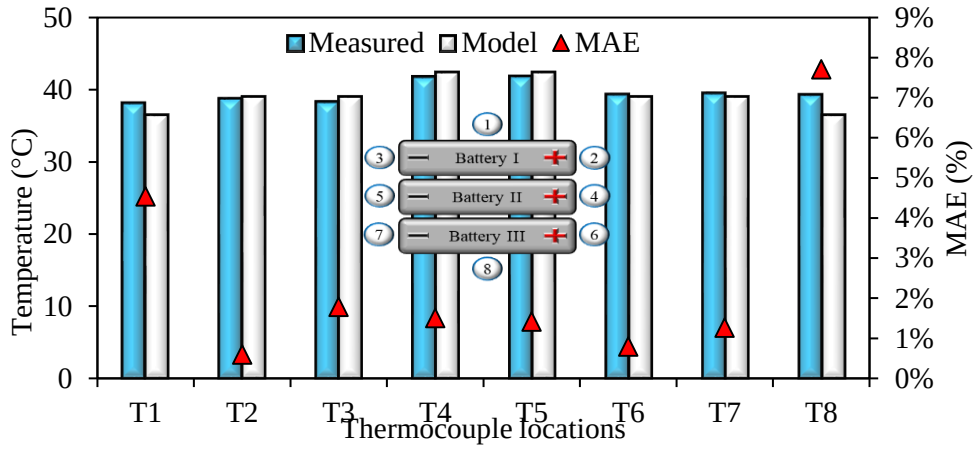

(b)

Figure IV.17 Comparison of experimental and numerical maximum temperatures for the battery pack. (a) battery core temperatures (b) surface temperatures.

The developed numerical model is used to estimate the maximum temperature obtained in the battery core for battery packs when tested under a constant current of 60A. Figure IV.18 illustrates a comparison of the calculated results for battery packs from 1 battery to 10 batteries. A rise of 4.79°C is noticed for two batteries pack comparing to only one battery. A symmetrical profile of temperature is remarked for more than 3 batteries and the batteries in the pack center temperatures' is higher compared to those exposed directly to air. This temperature rises for increasing batteries until attaining a temperature of about 48°C, after which a stabilization is noticed between all batteries.

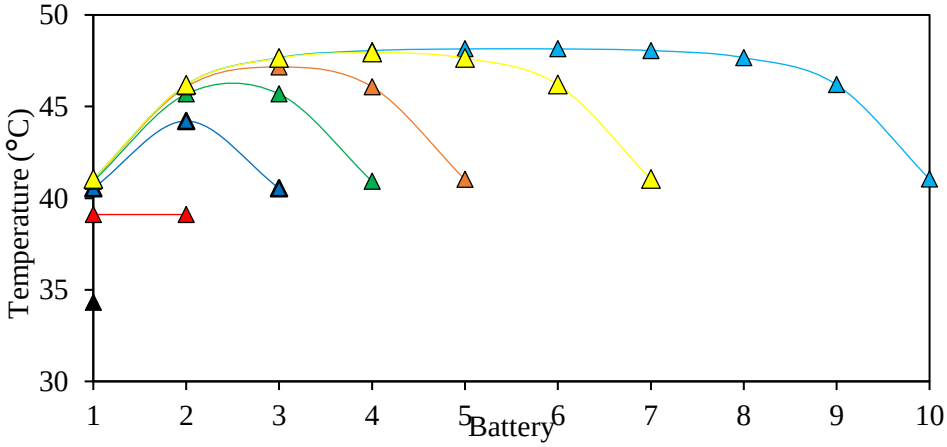

Figure IV.18 Comparison of maximum temperature of different battery packs.

IV.5 Battery pack combined with PCM

IV.5.1 Experimental results

During operating time, the current flow inside the battery causes heat generation and battery temperature rise. The amount of this generated heat as discussed in chapter III depends on the current rates. As battery packs are used as an energy source of EVs, the dissipation of this heat is primary to avoid any system deterioration. As recommended by Pesaran et al. [143] , the longer lifespan is ensured when the operating temperature of the battery is higher than 15°C and doesn't exceed 35°C. In this section a passive cooling method based on PCM is investigated to visualize the thermal behavior of a battery pack composed of three 60 Ah batteries. A microencapsulated PCM is used in this study as its presents higher security when used with electrical systems. The chosen PCM is Inertek 32 powder commercialized by MCI-technologies. A polymeric material was used as shell to the micro-encapsulated particles of PCM with a size range between 5 and 25 µm. The tested PCM is a non-paraffinic fatty ester, derived from organic vegetal wax (methyl hexadecanoate). The melting temperature of the tested PCM is 32°C which is chosen to ensure expanding the operating time of batteries under a temperature of 35°C. The thermal parameters of the tested PCM are experimentally measured by the heat flow meter (HFM446) and an illustration of the thermal conductivities and specific heat variation versus temperature is presented in Figure IV.19. The specific heat capacity was measured for five temperatures (0°C, 10°C, 20°C, 30°C and 40°C). Moreover, the thermal conductivity was determined also for five temperatures (20°C, 25°C, 30°C, 35°C and 40°C). The results show a strong increase of specific heat capacity for a temperature of 30°C comparing to other tested temperatures as it started the phase change process at this range of temperature. In addition, the thermal conductivity strongly decreases for increasing temperature especially for temperature equals and higher than 35°C in which the PCM is in liquid phase.

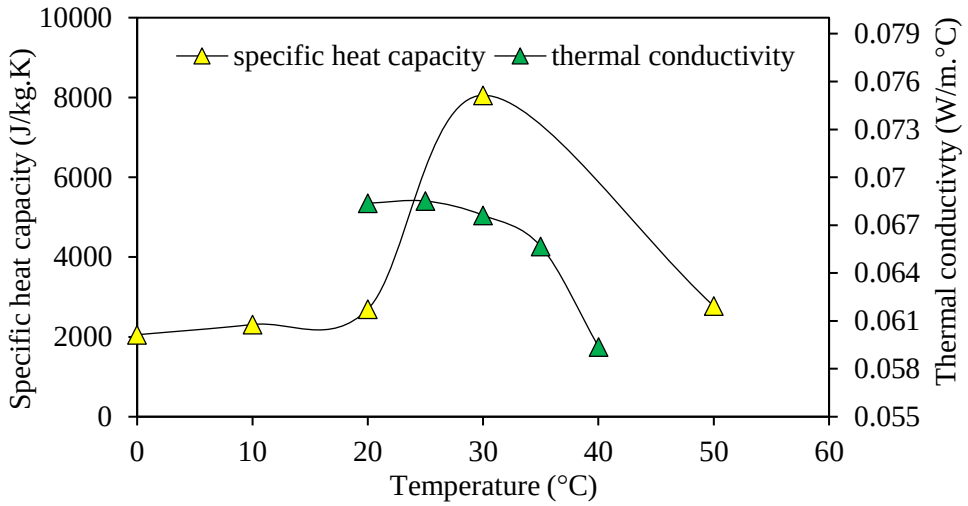

Figure IV.19. Measured thermal conductivities and specific heat of Inertek 32.

Two different configurations are proposed as illustrated in Figure IV.20. The Inertek 32 PCM is putted inside a box having same battery length and height (115 mm, 240 mm) and a thickness of 15mm. two boxes were made and two copper plates of 0.5mm were inserted in the lateral sides of the boxes to ensure the high thermal conduction. Furthermore, when studying a battery pack for transport application, the mass of cooling system is a key parameter to be taken in consideration as any increase of the vehicle mass will require an increase of the battery system capacity. For this reason, a quantity of 125 g is inserted in each PCM boxes which is equivalent to less than 5% of the battery pack system.

The purpose of the test described in this section is to define the more efficient cooling configuration. In the first configuration illustrated in Figure IV.20.a. the batteries were stacked together between the PCM boxes while in the second one presented in Figure IV.20.b. each box was placed between two batteries. Moreover, 15 K-type thermocouples were used to measure the temperature of the batteries. Three of them were inserted on the positive electrode of each one of the three batteries and 2 others were used to measure the temperature of each one of the two boxes. The Figure IV.21 shows a schematic diagram of the thermocouple's locations.

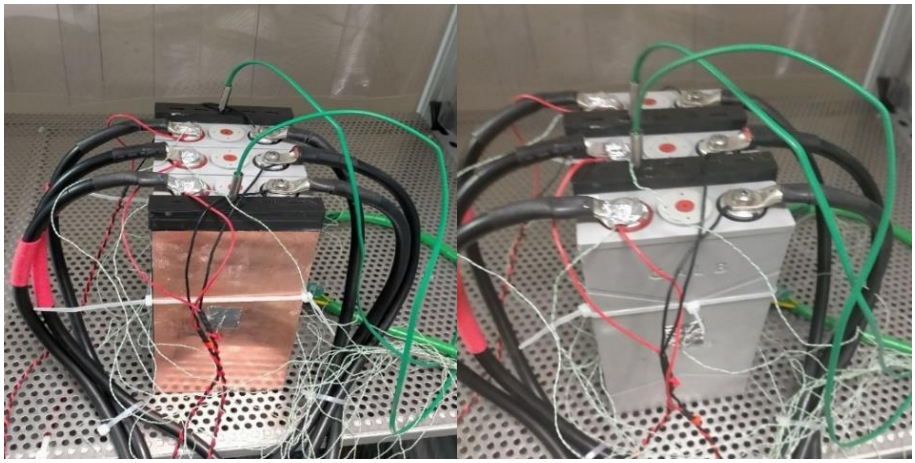

(a) (b)

Figure IV.20 Tested 60Ah Li-ion battery pack with PCM (a) configuration I (b) configuration II.

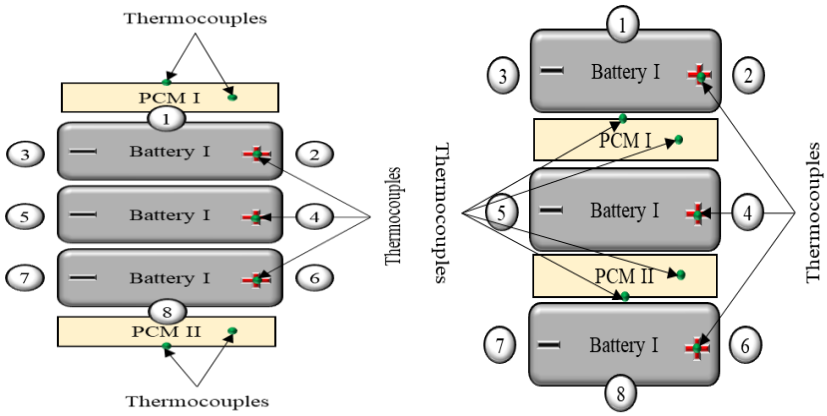

(a) (b)

Figure IV.21 Schematic diagram of thermocouples locations (a) configuration I (b) configuration II.

The battery pack composed of three batteries is tested under 60A constant current and consecutive charge and discharge cycles were applied until reaching the quasi-stationary regime. In experiment number one the three batteries were under air natural convection while in the second experiment the configuration I discussed previously is tested and finally the configuration II is tested in the third experiment. The experimental results obtained for the three studied experiments are presented in Figure IV.22. The temperature of positive electrodes gives the maximum temperature and best represents the battery core temperature as seen in chapter II. The results of the measurements show higher positive

electrode temperature in the second battery for all three tested cases as illustrated in Figure IV.22.a . Moreover, the results obtained during the test performed on configuration I are showing higher temperature in this experiment with the three batteries. This could be justified by a confinement of heat inside the batteries as the transmission via PCM boxes is slow. In addition, the lowest temperature was found during the application of the configuration II which is due basically to the ability of PCM boxes to store an amount of the heat generated by each battery directly. Indeed, even though the temperatures measured in battery surfaces and shown in Figure IV.22.b is lower for each battery than the temperature measured in positive electrode. Same remark is noticed and all thermocouples show higher temperature in case of configuration I comparing to the other cases. The results prove the importance of PCM disposition when combined with batteries.

To ensure the ability of each PCM boxes in storing heat energy generated by batteries an illustration is shown in Figure IV.23, presenting a comparison of temperature measurement inside PCM boxes. As the three batteries are tested under same current rates, the heat generation in each battery is supposed to be approximately the same and the temperature rise performed inside each PCM boxes could give an idea about this phenomenon. As shown in Figure IV.23 the temperature of PCM of the two boxes are approximately the same and a slight difference is remarked and the maximum temperature obtained for the PCM in box I is 33.3 °C while this temperature is equal to 32.4 °C in box II. This difference could be justified by the slight difference of heat generated by each battery after applying consecutive charge and discharge cycles as the state of health may not be the same for all batteries.

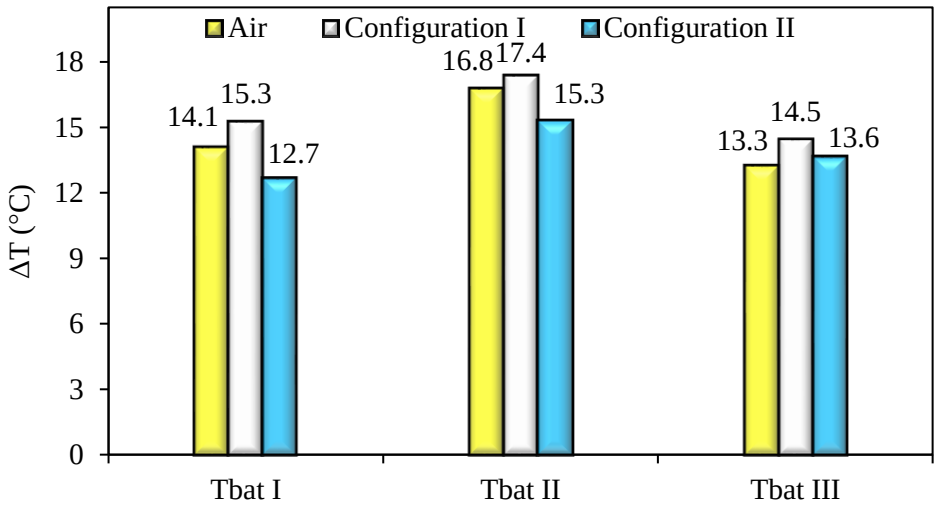

(a)

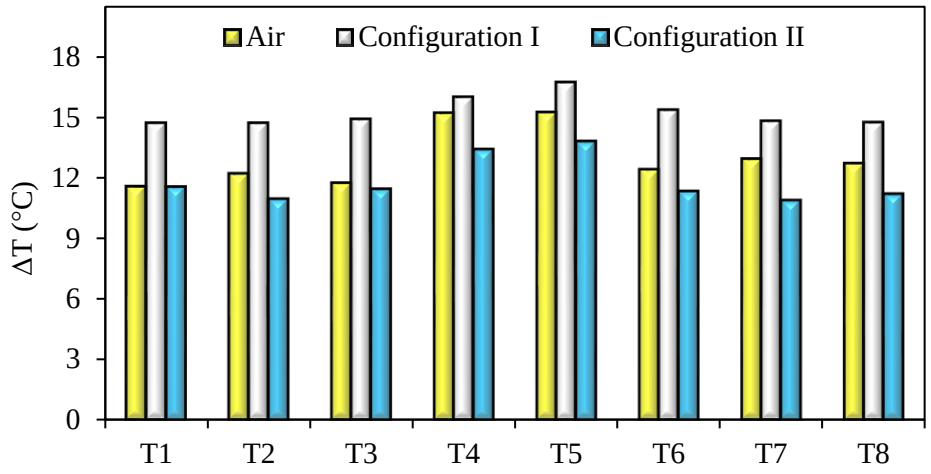

(b)

Figure IV.22 Comparison of experimental maximum temperature for battery pack with PCM (a) positive electrode temperatures (b) surface temperatures.

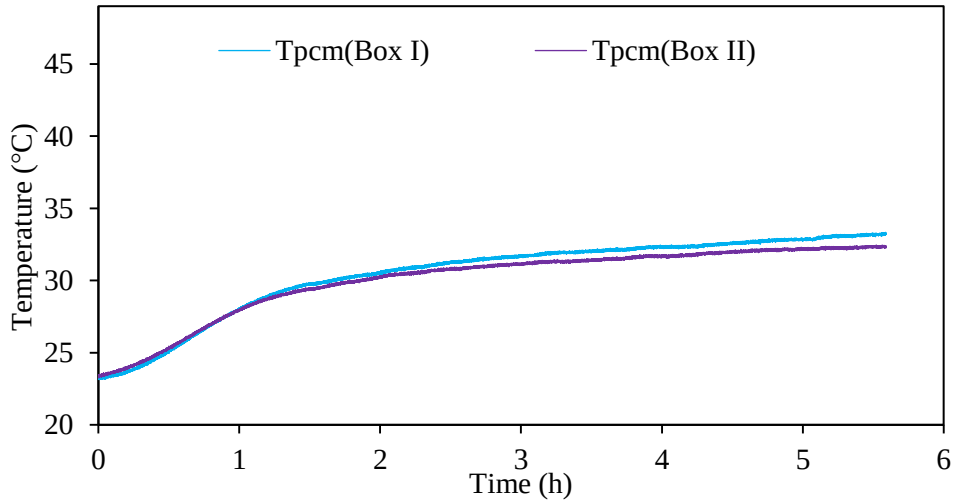

Figure IV.23 Comparison of temperature measurement inside PCM boxes in configuration I.

A comparison of the centered battery positive electrodes and PCM temperatures is performed to evaluate the difference in temperature rise profiles in both transient and quasi-stationary regimes. Figure IV.24 shows the profiles of temperatures obtained instantaneously when using PCM in configuration I (CI) and configuration II (CII). The results for battery electrodes in the first charge cycle show same temperature rise until exceeding a temperature of 32°C which presents the melting temperature of used

microencapsulated PCM. For temperatures higher than 32°C the temperature of battery in CI rises more than in CII. Inversely, The PCM temperature in CII is higher than in the case of CI which is justified by higher heat storage. Moreover, in the last cycle the PCM temperature started rising drastically due to the liquefaction of the PCM.

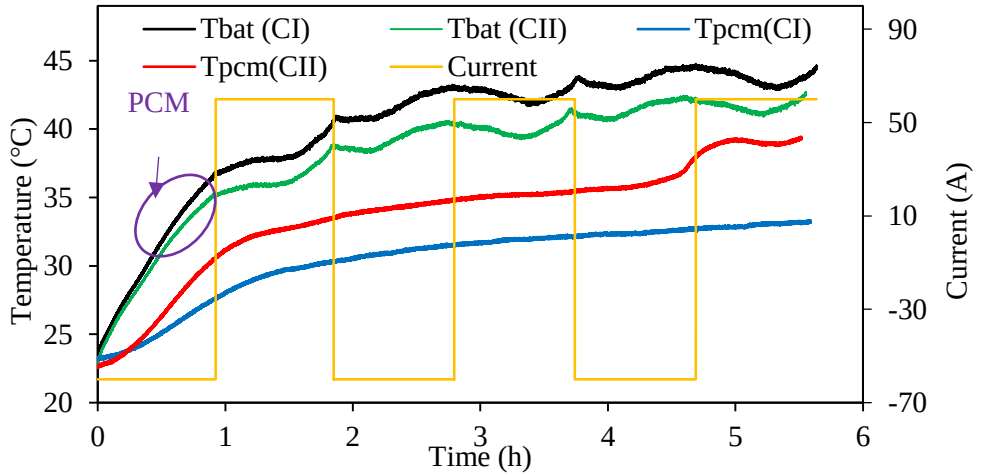

Figure IV.24 Battery and PCM temperatures profiles variation for both configuration I and II.

IV.5.2 Equivalent thermal network

In section IV.4 an equivalent thermal network is developed to simulate the thermal behavior of Li-ion battery pack while in this section the proposed model is extended and PCM is coupled with a battery pack and a novel equivalent thermal network is proposed. As seen in the previous section that the PCM has higher efficiency on the battery pack temperature control when it is inserted between batteries. For this reason, the proposed model suggests that the PCM confined between two batteries configuration is better. Furthermore, Figure IV.25 shows the proposed battery pack coupled with PCM configuration and the proposed 3D and 1D equivalent thermal networks. A system of ordinary differential equation is then used to describe the physical problem enabling the determination of battery core temperature in each battery when studying a battery pack. The system is defined in equation IV.21 and solved using Runge-Kutta 4th.

$$\begin{cases} RI^2 - IT_{in1}\dfrac{dU}{dT} - MCp\dfrac{dT_{in1}}{dt} = \dfrac{T_{in1} - T_{amb}}{R1} + \dfrac{T_{in1} - T_{pcm1}}{Req} \\ \dfrac{T_{in1} - T_{pcm1}}{Req} + \dfrac{T_{in2} - T_{pcm1}}{Req} = \rho_{pcm} V_{pcm} Cp_{pcm}\dfrac{dT_{1pcm}}{dt} + \dfrac{T_{pcm1} - T_{amb}}{R_{pcm}} \\ RI^2 - IT_{in2}\dfrac{dU}{dT} - MCp\dfrac{dT_{in2}}{dt} = \dfrac{T_{in2} - T_{pcm1}}{Req} + \dfrac{T_{in2} - T_{amb}}{R2} + \dfrac{T_{in2} - T_{pcm2}}{Req} \\ \vdots \\ RI^2 - IT_{inn}\dfrac{dU}{dT} - MCp\dfrac{dT_{inn}}{dt} = \dfrac{T_{inn} - T_{amb}}{Rn} + \dfrac{T_{inn} - T_{pcmn-1}}{Req} \end{cases} \quad \text{IV.21}$$

The thermal resistance enabling the resolution of the defined system are presented below in equation (IV.22, IV.23, IV.24 and IV.25):

$$R_1 = R_n = \frac{(R_x + R_{cx})(R_y + R_{cy})(R_z + R_{cz})}{2((R_x + R_{cx})(R_z + R_{cz}) + \frac{(R_y + R_{cy})(R_z + R_{cz})}{2} + (R_x + R_{cx})(R_y + R_{cy})} \quad \text{IV.22}$$

$$R_i = \frac{(R_y + R_{cy})(R_z + R_{cz})}{2(R_y + R_{cy} + R_z + R_{cz})} \quad \text{IV.23}$$

$$R_{pcm} = \frac{(R_{py} + R_{pcy})(R_{pz} + R_{pcz})}{2(R_{py} + R_{pcy} + R_{pz} + R_{pcz})} \quad \text{IV.24}$$

$$R_{eq} = R_x + R_{px} \quad \text{IV.25}$$

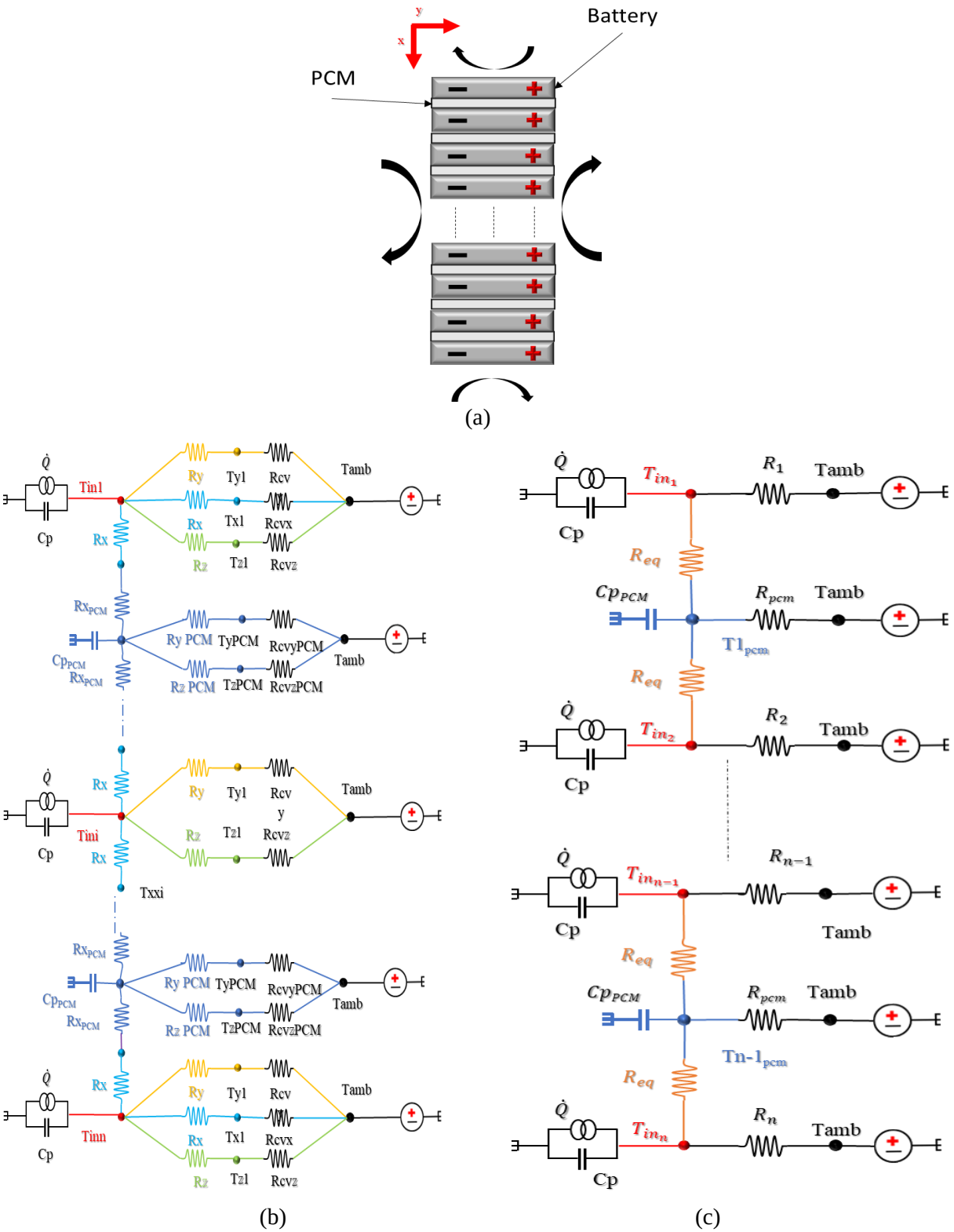

Figure IV.25 Equivalent thermal network of a battery pack coupled with PCM (a) battery disposition (b) 3D model (c) 1D model.

At this step, the novel proposed model, coupling a battery pack with PCM, is compared to the experimental results presented in the previous section for the PCM in configuration II. First, the thermal resistances are calculated for the given inputs of used microencapsulated PCM Inertek 32. The curve of thermal conductivity and specific heat capacity of PCM given in Figure IV.19 are correlated and inserted in the model. The Table IV.5 presented below define the used thermal properties of the PCM Inertek 32. In addition, the Figure IV.26 illustrates the numerical and experimental results obtained for the three tested battery pack combined with the microencapsulated PCM Inertek 32. The obtained mean absolute error (MAE) for the three batteries is lower than 5% which proves the accuracy of the proposed model. In the next section, the thermal behavior of battery pack under dynamic current is studied experimentally and numerically. Moreover, the efficiency of PCM cooling system when applied on battery pack used in three different cars is investigated.

Table IV.5 Micro encapsulated PCM Inertek 32 properties**.**

PCM	**Inertek 32**
Latent heat (J/g)	180
Density (kg/m^3)	333
$T_{melting}$ (°C)	32

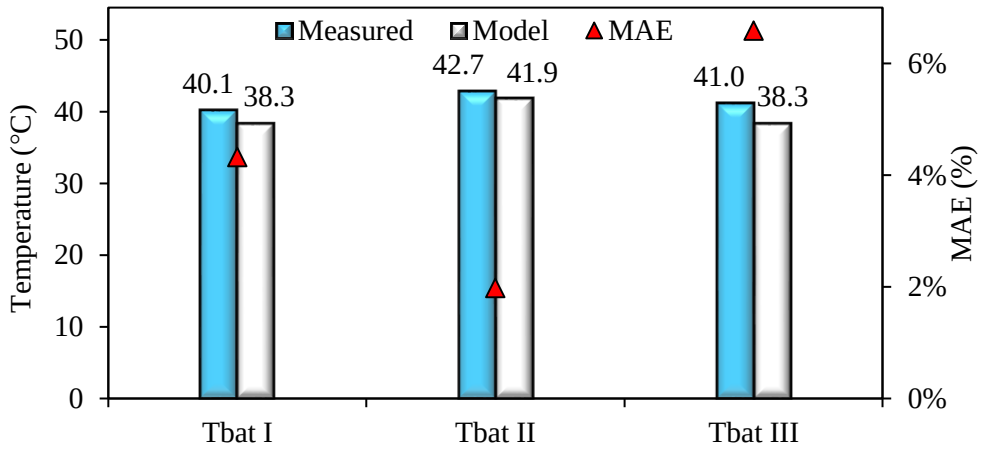

Figure IV.26 Comparison of experimental and numerical temperature for battery pack combined with PCM during 1C test.

IV.6 Normalized driving cycles

Applying consecutive charge and discharge cycles using constant current protocol is an import task to well describe the thermal behavior of Li-ion batteries. Nevertheless, testing the batteries thermal behavior during consecutive normalized driving cycles (NDC) is necessary as it is more near to the real use conditions. For this motive, in Table IV.6 the parameters of three different cars proposed to determine the dynamic current profiles are presented. Moreover, Table IV.7 shows a summary of the physical parameters used in the determination of the dynamic current profiles. Furthermore, equation IV.26 [144] is used to calculate current based on the NDCs shown in Figure IV.27. Three NDCs were chosen WLTC, US06 and JAP 15. Testing several protocols applied on different cars enables performing a comparison between the thermal behavior of Li-ion batteries packs and to propose efficient cooling solutions.

$$I = \frac{\rho_{air} S C_x V^3 + 2 C_g M g V + 2 M a V}{2 \eta U} \qquad \text{IV.26}$$

Table IV.6 Car's parameters used to define dynamic current profiles.

CAR	Capacity (Ah)	U(V)	Mass(kg)	Efficiency (%)	Area(m^2)
A	60	400	1516	93%	2.88
B	120	325	1800	87%	2.7
C	120	350	2100	85%	2.65

Table IV.7 Physical parameters used in the determination of dynamic current profiles.

Parameter	Value
ρ_{air}(kg/m^3)	1.225
C_x	0.35
C_g	0.012
g(m/s²)	9.81

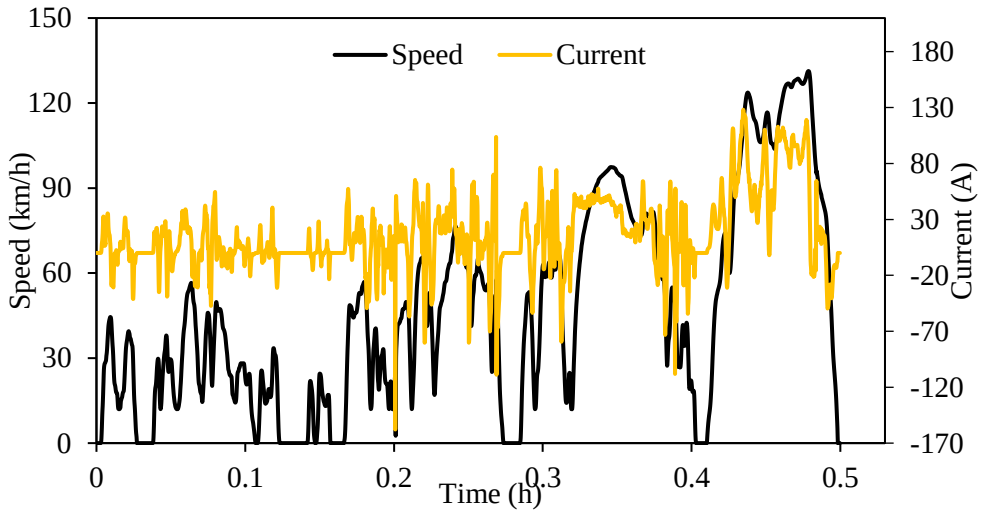

(a)

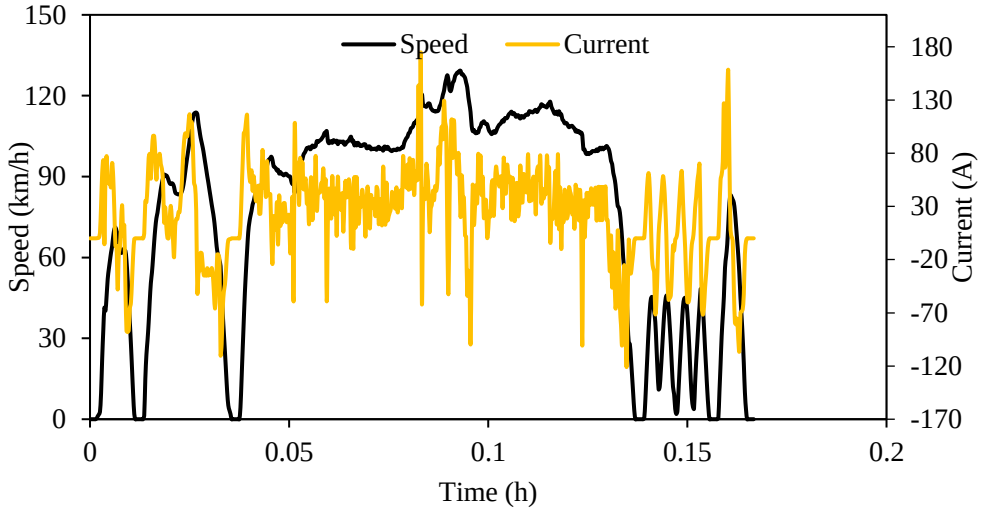

(b)

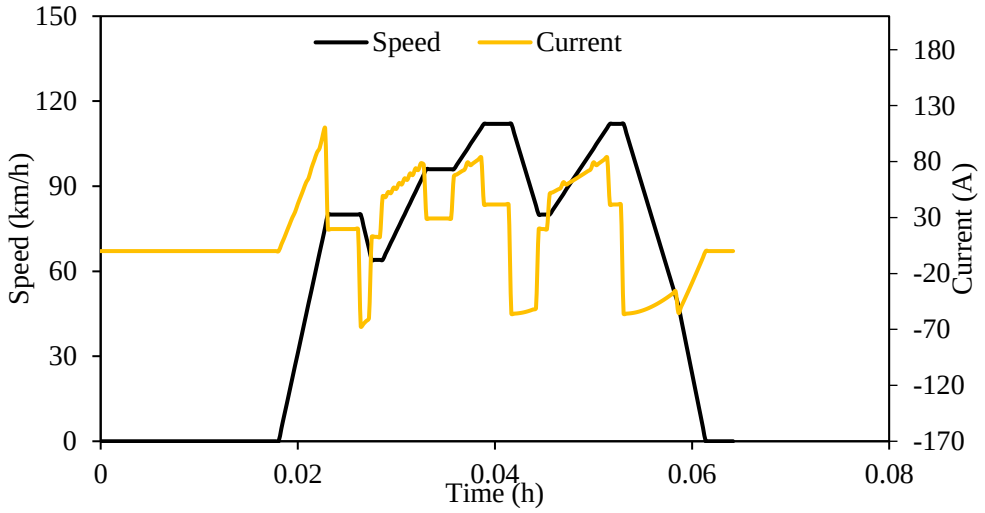

(c)

Figure IV.27 Example of normalized driving cycles profiles for (a) car A (WLTC) (b) car B (US06) (c) car C (JAP15).

One of the important steps to be performed is verifying the model accuracy when applying dynamic current. Figure IV.28 illustrates a comparison of experimental and numerical temperature for battery pack tested under dynamic current. In Figure IV.28.a. the dynamic current WLTC was applied consecutively by introducing the calculated profiles in the experimental test bench Chroma 17020 and as an input of the numerical model. Moreover, the measurement of temperature performed in battery

electrodes was compared to deduced battery core temperatures via the numerical model and the results are presented in Figure IV.28.b. A good accuracy is noticed with a mean absolute error lower than 3% obtained for the three tested batteries.

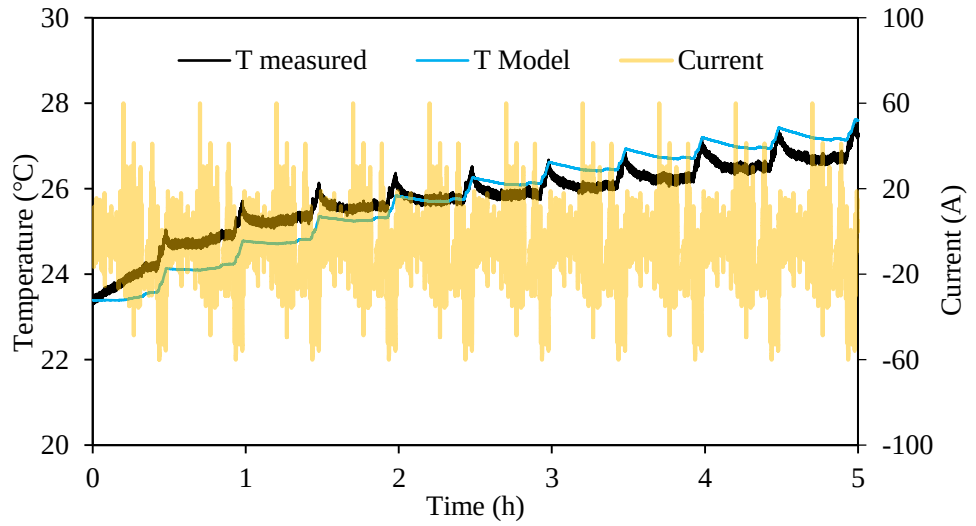

(a)

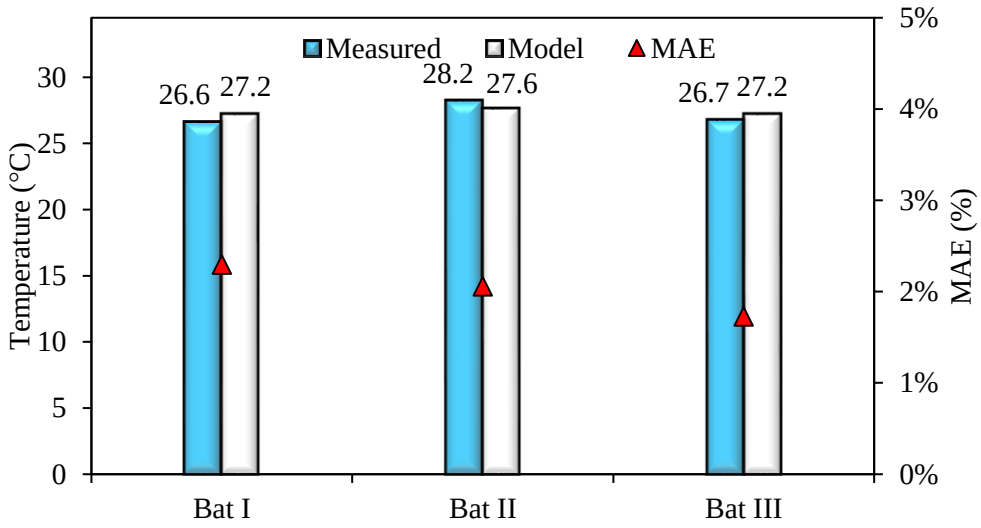

(b)

Figure IV.28 Comparison of experimental and numerical temperature for battery pack tested under dynamic current (a) consecutive cycles (b) maximum temperature.

The first step to be performed enabling the analysis of the thermal behavior of EVs battery pack is to determine the number of batteries in each of the cars presented in Table IV.6 following the steps described below.

The number of batteries N_B in a car is defined as the multiplication of the number of batteries in series N_{BS} and in parallel N_{BP} (equation IV.27).

$$N_B = N_{BS} N_{BP} \quad \text{IV.27}$$

The number of batteries in series is determined by calculating the ratio of the battery pack voltage (U_b) and batter cell voltage (U_{BC})as defined in equation IV.28

$$N_{BS} = \frac{U_B}{U_{BC}} \quad \text{IV.28}$$

Additionally, the number of batteries in parallel N_{BP} is defined as a division between the total energy of the battery pack E_B and the energy of the batteries in series (equation IV.29).

$$N_{BP} = \frac{E_B}{N_{BS} E_{BC}} \quad \text{IV.29}$$

Based on previous equations the number of batteries for each car defined in Table IV.5 is determined. Table IV.8 summarizes the number of batteries in each car.

Table IV.8 Number of batteries in each car

Car	Number of batteries
A	125
B	204
C	219

The developed model is used to predict the maximum temperature rise for each battery pack used in the chosen three car parameters for the three given normalized driving cycles current profiles and when batteries are exposed to natural convection and when combined with PCM. For each case the PCM mass was determined using the following proposed method based on the developed correlation in chapter III.

- First, the heat generation amount of battery pack is estimated

The correlation developed in chapter III enables the determination of a heat generation energy during a complete charge and discharge cycles for given constant current during charge and discharge. The applied current is dynamic during both charge and discharge cycles. An analogy between the dynamic current and constant current is then performed based on calculating an average of current for each tested cycle (WLTC, US06 and JAP15). Moreover, the current is equal to zero in some instances in each of the normalized driving cycle. For this reason, a coefficient characterizing the duration of each charge and discharge process regarding normalized cycle duration. After determining the averaged charge and discharge current, the amount of heat energy produced by each one of the batteries is given as described in equation IV.30

$$\mathrm{Q_g} = \left(-16.124 + 27.129{\mathrm{R_{CC}}}^{0.598} + 37.748{\mathrm{R_{DC}}}^{0.931} - 4.442{\mathrm{R_{CC}}}^{0.598}{\mathrm{R_{DC}}}^{0.931}\right) \times 1000 \qquad \text{IV.30}$$

- Second, the mass of PCM required for each cycle is calculated

Before calculating the PCM mass and to avoid any oversizing of PCM mass, the heat is transferred to PCM via only two sides in which the PCM are in contact. Thus, the maximum energy that could be stored in PCM is provided and transferred via battery front or back side. The determination of the contact area A_{Batt_PCM} between PCM and battery is essential. To determine the PCM mass, the equation IV.31 defined below is used in which N_{cycles} , N_B, Cp_{PCM}, T_{melt}, L present respectively the number of cycles, battery pack numbers, specific heat of PCM, melting temperature and latent heat. Table IV.9 presented below shows the calculated mass of PCM used in each cooling case.

$$\mathrm{M_{PCM}} = \frac{\mathrm{Q_g N_{cycles} A_{Batt\_PCM} N_B}}{\mathrm{Cp_{PCM}(T_{melt} + T_{amb}) + L}} \qquad \text{IV.31}$$

Table IV.9 Mass of PCM used in each cooling case.

CAR	Cycle	Averaged charge current (A)	Averaged discharge current (A)	PCM Mass (kg)	Battery pack mass (kg)
A	WLTC	4.55	21.12	9.4	246.2
	US06	10.2	45.91	75.7	
	JAP	9.12	31.71	77.6	
B	WLTC	3.74	14.9	28.9	401.9
	US06	8.46	31.9	43.9	
	JAP	7.73	22.72	16.4	
C	WLTC	4.28	15.41	27.7	431.4
	US06	9.8	32.75	63.6	
	JAP	8.97	23.84	28	

Figure IV.29 illustrates the obtained numerical results of the mean maximum temperature rise during consecutive normalized under natural convection (NC) and PCM cooling. The maximal difference between temperature in natural convection and with PCM is obtained for the case of car B tested under JAP15 driving cycles. The obtained difference is 2.49°C which presents a temperature reduction amount of 6.6% while the mass amount in this case calculated presents about 4%. A summary of percentage of temperature decrease versus PCM mass amount is shown in Figure IV.30. For the car A the maximum difference is obtained for WLTC cycle and it is equal to 1.98°C which presents a reduction of 5.7% with an increase of mass amount less than 4%. For car C the maximum difference is obtained also for the JAP15 cycle and it presents a temperature decrease of about 6% with an increase of mass estimated of 6.5%.

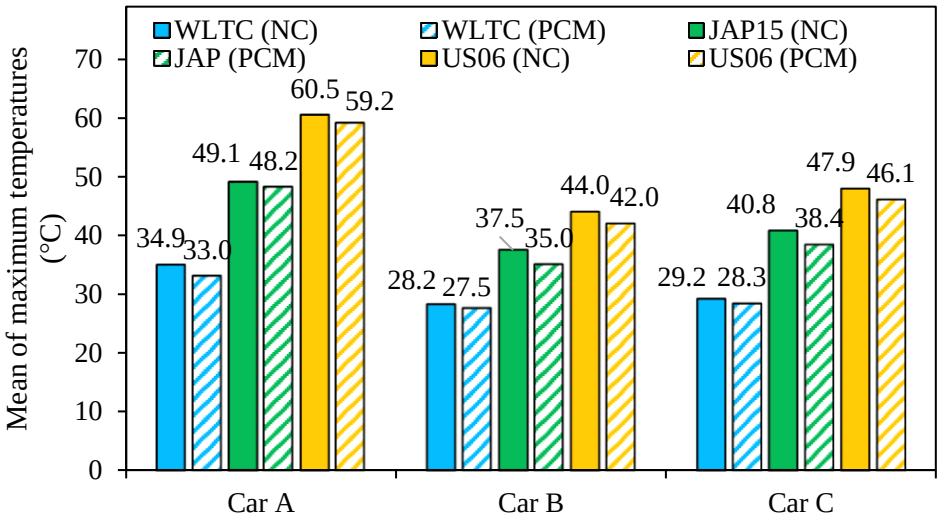

Figure IV.29 Numerical results of temperatures obtained for battery packs used in different EVs cars for natural convection and PCM cooling.

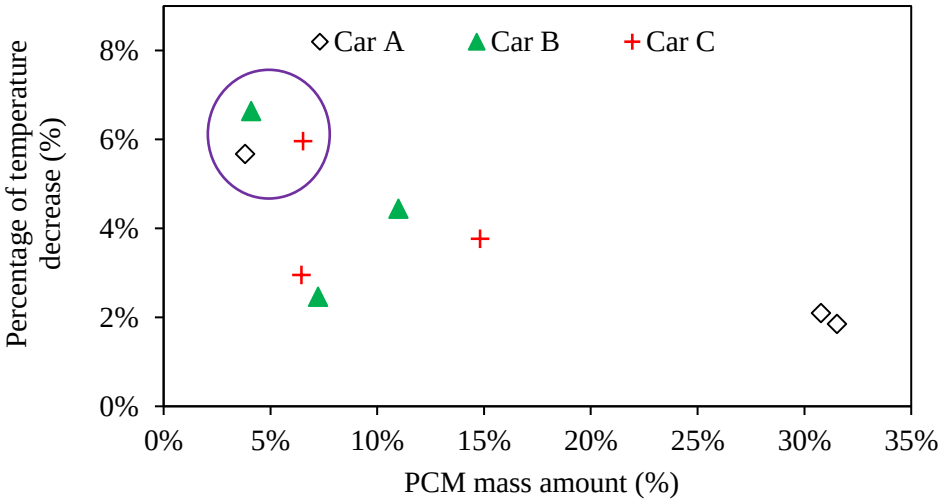

Figure IV.30 Percentage of temperature decrease versus mass amount.

IV.7 Conclusion

The chapter studied an experimental and numerical analysis of a Li-ion battery pack thermal behavior. First a simplified model based on equivalent thermal networks is developed and validated for the LFP 60Ah battery. Then a new test bench is implemented to carry out the novel series of tests. The

new test bench is composed of the Chroma 17020 system and a climate chamber Weiss-Technik. The Chroma 17020 system is used to ensure charge and discharge cycles during both constant and dynamic currents. While the climate chamber is devoted to apply different ambient temperatures. Moreover, a new experimental setup used to characterize the thermal conductivities and specific heat of batteries is also implemented.

Additionally, the thermal behavior of five Li-ion batteries is investigated for different ambient temperatures. The batteries tested are LFP/graphite and NMC/graphite. Two geometries were chosen: prismatic and cylindrical. Each battery was tested under 1C rate and consecutive charge and discharge cycles were applied in similar climate conditions in each test to enable an accurate comparison of the results. During operating time, the temperature of all batteries rises due to internal heat generation. It reaches after cycling a quasi-stationary state in which the temperature is not constant, but it presents a repetitive profile in each one of charge and discharge cycles. The profile of temperature in quasi-stationary regime has a "V" shape due to the strong dependency of the battery entropy to the SOC. The battery temperature depends strongly on applied climate conditions. Lower battery temperature increase is measured for higher ambient temperatures. This phenomenon is due mainly to the influence of ambient temperature on the internal chemical compositions of batteries which causes a change of battery thermal parameters. Furthermore, the battery specific heat capacity and thermal conductivity were experimentally measured. Obtained results show a linear increase of battery specific heat capacity for increasing applied temperature while no dependency of thermal conductivity to the ambient conditions was noticed.

After developing a new simplified model and validated for different condition applied to only one battery. The proposed model is extended to enable modeling a battery pack. Moreover, the battery pack model is validated for constant current and the maximum MAE is lower than 8%. For dynamic current and the maximum MAE is lower than 3%. In addition, the numerical results obtained for the temperature rise of different battery packs tested under different normalized driving cycles show the necessity of sizing an efficient cooling system to ensure the use of the battery pack under recommended operating conditions.

Furthermore, a PCM cooling system is studied experimentally and numerically. Two configurations were tested. In the first one, three 60Ah prismatic batteries were sandwiched between two microencapsulated PCM boxes while in the second configuration, each of the two PCM boxes were placed between two batteries. The experimental results of the two configurations were compared to the

tests under natural convection to evaluate the efficiency of PCM on battery temperature rise. The lowest temperature for the three batteries was obtained in the second configuration and a mean decrease of temperature comparing to natural convection of about 5.9% were obtained for a PCM mass amount comparing to battery pack mass of about 4.2%. An equivalent thermal network allowing the prediction of battery pack combined with PCM thermal behavior is proposed and validated. Finally, the developed model was used to analyze the efficiency of PCM when used with several sized battery packs, for three different given cars and under three different dynamic current cycles (WLTC, US06 and JAP15).

General conclusion

The objective of this thesis is to characterize the thermal behavior of Li-ion battery cell and pack for different current rates under both constant and dynamic currents. Experimental tests were performed besides the development of new numerical models. Based on the experimental database and the numerical study a passive cooling system using microencapsulated phase change material is proposed to ensure lower operating temperature.

In automotive applications, batteries must have high energy density and specific power at the same time. In addition, safety, lifetime and cost are three important factors in the choice of energy storage system. In this work, a 60Ah LFP prismatic battery thermal behavior is investigated experimentally and numerically. In addition, four other different batteries having different capacities, geometries and cathode materials were also tested to perform a comparative study between the thermal behavior of different tested batteries. The comparison is carried out in different climate conditions. The study performed in this thesis is structured in four chapters.

In the first chapter, a state of art describing two main modeling approaches to study the thermal behavior of Li-ion batteries is presented as it is the main key factor to enable sizing an efficient cooling system. In Addition, developing a numerical model requires the determination of several parameters characterizing the thermal behavior of a Li-ion battery such as the internal electrical resistance, the entropic heat coefficient, the specific heat capacity, the thermal conductivities and the heat transfer coefficients. Furthermore, many cooling systems were tested in different studies to ensure controlling the temperature rise of batteries during operating time and under different test conditions. The active cooling systems is widely used in EVs. Recently, researchers are more focusing on studying the efficiency of some passive cooling systems based on phase change material (PCM) and heat pipe as they present an advantage of no energy consumption.

The thermal characterization of a 60Ah prismatic Li-ion battery is carried out for three different charge currents (40A, 50A, and 60A) and different discharge currents (40A, 50A, 60A, 80A, and 100A) using an experimental test bench implemented in the LUSAC laboratory enabling charging and discharging batteries for different C-rates. The measurement of temperatures and heat fluxes performed on the tested battery allowed the determination of maximum temperature rise and heat dissipation. The

temperature measured on the positive electrode is the highest and it best characterizes the battery core temperature. The experimental study performed in the second chapter permits the determination of the entropic heat coefficient and the heat transfer coefficient. Moreover, the electrical internal resistance is measured during both charge and discharge cycles. The thermal parameters experimentally measured and extracted from literature are used as inputs parameters of the developed 3D numerical model proposed in the third chapter. Additionally, two correlations were developed in the third chapter enabling the prediction of maximum temperature rise and heat energy generation for given charge/discharge currents.

Finally, in the fourth chapter a numerical and experimental study is carried out to analyze the thermal behavior of a battery pack when tested under constant and dynamic current. Chroma 17020 system is implemented to enable testing the battery under dynamic current. A numerical model is developed based on equivalent thermal networks and validated for both constant and dynamic currents. Finally, a case study is proposed to size cooling system based on PCM to ensure the control of temperature of battery packs of three given cars parameters and for three normalized driving cycles (WLTC, US06 and JAP15).

The presented work in this PhD gave rise to additional research opportunities concerning the following issues:

- The thermal and electrical parameterization performed on the prismatic 60Ah battery could be carried out on the other tested batteries in this work which will enable the validation of the numerical model for different batteries capacities and geometries.
- The proposed correlations enabling the determination of the maximum temperature rise and heat energy generation should be extended to several commercialized batteries data to rise its validation domain.
- The efficiency of proposed cooling system may be investigated experimentally and numerically for different climate conditions.

References

[1] IEA, “Tracking Transport 2020.” https://www.iea.org/reports/tracking-transport-2020.

[2] S. F. Tie and C. W. Tan, “A review of energy sources and energy management system in electric vehicles,” *Renewable and Sustainable Energy Reviews*, vol. 20. 2013, doi: 10.1016/j.rser.2012.11.077.

[3] S. Panchal, M. Haji Akhoundzadehr, K. Raahemifar, M. Fowler, and R. Fraser, “Heat and mass transfer modeling and investigation of multiple LiFePO4/graphite batteries in a pack at low C-rates with water-cooling,” *Int. J. Heat Mass Transf.*, vol. 135, pp. 368–377, Jun. 2019, doi: 10.1016/j.ijheatmasstransfer.2019.01.076.

[4] “Li-ion batteries: basics, progress, and challenges.”

[5] M. Xu, Z. Zhang, X. Wang, L. Jia, and L. Yang, “A pseudo three-dimensional electrochemical-thermal model of a prismatic LiFePO4 battery during discharge process,” *Energy*, vol. 80, pp. 303–317, Feb. 2015, doi: 10.1016/j.energy.2014.11.073.

[6] A. K. Thakur *et al.*, “A state of art review and future viewpoint on advance cooling techniques for Lithium–ion battery system of electric vehicles,” *J. Energy Storage*, vol. 32, p. 101771, Dec. 2020, doi: 10.1016/J.EST.2020.101771.

[7] Z. Wang, J. Ma, and L. Zhang, “Finite Element Thermal Model and Simulation for a Cylindrical Li-Ion Battery,” *IEEE Access*, vol. 5, pp. 15372–15379, 2017, doi: 10.1109/ACCESS.2017.2723436.

[8] M. Mastali *et al.*, “Electrochemical-thermal modeling and experimental validation of commercial graphite/LiFePO4 pouch lithium-ion batteries,” *Int. J. Therm. Sci.*, vol. 129, pp. 218–230, Jul. 2018, doi: 10.1016/J.IJTHERMALSCI.2018.03.004.

[9] J. Vetter *et al.*, “Ageing mechanisms in lithium-ion batteries,” *J. Power Sources*, vol. 147, no. 1–2, pp. 269–281, Sep. 2005, doi: 10.1016/J.JPOWSOUR.2005.01.006.

[10] S. Chacko and Y. M. Chung, “Thermal modelling of Li-ion polymer battery for electric vehicle drive cycles,” *J. Power Sources*, vol. 213, pp. 296–303, Sep. 2012, doi: 10.1016/J.JPOWSOUR.2012.04.015.

[11] F. Richter, S. Kjelstrup, P. J. S. Vie, and O. S. Burheim, “Thermal conductivity and internal temperature profiles of Li-ion secondary batteries,” *J. Power Sources*, vol. 359, pp. 592–600, Aug. 2017, doi: 10.1016/J.JPOWSOUR.2017.05.045.

[12] S. J. Drake, D. A. Wetz, J. K. Ostanek, S. P. Miller, J. M. Heinzel, and A. Jain, "Measurement of anisotropic thermophysical properties of cylindrical Li-ion cells," *J. Power Sources*, vol. 252, pp. 298–304, Apr. 2014, doi: 10.1016/J.JPOWSOUR.2013.11.107.

[13] J. Huang, P. Xu, and P. Wang, "Experimental measurement of anisotropic thermal conductivity of 18650 lithium battery," *J. Phys. Conf. Ser.*, vol. 1509, no. 1, pp. 0–8, 2020, doi: 10.1088/1742-6596/1509/1/012013.

[14] Y. Tang, T. Li, and X. Cheng, "Review of Specific Heat Capacity Determination of Lithium-Ion Battery," *Energy Procedia*, vol. 158, pp. 4967–4973, Feb. 2019, doi: 10.1016/J.EGYPRO.2019.01.671.

[15] C. Lin, S. Xu, Z. Li, B. Li, G. Chang, and J. Liu, "Thermal analysis of large-capacity LiFePO4 power batteries for electric vehicles," *J. Power Sources*, vol. 294, pp. 633–642, Oct. 2015, doi: 10.1016/J.JPOWSOUR.2015.06.129.

[16] J. Zhang *et al.*, "Comparison and validation of methods for estimating heat generation rate of large-format lithium-ion batteries," *J. Therm. Anal. Calorim.*, vol. 117, no. 1, pp. 447–461, 2014, doi: 10.1007/s10973-014-3672-z.

[17] K. Jalkanen, T. Aho, and K. Vuorilehto, "Entropy change effects on the thermal behavior of a LiFePO4/graphite lithium-ion cell at different states of charge," *J. Power Sources*, vol. 243, pp. 354–360, Dec. 2013, doi: 10.1016/J.JPOWSOUR.2013.05.199.

[18] L. Sheng, L. Su, H. Zhang, Y. Fang, H. Xu, and W. Ye, "An improved calorimetric method for characterizations of the specific heat and the heat generation rate in a prismatic lithium ion battery cell," *Energy Convers. Manag.*, vol. 180, pp. 724–732, Jan. 2019, doi: 10.1016/J.ENCONMAN.2018.11.030.

[19] D. Pan *et al.*, "Evaluating the accuracy of electro-thermal coupling model in lithium-ion battery via altering internal resistance acquisition methods," *J. Power Sources*, vol. 463, p. 228174, Jul. 2020, doi: 10.1016/J.JPOWSOUR.2020.228174.

[20] M. Akbarzadeh *et al.*, "Thermal modeling of a high-energy prismatic lithium-ion battery cell and module based on a new thermal characterization methodology," *J. Energy Storage*, vol. 32, p. 101707, Dec. 2020, doi: 10.1016/j.est.2020.101707.

[21] M. Toman, R. Cipin, P. Vorel, and D. Cervinka, "Dynamic Thermal Model for Cylindrical Battery Cell Temperature Modeling," *ECS Trans.*, vol. 95, no. 1, pp. 371–377, 2019, doi: 10.1149/09501.0371ecst.

[22] S. Dey *et al.*, "Model-based real-time thermal fault diagnosis of Lithium-ion batteries," *Control*

Eng. Pract., vol. 56, pp. 37–48, Nov. 2016, doi: 10.1016/j.conengprac.2016.08.002.

[23] C. Forgez, D. Vinh Do, G. Friedrich, M. Morcrette, and C. Delacourt, "Thermal modeling of a cylindrical LiFePO4/graphite lithium-ion battery," *J. Power Sources*, vol. 195, no. 9, pp. 2961–2968, May 2010, doi: 10.1016/j.jpowsour.2009.10.105.

[24] E. Paccha-Herrera, W. R. Calderón-Muñoz, M. Orchard, F. Jaramillo, and K. Medjaher, "Thermal modeling approaches for a licoo2 lithium-ion battery—a comparative study with experimental validation," *Batteries*, vol. 6, no. 3, pp. 1–23, 2020, doi: 10.3390/batteries6030040.

[25] J. Tian, Y. Wang, and Z. Chen, "Sensor fault diagnosis for lithium-ion battery packs based on thermal and electrical models," *Int. J. Electr. Power Energy Syst.*, vol. 121, no. April, p. 106087, 2020, doi: 10.1016/j.ijepes.2020.106087.

[26] K. Chen, S. Wang, M. Song, and L. Chen, "Configuration optimization of battery pack in parallel air-cooled battery thermal management system using an optimization strategy," *Appl. Therm. Eng.*, vol. 123, pp. 177–186, Aug. 2017, doi: 10.1016/j.applthermaleng.2017.05.060.

[27] K. Chen, M. Song, W. Wei, and S. Wang, "Design of the structure of battery pack in parallel air-cooled battery thermal management system for cooling efficiency improvement," *Int. J. Heat Mass Transf.*, vol. 132, pp. 309–321, Apr. 2019, doi: 10.1016/j.ijheatmasstransfer.2018.12.024.

[28] K. Chen, W. Wu, F. Yuan, L. Chen, and S. Wang, "Cooling efficiency improvement of air-cooled battery thermal management system through designing the flow pattern," *Energy*, vol. 167, pp. 781–790, Jan. 2019, doi: 10.1016/j.energy.2018.11.011.

[29] W. Li, M. Xiao, X. Peng, A. Garg, and L. Gao, "A surrogate thermal modeling and parametric optimization of battery pack with air cooling for EVs," *Appl. Therm. Eng.*, vol. 147, pp. 90–100, Jan. 2019, doi: 10.1016/j.applthermaleng.2018.10.060.

[30] N. Yang, X. Zhang, G. Li, and D. Hua, "Assessment of the forced air-cooling performance for cylindrical lithium-ion battery packs: A comparative analysis between aligned and staggered cell arrangements," *Appl. Therm. Eng.*, vol. 80, pp. 55–65, Apr. 2015, doi: 10.1016/j.applthermaleng.2015.01.049.

[31] X. Li, F. He, G. Zhang, Q. Huang, and D. Zhou, "Experiment and simulation for pouch battery with silica cooling plates and copper mesh based air cooling thermal management system," *Appl. Therm. Eng.*, vol. 146, pp. 866–880, Jan. 2019, doi: 10.1016/j.applthermaleng.2018.10.061.

[32] H. Sun and R. Dixon, "Development of cooling strategy for an air cooled lithium-ion battery pack," *J. Power Sources*, vol. 272, pp. 404–414, Dec. 2014, doi: 10.1016/j.jpowsour.2014.08.107.

[33] L. Fan, J. M. Khodadadi, and A. A. Pesaran, “A parametric study on thermal management of an air-cooled lithium-ion battery module for plug-in hybrid electric vehicles,” *J. Power Sources*, vol. 238, pp. 301–312, Sep. 2013, doi: 10.1016/j.jpowsour.2013.03.050.

[34] H. Park, “A design of air flow configuration for cooling lithium ion battery in hybrid electric vehicles,” *J. Power Sources*, vol. 239, pp. 30–36, Oct. 2013, doi: 10.1016/j.jpowsour.2013.03.102.

[35] E. Jiaqiang *et al.*, “Effects of the different air cooling strategies on cooling performance of a lithium-ion battery module with baffle,” *Appl. Therm. Eng.*, vol. 144, pp. 231–241, Nov. 2018, doi: 10.1016/j.applthermaleng.2018.08.064.

[36] J. Cen, Z. Li, and F. Jiang, “Experimental investigation on using the electric vehicle air conditioning system for lithium-ion battery thermal management,” *Energy Sustain. Dev.*, vol. 45, pp. 88–95, Aug. 2018, doi: 10.1016/j.esd.2018.05.005.

[37] M. R. Giuliano, A. K. Prasad, and S. G. Advani, “Experimental study of an air-cooled thermal management system for high capacity lithium-titanate batteries,” *J. Power Sources*, vol. 216, pp. 345–352, Oct. 2012, doi: 10.1016/j.jpowsour.2012.05.074.

[38] Y. W. Wang, J. M. Jiang, Y. H. Chung, W. C. Chen, and C. M. Shu, “Forced-air cooling system for large-scale lithium-ion battery modules during charge and discharge processes,” *J. Therm. Anal. Calorim.*, 2019, doi: 10.1007/s10973-018-7646-4.

[39] T. Yang, N. Yang, X. Zhang, and G. Li, “Investigation of the thermal performance of axial-flow air cooling for the lithium-ion battery pack,” *Int. J. Therm. Sci.*, vol. 108, pp. 132–144, Oct. 2016, doi: 10.1016/j.ijthermalsci.2016.05.009.

[40] M. Li, Y. Liu, X. Wang, and J. Zhang, “Modeling and optimization of an enhanced battery thermal management system in electric vehicles,” *Front. Mech. Eng.*, 2019, doi: 10.1007/s11465-018-0520-z.

[41] J. Xun, R. Liu, and K. Jiao, “Numerical and analytical modeling of lithium ion battery thermal behaviors with different cooling designs,” *J. Power Sources*, vol. 233, pp. 47–61, Jul. 2013, doi: 10.1016/j.jpowsour.2013.01.095.

[42] Z. Lu *et al.*, “Parametric study of forced air cooling strategy for lithium-ion battery pack with staggered arrangement,” *Appl. Therm. Eng.*, vol. 136, pp. 28–40, May 2018, doi: 10.1016/j.applthermaleng.2018.02.080.

[43] R. Mahamud and C. Park, “Reciprocating air flow for Li-ion battery thermal management to improve temperature uniformity,” *J. Power Sources*, vol. 196, no. 13, pp. 5685–5696, Jul. 2011, doi:

10.1016/j.jpowsour.2011.02.076.

[44] X. Na, H. Kang, T. Wang, and Y. Wang, “Reverse layered air flow for Li-ion battery thermal management,” *Appl. Therm. Eng.*, vol. 143, pp. 257–262, Oct. 2018, doi: 10.1016/j.applthermaleng.2018.07.080.

[45] J. Xie, Z. Ge, M. Zang, and S. Wang, “Structural optimization of lithium-ion battery pack with forced air cooling system,” *Appl. Therm. Eng.*, vol. 126, pp. 583–593, Nov. 2017, doi: 10.1016/j.applthermaleng.2017.07.143.

[46] K. Yu, X. Yang, Y. Cheng, and C. Li, “Thermal analysis and two-directional air flow thermal management for lithium-ion battery pack,” *J. Power Sources*, 2014, doi: 10.1016/j.jpowsour.2014.07.086.

[47] Y. Fan, Y. Bao, C. Ling, Y. Chu, X. Tan, and S. Yang, “Experimental study on the thermal management performance of air cooling for high energy density cylindrical lithium-ion batteries,” *Appl. Therm. Eng.*, vol. 155, pp. 96–109, Jun. 2019, doi: 10.1016/j.applthermaleng.2019.03.157.

[48] S. Shahid and M. Agelin-Chaab, “Development and analysis of a technique to improve air-cooling and temperature uniformity in a battery pack for cylindrical batteries,” *Therm. Sci. Eng. Prog.*, vol. 5, pp. 351–363, Mar. 2018, doi: 10.1016/j.tsep.2018.01.003.

[49] T. Wang, K. J. Tseng, J. Zhao, and Z. Wei, “Thermal investigation of lithium-ion battery module with different cell arrangement structures and forced air-cooling strategies,” *Appl. Energy*, vol. 134, pp. 229–238, Dec. 2014, doi: 10.1016/j.apenergy.2014.08.013.

[50] L. H. Saw, Y. Ye, A. A. O. Tay, W. T. Chong, S. H. Kuan, and M. C. Yew, “Computational fluid dynamic and thermal analysis of Lithium-ion battery pack with air cooling,” *Appl. Energy*, vol. 177, pp. 783–792, Sep. 2016, doi: 10.1016/j.apenergy.2016.05.122.

[51] K. Chen, M. Song, W. Wei, and S. Wang, “Structure optimization of parallel air-cooled battery thermal management system with U-type flow for cooling efficiency improvement,” *Energy*, vol. 145, pp. 603–613, Feb. 2018, doi: 10.1016/j.energy.2017.12.110.

[52] K. Chen, Y. Chen, Y. She, M. Song, S. Wang, and L. Chen, “Construction of effective symmetrical air-cooled system for battery thermal management,” *Appl. Therm. Eng.*, vol. 166, p. 114679, Feb. 2020, doi: 10.1016/j.applthermaleng.2019.114679.

[53] F. Arrangements, “Transient Thermal Analysis of a Li-Ion Battery,” 2020.

[54] J. Xu, C. Lan, Y. Qiao, and Y. Ma, “Prevent thermal runaway of lithium-ion batteries with

minichannel cooling," *Appl. Therm. Eng.*, vol. 110, pp. 883–890, Jan. 2017, doi: 10.1016/j.applthermaleng.2016.08.151.

[55] C. Lan, J. Xu, Y. Qiao, and Y. Ma, "Thermal management for high power lithium-ion battery by minichannel aluminum tubes," *Appl. Therm. Eng.*, vol. 101, pp. 284–292, May 2016, doi: 10.1016/j.applthermaleng.2016.02.070.

[56] Y. Huo, Z. Rao, X. Liu, and J. Zhao, "Investigation of power battery thermal management by using mini-channel cold plate," *Energy Convers. Manag.*, vol. 89, pp. 387–395, Jan. 2015, doi: 10.1016/j.enconman.2014.10.015.

[57] A. Jarrett and I. Y. Kim, "Influence of operating conditions on the optimum design of electric vehicle battery cooling plates," *J. Power Sources*, vol. 245, pp. 644–655, Jan. 2014, doi: 10.1016/j.jpowsour.2013.06.114.

[58] B. Ye, M. R. H. Rubel, and H. Li, "Design and optimization of cooling plate for battery module of an electric vehicle," *Appl. Sci.*, 2019, doi: 10.3390/app9040754.

[59] Z. An, L. Jia, X. Li, and Y. Ding, "Experimental investigation on lithium-ion battery thermal management based on flow boiling in mini-channel," *Appl. Therm. Eng.*, vol. 117, pp. 534–543, May 2017, doi: 10.1016/j.applthermaleng.2017.02.053.

[60] C. Wang *et al.*, "Liquid cooling based on thermal silica plate for battery thermal management system," *Int. J. Energy Res.*, 2017, doi: 10.1002/er.3801.

[61] Z. Shang, H. Qi, X. Liu, C. Ouyang, and Y. Wang, "Structural optimization of lithium-ion battery for improving thermal performance based on a liquid cooling system," *Int. J. Heat Mass Transf.*, vol. 130, pp. 33–41, Mar. 2019, doi: 10.1016/j.ijheatmasstransfer.2018.10.074.

[62] T. Deng, Y. Ran, G. Zhang, and Y. Yin, "Novel leaf-like channels for cooling rectangular lithium ion batteries," *Appl. Therm. Eng.*, vol. 150, pp. 1186–1196, Mar. 2019, doi: 10.1016/j.applthermaleng.2019.01.065.

[63] Z. Rao, Z. Qian, Y. Kuang, and Y. Li, "Thermal performance of liquid cooling based thermal management system for cylindrical lithium-ion battery module with variable contact surface," *Appl. Therm. Eng.*, vol. 123, pp. 1514–1522, 2017, doi: 10.1016/j.applthermaleng.2017.06.059.

[64] S. Panchal, R. Khasow, I. Dincer, M. Agelin-chaab, R. Fraser, and M. Fowler, "Thermal design and simulation of mini-channel cold plate for water cooled large sized prismatic lithium-ion battery," *Appl. Therm. Eng.*, vol. 122, pp. 80–90, 2017, doi: 10.1016/j.applthermaleng.2017.05.010.

[65] H. Zhou, F. Zhou, Q. Zhang, Q. Wang, and Z. Song, “Thermal management of cylindrical lithium-ion battery based on a liquid cooling method with half-helical duct,” *Appl. Therm. Eng.*, vol. 162, no. July, p. 114257, 2019, doi: 10.1016/j.applthermaleng.2019.114257.

[66] M. Al-zareer, I. Dincer, and M. A. Rosen, “Comparative assessment of new liquid-to-vapor type battery cooling systems,” *Energy*, vol. 188, p. 116010, 2019, doi: 10.1016/j.energy.2019.116010.

[67] Y. Wang, G. Zhang, and X. Yang, “Optimization of liquid cooling technology for cylindrical power battery module,” *Appl. Therm. Eng.*, vol. 162, p. 114200, Nov. 2019, doi: 10.1016/j.applthermaleng.2019.114200.

[68] H. Wang, T. Tao, J. Xu, X. Mei, X. Liu, and P. Gou, “Cooling capacity of a novel modular liquid-cooled battery thermal management system for cylindrical lithium ion batteries,” *Appl. Therm. Eng.*, vol. 178, no. February, p. 115591, 2020, doi: 10.1016/j.applthermaleng.2020.115591.

[69] Z. Zhu, X. Wu, H. Zhang, Y. Guo, and G. Wu, “International Journal of Heat and Mass Transfer Multi-objective optimization of a liquid cooled battery module with collaborative heat dissipation in both axial and radial directions,” *Int. J. Heat Mass Transf.*, vol. 155, p. 119701, 2020, doi: 10.1016/j.ijheatmasstransfer.2020.119701.

[70] Y. Huang, S. Wang, Y. Lu, R. Huang, and X. Yu, “Study on a liquid cooled battery thermal management system pertaining to the transient regime,” *Appl. Therm. Eng.*, vol. 180, no. April, p. 115793, 2020, doi: 10.1016/j.applthermaleng.2020.115793.

[71] N. Javani, I. Dincer, G. F. Naterer, and G. L. Rohrauer, “Modeling of passive thermal management for electric vehicle battery packs with PCM between cells,” *Appl. Therm. Eng.*, vol. 73, no. 1, pp. 307–316, Dec. 2014, doi: 10.1016/j.applthermaleng.2014.07.037.

[72] W. Q. Li, Z. G. Qu, Y. L. He, and Y. B. Tao, “Experimental study of a passive thermal management system for high-powered lithium ion batteries using porous metal foam saturated with phase change materials,” *J. Power Sources*, vol. 255, pp. 9–15, Jun. 2014, doi: 10.1016/j.jpowsour.2014.01.006.

[73] S. A. Khateeb, S. Amiruddin, M. Farid, J. R. Selman, and S. Al-Hallaj, “Thermal management of Li-ion battery with phase change material for electric scooters: Experimental validation,” *J. Power Sources*, vol. 142, no. 1–2, pp. 345–353, Mar. 2005, doi: 10.1016/j.jpowsour.2004.09.033.

[74] A. Babapoor, M. Azizi, and G. Karimi, “Thermal management of a Li-ion battery using carbon fiber-PCM composites,” *Appl. Therm. Eng.*, vol. 82, pp. 281–290, May 2015, doi: 10.1016/j.applthermaleng.2015.02.068.

[75] Y. Azizi and S. M. Sadrameli, “Thermal management of a LiFePO4 battery pack at high temperature environment using a composite of phase change materials and aluminum wire mesh plates,” *Energy Convers. Manag.*, vol. 128, pp. 294–302, Nov. 2016, doi: 10.1016/j.enconman.2016.09.081.

[76] G. Jiang, J. Huang, Y. Fu, M. Cao, and M. Liu, “Thermal optimization of composite phase change material/expanded graphite for Li-ion battery thermal management,” *Appl. Therm. Eng.*, vol. 108, pp. 1119–1125, Sep. 2016, doi: 10.1016/j.applthermaleng.2016.07.197.

[77] Y. Lv, X. Yang, X. Li, G. Zhang, Z. Wang, and C. Yang, “Experimental study on a novel battery thermal management technology based on low density polyethylene-enhanced composite phase change materials coupled with low fins,” *Appl. Energy*, vol. 178, pp. 376–382, Sep. 2016, doi: 10.1016/j.apenergy.2016.06.058.

[78] J. Yan, K. Li, H. Chen, Q. Wang, and J. Sun, “Experimental study on the application of phase change material in the dynamic cycling of battery pack system,” *Energy Convers. Manag.*, vol. 128, pp. 12–19, Nov. 2016, doi: 10.1016/j.enconman.2016.09.058.

[79] P. Ping, R. Peng, D. Kong, G. Chen, and J. Wen, “Investigation on thermal management performance of PCM-fin structure for Li-ion battery module in high-temperature environment,” *Energy Convers. Manag.*, vol. 176, pp. 131–146, Nov. 2018, doi: 10.1016/j.enconman.2018.09.025.

[80] W. Wang, X. Zhang, C. Xin, and Z. Rao, “An experimental study on thermal management of lithium ion battery packs using an improved passive method,” *Appl. Therm. Eng.*, vol. 134, pp. 163–170, Apr. 2018, doi: 10.1016/j.applthermaleng.2018.02.011.

[81] Z. Ling, X. Wen, Z. Zhang, X. Fang, and X. Gao, “Thermal management performance of phase change materials with different thermal conductivities for Li-ion battery packs operated at low temperatures,” *Energy*, vol. 144, pp. 977–983, Feb. 2018, doi: 10.1016/j.energy.2017.12.098.

[82] A. Hussain, I. H. Abidi, C. Y. Tso, K. C. Chan, Z. Luo, and C. Y. H. Chao, “Thermal management of lithium ion batteries using graphene coated nickel foam saturated with phase change materials,” *Int. J. Therm. Sci.*, vol. 124, pp. 23–35, Feb. 2018, doi: 10.1016/j.ijthermalsci.2017.09.019.

[83] D. Zou *et al.*, “Preparation of a novel composite phase change material (PCM) and its locally enhanced heat transfer for power battery module,” *Energy Convers. Manag.*, vol. 180, pp. 1196–1202, Jan. 2019, doi: 10.1016/j.enconman.2018.11.064.

[84] Y. H. Huang, W. L. Cheng, and R. Zhao, “Thermal management of Li-ion battery pack with the application of flexible form-stable composite phase change materials,” *Energy Convers. Manag.*, vol. 182, pp. 9–20, Feb. 2019, doi: 10.1016/j.enconman.2018.12.064.

[85] M. Nofal, S. Al-Hallaj, and Y. Pan, “Thermal management of lithium-ion battery cells using 3D printed phase change composites,” *Appl. Therm. Eng.*, vol. 171, p. 115126, May 2020, doi: 10.1016/j.applthermaleng.2020.115126.

[86] W. H. Zhu, H. Yang, K. Webb, T. Barron, P. Dimick, and B. J. Tatarchuk, “A novel cooling structure with a matrix block of microfibrous media / phase change materials for heat transfer enhancement in high power Li-ion battery packs,” *J. Clean. Prod.*, vol. 210, pp. 542–551, Feb. 2019, doi: 10.1016/j.jclepro.2018.11.043.

[87] S. Arora, A. Kapoor, and W. Shen, “A novel thermal management system for improving discharge/charge performance of Li-ion battery packs under abuse,” *J. Power Sources*, vol. 378, pp. 759–775, Feb. 2018, doi: 10.1016/j.jpowsour.2017.12.030.

[88] F. F. Liu, F. C. Lan, J. Q. Chen, and Y. G. Li, “Experimental investigation on cooling/heating characteristics of ultra-thin micro heat pipe for electric vehicle battery thermal management,” *Chinese J. Mech. Eng. (English Ed.*, vol. 31, no. 3, Jun. 2018, doi: 10.1186/s10033-018-0255-0.

[89] Y. C. Weng, H. P. Cho, C. C. Chang, and S. L. Chen, “Heat pipe with PCM for electronic cooling,” *Appl. Energy*, vol. 88, no. 5, pp. 1825–1833, May 2011, doi: 10.1016/j.apenergy.2010.12.004.

[90] Z. Rao, S. Wang, M. Wu, Z. Lin, and F. Li, “Experimental investigation on thermal management of electric vehicle battery with heat pipe,” *Energy Convers. Manag.*, vol. 65, pp. 92–97, Jan. 2013, doi: 10.1016/j.enconman.2012.08.014.

[91] A. Greco, D. Cao, X. Jiang, and H. Yang, “A theoretical and computational study of lithium-ion battery thermal management for electric vehicles using heat pipes,” *J. Power Sources*, vol. 257, pp. 344–355, Jul. 2014, doi: 10.1016/j.jpowsour.2014.02.004.

[92] Q. Wang *et al.*, “Experimental investigation on EV battery cooling and heating by heat pipes,” *Appl. Therm. Eng.*, vol. 88, pp. 54–60, Jun. 2014, doi: 10.1016/j.applthermaleng.2014.09.083.

[93] L. Batteries, “Heat Pipe Thermal Management Based on High-Rate,” 2019.

[94] T. H. Tran, S. Harmand, B. Desmet, and S. Filangi, “Experimental investigation on the feasibility of heat pipe cooling for HEV/EV lithium-ion battery,” *Appl. Therm. Eng.*, vol. 63, no. 2, pp. 551–558, Feb. 2014, doi: 10.1016/j.applthermaleng.2013.11.048.

[95] T. H. Tran, S. Harmand, and B. Sahut, “Experimental investigation on heat pipe cooling for Hybrid Electric Vehicle and Electric Vehicle lithium-ion battery,” *J. Power Sources*, vol. 265, pp. 262–272, Nov. 2014, doi: 10.1016/j.jpowsour.2014.04.130.

[96] Y. Ye, L. H. Saw, Y. Shi, and A. A. O. Tay, “Numerical analyses on optimizing a heat pipe thermal management system for lithium-ion batteries during fast charging,” *Appl. Therm. Eng.*, vol. 86, pp. 281–291, Jul. 2015, doi: 10.1016/j.applthermaleng.2015.04.066.

[97] H. Zou, W. Wang, G. Zhang, F. Qin, C. Tian, and Y. Yan, “Experimental investigation on an integrated thermal management system with heat pipe heat exchanger for electric vehicle,” *Energy Convers. Manag.*, vol. 118, pp. 88–95, Jun. 2016, doi: 10.1016/j.enconman.2016.03.066.

[98] R. G. Chi, W. S. Chung, and S. H. Rhi, “Thermal characteristics of an oscillating heat pipe cooling system for electric vehicle Li-ion batteries,” *Energies*, 2018, doi: 10.3390/en11030655.

[99] J. Qu, C. Wang, X. Li, and H. Wang, “Heat transfer performance of flexible oscillating heat pipes for electric/hybrid-electric vehicle battery thermal management,” *Appl. Therm. Eng.*, vol. 135, pp. 1–9, May 2018, doi: 10.1016/j.applthermaleng.2018.02.045.

[100] L. Feng *et al.*, “Experimental investigation of thermal and strain management for lithium-ion battery pack in heat pipe cooling,” *J. Energy Storage*, vol. 16, pp. 84–92, Apr. 2018, doi: 10.1016/j.est.2018.01.001.

[101] R. Rizk, H. Louahlia, H. Gualous, and P. Schaetzel, “Passive cooling of high capacity lithium-ion batteries,” 2019, doi: 10.1109/INTLEC.2018.8612368.

[102] A. Wei, J. Qu, H. Qiu, C. Wang, and G. Cao, “Heat transfer characteristics of plug-in oscillating heat pipe with binary-fluid mixtures for electric vehicle battery thermal management,” *Int. J. Heat Mass Transf.*, vol. 135, pp. 746–760, Jun. 2019, doi: 10.1016/j.ijheatmasstransfer.2019.02.021.

[103] D. Chen, J. Jiang, G. H. Kim, C. Yang, and A. Pesaran, “Comparison of different cooling methods for lithium ion battery cells,” *Appl. Therm. Eng.*, vol. 94, pp. 846–854, Feb. 2016, doi: 10.1016/j.applthermaleng.2015.10.015.

[104] R. Zhao, J. Gu, and J. Liu, “An experimental study of heat pipe thermal management system with wet cooling method for lithium ion batteries,” *J. Power Sources*, vol. 273, pp. 1089–1097, Jan. 2015, doi: 10.1016/j.jpowsour.2014.10.007.

[105] Z. Ling, F. Wang, X. Fang, X. Gao, and Z. Zhang, “A hybrid thermal management system for lithium ion batteries combining phase change materials with forced-air cooling,” *Appl. Energy*, vol. 148, pp. 403–409, Jun. 2015, doi: 10.1016/j.apenergy.2015.03.080.

[106] W. Wu, X. Yang, G. Zhang, K. Chen, and S. Wang, “Experimental investigation on the thermal performance of heat pipe-assisted phase change material based battery thermal management system,” *Energy Convers. Manag.*, vol. 138, pp. 486–492, Apr. 2017, doi: 10.1016/j.enconman.2017.02.022.

[107] T. Yamada, T. Koshiyama, M. Yoshikawa, T. Yamada, and N. Ono, “Analysis of a lithium-ion battery cooling system for electric vehicles using a phase-change material and heat pipes,” *J. Therm. Sci. Technol.*, 2017, doi: 10.1299/jtst.2017jtst0011.

[108] J. Zhao, P. Lv, and Z. Rao, “Experimental study on the thermal management performance of phase change material coupled with heat pipe for cylindrical power battery pack,” *Exp. Therm. Fluid Sci.*, vol. 82, pp. 182–188, Apr. 2017, doi: 10.1016/j.expthermflusci.2016.11.017.

[109] Y. Wei and M. Agelin-Chaab, “Experimental investigation of a novel hybrid cooling method for lithium-ion batteries,” *Appl. Therm. Eng.*, vol. 136, pp. 375–387, May 2018, doi: 10.1016/j.applthermaleng.2018.03.024.

[110] Q. Huang, X. Li, G. Zhang, J. Zhang, F. He, and Y. Li, “Experimental investigation of the thermal performance of heat pipe assisted phase change material for battery thermal management system,” *Appl. Therm. Eng.*, vol. 141, pp. 1092–1100, Aug. 2018, doi: 10.1016/j.applthermaleng.2018.06.048.

[111] Z. Ling, J. Cao, W. Zhang, Z. Zhang, X. Fang, and X. Gao, “Compact liquid cooling strategy with phase change materials for Li-ion batteries optimized using response surface methodology,” *Appl. Energy*, vol. 228, pp. 777–788, Oct. 2018, doi: 10.1016/j.apenergy.2018.06.143.

[112] F. Bai *et al.*, “Investigation of thermal management for lithium-ion pouch battery module based on phase change slurry and mini channel cooling plate,” *Energy*, vol. 167, pp. 561–574, Jan. 2019, doi: 10.1016/j.energy.2018.10.137.

[113] J. Qu, Z. Ke, A. Zuo, and Z. Rao, “Experimental investigation on thermal performance of phase change material coupled with three-dimensional oscillating heat pipe (PCM/3D-OHP) for thermal management application,” *Int. J. Heat Mass Transf.*, vol. 129, pp. 773–782, Feb. 2019, doi: 10.1016/j.ijheatmasstransfer.2018.10.019.

[114] M. Mashayekhi, E. Houshfar, and M. Ashjaee, “Development of hybrid cooling method with PCM and Al 2 O 3 nanofluid in aluminium minichannels using heat source model of Li-ion batteries,” *Appl. Therm. Eng.*, vol. 178, no. January, p. 115543, 2020, doi: 10.1016/j.applthermaleng.2020.115543.

[115] H. Behi, D. Karimi, M. Behi, and M. Ghanbarpour, “A new concept of thermal management system in Li-ion battery using air cooling and heat pipe for electric vehicles,” *Appl. Therm. Eng.*, vol. 174, no. November 2019, p. 115280, 2020, doi: 10.1016/j.applthermaleng.2020.115280.

[116] M. Mahdi, S. Mousavi, and M. Siavashi, “Battery thermal management with thermal energy storage composites of PCM , metal foam , fin and nanoparticle,” *J. Energy Storage*, vol. 28, no.

December 2019, p. 101235, 2020, doi: 10.1016/j.est.2020.101235.

[117] D. Kong, R. Peng, P. Ping, J. Du, G. Chen, and J. Wen, “A novel battery thermal management system coupling with PCM and optimized controllable liquid cooling for di ff erent ambient temperatures,” *Energy Convers. Manag.*, vol. 204, no. November 2019, p. 112280, 2020, doi: 10.1016/j.enconman.2019.112280.

[118] M. Kiani, S. Omiddezyani, E. Houshfar, S. Rahman, M. Ashjaee, and A. Mahdavi, “Lithium-ion battery thermal management system with Al 2 O 3 / AgO / CuO nano fl uids and phase change material,” *Appl. Therm. Eng.*, vol. 180, no. February, p. 115840, 2020, doi: 10.1016/j.applthermaleng.2020.115840.

[119] D. Dan, C. Yao, Y. Zhang, H. Zhang, Z. Zeng, and X. Xu, “Dynamic thermal behavior of micro heat pipe array-air cooling battery thermal management system based on thermal network model,” *Appl. Therm. Eng.*, vol. 162, Nov. 2019, doi: 10.1016/j.applthermaleng.2019.114183.

[120] Y. Gan, J. Wang, J. Liang, Z. Huang, and M. Hu, “Development of thermal equivalent circuit model of heat pipe-based thermal management system for a battery module with cylindrical cells,” *Appl. Therm. Eng.*, vol. 164, Jan. 2020, doi: 10.1016/j.applthermaleng.2019.114523.

[121] S. K. Mohammadian, Y. L. He, and Y. Zhang, “Internal cooling of a lithium-ion battery using electrolyte as coolant through microchannels embedded inside the electrodes,” *J. Power Sources*, vol. 293, pp. 458–466, Jun. 2015, doi: 10.1016/j.jpowsour.2015.05.055.

[122] K. Shah, C. McKee, D. Chalise, and A. Jain, “Experimental and numerical investigation of core cooling of Li-ion cells using heat pipes,” *Energy*, vol. 113, pp. 852–860, Oct. 2016, doi: 10.1016/j.energy.2016.07.076.

[123] R. Zhao, J. Gu, and J. Liu, “Optimization of a phase change material based internal cooling system for cylindrical Li-ion battery pack and a hybrid cooling design,” *Energy*, vol. 135, pp. 811–822, Sep. 2017, doi: 10.1016/j.energy.2017.06.168.

[124] J. Gou, W. Liu, and Y. Luo, “The thermal performance of a novel internal cooling method for the electric vehicle battery: An experimental study,” *Appl. Therm. Eng.*, vol. 161, p. 114102, Oct. 2019, doi: 10.1016/j.applthermaleng.2019.114102.

[125] C. Zhu, X. Li, L. Song, and L. Xiang, “Development of a theoretically based thermal model for lithium ion battery pack,” *J. Power Sources*, vol. 223, 2013, doi: 10.1016/j.jpowsour.2012.09.035.

[126] W.-Y. Chang, “The State of Charge Estimating Methods for Battery: A Review,” *ISRN Appl. Math.*, vol. 2013, no. 1, pp. 1–7, 2013, doi: 10.1155/2013/953792.

[127] A. Samba *et al.*, “Development of an advanced two-dimensional thermal model for large size lithium-ion pouch cells,” *Electrochim. Acta*, vol. 117, pp. 246–254, Jan. 2014, doi: 10.1016/j.electacta.2013.11.113.

[128] S. Goutam, J. M. Timmermans, N. Omar, P. Van den Bossche, and J. Van Mierlo, “Comparative study of surface temperature behavior of commercial li-ion pouch cells of different chemistries and capacities by infrared thermography,” *Energies*, vol. 8, no. 8, pp. 8175–8192, 2015, doi: 10.3390/en8088175.

[129] D. H. Jeon and S. M. Baek, “Thermal modeling of cylindrical lithium ion battery during discharge cycle,” *Energy Convers. Manag.*, vol. 52, no. 8–9, pp. 2973–2981, Aug. 2011, doi: 10.1016/J.ENCONMAN.2011.04.013.

[130] K. E. Thomas and J. Newman, “Heats of mixing and of entropy in porous insertion electrodes,” *J. Power Sources*, vol. 119–121, pp. 844–849, Jun. 2003, doi: 10.1016/S0378-7753(03)00283-0.

[131] S. Panchal, I. Dincer, M. Agelin-Chaab, R. Fraser, and M. Fowler, “Experimental and theoretical investigation of temperature distributions in a prismatic lithium-ion battery,” *Int. J. Therm. Sci.*, vol. 99, 2016, doi: 10.1016/j.ijthermalsci.2015.08.016.

[132] C. Lin, S. Xu, and J. Liu, “Measurement of heat generation in a 40 Ah LiFePO4 prismatic battery using accelerating rate calorimetry,” *Int. J. Hydrogen Energy*, 2018, doi: 10.1016/j.ijhydene.2018.03.057.

[133] D. Bernardi, E. Pawlikowski, and J. Newman, “Bernardi1985,” vol. 132, no. 1, 1970.

[134] A. M. Society, “Stability and Convergence of the Peaceman-Rachford ADI Method for Initial-Boundary Value Problems Author (s): W . H . Hundsdorfer and J . G . Verwer Published by : American Mathematical Society Stable URL : https://www.jstor.org/stable/2008350 REFERENCE,” vol. 53, no. 187, pp. 81–101, 1989.

[135] S. C. Chen, C. C. Wan, and Y. Y. Wang, “Thermal analysis of lithium-ion batteries,” *J. Power Sources*, vol. 140, no. 1, pp. 111–124, 2005, doi: 10.1016/j.jpowsour.2004.05.064.

[136] R. Rizk, H. Louahlia, H. Gualous, and P. Schaetzel, “Experimental analysis and transient thermal modelling of a high capacity prismatic lithium-ion battery,” *Int. Commun. Heat Mass Transf.*, 2018, doi: 10.1016/j.icheatmasstransfer.2018.03.018.

[137] T. Inl, “Battery Test Manual for Plug-In Hybrid Electric Vehicles,” *Contract*, vol. 158, no. March, pp. 1720–1723, 2010, [Online]. Available: http://www.inl.gov/technicalpublications/Documents/3952791.pdf.

[138] E. Schuster, C. Ziebert, A. Melcher, M. Rohde, and H. J. Seifert, “Thermal behavior and electrochemical heat generation in a commercial 40 Ah lithium ion pouch cell,” *J. Power Sources*, 2015, doi: 10.1016/j.jpowsour.2015.03.170.

[139] F. Geifes, C. Bolsinger, P. Mielcarek, and K. Peter, “Determination of the entropic heat coe ffi cient in a simple electro-thermal lithium-ion cell model with pulse relaxation measurements and least squares algorithm,” *J. Power Sources*, vol. 419, no. November 2018, pp. 148–154, 2019, doi: 10.1016/j.jpowsour.2019.02.072.

[140] X. Wu, Z. Chen, and Z. Wang, “Analysis of low temperature preheating effect based on battery temperature-rise model,” *Energies*, vol. 10, no. 8, 2017, doi: 10.3390/en10081121.

[141] S. J. Bazinski and X. Wang, “The Influence of Cell Temperature on the Entropic Coefficient of a Lithium Iron Phosphate (LFP) Pouch Cell,” *J. Electrochem. Soc.*, vol. 161, no. 1, pp. A168–A175, 2014, doi: 10.1149/2.082401jes.

[142] G. Zheng, W. Zhang, and X. Huang, “Lithium-Ion Battery Electrochemical-Thermal Model Using Various Materials as Cathode Material: A Simulation Study,” *ChemistrySelect*, vol. 3, no. 41, pp. 11573–11578, 2018, doi: 10.1002/slct.201802556.

[143] A. A. Pesaran, M. Keyser, G. Kim, S. Santhanagopalan, and K. Smith, “Tools for Designing Thermal Management of Batteries in Electric Drive Vehicles Battery Temperature in xEVs,” *Adv. Automot. Batter. Conf.*, 2013.

[144] S. Goutam *et al.*, “Three-dimensional electro-thermal model of li-ion pouch cell: Analysis and comparison of cell design factors and model assumptions,” *Appl. Therm. Eng.*, vol. 126, pp. 796–808, Nov. 2017, doi: 10.1016/J.APPLTHERMALENG.2017.07.206.